

https://dspace.org/

The development of whisker and cubic boron nitride reinforced titanium carbide ceramic matrix composites

Petersen, Shaheeda

2024
https://hdl.handle.net/10539/37369

Downloaded from a DSpace repository. https://dspace.org/



The Development of Whisker and Cubic Boron Nitride Reinforced Titanium Carbide Ceramic Matrix Composites

A Thesis submitted in fulfilment of the requirements of the degree of Master of Science in Metallurgy and Materials Engineering

Prepared by

Shaheeda Petersen (693270)

Submitted to

School of Chemical and Metallurgical Engineering, Faculty of Engineering and the Built Environment, University of the Witwatersrand, Johannesburg, South Africa

Supervisor: Professor I. Sigalas

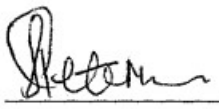
March, 2023

DECLARATION

PLAGIARISM DECLARATION

I, Shaheeda Petersen (Student number: 693270) am a student registered for MSc. Engineering in Metallurgy and Materials in the year 2023. I hereby declare the following:

- I am aware that plagiarism (the use of someone else's work without their permission and/or without acknowledging the original source) is wrong.
- I confirm that the work submitted for assessment for the above course is my own unaided work except where I have explicitly indicated otherwise.
- I have followed the required conventions in referencing the thoughts and ideas of others.
- I understand that the University of the Witwatersrand may take disciplinary action against me if there is a belief that this was not my own unaided work or that I have failed to acknowledge the source of the ideas or words in my writing.

Signature:  Date: 20 March 2023

ABSTRACT

TiC as the matrix in ceramic matrix composites (CMC's) is limited due to its poor fracture toughness. In order to increase their use in interrupted cutting applications, it is necessary to improve their fracture toughness and hardness. The purpose of this study was to improve the fracture toughness of TiC without causing a decrease in its other mechanical properties by adding SiC whiskers to the starting TiC powder before Spark Plasma Sintering (SPS). To improve the hardness cBN was also added as a secondary hard phase prior to sintering. The reinforced powders where then sintered at temperatures between 1550°C and 1650°C, under pressures of 50-70 MPa and hold times between 5-20 minutes. The resulting materials were then characterized by density, hardness, fracture toughness, biaxial strength, sliding wear testing and scanning electron microscopy.

Analysis of the hardness and fracture toughness of the sintered TiC matrix compacts with/without SiO_2 concluded that the sintered sample with the highest hardness was found to be 90TiC-8Al_2O_3-2Y_2O_3 SPS'd at 1625°C, 70MPa and the sintered sample with the highest fracture toughness was determined to be 90TiC-8Al_2O_3-2Y_2O_3 SPS'd at 1625°C, 50MPa. From the XRD results we observed that the SPS material with the highest fracture toughness had formed YAP instead of YAG during sintering.

The 77.8TiC-6.9Al_2O_3-1.7Y_2O_3-14 (20 vol.%) SiCw composition had the greatest ultimate fracture strength of 152.67 GPa and a Weibull modulus of 26.973 which is higher than unreinforced engineering ceramics but similar to other CMC's reinforced with ceramic fibres. Out of all the compositions tested the 78.6TiC-3.5Al_2O_3-5.6Y_2O_3-4.9SiO_2-7.5 (10 vol.%) cBN removed the most material and had the lowest frictional coefficient making it suitable for use as a cutting blade.

ACKNOWLEDGMENTS

This research was made possible by the financial support of Element Six Production (Pty) Limited, South Africa and the Department of Science and Technology/ National Research Foundation: Centre of Excellence in Strong Materials, South Africa.

I would like to express my sincere gratitude to my academic supervisor Prof Iakovos Sigalas, School of Chemical and Metallurgical Engineering, University of the Witwatersrand, Johannesburg, South Africa and my research advisor Dr Mathias Herrmann, IKTS Fraunhofer Institute for Ceramic Technology and Systems, Dresden, Germany for their continuous support, motivation and immense knowledge. I would also like to thank the academic staff, technical staff and my fellow postgraduate students at the School of Chemical and Metallurgical Engineering, University of the Witwatersrand for their assistance, guidance and encouragement during the duration of my research and beyond.

I am eternally grateful for the emotional support and encouragement I have received from my colleagues and management at the Department of Mechanical Engineering, Cape Peninsula University of Technology and also the Mellon Mays Undergraduate Fellowship program for their guidance throughout the early stages of my academic undertakings until now.

And last, but not least I would like to thank my family for their unparalleled emotional, financial and spiritual support during my academic journey. I am immeasurably grateful to you all.

TABLE OF CONTENTS

Declaration ii

Abstract iii

Acknowledgments iv

List of figures xii

List of tables xix

1. INTRODUCTION 1

1.1 Subject of the thesis 1

1.2 Background to the thesis 1

1.3 Problem Statement 2

1.4 Objectives of the thesis 3

1.5 Plan of development 4

2. LITERATURE REVIEW 5

2.1 Titanium Carbide 5

2.1.1 Background 5

2.1.2 Structure of TiC 5

2.1.3 Properties of TiC 6

2.1.4 Sintering TiC 6

2.1.5 Liquid phase sintering aids 7

2.1.6 Sintering TiC with liquid phase sintering aids 8

2.1.7 Interaction between TiC and SiC 9

2.1.8 Interaction of SiO_2 and liquid phase sintering aids 9

2.1.9 Interaction between SiC and liquid phase sintering aids 9

2.1.10 Interaction between TiC and Cubic Boron Nitride (cBN) 10
2.1.11 Interaction between cBN and liquid phase sintering aids (SiO_2) 10
2.2 Whisker reinforcement of ceramics 11
2.2.1 Processing of whisker reinforced ceramics 11
2.2.2 Whisker/powder mixing 11
2.2.3 Whisker toughening in ceramic materials 11
2.2.4 Proposed toughening mechanisms for whisker reinforced CMC's 12
2.3 Sintering and densification of ceramics 15
2.3.1 Spark Plasma Sintering (SPS) 15
2.4 Reinforcement materials 15
2.4.1 Silicon Carbide Whiskers (SiC_w) 15
2.4.2 Boron Nitride 17
2.5 Fracture in ceramics 19
2.5.1 Contact failure 19
2.5.2 Ball on three balls (B3B) biaxial strength testing 20
2.6 Wear by hard particles 21
2.6.1 Models for abrasive wear 22
2.6.2 Types of physical interactions that occur during abrasive wear 25
2.6.3 Factors that affect abrasive wear 26
2.6.4 Testing methods for abrasive wear 28
2.6.5 Effect of secondary phases on abrasive wear 29
3. METHODOLOGY 30
3.1 Experimental Approach 30
3.2 Materials used and their characterization 31
3.2.1 Scanning Electron Microscopy of Reinforcement Materials 31

3.3 Experimental Apparatus 32
3.3.1 Planetary ball mill 33
3.3.2 Attritor mill 33
3.3.3 Turbula mixer 34
3.3.4 Spark plasma sintering (SPS) machine 34
3.3.5 Materialography (Sample preparation) equipment 35
3.3.6 X-ray Diffractometry (XRD) 35
3.3.7 Scanning Electron miscroscopy (SEM) and Energy Dispersive Spectroscopy (EDX) 35
3.4 Powder processing 36
3.4.1 Preparation of matrix powders 36
3.4.2 Preparation of reinforced matrix powders 36
3.5 Analysis of sintered samples 38
3.5.1 Density Measurements 38
3.5.2 Vickers Hardness Testing 39
3.5.3 B3B Biaxial strength testing ..... Error! Bookmark not defined.
3.5.4 Sliding wear testing 41
4. Analysis of unreinforced TiC with Al_2O_3, Y_2O_3 AND SiO_2 sINTERING AIDS 43
4.1 Particle size analysis of TiC, liquid phase sintering aids and reinforcement material 43
4.2 Analysis of the TiC Matrix powders 44
4.2.1 XRD results of Milled TiC matrix powders with/without SiO_2 44
4.2.2 SEM analysis of the TiC Matrix powders 45
4.3 SPS Sintering of TiC matrix powders 46
4.3.1 Theoretical densities of TiC powder mixes without SiO_2 46
4.3.2 Theoretical densities of TiC powder mixes with the addition of Al_2O_3, Y_2O_3 and SiO_2 46
4.3.3 SPS sintering parameters for TiC mixes without SiO_2 46

4.3.4 SPS sintering parameters for TiC mixes with the addition of SiO_2 48

4.3.5 Percentage of theoretical density of TiC mix sintered samples with/without SiO_2 48

4.4 Phases identified by XRD measurements of SPS sintered samples 52

4.5 Microstructural Analysis 54

4.5.1 Scanning Electron Microscopy TiC mix sintered samples with/without SiO_2 54

4.5.2 Energy-dispersive X-ray spectroscopy on TiC mix sintered samples with/without SiO_2 54

4.6 Hardness and fracture toughness of sintered samples 57

5. Analysis of TiC based CMC's with SiC whisker or cBN particle reinforcement 59

5.1 Analysis of the TiC Matrix powders with/without SiO_2 and the addition of SiC whiskers and cBN respectively 59

5.1.1 Examples of typical XRD patterns XRD of milled TiC matrix powders with/without SiO_2 and the addition of SiC whiskers and cBN respectively 59

5.2 SPS Sintering of TiC matrix powders with/without SiO_2 and the addition of SiC whiskers and cBN 63

5.2.1 Theoretical density of TiC matrices with/without SiO_2 and the addition of SiC whiskers and cBN respectively 63

5.2.2 SEM analysis of TiC matrix powder samples with the addition of reinforcing materials 64

5.2.3 SPS sintering parameters for TiC mixes using TiC powder without SiO_2 and with the addition of cBN 65

5.2.4 SPS sintering parameters for TiC mixes using TiC powder with SiO_2 and with the addition of cBN 65

5.2.5 SPS sintering parameters for TiC mixes using 2µm TiC powder without SiO_2 and with the addition of SiC whiskers 65

5.2.6 SPS sintering parameters for TiC mixes using TiC powder with SiO_2 and with the addition of SiC whiskers 65

5.3 Density of SPS sintered samples 66

5.3.1 Densities of TiC powder mixes without SiO_2 and with the addition of SiC whiskers 66

5.3.2 Densities of TiC powder mixes with SiO_2 and with the addition of SiC whiskers 69

5.3.3 Densities of TiC powder mixes with/without SiO_2 and with the addition of cBN 71

5.4 Phases identified by XRD measurements of SPS sintered samples 75

5.4.1 Phases identified by XRD analysis of SPS'd samples of TiC + SiCw with the highest percentage theoretical density 75

5.4.2 Phases identified by XRD analysis of SPS'd samples of TiC + cBN with the highest percentage theoretical density 79

5.5 Microstructural Analysis by SEM 82

5.5.1 SEM analysis of SPS sintered samples with 85 wt. % TiC, liquid phase sintering aids (Al_2O_3-Y_2O_3) and SiC whiskers of various compositions and sintering parameters 82

5.5.2 SEM analysis of SPS sintered samples with 85 wt. % TiC, liquid phase sintering aids (Al_2O_3-Y_2O_3-SiO_2) and SiC whiskers of various compositions and sintering parameters 83

5.5.3 SEM analysis of SPS sintered samples with 90 wt. % TiC, liquid phase sintering aids (Al_2O_3-Y_2O_3) and SiC whiskers of various compositions and sintering parameters 84

5.5.4 SEM analysis of SPS sintered samples with 90 wt. % TiC, liquid phase sintering aids (Al_2O_3-Y_2O_3-SiO_2) and SiC whiskers of various compositions and sintering 84

5.5.5 SEM analysis of SPS sintered samples with 85 wt. % TiC, liquid phase sintering aids (Al_2O_3-Y_2O_3-SiO_2) and cBN of various compositions and sintering parameters 85

5.5.6 SEM analysis of SPS sintered samples with 90 wt. % TiC, liquid phase sintering aids (Al_2O_3-Y_2O_3-SiO_2) and cBN of various compositions and sintering 86

5.6 Hardness and fracture toughness 88

5.6.1 Hardness and fracture toughness of SPS sintered samples with 85 wt.% TiC, liquid phase sintering aids and SiC whiskers with the highest density 88

5.6.2 Hardness and fracture toughness of SPS sintered samples with 85 wt.% TiC, liquid phase sintering aids and cBN with the highest density 90

5.6.3 Hardness and fracture toughness of SPS sintered samples with 90 wt.% TiC, liquid phase sintering aids and SiC whiskers with the highest density 91

5.6.4 Hardness and fracture toughness of SPS sintered samples with 90 wt.% TiC, liquid phase sintering aids and cBN with the highest density 92

6. Biaxial strength testing using Ball on 3 Ball testing 94

6.1 Analysis of the flexural strength tests of sintered TiC samples with the best combination of density and fracture toughness. 94

6.1.1 85TiC-12Al_2O_3-3Y_2O_3 SPS'd at 1610°C, 70MPa and 10 min hold 96

6.1.2 79TiC-11Al_2O_3-3Y_2O_3-7(10 vol.%) SiCw SPS'd at 1600°C, 70MPa and 10 min hold 98

6.1.3 73TiC-10Al_2O_3-3Y_2O_3-14(20 vol.%) SiCw SPS'd at 1625°C, 70MPa and 10 min hold 100

6.1.4 79TiC-4.5Al_2O_3-5.6Y_2O_3-4.9SiO_2-7.1(10 vol.%) SiCw SPS'd at 1600°C, 70MPa and 10 min hold 102

6.1.5 78.6TiC-3.5Al_2O_3-5.6Y_2O_3-4.9SiO_2-7.5 (10 vol.%) cBN SPS'd at 1575°C, 70MPa and 5 min hold 105

6.1.6 77.8TiC-6.9Al_2O_3-1.7Y_2O_3-14(20 vol.%) SiCw SPS'd at 1625°C, 70MPa and 20 min hold 107

6.1.7 Comparison of the Weibull moduli of sintered TiC with various liquid phase sintering aids and with/without the addition of reinforcement materials 110

7. Ball on Disc sliding wear testing 112

7.1 85TiC-12Al_2O_3-3Y_2O_3 SPS'd at 1610°C, 70MPa and 10 min hold 113

7.2 79TiC-11Al_2O_3-3Y_2O_3-7(10 vol.%) SiCw SPS'd at 1600°C, 70MPa and 10 min hold 116

7.3 73TiC-10Al_2O_3-3Y_2O_3-14(20 vol.%) SiCw SPS'd at 1625°C, 70MPa and 10 min hold 119

7.4 79TiC-4.5Al_2O_3-5.6Y_2O_3-4.9SiO_2-7.1(10 vol.%) SiCw SPS'd at 1600°C, 70MPa and 10 min hold 122

7.5 78.6TiC-3.5Al_2O_3-5.6Y_2O_3-4.9SiO_2-7.5 (10 vol.%) cBN SPS'd at 1575°C, 70MPa and 5 min hold 125

7.6 77.8TiC-6.9Al_2O_3-1.7Y_2O_3-14 (20 vol.%) SiCw SPS'd at 1625°C, 70MPa and 20 min hold 128

7.7 Mass lost on ball bearing during wear testing 131

7.8 Friction and sliding wear results from CSM Tribometer 132

8 Conclusions and Recommendations 134

8.1 Conclusions 134

8.1.1 Results of the analysis of the TiC matrices with/without SiO_2 134

8.1.2 Results of the analysis of the TiC Matrices with/without SiO_2 and the addition of SiC whiskers and cBN respectively 135

8.1.3 Results of the analysis of the biaxial strength tests of sintered TiC samples with the best combination of density and fracture toughness. 137

8.1.4 Results of the analysis of the friction and sliding wear tests of sintered TiC samples with the best combination of density and fracture toughness. 138

8.2 Recommendations 139

Bibliography 140

Appendices 147

Appendix A – Theoretical Density calculations 147

Appendix B – SPS sintering parameters for TiC mixes without SiO_2 148

Appendix C – Preliminary Densification results of Sintered TiC mixes with Al_2O_3 and Y_2O_3 151

Appendix D – SPS sintering parameters for TiC mixes with the addition of SiO_2 152

Appendix E - SPS sintering parameters for TiC mixes using TiC powder without SiO_2 and with the addition of cBN 154

Appendix F - SPS sintering parameters for TiC mixes using TiC powder with SiO_2 and with the addition of cBN 156

Appendix G -SPS sintering parameters for TiC mixes using 2μm TiC powder without SiO_2 and with the addition of SiC whiskers 157

Appendix H -SPS sintering parameters for TiC mixes using TiC powder with SiO_2 and with the addition of SiC whiskers 158

LIST OF FIGURES

Figure 2.1 (a) Crystal structure of TiC and (b) Projection of Ti–C atoms along [111] direction 5

Figure 2.2 Displacement rate Vs temperature for powder processed with the initial pressure and densification mechanisms. 7

Figure 2.3 Alumina-Yttria phase diagram..... 7

Figure 2.4 Alumina-Yttria phase diagram of the Alumina rich portion of the Al_2O_3-Y_2O_3 system. The metastable phase diagram is superimposed with dashed lines and the phase fields are labelled 8

Figure 2.5 Phase relation in the ternary system SiC–Al_2O_3–Y_2O_3 at 1400°C..... 10

Figure 2.6 Typical processes occurring during crack propagation in whisker reinforced ceramics 13

Figure 2.7 Schematic representation of the spark plasma sintering apparatus 15

Figure 2.8 SEM images of Silicon Carbide whiskers..... 16

Figure 2.9 Crystal structures of Boron Nitride 17

Figure 2.10 SEM morphologies of cBN powders..... 18

Figure 2.11 Contact damage/cracks on the surface of ceramics: a) Hertzian ring crack in silicon nitride and b) crack caused in operation by the rolling of high alloyed steel wires. c) Radial cracks in the corners of a Vickers indent in silicon nitride and d) breakout due to lateral crackers under a Vickers indent in silicon carbide. ... 19

Figure 2.12-1 a) and b) Experimental setup of the B3B test: a) shows the set-up with applied pre-load b) the set up (with the guide lowered) just before the start of the fracture. 20

Figure 2.13 Graphs of wear loss by hard particles as a function of material properties and operating parameters a) hardness of the abrasive particle, b) ratio of hardness of the abrasive particle and hardness of the wearing material, c) abrasive particle size, normal load and impact velocity and d) impact angle without considering lubrication. 21

Figure 2.14 Geometry of contact between an idealised conical abrasive particle and a surface: (a) in elevation; (b) in the plane view 22

Figure 2.15 Diagram showing crack formation in a brittle material due to point indentation. The normal load increases from (a) to (c), and is then progressively reduced from (d) to (f) 23

Figure 2.16 Schematic representation of different interactions between sliding abrasive particles and the surface of materials, scanning electron micrograph of a wear groove on an austenitic steel and a draft of a taper section through the wear groove. 24

Figure 2.17 Ratio of microcutting to microploughing as a function of the ratio of the attack angle to the critical attack angle. 25

Figure 2.18 Schematic illustrations of four common methods used to measure abrasive wear rates of materials: (a) Pin on abrasive disc; (b) pin on abrasive plate; (c) pin on abrasive drum; (d) rubber wheel abrasion test.27

Figure 2.19 Schematic representation of abrasive wear resistance of two-phase structures as a function of volume fraction of a reinforcing phase. 28

Figure 3.1 A brief outline of the experimental approach 29

Figure 3.2 SEM image of SiC whiskers 31
Figure 3.3 SEM images of SiC whiskers (higher magnification) 31
Figure 3.4 A SEM image of cBN crush grade 6 31
Figure 3.5 SEM image of cBN crush grade 6 (higher magnification) 31
Figure 3.6 Fritsch Pulverisette 6 planetary ball mill 32
Figure 3.7 FCT group Systeme GmbH Spark Plasma Sintering Machine 33
Figure 3.8 Sketch of the B3B experimental setup 39
Figure 3.9 Ball on disc sliding wear testing rig 41
Figure 3.10 Diagram of the positioning of the sample disc and wear ball in a ball on disc sliding wear testing rig 41
Figure 3.11 Diagram of a spherical cap region of a sphere 41
Figure 4.2a) 85 wt. % TiC +12 wt. % Al_2O_3 + 3 wt. % Y_2O_3 powder 43
Figure 4.2b)85 wt. % TiC-3.75 wt. % Al_2O_3-6wt. % Y_2O_3-5.25 wt. % SiO_2 powder 43
Figure 4.3A Micrograph of 95% TiC mix 44
Figure 4.3B Micrograph of 90% TiC mix 44
Figure 4.3C Micrograph of 85% TiC mix 44
Figure 4.3D Micrograph of 80% TiC mix 44
Figure 4.4 Graph of the trends in the density of SPS sintered samples with 85 wt. % TiC and liquid phase sintering aids 48
Figure 4.5 Graph of the rends in the density of SPS sintered samples with 90 wt. % TiC and liquid phase sintering aids 50
Figure 4.6 Y_2O_3-Al_2O_3 phase diagram) 52
Figure 4.7 Isothermal section of the system Y_2O_3-Al_2O_3-SiO_2 at 1600°C in air (in mol. %) 52
Figure 4.8A: SEM image of the microstructure of 85TiC-12Al_2O_3-3Y_2O_3 SPS'd at 1550 °C, 50MPa and 10 min hold. 53
Figure 4.8B: SEM image of 85TiC-3.75Al_2O_3-6Y_2O_3-5.25SiO_2 SPS'd at 1610°C, 70MPa and 10 min hold. 53
Figure 4.8C: SEM image of 90TiC-8Al_2O_3-2Y_2O_3 SPS'd at 1550°C, 50MPa and 10 min hold 53
Figure 4.8D: SEM image of 90TiC-2.5Al_2O_3-4Y_2O_3-3.5SiO_2 SPS'd at 1625°C, 70MPa and 10 min hold 53
Figure 4.9 A: Image of the area of sintered 85TiC-12Al_2O_3-3Y_2O_3 SPS'd at 1550 °C, 50MPa and 10 min hold scanned by EDS for composition 54
Figure 4.9 B: Results of EDS qualitative analysis on the area highlighted in Fig. 4.9 A 54
Figure 4.10 A: Image of the area of sintered 85TiC-12Al_2O_3-3Y_2O_3 SPS'd at 1550 °C, 50MPa and 10 min hold scanned by EDS for composition 54

Figure 4.10 B: Results of EDS qualitative analysis on the area highlighted in Fig. 4.110 A 54

Figure 4.11 A: Image of the area of sintered 85TiC-12Al_2O_3-3Y_2O_3 SPS'd at 1550 °C, 50MPa and 10 min hold scanned by EDS for composition 54

Figure 4.11 B: Results of EDS qualitative analysis on the area highlighted in Fig. 4.11 A 54

Figure 4.12 A: Image of the area of sintered 90TiC-2.5Al_2O_3-4Y_2O_3-3.5SiO_2 SPS'd at 1625°C, 70MPa and 10 min hold scanned by EDS for composition 55

Figure 4.12 B: Results of EDS qualitative analysis on the area highlighted in Fig. 4.12 A 55

Figure 4.13 A: Image of the area of sintered 90TiC-2.5Al_2O_3-4Y_2O_3-3.5SiO_2 SPS'd at 1625°C, 70MPa and 10 min hold scanned by EDS for composition 55

Figure 4.13: Results of EDS qualitative analysis on the area highlighted in Fig. 4.13 A 55

Figure 4.14 A: Image of the area of sintered 90TiC-2.5Al_2O_3-4Y_2O_3-3.5SiO_2 SPS'd at 1625°C, 70MPa and 10 min hold scanned by EDS for composition 56

Figure 4.14 B: Results of EDS qualitative analysis on the area highlighted in Fig. 4.14 A 56

Figure 4.15 Comparison of % of full density of 85 wt.% TiC vs. 85 wt.% TiC(SiO_2) at various sintering parameters 57

Figure 4.16 Comparison of % of full density of 90 wt.% TiC vs. 90 wt.% TiC(SiO_2) at various sintering parameters 57

Figure 5.1 a) 90 wt.% TiC (2µm) + 10 vol.% SiCw powder 59

Figure 5.1 b) 90 wt.% TiC (2µm) + 7 vol.% cBN powder 59

Figure 5.1 c) 90 wt.% TiC (+SiO2) (5:8:7) + 20 vol.% SiCw powder 60

Figure 5.1 d) 90 wt.% TiC (+SiO2) (5:8:7) + 10 vol.% cBN powder 60

Figure 5.2 SEM images of TiC matrix powder mixes after the addition of SiC whiskers 63

Figure 5.3 Densification rate of 85 wt.% TiC matrices with/without SiO_2 and 10 vol.% cBN SPS'd at 1575°C72

Figure 5.4 Y_2O_3-Al_2O_3 phase diagram 75

Figure 5.5 Isothermal section of the system Y_2O_3-Al_2O_3-SiO2 at 1600°C in air (in mol. %) ♦ - Represents liquid phase sintering aid composition used. 75

Figure 5.6 Phase relation in the ternary system SiC- Al_2O_3-Y_2O_3 at 1400°C 75

Figure 5.7 SEM micrographs of A - crack path from Vickers Hardness indentation in a sample with the composition 79TiC-11Al_2O_3-3Y_2O_3-7 (10 vol.%) SiCw SPS'd at 1600°C, 70MPa and 10 min hold time and B - crack path from Vickers Hardness indentation in a sample with the composition 73TiC-10Al_2O_3-3Y_2O_3-14 (20 vol.%) SiCw SPS'd at 1625°C, 70MPa and 10 min hold. 81

Figure 5.8 SEM micrographs of A - 85TiC-3.75Al_2O_3-6Y_2O_3-5.25SiO_2 SPS'd at 1610°C, 70MPa and 10 min hold time and B - crack path from Vickers Hardness indentation in 73TiC-3Al_2O_3-5Y_2O_3-4SiO_2-15 (20 vol.%) SiCw SPS'd at 1625°C, 70MPa and 10 min 82

Figure 5.9 SEM micrographs of A – 77.2TiC-6.9Al_2O_3-1.7Y_2O_3-14.2 (20 vol.%) SiCw SPS'd at 1625°C, 70MPa and 20 min hold time and B - crack path from Vickers Hardness indentation in 77.2TiC-6.9Al_2O_3-1.7Y_2O_3-14.2 (20 vol.%) SiCw SPS'd at 1625°C, 70MPa and 20 min hold time magnified by 15 K X. 83

Figure 5.10 SEM micrographs of A – 77TiC-2.1Al_2O_3-3.4Y2O3-3SiO_2-14.5 (20 vol.%) SiCw SPS'd at 1640°C, 70MPa and 10 min hold time and B - crack path from Vickers Hardness indentation in 77TiC-2.1Al_2O_3-3.4Y_2O_3-3SiO_2-14.5 (20 vol.%) SiCw SPS'd at 1640°C, 70MPa and 10 min hold time magnified by 10 K X 83

Figure 5.11 SEM micrographs of A – 78.6TiC-3.5Al_2O_3-5.6Y_2O_3-4.9SiO_2-7.5 (10 vol.%) cBN SPS'd at 1625°C, 70MPa and 10 min hold time and B - crack path from Vickers Hardness indentation in 78.6TiC-3.5Al_2O_3-5.6Y_2O_3-4.9SiO_2-7.5 (10 vol.%) cBN SPS'd at 1625°C, 70MPa and 10 min hold time magnified by 10 K X 84

Figure 5.12 SEM micrographs of A – 78.6TiC-3.5Al_2O_3-5.6Y_2O_3-4.9SiO_2-7.5 (10 vol.%) cBN SPS'd at 1575°C, 70MPa and 10 min hold time viewed with the Secondary detector magnified by 15 K X and B - 78.6TiC-3.5Al_2O_3-5.6Y_2O_3-4.9SiO_2-7.5 (10 vol.%) cBN SPS'd at 1575°C, 70MPa and 10 min hold time viewed via Backscatter detector magnified by 15 K X 84

Figure 5.13 SEM micrographs of A – 83.3TiC-2.3Al_2O_3-3.7Y_2O_3-3.2SiO_2-7.5 (10 vol.%) cBN SPS'd at 1575°C, 70MPa and 10 min hold time and B - crack path from Vickers Hardness indentation in 83.3TiC-2.3Al_2O_3-3.7Y_2O_3-3.2SiO_2-7.5 (10 vol.%) cBN SPS'd at 1575°C, 70MPa and 10 min hold time magnified by 10.00 KX 85

Figure 5.14 SEM micrographs of A – 83.3TiC-2.3Al_2O_3-3.7Y_2O_3-3.2SiO_2-7.5 (10 vol.%) cBN SPS'd at 1575°C, 70MPa and 10 min hold time viewed with the Secondary detector magnified at 15.1 K X and B - 83.3TiC-2.3Al_2O_3-3.7Y_2O_3-3.2SiO_2-7.5 (10 vol.%) cBN SPS'd at 1575°C, 70MPa and 10 min hold time viewed via Backscatter detector magnified by 15.1 K X 86

Figure 6.1 Photograph of fractured sample of 85TiC-12Al_2O_3-3Y_2O_3 95

Figure 6.2 A- Outer limit of fractured edge (outside circumference of sample furthest from the site of loading), B- mid-length of fractured edge and C-inner edge of fracture of edge (center of sample directly under the site of loading) 96

Figure 6.3 A - Fracture surface analysed under high magnification (10.0 K X) using Backscatter Detector and B- same surfaced analysed under high magnification using Secondary Electron Detector 96

Figure 6.4 Graph of the regression line used to determine the Weibull modulus for 85TiC-12Al_2O_3-3Y_2O_3 . 97

Figure 6.5 Photograph of fractured sample of 79TiC-11Al_2O_3-3Y_2O_3-7 (10.0 vol.%) SiCw 97

Figure 6.6 A- Outer limit of fractured edge (outside circumference of sample furthest from the site of loading), B- mid-length of fractured edge and C-inner edge of fracture of edge (center of sample directly under the site of loading) 98

Figure 6.7 A - Fracture surface analysed under high magnification (10.0 K X) using Backscatter Detector and B- same surfaced analysed under high magnification using Secondary Electron Detector 98

Figure 6.8 Graph of the regression line used to determine the Weibull modulus for 79TiC-11Al_2O_3-3Y_2O_3-7(10.0 vol.%) SiCw 99

Figure 6.9 Photograph of fractured sample of 73TiC-10Al_2O_3-3Y_2O_3-14 (20.0 vol.%) SiCw 100

Figure 6.10 A- Outer limit of fractured edge (outside circumference of sample furthest from the site of loading), B- mid-length of fractured edge and C-inner edge of fracture of edge (center of sample directly under the site of loading) 100

Figure 6.11 A - Fracture surface analysed under high magnification (10.0 K X) using Backscatter Detector and B- same surfaced analysed under high magnification using Secondary Electron Detector 100

Figure 6.12 Graph of the regression line used to determine the Weibull modulus for 73TiC-10Al_2O_3-3Y_2O_3-14 (20.0 vol.%) SiCw 101

Figure 6.13 Photograph of fractured sample of 79TiC-4.5Al_2O_3-5.6Y_2O_3-4.9SiO_2-7.1 (10.0 vol.%) SiCw .. 101

Figure 6.14 A- Outer limit of fractured edge (outside circumference of sample furthest from the site of loading), B- mid-length of fractured edge and C-inner edge of fracture of edge (center of sample directly under the site of loading) 102

Figure 6.15 A - Fracture surface analysed under high magnification (10.0 K X) using Backscatter Detector and B- same surfaced analysed under high magnification using Secondary Electron Detector 102

Figure 6.16 Graph of the regression line used to determine the Weibull modulus for 79TiC-4.5Al_2O_3-5.6Y_2O_3-4.9 SiO_2-7.1 (10.0 vol.%) SiCw 103

Figure 6.17 Photograph of fractured sample of 78.6TiC-3.5Al_2O_3-5.6Y_2O_3-4.9SiO_2-7.5 (10.0 vol.%) cBN. 104

Figure 6.18 A- Outer limit of fractured edge (outside circumference of sample furthest from the site of loading), B- mid-length of fractured edge and C-inner edge of fracture of edge (center of sample directly under the site of loading) 104

Figure 6.19 A - Fracture surface analysed under high magnification (10.0 K X) using Backscatter Detector and B- same surfaced analysed under high magnification using Secondary Electron Detector 105

Figure 6.20 Graph of the regression line used to determine the Weibull modulus for 78.6TiC-3.5Al_2O_3-5.6Y_2O_3-4.9SiO_2-7.5 (10.0 vol.%) cBN 106

Figure 6.21 Photograph of fractured sample of 77.8TiC-6.9Al_2O_3-7Y_2O_3-14 (20.0 vol.%) SiCw 106

Figure 6.22 A- mid-length of fractured edge and B- inner edge of fracture of edge (center of sample directly under the site of loading) 107

Figure 6.23 A - Fracture surface analysed under high magnification (10.0 K X) using Backscatter Detector and B- same surfaced analysed under high magnification using Secondary Electron Detector 107

Figure 6.24 Graph of the regression line used to determine the Weibull modulus for 77.8TiC-6.9Al_2O_3-1.7Y_2O_3-14 (20.0 vol.%) SiCw 108

Figure 7.1 A: wear track on the surface of the 85TiC-12Al_2O_3-3Y_2O_3 matrix only sample disc. B: High magnification image of the wear track on the 82.6 vol.%TiC-14.6 vol.%Al_2O_3-2.9 vol.%Y_2O_3 matrix only sample disc..... 112

Figure 7.2 A: Spectrum 2 Area alongside the wear track scanned by EDS for composition B: Results of EDS qualitative analysis on Spectrum 2. 112

Figure 7.3 A: Spectrum 1 Area on the wear track scanned by EDS for composition B: Results of EDS qualitative analysis on Spectrum 1 113

Figure 7.4 A: Wear scar on the surface of the worn AISI 52100 steel ball bearing. B: Diameter and area of the wear scar on the worn AISI 52100 steel ball bearing. (Diameter: 1.041mm and Area: 0.850mm2) 113

Figure 7.5 A: High magnification image of the edge of the wear scar on the worn AISI 52100 steel ball bearing. B: Higher magnification image of the center of the wear scar on the worn AISI 52100 steel ball bearing.. 114

Figure 7.6 A: Spectrum 2 Area inside the wear scar on the worn AISI 52100 steel ball bearing scanned by EDS for composition B: Results of EDS qualitative analysis on Spectrum 2 114

Figure 7.7 A: wear track on the surface of the 79TiC-11Al_2O_3-3Y_2O_3-7 (10.0 vol.%) SiCw sample disc. B: High magnification image of the wear track on the 79TiC-11Al_2O_3-3Y_2O_3-7 (10.0 vol.%) SiCw sample disc..... 115

Figure 7.8 A: Spectrum 2 Area alongside the wear track scanned by EDS for composition B: Results of EDS qualitative analysis on Spectrum 2 115

Figure 7.9 A: Spectrum 1 Area on the wear track scanned by EDS for composition B: Results of EDS qualitative analysis on Spectrum 1. 116

Figure 7.10 A: Wear scar on the surface of the worn AISI 52100 steel ball bearing. B: Diameter and area of the wear scar on the worn AISI 52100 steel ball bearing. (Diameter: 1.032mm and Area: 0.837mm^2)..... 116

Figure 7.11 A: High magnification image of the edge of the wear scar on the worn AISI 52100 steel ball bearing. B: Higher magnification image of the center of the wear scar on the worn AISI 52100 steel ball bearing 117

Figure 7.12 A: Spectrum 2 Area inside the wear scar on the worn AISI 52100 steel ball bearing scanned by EDS for composition B: Results of EDS qualitative analysis on Spectrum 2 117

Figure 7.13 A: wear track on the surface of the 73TiC-10Al_2O_3-3Y_2O_3-14 (20 vol.%) SiCw sample disc. B: High magnification image of the wear track on the 73TiC-10Al_2O_3-3Y_2O_3- 14 (20.0 vol.%) SiCw sample disc... 118

Figure 7.14 A: Spectrum 2 Area alongside the wear track scanned by EDS for composition B: Results of EDS qualitative analysis on Spectrum 2 118

Figure 7.15 A: Spectrum 1 Area on the wear track scanned by EDS for composition B: Results of EDS qualitative analysis on Spectrum 1 119

Figure 7.16 A: Wear scar on the surface of the worn AISI 52100 steel ball bearing. B: Diameter and area of the wear scar on the worn AISI 52100 steel ball bearing. (Diameter: 0.929mm and Area: 0.678mm^2)..... 119

Figure 7.17 A: High magnification image of the edge of the wear scar on the worn AISI 52100 steel ball bearing. B: Higher magnification image of the center of the wear scar on the worn AISI 52100 steel ball bearing 120

Figure 7.18 A: Spectrum 3 Area inside the wear scar on the worn AISI 52100 steel ball bearing scanned by EDS for composition B: Results of EDS qualitative analysis on Spectrum 3 120

Figure 7.19 A: wear track on the surface of the 79TiC-4.5Al_2O_3-5.6Y_2O_3-4.9SiO_2-7.1(10.0 vol.%) SiCw sample disc. B: High magnification image of the wear track on the 79TiC-4.5Al_2O_3-5.6Y_2O_3-4.9 SiO_2-7.1(10.0 vol.%) SiCw sample disc 121

Figure 7.20 A: Spectrum 2 Area alongside the wear track scanned by EDS for composition B: Results of EDS qualitative analysis on Spectrum 2 121

Figure 7.21 A: Spectrum 1 Area on the wear track scanned by EDS for composition B: Results of EDS qualitative analysis on Spectrum 1 122

Figure 7.22 A: Wear scar on the surface of the worn AISI 52100 steel ball bearing. B: Diameter and area of the wear scar on the worn AISI 52100 steel ball bearing. (Diameter: 0.798mm and Area: 0.500mm^2)..... 122

Figure 7.23 A: High magnification image of the edge of the wear scar on the worn AISI 52100 steel ball bearing. B: Higher magnification image of the center of the wear scar on the worn AISI 52100 steel ball bearing 123

Figure 7.24 A: Spectrum 2 Area inside the wear scar on the worn AISI 52100 steel ball bearing scanned by EDS for composition B: Results of EDS qualitative analysis on Spectrum 2 123

Figure 7.25 A: wear track on the surface of the 78.6TiC-3.5Al_2O_3-5.6Y_2O_3-4.9 SiO_2-7.5(10.0 vol.%) cBN sample disc. B: High magnification image of the wear track on the 78.6TiC-3.5Al_2O_3-5.6Y_2O_3-4.9SiO_2-7.5(10.0 vol.%) cBN sample disc..... 124

Figure 7.26 A: Spectrum 1 Area alongside the wear track scanned by EDS for composition B: Results of EDS qualitative analysis on Spectrum 1 124

Figure 7.27 A: Spectrum 2 Area on the wear track scanned by EDS for composition B: Results of EDS qualitative analysis on Spectrum 2. 125

Figure 7.28 A: Wear scar on the surface of the worn AISI 52100 steel ball bearing. B: Diameter and area of the wear scar on the worn AISI 52100 steel ball bearing. (Diameter: 1.376mm and Area: 1.486mm^2)..... 125

Figure 7.29 A: High magnification image of the edge of the wear scar on the worn AISI 52100 steel ball bearing. B: Higher magnification image of the center of the wear scar on the worn AISI 52100 steel ball bearing 126

Figure 7.30 A: Spectrum 3 Area inside the wear scar on the worn AISI 52100 steel ball bearing scanned by EDS for composition B: Results of EDS qualitative analysis on Spectrum 3 126

Figure 7.31 A: wear track on the surface of the 77.8TiC-6.9Al_2O_3-1.7Y_2O_3-14(20.0 vol.%) SiCw sample disc. B: High magnification image of the wear track on the 77.8TiC-6.9Al_2O_3-1.7Y_2O_3-14(20.0 vol.%) SiCw sample disc 127

Figure 7.32 A: Spectrum 2 Area alongside the wear track scanned by EDS for composition B: Results of EDS qualitative analysis on Spectrum 2. 127

Figure 7.33 A: Spectrum 1 Area on the wear track scanned by EDS for composition B: Results of EDS qualitative analysis on Spectrum 1 128

Figure 7.34 A: Wear scar on the surface of the worn AISI 52100 steel ball bearing. B: Diameter and area of the wear scar on the worn AISI 52100 steel ball bearing. (Diameter: 0.876mm and Area: 0.603mm^2)..... 128

Figure 7.35 A: High magnification image of the edge of the wear scar on the worn AISI 52100 steel ball bearing. B: Higher magnification image of the center of the wear scar on the worn AISI 52100 steel ball bearing 129

Figure 7.36 A: Spectrum 2 Area inside the wear scar on the worn AISI 52100 steel ball bearing scanned by EDS for composition B: Results of EDS qualitative analysis on Spectrum 2 129

Figure 7.37 Graphs for results given by the CSM Tribometer for the sliding wear tests of the sintered TiC discs with/without reinforcements 131

LIST OF TABLES

Table 2.1 Properties of TiC 6

Table 2.2 Typical properties for hexagonal and cubic boron nitride 18

Table 3.1: Materials used for processing 31

Table 3.2: Preparation method for grinding sintered TiC matrices samples 35

Table 3.3: Preparation method for polishing sintered TiC matrices samples 35

Table 3.4: Components TiC matrices 36

Table 3.5: Components TiC matrices with SiC whisker (SiCw) reinforcements 37

Table 3.6: Components TiC matrices with Cubic boron nitride (cBN) reinforcements 37

Table 4.1 Results of the Particle size analysis of the starting powders 43

Table 4.2: Results for XRD patterns for milled TiC matrix powders 45

Table 4.3: Theoretical densities of TiC mixes with Al_2O_3 and Y_2O_3 46

Table 4.4: Theoretical densities of TiC mixes with Al_2O_3, Y_2O_3 the addition of SiO_2 46

Table 4.5: Average density measurements for samples of TiC mixes with Al_2O_3 and Y_2O_3 sintered at 1450°C 47

Table 4.6: Average density measurements for samples of TiC mixes with Al_2O_3 and Y_2O_3 sintered at 1550°C 47

Table 4.7: Average density measurements for samples of TiC mixes with Al_2O_3 and Y_2O_3 sintered at 1650°C 47

Table 4.8: Density of SPS sintered samples with 85 wt. % TiC and liquid phase sintering aids 48

Table 4.9: Density of SPS sintered samples with 90 wt. % TiC and liquid phase sintering aids 50

Table 4.10: Phases identified by XRD analysis of SPS's samples with the highest percentage theoretical density. (YAG-$Y_3Al_5O_{12}$, YAP- $YAlO_3$ and $Y_2Si_2O_7$) 52

Table 4.11 Hardness and Fracture Toughness of SPS samples with highest percentage of Theoretical Density 58

Table 5.1 of Results for XRD patterns for milled 90 wt.% TiC matrix powders with/without SiO_2 and the addition of SiC whiskers and cBN respectively 62

Table 5.2 Results for XRD patterns for milled 85 wt.% TiC matrix powders with/without SiO_2 and the addition of SiC whiskers and cBN respectively 62

Table 5.3 Composition of TiC matrix samples without SiO_2 and with the addition of SiC whiskers and cBN respectively 63

Table 5.4 Composition of 85 wt.% TiC matrix samples with SiO_2 and with the addition of SiC whiskers and cBN respectively 63

Table 5.5 Composition of 90 wt.% TiC matrix samples with SiO_2 and with the addition of SiC whiskers and cBN respectively 64

Table 5.6: Density of SPS sintered samples with 85 wt. % TiC, liquid phase sintering aids (Al_2O_3-Y_2O_3), SiC whiskers and cBN respectively of various compositions and sintering parameters 66

Table 5.7: Density of SPS sintered samples with 90 wt. % TiC, liquid phase sintering aids (Al_2O_3-Y_2O_3), SiC whiskers and cBN respectively of various compositions and sintering parameters 67

Table 5.8: Density of SPS sintered samples with 85 wt. % TiC, liquid phase sintering aids (Al_2O_3-Y_2O_3-SiO_2) and SiC whiskers of various compositions and sintering parameters 69

Table 5.9: Density of SPS sintered samples with 90 wt. % TiC, liquid phase sintering aids (Al_2O_3-Y_2O_3-SiO_2) and SiC whiskers of various compositions and sintering parameters 70

Table 5.10: Density of SPS sintered samples with 85 wt. % TiC, liquid phase sintering aids (Al_2O_3-Y_2O_3-SiO_2) and cBN of various compositions and sintering parameters..... 71

Table 5.11: Density of SPS sintered samples with 90 wt. % TiC, liquid phase sintering aids (Al_2O_3-Y_2O_3-SiO_2) and cBN of various compositions and sintering parameters..... 73

Table 5.12 Phases identified by XRD analysis of SPS'd samples of 85 wt. % TiC + SiCw with the highest percentage theoretical density. (YAG-$Y_3Al_5O_{12}$, YAP- $YAlO_3$) 75

Table 5.13 Phases identified by XRD analysis of SPS'd samples of 90 wt. % TiC + SiCw with the highest percentage theoretical density. (YAG-$Y_3Al_5O_{12}$, YAP- $YAlO_3$) 77

Table 5.14 Phases identified by XRD analysis of SPS'd samples of 85 wt. % TiC + cBN with the highest percentage theoretical density. (YAG-$Y_3Al_5O_{12}$, YAP- $YAlO_3$) 79

Table 5.15 Phases identified by XRD analysis of SPS'd samples of 90 wt. % TiC + cBN with the highest percentage theoretical density. (YAG-$Y_3Al_5O_{12}$, YAP- $YAlO_3$) 81

Table 5.16: Hardness and fracture toughness of SPS sintered samples with 85 wt. % TiC, liquid phase sintering aids (Al_2O_3-Y_2O_3) and SiC whiskers with the highest density 88

Table 5.17: Hardness and fracture toughness of SPS sintered samples with 85 wt. % TiC, liquid phase sintering aids (Al_2O_3-Y_2O_3-SiO_2) and SiC whiskers with the highest density..... 89

Table 5.18: Hardness and fracture toughness of SPS sintered samples with 85 wt.% TiC, liquid phase sintering aids (Al_2O_3-Y_2O_3-SiO_2) and cBN with the highest density..... 90

Table 5.19: Hardness and fracture toughness of SPS sintered samples with 90 wt. % TiC, liquid phase sintering aids (Al_2O_3-Y_2O_3) and SiC whiskers with the highest density 91

Table 5.20: Hardness and fracture toughness of SPS sintered samples with 90 wt. % TiC, liquid phase sintering aids (Al_2O_3-Y_2O_3-SiO_2) and SiC whiskers with the highest density..... 92

Table 5.21: Hardness and fracture toughness of SPS sintered samples with 90 wt.% TiC, liquid phase sintering aids (Al_2O_3-Y_2O_3-SiO_2) and cBN with the highest density..... 92

Table 6.1. Table of sintering parameters, sintering density and fracture toughness for selected sample compositions 94

Table 6.2. Table of results for the force at the moment of fracture for samples of various compositions 94

Table 6.3 Table of Poisson's Ratios and Young's moduli for the constituents of the composite materials .. 95

Table 6.4 Table of results for theoretical Poisson's Ratios and Young's moduli of various compositions based on Rule of Mixtures..... 95

Table 6.5 Table of results for the calculation of Poisson's Ratio (υ), Young's Modulus (E) and maximum tensile stress (σ_{max}) for samples of various composition and sintering parameters..... 96

Table 6.6 Table of results for the calculation of the probability of fracture and Weibull modulus of 85TiC-12Al_2O_3-3Y_2O_3..... 98

Table 6.7 Table of results for the calculation of the probability of fracture and Weibull modulus of 79TiC-11Al_2O_3-3Y_2O_3-7(10.0 vol.%) SiCw..... 100

Table 6.8 Table of results for the calculation of the probability of fracture and Weibull modulus of 73TiC-10Al_2O_3-3Y_2O_3-14(20.0 vol.%) SiCw..... 102

Table 6.9 Table of results for the calculation of the probability of fracture and Weibull modulus of 79TiC-4.5Al_2O_3-5.6Y_2O_3-4.9SiO_2-7.1(10.0 vol.%) SiCw
……..…104

Table 6.10 Table of results for the calculation of the probability of fracture and Weibull modulus of 78.6TiC-3.5Al_2O_3-5.6Y_2O_3-4.9 SiO_2-7.5 (10.0 vol.%)
cBN……106

Table 6.11 Table of results for the calculation of the probability of fracture and Weibull modulus of 77.8TiC-6.9Al_2O_3-1.7Y_2O_3-14(20.0 vol.%) SiCw..... 109

Table 6.12: Typical values of the Weibull modulus m for some materials 110

Table 6.13: Weibull moduli of sintered TiC with various liquid phase sintering aids and with/without the addition of reinforcement materials 110

Table 7.1 Mass lost on ball bearing during wear testing..... 131

Table 7.2 Coefficient of friction (μ) for the sliding wear testing of sintered TiC discs with/without reinforcement materials..... 133

1. INTRODUCTION

1.1 Subject of the thesis

Titanium carbide (TiC) is successfully used as a component of heat resistant materials intended for parts operating at high temperature. In addition to high hardness and wear resistance, TiC is readily available at a comparatively low cost. As a result of its low comparative cost it is commonly used as a matrix of sintered hard alloys for wear resistant parts and cutting tools (Samsonov & Sergeev, 1971). However, the widespread use of TiC in cutting tools and other applications has been limited because the fracture strength of the material has resulted in poor fracture toughness. (Sorrell, 2001) The insufficient fracture toughness of conventionally produced TiC is a characteristic that could possibly be overcome by the use of TiC as a matrix in ceramic matrix composites (CMC's).

The use of TiC matrices in ceramic matrix composites (CMC's) is limited because of the methods used to produce CMC's. Complex microstructures, changeability of the distribution of reinforcement materials, sintering defects and unusual material behaviour can be created during the production processes. This results in a large obstacle to the use of CMC's as there is limited knowledge with regards to the relationship between sintering parameters, microstructure and physical properties (Gowayed et al., 2018).

This project intended to determine the suitability of TiC based CMC's as a material for cutting tools. The research was aimed at improving the fracture toughness of TiC without causing a decrease in its other mechanical properties by introducing and comparing two types of reinforcing phases in the TiC matrix i.e. SiC whiskers and cubic boron nitride (cBN) particles. The project will span the processing of the TiC matrix powders and Spark Plasma Sintering (SPS) of such materials, followed by characterization and mechanical property evaluation; particularly in terms of density, hardness, fracture toughness, biaxial flexural strength and sliding wear resistance.

1.2 Background to the thesis

Various toughening methods have been considered in order to increase the toughness of ceramics to levels where they can be used as engineering components.The addition of whiskers to many ceramics have a significant effect on their toughening (Wei & Becher, 1984) (Claussen, Petow 1986) (Buljan, Pasto & Kim 1989) (Lio et al. 1989, Gadkaree, Chyung 1986). The ease of fabrication and higher degree of isotropy in material properties of whisker reinforced ceramics are directly related to the smaller aspect ratios involved. Due to chemical incompatibility issues between matrices and fibers, only a few fibers have the potential to be used as reinforcements, especially under the high temperatures experienced during the sintering process. One of the possible candidates as a reinforcement material for ceramic matrix composites is SiC whiskers (Lundberg et al. 1987).

SiC whiskers have been shown to be an exceptional reinforcement material in glass and ceramic composites, giving improved high temperature properties and preparing the materials for use as high temperature engineering composites (Becher et al. 1988, Chokshi, Porter 1985, Homeny, Vaughn & Ferber 1987, Tiegs, Becher 1986). SiC fiber composites possessed a high potential for significantly improving the fracture toughness as well as the tendency towards catastrophic failure in brittle load bearing systems (Petrovic et al., 1985).

Cubic boron nitride was commonly used as 2nd hard phase in the TiC composites. Cubic boron nitride (cBN) is the second hardest material next to diamond. It has many desirable physical and chemical properties (thermal stability up to 1200°C) and is highly resistant to chemical damage. Cubic boron nitride (cBN); characterized both by high compressive strength, hardness and oxidative resistance, is extensively used in applications in the manufacturing industry. Tools fabricated for cutting hardened steel, cast iron or other materials can be difficult to process. cBN compacts are commonly bonded with Ti-based alloys or compounds (Benko et al., 2003). Composites with metals of the elements in groups IV-VI of the period table or their compounds are most usually used as a binding phase. TiC and TiN display the highest chemical activity towards Boron Nitride. Previously experimental cBN-TiN/TiC composites were prepared by high pressure hot (HPHT) pressing and then followed by heat treatments. Those samples were found to have a dense polycrystalline microstructure and a thin layer of TiB_2 which was visible at the interface between the BN and the binder. It was also found that after the heat treatment there was a significant decrease in the hardness (Benko et al., 1999).

1.3 Problem Statement

TiC compacts can be sintered by hot pressing TiC powder with a ceramic binder (Al_2O_3 and/or Y_2O_3) at temperatures in the range of 1850-2100°C. During sintering, the plastic deformation of the powder particles occurs simultaneously with the chemical reaction with the binder in a complicated process. The microhardness of TiC prepared by spark plasma sintering (SPS) at a temperature range of 1450-1600°C was between 24-30 GPa, and its fracture toughness K_{IC} was from 3.7-5 MPa.m$^{1/2}$ (Cheng et al., 2012).

Previous research has shown that addition of whiskers to CMC's at a volume fraction exceeding 30 vol. % results in a significant decrease in the relative density of the composites (Dusza et al., 1992); nevertheless there is a tendency of higher volume percentages of whiskers in CMC's resulting in higher fracture toughness (Evans & Faber, 1984). Therefore, determining the correct ratio of whiskers to matrix material is essential. Consideration will also need to be given to the fact that the different whiskers will have different mechanical and chemical properties which could also affect the ratio of whiskers to matrix material needed to significantly improve the fracture toughness of the TiC composite (Cheng et al., 2012). Shahedi Asl et. al produced SiCw reinforced TiC via SPS sintering at a temperature of 1900°C. The specimens with 20 volume % SiC whiskers showed the highest flexural strength. They also found that the SiC whiskers could act as a grain growth inhibitor (Shahedi Asl et al., 2019). Grain growth was a concern during the study due to the high sintering temperature required in order to achieve full density.

In studies that analysed the behaviour of cBN reinforced α-Sialon ceramic produced by SPS sintering it was found that higher densities were achieved at a sintering temperature 1550°C as it was below the temperature at which hexagonalization occurs. The addition of cBN to the α-Sialon increased the hardness and fracture toughness at sintering temperatures of 1550°C (Garrett et al., 2015) To improve the hardness and potential use as a cutting tool material cBN would be added as a secondary hard phase. CBN is commonly bonded with Ti based compounds. The more reactive the binding phase is with the cBN crysrallites the better the properties of the composite. (Benko et al., 2003)

The purpose of this study is to improve the fracture toughness of TiC without causing a decrease in its other mechanical properties by adding SiC whiskers and cBN powder allong with liquid phase sintering aids to the starting TiC powder before sintering. In order to produce a TiC composite material with the best possible mechanical properties it will be essential to achieve the highest possible density. At a sintering temperature of 1450°C, and pressure of 50MPa, a relative density of ±96% can be achieved for TiC only material (no whiskers) (Cheng et al., 2012). With the addition of whiskers, the density will most likely decrease and therefore higher temperatures (> 1450°C) and pressures (> 50MPa) will be needed to produce samples of equal or similar density. To further increase the fracture toughness and facilitate the densification of the whisker-reinforced TiC liquid phase sintering aids will be added that will bind with the TiC to form new phases which will increase densification. cBN would be added to the TiC powder before sintering to increase the hardness and fracture toughness .

1.4 Objectives of the thesis

The objectives of this project are:

- To analyse the TiC-based (with liquid phase sintering aids) matrix powders with/without reinforcement materials after milling prior to sintering using SEM, EDS and XRD phase analysis
- To compare the SPS sintering parameters of TiC-based (with liquid phase sintering aids) matrix powders with/without reinforcement materials
- To analyse TiC-based (with liquid phase sintering aids) matrix with/without reinforcement materials after SPS sintering using SEM, EDS and XRD microstructure and phase analysis
- To determine the Density, Vickers Hardness and Fracture Toughness of the sintered TiC-based (with liquid phase sintering aids) matrix with/without reinforcement materials
- To select the TiC-based CMC compositions with the best combination of Density, Vickers Hardness and Fracture toughness for additional testing
- To determine the Biaxial Flexural Strength, Weibull Modulii and analyse the fracture surfaces of the selected TiC-based CMC’s

- To perform Sliding Wear Testing and determine the wear resistance and co-efficent of friction of the selected TiC-based CMC's

1.5 Plan of development

An overview of the TiC, SiC whiskers and cBN materials are presented in Chapter 2. The preparation and properties of TiC-based materials are also reviewed in this chapter. At the end of chapter 2 some relevant phase diagrams (binary Al_2O_3-Y_2O_3, BN-TiC and ternary Al_2O_3-Y_2O_3-SiO_2 and Al_2O_3-Y_2O_3-SiC) are discussed. Chapter 2 also summarizes the findings and develops the strategy for the research on which this thesis is based. Chapter 3 describes the powders, the equipment and the experimental techniques used. The results of the investigation into the density, microstructure, hardness and fracture toughness of the sintered TiC matrices are given in Chapter 4, which includes the results of the investigation into the reactions between TiC, Al_2O_3, Y_2O_3 and SiO_2. Chapter 5 focuses on the sintering of TiC matrices with the addition of SiC whiskers and cBN respectively. The hardness and fracture toughness properties of the resultant TiC-based CMC's and their microstructures are analysed and discussed at the end of this chapter. Chapter 6 summarizes the preliminary studies of the Ball-on-3 ball biaxial strength testing allong with the calculations for the Weibull Moduli of the TiC-based CMC's. Chapter 7 focuses on ball-on-disc sliding wear testing on the TiC-based CMC's for the determination of their co-efficients of friction. The results are discussed at the end of each chapter. The conclusions and recommendations for necessary future work are presented in Chapter 8. Appendices with additional tables and graphs can be found at the back of the document.

2. LITERATURE REVIEW

2.1 Titanium Carbide

2.1.1 Background

Titanium carbide (TiC) is an ideal structural material due to its stability at high temperatures, low density and high hardness. The extensive use of TiC in cutting tools and similar applications has been limited because the high production cost of TiC and poor fracture toughness of the material (Sorrell, 2001).

2.1.2 Structure of TiC

TiC is a standard faceted crystal with a NaCl type crystal structure. It has been hypothesised that the growth unit of TiC is a TiC_6 octahedron. An ideal morphology of TiC particles would be an octahedral shape if the TiC_6 grew freely in liquid under equilibrium during solidification. Different growth kinetics, conditions and mechanisms can however affect the growth morphology. TiC particles with dendritic, whisker/fibre, rod and hollow spherical shapes, etc. have reportedly been found (Li et al., 2008).

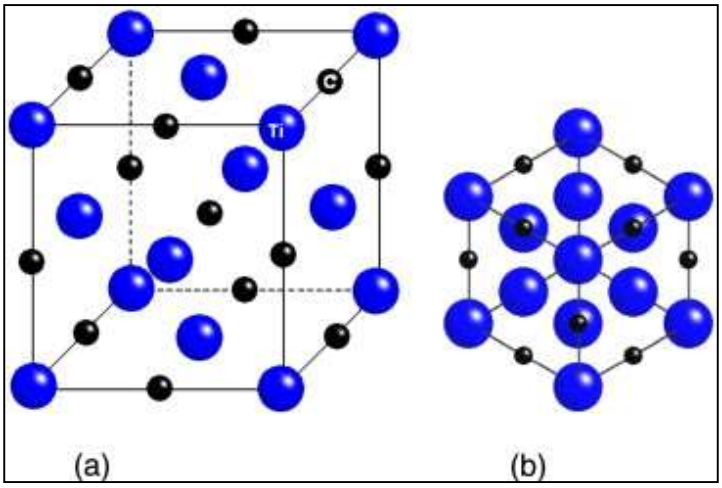


Figure 2.1 (a) Crystal structure of TiC and (b) Projection of TiC atoms along [111] direction. The blue atoms are Ti and the black atoms are C atoms (Li et al., 2008)**.**

2.1.3 Properties of TiC

Table 2.1 Properties of TiC

Mechanical Properties		
Property	**Value**	**Unit**
Young's modulus	430 - 451	GPa
Compressive strength	2500 - 2500	MPa
Bending strength	420 - 420	MPa
Physical Properties		
Property	**Value**	**Unit**
Thermal expansion	4.1 - 7.7	e^{-6}/K
Thermal conductivity	110 - 110	W/m.K
Melting temperature	3100 - 3100	°C
Service temperature	20 - 1600	°C
Density	4940 - 4940	kg/m^3
Resistivity	0.2 - 100	Ohm.mm^2/m
Friction coefficient	0.07 - 0.07	-

Reference: (Matweb - Material Property Database, “Titanium Carbide / TiC Chemical, mechanical, physical and environmental properties of materials,” n.d.)

2.1.4 Sintering TiC

TiC has strong covalent bonds which makes it difficult to obtain fully dense ceramics using traditional sintering methodologies without substantial amounts of sintering aids and sintering temperatures upwards of 2000°C. High temperatures and lengthy heat treatments are unsuitable for use as they limit the types of reinforcements which can be added to the matrix. A rapid densification method is therefore more desirable. Spark plasma sintering (SPS) allows for rapid densification of metal and/or ceramic powders at considerably lower temperatures. The advantage of SPS is that highly dense samples can be produced within a few minutes under a high mechanical pressure although it does require a large electric current. SPS technology is broadly used in the sintering of carbides, nitrides and nano-ceramics (Cheng et al., 2013).

The graph below shows examples of the densification curves produced during SPS sintering. The peaks seen represent localized deformation, bulk deformation and mass transport phenomena (Diouf & Molinari, 2012).

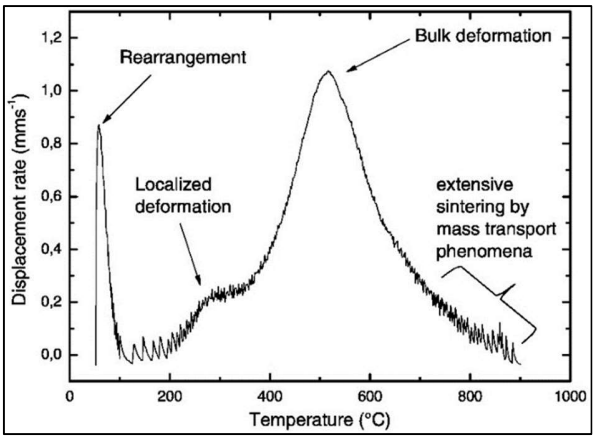


Figure 2.2 Displacement rate Vs temperature for powder processed with the initial pressure and densification mechanisms (Diouf & Molinari, 2012).

2.1.5 Liquid phase sintering aids

Alumina and Yttria are used as additives for liquid phase sintering of Si_3N_4, SiC and SiAlON ceramics. Phase interactions in the Y_2O_3-Al_2O_3 system are of importance due to even small changes in the physico-chemical conditions during sintering could result in the generation of new phase equilibria and the development of alternative microstructures which would thus influence the properties of the resulting sintered materials. It was discovered that the $Y_3Al_5O_{12}$ (YAG) phase and the YAG-Al_2O_3 eutectic are potential materials for the reinforcement of ceramics and intermetallic matrix composites for use in structural applications (Fabrichnaya & Seifert, 2001).

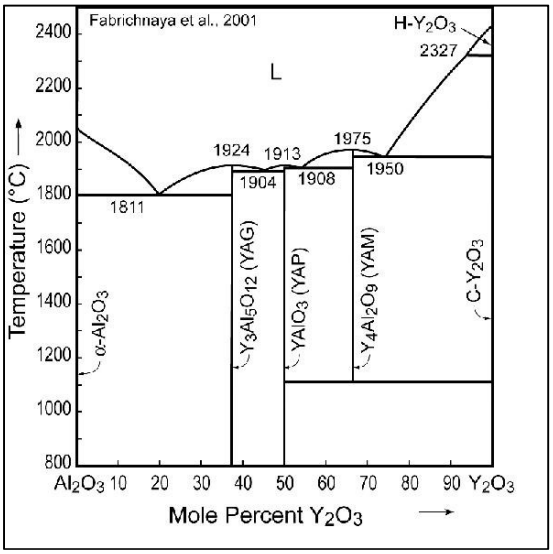


Figure 2.3 Alumina-Yttria phase diagram (Fabrichnaya & Seifert, 2001)

Metastable eutectics of Yttrium-Aluminium Perovskite (YAP, $YAlO_3$) and alumina (Al_2O_3) were initially determined by Caslavsky and Viechnicki (Caslavsky & Viechnicki, 1980). The method of formation of metastable eutectics is not well defined but it has been suggested that it is carried out via the solidification of immiscible eutectic liquids heated at a minimum 40°C above the liquidus point (Caslavsky & Viechnicki, 1980).

A resurgence in interest in the YAP-Alumina eutectic was driven by its potential use as a high temperature stable structural ceramic. It was noted that after extended periods of time at temperatures above 1200°C, deformation accompanying a reaction to YAG prevented the consideration of this eutectic ceramicfor high temperature stable structural applications (Hay, 1994).

$$Al_2O_3 + 3YAlO_3 = Y_3Al_5O_{12}$$

$$alumina + YAP = YAG$$

The reactants and reaction products have equivalent stiffness and creep resistance and hence the strain energy effects should be of greater importance (Hay, 1994).

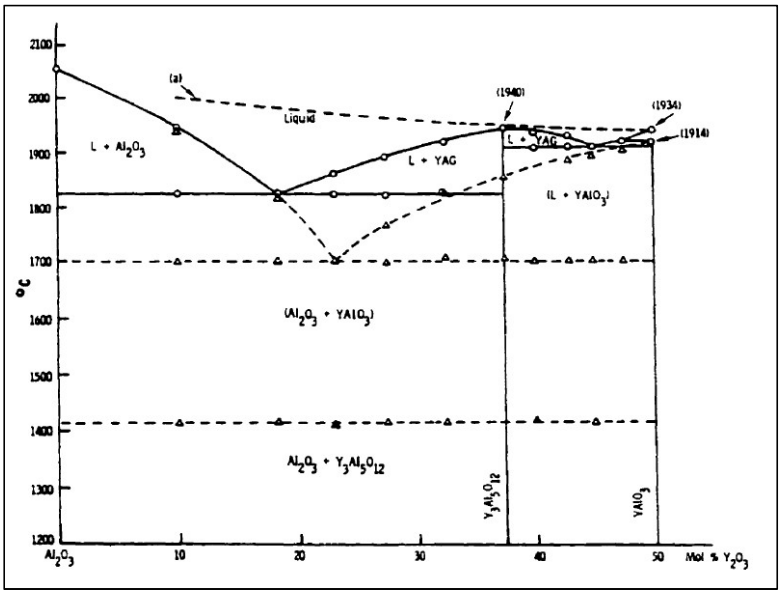


Figure 2.4 Alumina-Yttria phase diagram of the Alumina rich portion of the Al_2O_3-Y_2O_3 system. The metastable phase diagram is superimposed with dashed lines and the phase fields are labelled (Caslavsky & Viechnicki, 1980)**.**

Porosity can develop during sintering adjacent to the alumina-YAG interface and can be deduced to be Kirkendall porosity. This porosity results from the Aluminium and Oxygen diffusion through the YAG phase or is related to stresses developed during the reaction. Yttrium is the slowest diffusing of the species which supports the Kirkendall porosity hypothesis (Hay, 1994).

2.1.6 Sintering TiC with liquid phase sintering aids

In their investigations, Chae *et al*. have shown that the addition of Y_2O_3 in small amounts is very effective in the densification of TiC-Al_2O_3 composite during sintering at 1700°C. The added Y_2O_3 had been shown to form a solid solution film at the surface of the alumina particles and to suppress the gas generating reaction that occurs during sintering (Chae & Kim, 1993). Since the eutectic reaction in the Al_2O_3-Y_2O_3 has been reported to occur at 1760°C, the sintering of Al_2O_3- TiC composite with Y_2O_3 additive at higher temperatures is expected to occur in the presence of liquid and result in enhanced densification (Chae et al., 1995).

In the sintering of Al_2O_3- TiC composites, it has been suggested that vacuum atmosphere is detrimental for densification because of the gas generating reactions. Among the various possible reactions, the following is known to be the most severe:

$$Al_2O_3 + TiC = Al_2O + TiO + CO$$

The equilibrium partial pressure for CO for the above reaction is reported to be around 24 Pa at 2000K and thus the vacuum atmosphere which enhances the reaction will have an adverse effect on densification. However, under the conditions of rapid heating and where the gas generating reaction of Al_2O_3 with TiC is sufficiently suppressed by the addition of Y_2O_3, vacuum sintering is expected to provide better densification than sintering in an inert gas atmosphere. There is also a possibility of formation of YAG ($Y_3Al_5O_{12}$) in the cooled liquid phase after sintering (Chae et al., 1995).

2.1.7 Interaction between TiC and SiC

TiC-SiC composites are hard to densify owing to the low self-diffusion rate of SiC into TiC. TiC-SiC composites are usually produced by hot pressing techniques, including SPS. The properties of these composites largely depend on their microstructure. The intragranular nature of the microstructure is effective in improving the mechanical properties of the composite material. Intragranular composites are challenging to fabricate by the previously mentioned sintering methods (Chen et al., 2009).

2.1.8 Interaction of SiO_2 and liquid phase sintering aids

The system Y_2O_3-Al_2O_3-SiO_2 is important as a system as it involves the most widely used sintering additives for sintering Si_3N_4, SiAlON and SiC ceramics. Y_2O_3-Al_2O_3-SiO_2 based glasses have become more important for technical use due to their astonishing physico-chemical properties (Kolitsch et al., 1999). The system Y_2O_3-Al_2O_3 features the monoclinic compound $Y_4Al_2O_9$ (YAM), the Perovskite-type $YAlO_3$ (YAP), and the garnet-type $Y_3Al_5O_{12}$ (YAG), with mole ratio Y_2O_3:Al_2O_3 of 2:1, 1:1 and 3:5 respectively. Because of the very complex (and partly metastable) behaviour of this system, many different interpretations of the phase diagram had been published. Even though an extensive amount of experimental work performed on this system, there still are some inconsistencies concerning the melting and crystallization behaviour of YAP and YAG, the composition and the temperature of specific eutectics, the liquidus data on the Y_2O_3-rich side, and the thermal stability of YAP at lower temperature (Kolitsch et al., 1999).

2.1.9 Interaction between SiC and liquid phase sintering aids

The traditional method of solid-state sintering SiC is by sintering at temperatures up to 2200°C where additions of small amounts of boron, aluminium and carbon are added to improve densification. Instead, liquid phase sintering with the use of rare earth metals together with alumina and AlN, allow for sintering at lower temperatures and improve fracture toughness and mechanical strength (Neher et al., 2011). The observed phase relations in the SiC-Al_2O_3-Y_2O_3 system indicates that at least some dissolution of SiC in the liquid phase is required. The

observed integration of minute amounts of alumina into the SiC grains and the quick phase transformation from β- to α-SiC during liquid phase sintering are evidence of the existence of this solution. The ratios and the melting temperature of the various components are shown to have an effect on the low solubility of SiC in the oxide solution (Neher et al., 2011).

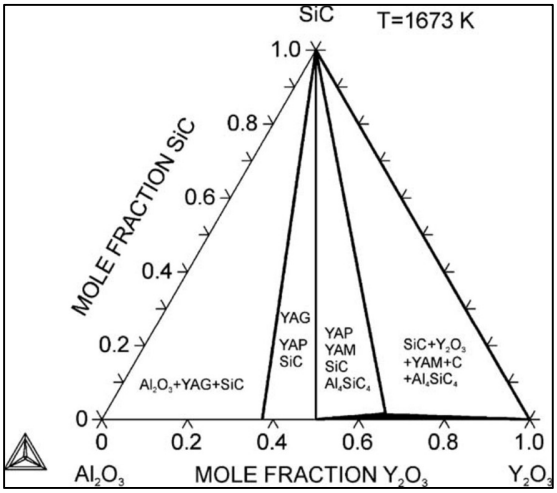


Figure 2.5 Phase relation in the ternary system SiC–Al_2O_3–Y_2O_3 at 1400˚C (Neher et al., 2011)

2.1.10 Interaction between TiC and Cubic Boron Nitride (cBN)

One of the most essential criteria for selecting the matrix phase for sintering cBN-containing composites is the nature of chemical reaction occurring at the BN-matrix interface. Formation of new phases on the-BN-matrix interface can give rise to composite materials with advantageous mechanical properties.

Exploring the reactions taking place at the BN-matrix interface is also of interest from a technological perspective. The TiC matrix material reacts with BN to form two new phases, TiB_2 and TiN (Benko et al., 2001).

BN-TiC with a molar ratio equating to 1:1 and at a temperature of 1400°C, co-exists as four phases in the system at constant pressure (10^2 Pa). These are as follows: cBN(solid), $TiC_{0.8}N_{0.2}$(solid); TiB_2(solid), C(solid). Under low pressure three solid phases co-exist in the system: TiB_2, C and $TiC_{0.8}N_{0.2}$ in molar quantities of 0.50 mol, 0.60 mol and 0.50 mol respectively, as well as Nitrogen (gas) at the amount 0.45 mol. At pressures higher than $1X10^{-1}$ Pa, four solid phases exist in the system. These are TiB_2, C, $TiC_{0.8}N_{0.2}$ and BN in molar quantities of 0.09 mol, 0.27 mol, 0.90 mol, and 0.82 mol respectively (Benko et al., 2001).

2.1.11 Interaction between cBN and liquid phase sintering aids (SiO_2)

CBN and SiO_2 have low coefficients of thermal expansion and electrical conductivity. But cBN has high hardness values and thermal conductivity unlike SiO_2. cBN does not readily react with SiO_2. Spark plasma sintering would restrict the cBN to hBN phase transformation due to the short sintering time involved. The phase transformation temperature was higher than usual (1973 K) in the presence of SiO_2 than with other secondary phases (Zhang et al., 2014).

2.2 Whisker reinforcement of ceramics

2.2.1 Processing of whisker reinforced ceramics

Reinforcement using fibre has been successfully used to increase the fracture toughness of ceramics. Only a few types of fibres can be considered possible candidates for the reinforcement of high performance ceramics due to the effects of chemical incompatibility between fibres and the matrix and/or the high temperatures required during sintering and/or use. Silicon carbide whiskers are accepted as the most promising fibres thus far since they retain their high strength at high temperatures up to at least 1600ºC. Scanning electron microscopy (SEM) of multiple whiskers showed that the whiskers contained both particulate material in the form of smooth crystals and in the form of bundles of fibres. These particulates could possibly act as flaws in a ceramic matrix composite structure (Lundberg et al., 1987).

2.2.2 Whisker/powder mixing

A wet processing method has been used to ensure a homogeneous distribution of whiskers in the whisker/powder mixture. Mixing can be carried out in either a dispersed or flocced state depending on which technique is used to form the composite. In slip casting a properly stabilized and dispersed slip mixture with a low viscosity and high solids content must be used to reach high green densities after casting. This can be obtained by choosing a pH where both the matrix and the whiskers have a high zeta potential with an identical charge. Surfactants can be used to increase the stability and change the zeta potential curve for one or both components so that a wider range of pH can be used. For the remaining forming methods such as pressing, flocced mixing must be considered. Systems consisting of multiple components can be effectively mixed in a few minutes in a flocced state. Flocculation occurs when whiskers and matrix powders are differently charged or have zeta potentials near zero. The aggregates of the flocs formed contain both components but they are not very homogeneously mixed.

The flocs may be broken up with a mixer with relatively high shear rate but only if the shearing continues. Once the flocs leave the high shear-rate field they reform and “freeze” the in the homogeneous state the mixture achieved. The best possible mixers are high speed homogenizers and ball mills with plastic or even ceramic balls. Once a mixed floc has formed it remains stable for several weeks and will not segregate (Lundberg et al., 1987).

2.2.3 Whisker toughening in ceramic materials

The inclusion of whiskers in many ceramics has resulted in significant benefits being achieved. Whisker toughening is just as effective as ZrO_2 toughening at an ambient temperature. In comparison to ZrO_2 toughening, the amount of toughening remains relatively consistent at high (>1000ºC) temperatures. Fracture toughness values can further be increased by the incorporation of both ZrO_2 and whiskers and in some cases both types of toughening has also been observed.

Fracture toughness levels in fibre reinforced ceramic matrix composites (CMCs) are the highest among all ceramic composites. The shorter whisker reinforcement offers many advantages i.e. easier fabrication and a higher degree of isotropy in material properties due to the smaller aspect ratios involved (Bengisu et al., 1991).

To achieve maximum toughening the following parameters need to be considered:

- *τi* (interface shear stress): partial resistance to slip is needed but it should not be too high otherwise pull-out will not occur. Lower shear stresses are preferable in order to increase pull-out and debonding lengths.
- *lpo* (pull-out length) pull-out lengths should be increased for maximum toughening. This can be accomplished by minimizing the compressive stresses acting on the whiskers, lowering the mechanical clamping force by using smooth surfaced whiskers and coating the whiskers with lubricants to prevent chemical reactions at the interface and decrease interfacial friction.
- *r* (whisker radius) decreasing whisker radii provide higher toughening.
- *Vf* (whisker volume fraction): the quantity of whiskers should be as high as processing method allows.
- *σw* (whisker strength): high whisker strengths are most favourable since higher strengths provide more significant improvements in toughening.
- *lDB* (debond length): this factor should be maximized as much as possible by decreasing whisker/matrix interaction.
- *Φ* (deflection angle): deflection angles should also be maximized by monitoring whisker/matrix interface characteristics (Bengisu et al., 1991).

2.2.4 Proposed toughening mechanisms for whisker reinforced CMC's

Observations in whisker toughening in whisker reinforced CMC's allude to the possibility of five toughening mechanisms to be taking place. These mechanisms are crack deflection, micro-cracking, whisker pull-out, crack bowing and crack bridging (Bengisu et al., 1991).

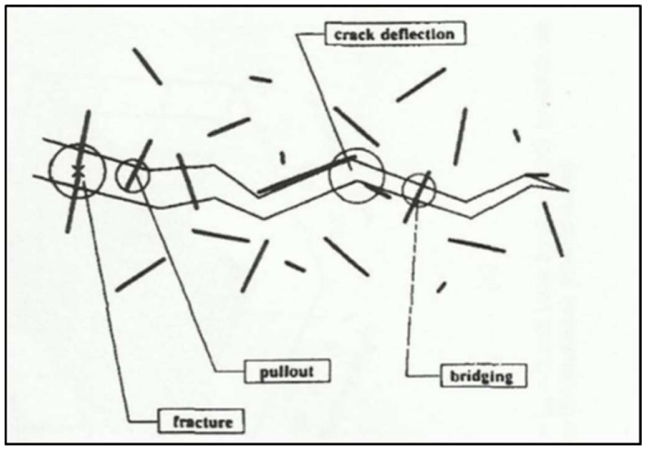


Figure 2.6 Typical processes occurring during crack propagation in whisker reinforced ceramics (Bengisu et al., 1991).

2.2.4.1 Microcracking

Microcracking is not uncommon in ceramics reinforced with whiskers. Recent experimental and theoretical analyses show that toughening due to microcracking in non-transformational ceramics is negligible at best.

Evans and Farber's Model of microcracking induced toughening is based on the concept that microcracking leads to dilatations in the material which produces compressive stresses on a macrocrack. Their model predicted that toughness only increased by 10% (Evans & Faber, 1984). Another model by Dolgopolsky et al. considers the possibility of two opposing effects due to microcracking. One effect is the diminishing of crack growth resistance due to linking of microcracks and the other effect is crack shielding by nucleated microcracks (Dolgopolsky et al., 1989).

2.2.4.2 Crack bowing

Crack bowing initiates from resistant second phase species in the path of a propagating crack. Faber and Evans' calculated that the highest toughening by this mechanism is achieved in the case of discs with high aspect ratios whereas the lowest toughening is achieved in the case of rods (Evans & Faber, 1984). The crack bowing theory postulates that toughening is predominantly a function of obstacle penetrability (related to an obstacles toughness, strength and the coherency of said obstacle/matrix interface), the volume fraction of second phase and the size obstacle itself. Following that, whiskers are therefore theoretically less effective in bowing a crack front than e.g. metal discs/inclusions as the whiskers have a rod-like shapes and hence easier to penetrate by the crack due to their lower comparative fracture toughness. Furthermore, it can be debated that crack bowing is not a major contributor as a toughening mechanism in whisker reinforcement, although it should not be disregarded completely.

Crack pinning observations suggest that a minor contribution is possible although, though crack bowing theory is not fully established it can be used to calculate this contribution with any confidence. (Dolgopolsky et al., 1989)

2.2.4.3 Whisker pull-out

Becher et al. determined whisker pull-out toughening can be considered as the work done by the sliding of whiskers within the matrix. Whisker pull-out is often seen in whisker reinforced CMC's even though in many cases pull-out length is limited to 1-2μm. Becher et al. calculated the average pull-out lengths as 1.2-2.0 μm in Al_2O_3 or SiC_w, 0.4-0.8μm in mullite or SiC_w, and 0.2-0.4μm in glass or SiC_w composites, where whiskers are untreated (P. Becher & Hsueh, 1989). Pull-out toughening can be encouraged by increasing the pull-out lengths.

This can be done by preventing the formation of interaction layers between the matrix and the whiskers and using whiskers with smooth surfaces to prevent mechanical keying. Chemical interaction layers have been observed by careful examination of whisker matrix interfaces.

Thin amorphous layers have been observed in Si_3N_4/SiC_w composites formed due to chemical reaction at high sintering temperatures. High temperature oxidation or reaction was also found to produce a surface oxide scale on the SiC_w in alumina matrices, resulting in mullite interfaces. When oxygen content on the surface of SiC whiskers is high the resulting composite toughness is lower overall (Bengisu et al., 1991).

2.2.4.4 Crack deflection

Crack deflection is frequently seen in whisker reinforced ceramics irrespective of the matrix types. Liu et al. modelled toughening by crack deflection for whisker reinforced CMC's with whiskers randomly positioned in two dimensions. To compensate for whisker orientation in hot pressed composites. Liu et al. compared their predictions to experimental results from the literature. Accrediting all of the observed toughening in whisker reinforced ceramics to only crack deflection over stresses the importance of the mechanism (Liu et al., 2002).

Carter and Hurley determined crack deflection angles in $MoSi_2$/SiCw composites and deduced that a 20 vol. % whisker reinforcement to the matrix increases median deflection angles from 7.2° to almost 13.0° while the toughness was increased from 5.3 to 8.2 $MPa.m^{1/2}$ (Carter & Hurley, 1987).

Seshadri et al. used computer simulations to show that significantly lower toughening should be anticipated from crack deflection than originally projected by Faber and Evans as their deflection angles were overvalued by their model. The analytical model proposes that the main crack is deflected at all angles evenly up to a maximum angle of 90º, disregarding a large input of 0° angle i.e. un-deflected cracks (Seshadri et al., 2008).

2.2.4.5 Crack bridging

Crack bridging phenomena have been seen in multiple composites and are well defined in rubber toughened polymers, in coarse grained Al_2O_3 and in cermets (P. Becher & Hsueh, 1989). In coarse grained, single phase ceramics toughening is suggested to take place via two mechanisms. The first mechanism at work is frictional interlocking of opposing fracture surfaces as the main crack tends to grow and the crack opening displacement (COD) increases. The second of the two mechanisms involve the formation of ligamentary bridges.

The fracture resistance is amplified by this phenomenon given that propagation of the crack can only occur if these ligaments are fractured. Whiskers and fibres can act as locations for crack bridging just as coarse grains do. Experimental research involving TEM and SEM concluded that the existence of crack bridging in many whisker-toughened composites e.g. Al_2O_3-SiC_w, mullite-SiC_w and glass-SiCw. Becher et al. regarded the toughening phenomenon in whisker reinforced ceramics, largely attributing toughening to the crack bridging mechanism (P. Becher & Hsueh, 1989).

2.3 Sintering and densification of ceramics

2.3.1 Spark Plasma Sintering (SPS)

Spark plasma sintering (SPS) is a process by which ceramic powders can be sintered at a rapid rate to fully achieve density. It is very similar to hot pressing as graphite dies are used as well, but the heating is done differently. If the green body is made up of an electrically conductive material; the resultant energy is dissipated within the sample and the electrically conductive sections of the pressing tool. If the green body is made up of a non-conductive material, the conductive pressing tool needs to transmit the heat produced by Joule heating via conduction to the powder (Guillon et al., 2014).

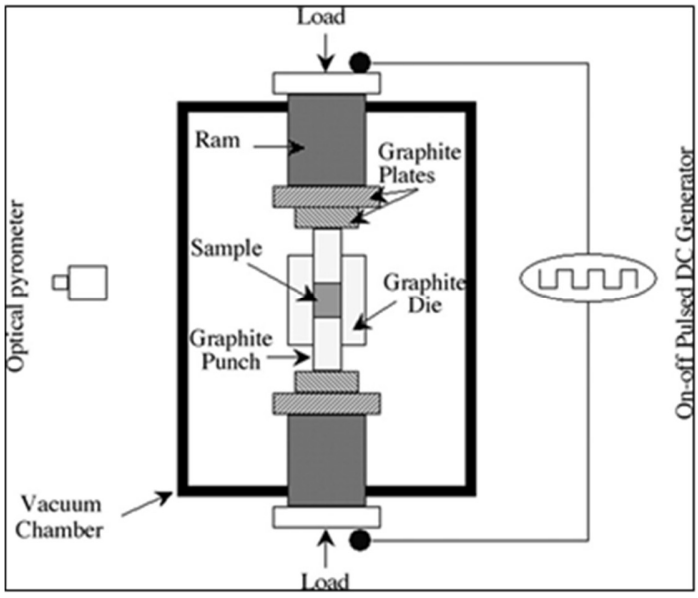


Figure 2.7 Schematic representation of the spark plasma sintering apparatus (Zhao & Wang, 2009)

2.4 Reinforcement materials

2.4.1 Silicon Carbide Whiskers (SiC_w)

Silicon Carbide (SiC) ranks superior to alumina in terms of its higher thermal conductivity, refractoriness, abrasive resistance and chemical inertness (Bertram & Gerhardt, 2011). SiC in whisker form has been revealed to be an outstanding reinforcement material in comparison with particulates, in ceramic and glass matrix composites.

Whiskers gave better high temperature properties and hence improving the potential of the materials for use in high temperature engineering applications.

SiC whisker reinforced composites of alumina, mullite and zirconia matrices have been studied in depth and Al_2O_3-SiCw composites have been tested in machining and tool application. β-SiC is less brittle and less susceptible to damage during fabrication in comparison with the alpha form (Raju & Verma, 1997).

2.4.1.1 Formation of SiC_w

Several methods are used for the production of SiC whiskers including sol-gel, plasma deposition, chemical vapour deposition (CVD), reaction of Silicon-carbon (coal tar pitch) mixtures, silica methane pyrolysis of rice-hulls and silicon nitride. Whiskers produced from rice hulls at 1300-1500ºC contain a mixture of alpha and beta modifications or are predominately in the cubic beta form along with particulates. Many investigations used catalysts such as Pd, Ni or Co. Beta silicon carbide whiskers have been observed on a carbon substrate over which a mixture of N_2 and methyl-trichlorosilane vapour was passed at 1500ºC.

Ultrafine silicon carbide powders have also been produced by gas phase synthesis in an argon/hydrogen plasma jet from silicon tetrachloride and methane. The morphology and surface chemistry of SiC whiskers are very much dependant on the method of manufacture and the raw materials used, and eventually control the properties of the SiC reinforced composites. Whisker reinforcements considerably increase the fracture toughness and strength of simple matrix materials.

Despite the environment problems and health hazards in handling whiskers, their use is beneficial in view of the tribological and mechanical properties. Beta SiC whiskers have been produced from rice-hulls in pure form without the use of a catalyst and extra carbon (Raju & Verma, 1997).

2.4.1.2 Characterization of SiCw

Pyrolysed products are characterized by X-ray Diffraction (XRD), Infrared Spectroscopy (IR), Scanning Electron Microscopy (SEM) and Thermal Analysis (TA). The X-ray powder diffraction analysis was carried out using CuKα radiation with a nickel target. The density of the material was determined by the specific gravity bottle method and surface area by micron photosizer (Raju & Verma, 1997).

2.4.1.3 Microstructure of SiC_w

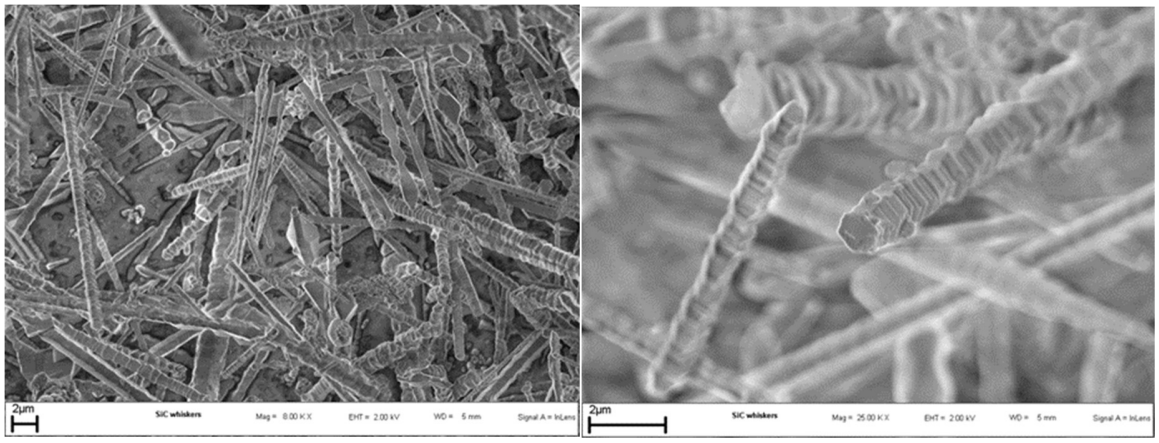


Figure 2.8 SEM images of Silicon Carbide whiskers

2.4.2 Boron Nitride

Boron and Nitrogen are in the same row as Carbon on the periodic table of elements. When combined Boron and Nitrogen have the same number of outer shell electrons as Carbon. The atomic radii of Boron and Nitrogen are also like Carbon. Therefore, Boron nitride can exhibit the same crystal structures as carbon. Just as carbon exists as graphite and diamond, boron nitride can be synthesized in hexagonal and cubic forms. Hexagonal boron nitride powder is synthesized by nitridation or ammonolysis of boric acid at elevated temperature (*Boron Nitride (BN) - Properties and Information on Boron Nitride*, 2001).

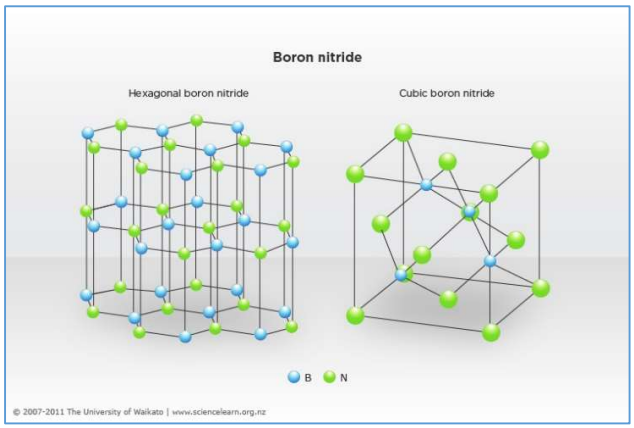


Figure 2.9 Crystal structures of Boron Nitride (*Boron Nitride* | *Sciencelearn Hub*, n.d.)

Cubic boron nitride (cBN) has the same structure as diamond and its properties are like those of diamond. CBN is the second hardest material next to diamond. It was first synthesized in 1957 (*Boron Nitride (BN) - Properties and Information on Boron Nitride*, 2001).

Table 2.2 Typical properties for hexagonal and cubic boron nitride

Property	hBN	cBN
Density ($g.cm^{-3}$)	2.00-2.28	3.45
Hardness (Mohs)	1.5	9.5
Surface Microhardness - Knoop's pyramid test ($kg.mm^{-2}$ at 300K)	-	4500
Bulk Modulus (GPa)	36.5	400
Melting Point (°C)	2800 (decomposes)	2973
Specific Heat (J.g-1.°C-1)	±0.8	±0.6
Thermal Conductivity ($W.cm^{-1}.°C^{-1}$)	≤0.6 Parallel to the C axis ≤6 Perpendicular to the C axis	7.4
Linear Thermal Expansion ($°C^{-1}$)	3×10^{-6} Parallel to the C axis -2.7×10^{-6} Perpendicular to the C axis	1.2×10^{-6}

Reference: ("NSM Archive - Boron Nitride (BN) - Mechanical Properties, Elastic Constants, Lattice Vibrations," n.d.), ("NSM Archive - Boron Nitride (BN) - Thermal properties," n.d.)

2.4.2.1 Formation of cBN

Cubic boron nitride is formed by high pressure-high temperature (HPHT) treatment of hexagonal boron nitride. Hexagonal boron nitride (hBN) has the equivalent structure of graphite and like graphite it has a plate like microstructure. The layered lattice structure gives it excellent lubricating properties. HBN is resistant to sintering and is usually formed by hot pressing ("AZO Materials - *Boron Nitride (BN) - Properties and Information on Boron Nitride"*, 2001).

2.4.2.2 Characterization of cBN

Prepared cBN or Polycrystalline cBN (PcBN) is characterized by measuring physical properties such as density, microhardness, fracture toughness and by phase and microstructural analysis. Densities are measured by weight and volume which are determined by immersion in distilled water using the Archimedes principle. Measurements of microhardness and fracture toughness are made using a hardness tester by making indentations with a diamond pyramidal indenter. Microstructure was examined by using a scanning electron microscope (SEM) and a transmission electron microscope (TEM). An x-ray diffraction (XRD) study would be carried out to identify existing phases in sintered samples (Zhao & Wang, 2009).

2.4.2.3 Microstructure of cBN

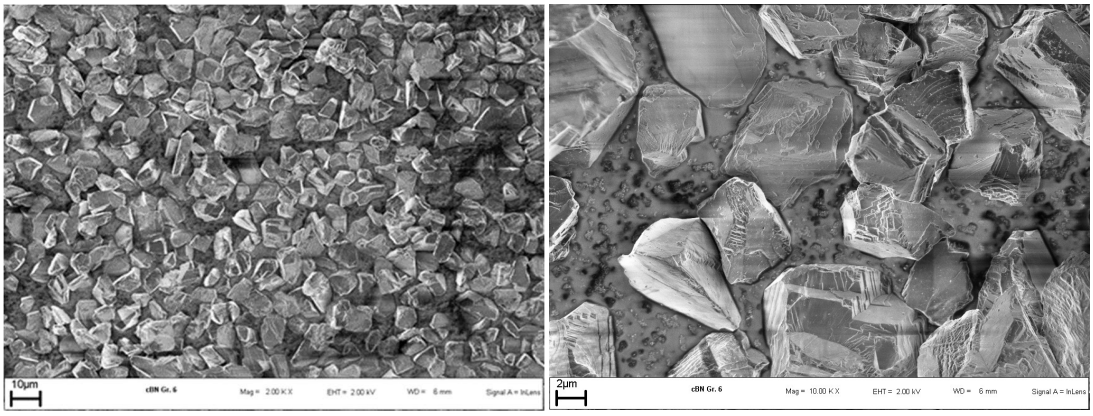


Figure 2.10 SEM morphologies of cBN powders

2.5 Fracture in ceramics

In ceramic materials dislocations are reasonably immobile and dislocation induced plasticity does not usually occur in standard temperature conditions. This is the basis for their high hardness and inherent brittleness. Because localized stress concentrations cannot be relaxed by yielding, careful design is needed with regards to highly loaded ceramic parts. This suggests the need for more precise tolerances and for very careful handling of those parts. At the region of load transfer onto the component a high stress may occur, and detrimental tensile stresses may even exist around the compressive contact zones. Mechanical testing is far more complex for ceramic materials than ductile materials since the challenges arising from any misalignment of samples can be extreme (Danzer et al., 2008).

2.5.1 Contact failure

Loading contact of hard surfaces via dynamic and/or static impingement of bodies can lead to cracking if the critical values for the stresses are exceeded. This type of damage generally occurs in one of the two modes: local area loading (blunt contact) or point loading (sharp contact). Local area loading occurs when the surfaces of two bodies touch each other in such a way that they deform elastically and form a circular contact area.

The material under this contact area experiences compressive stresses whose amplitude is a function of the elasticity of the two and which increases with both applied load and decreasing radius of the sphere. The contact zone is encircled by a narrow ring shaped region where significant tensile stresses occur (Danzer et al., 2008).

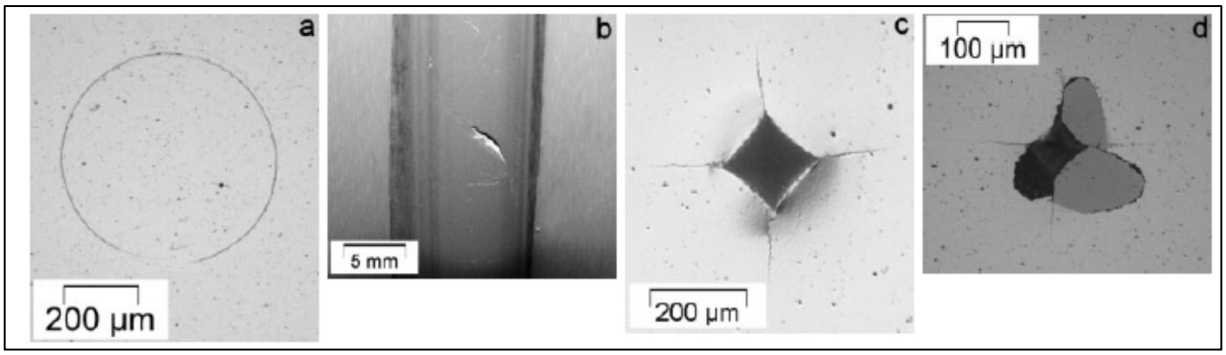


Figure 2.11 Contact damage/cracks on the surface of ceramics: a) Hertzian ring crack in silicon nitride and b) crack caused in operation by the rolling of high alloyed steel wires. These cracks were caused by blunt contact. c) Radial cracks in the corners of a Vickers indent in silicon nitride and d) breakout due to lateral crackers under a Vickers indent in silicon carbide. These cracks were caused by a sharp indenter (Danzer et al., 2008).

2.5.2 Ball on three balls (B3B) biaxial strength testing

The Ball on three balls (B3B) test is a biaxial strength test for brittle materials. This type of testing can be applied on specimens having a wide range of shapes (most frequently discs and plates) and sizes. In-service biaxial stress states are very common e.g. in thermal shock load. Biaxial testing is more realistic in many cases compared to conventional bending testing (where a uniaxial stress state is used). In brittle materials failure is generally initiated from crack like defects which are present in the volume or on the surface of the specimens. Surface flaws are often caused by the machining and/or finishing of specimens or components. In biaxial testing surface cracks in any given direction are loaded in Mode I and can consequently cause failure in the specimen. Biaxial strength testing results in much lower strength values than uniaxial testing. The B3B test creates a biaxial stress state on the specimen which is more sensitive to defects than the uniaxial one. Therefore, it stands to reason that in B3B testing surface defects are a more critical factor (Harrer et al., 2011).

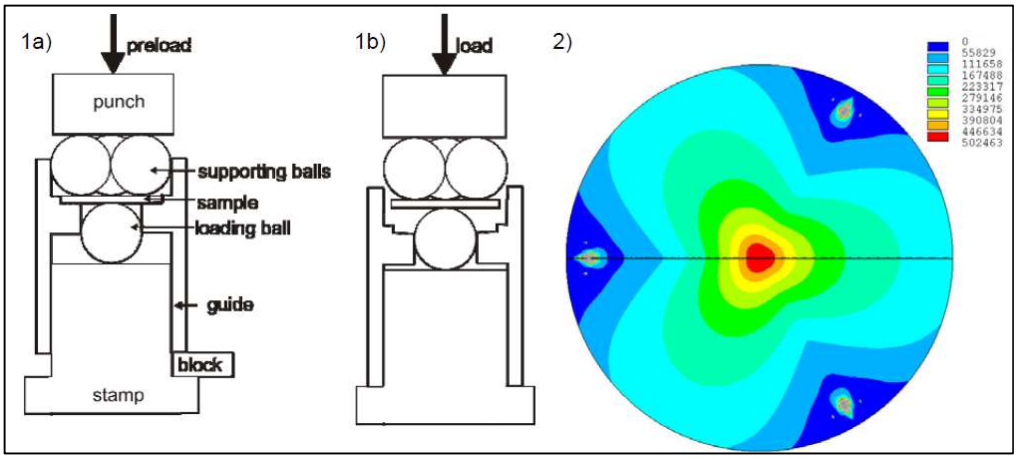


Figure 2.12-1 a) and b) Experimental setup of the B3B test: a) shows the set-up with applied pre-load b) the set up (with the guide lowered) just before the start of the fracture. Figure 2.11-1 First principal stress field for F=1N [in Pa] bottom view of the tensile stress surface of the disc for a silicon nitride specimen with the diameter of 20 mm and a thickness of 2 mm (Harrer et al., 2011).

The stress field of the specimen in B3B testing has a cloverleaf symmetry and can only be determined numerically. The maximum tensile stress appears concentrated in the centre of the disc on the opposing side of the loading ball where the biaxial stress state exists. The maximum tensile stress σ_{max} can be determined by the following equation:

$$\sigma_{max} = f.\frac{F}{t^2}$$

F is the load at the moment of fracture, t is the thickness of the disc and f a dimensionless factor which depends on the t/R ration (ratio of sample thickness to sample radius, R_a/R ratio (ratio of the support radius to the sample radius) and on v the Poisson's ratio of the tested material (Harrer et al., 2011).

2.6 Wear by hard particles

Abrasive wear is the removal of material caused by the presence of hard particles, of hard particles between or embedded in one or both surfaces in relative motion, or by the presence of hard protuberances on one or both of the relatively moving surfaces (Rigney, 2003). A "hard particle" can be the product of processing or arise from particles that enter from outside the tribosystem, such as dirt particles. Protuberances such as surface roughness on machined surfaces act as "hard particles" if the surface is significantly harder than the counter surface (K.-H. Zum Gahr, 1987).

Abrasive wear may be categorized as two-body or three-body abrasion. In two-body abrasion, abrasive particles move freely over a material surface e.g. sand sliding down a chute or in the dredging of sand/gravel. In three-body abrasion, abrasive particles act as interfacial elements between the solid body and the counter body. Examples of this type of abrasion are the extrusion of plastics containing abrasive particles and jaw crushers. The wear in the three-body abrasion is much smaller than in two-body abrasion. This is because in three-body abrasion only a small portion of the abrasive particles cause wear, due to variations in the angle of attack (K.-H. Zum Gahr, 1987). A theoretical understanding of abrasive wear is based on distinguishing between the different physical processes that occur during abrasion, namely microploughing, microcutting, microfatigue and microcracking. These processes occur when the abrasive material is harder than the surface which is being abraded. Abrasive wear occurs at a low or a high level depending on the ratio of hardness of the abrasive to hardness of the surface being worn. For homogenous material of equal hardness, the transitions from the lower to the higher wear level can clearly be seen (K.-H. Z. Gahr, 1998).

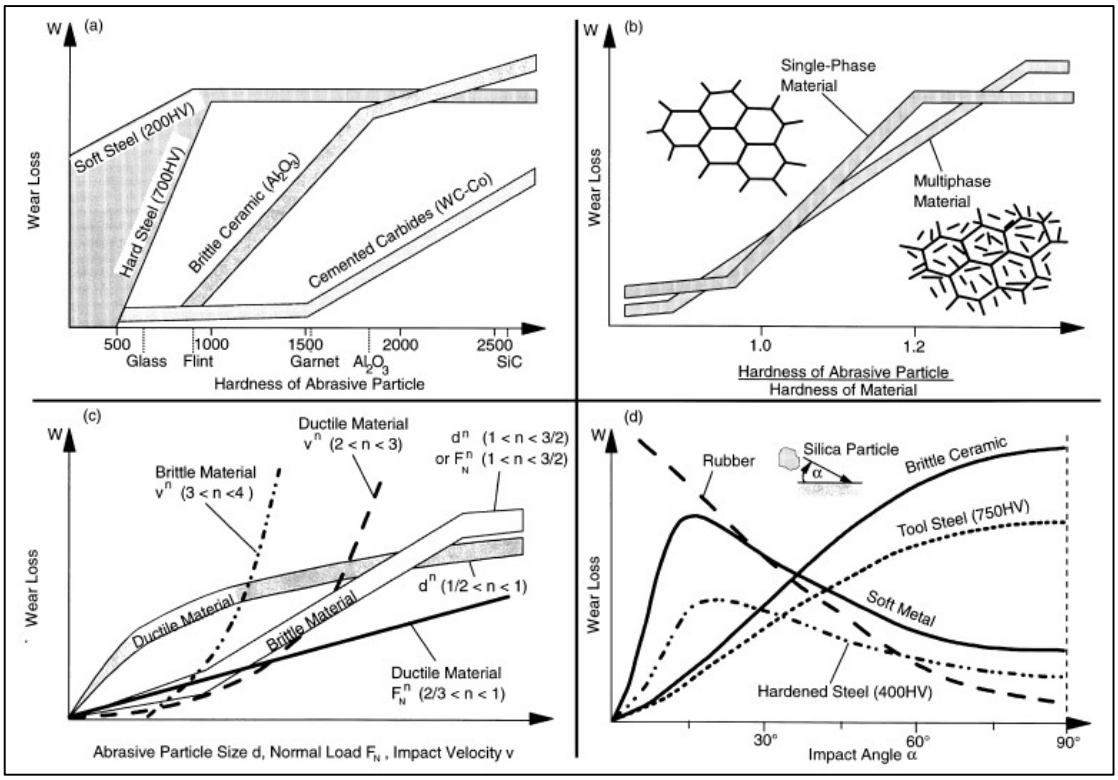


Figure 2.13 Graphs of wear loss by hard particles as a function of material properties and operating parameters such as: a) hardness of the abrasive particle, b) ratio of hardness of the abrasive particle and hardness of the wearing material, c) abrasive particle size, normal load and impact velocity and d) impact angle without considering lubrication (K.-H. Z. Gahr, 1998).

At equivalent bulk hardness, the matrix of the material containing hard carbides is softer than the matrix of the homogenous material. The transition from a lower to a higher wear level of inhomogeneous materials begins when the hardness of the matrix and the hardness of the carbides are respectively exceeded by the hardness of the abrasive. An abrasive of hardness less than or equal that of worn surface is called a “soft abrasive” and an abrasive harder than the worn surface a “hard abrasive” (K.-H. Zum Gahr, 1987).

2.6.1 Models for abrasive wear

2.6.1.1 Abrasive wear by plastic deformation

A simplistic model for abrasive wear entails the removal of material by plastic deformation. This model, Fig. 2.14, shows an abrasive particle, defined as a cone of semi-angle α, being drawn across the surface of a ductile material which moves away under an indentation pressure P. It forms a channel in the material, and wear occurs by the removal of some proportion of the material which is displaced by the particle from the channel. The normal load W carried by the particle is supported by plastic flow beneath the particle, which causes pressure P to act over the area of contact between the particle and the surface (K.-H. Zum Gahr, 1987).

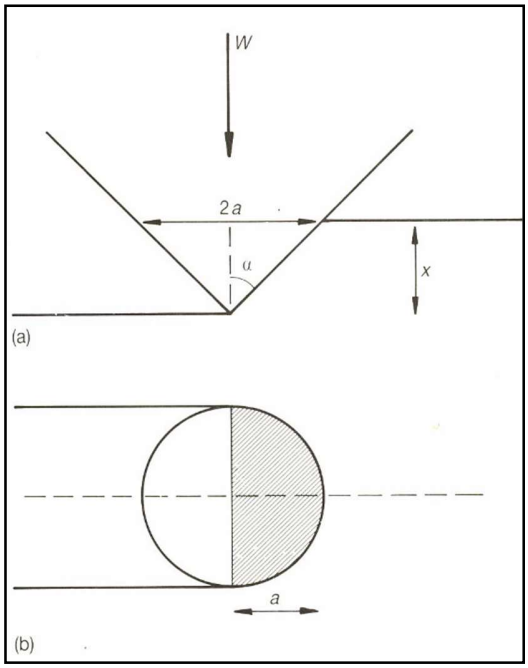


Figure 2.14 Geometry of contact between an idealised conical abrasive particle and a surface: (a) in elevation; (b) in the plane view (K.-H. Zum Gahr, 1987)

2.6.1.2 Abrasive wear by brittle fracture

Another predicted model for abrasive wear is one in which material removal takes place by brittle fracture, with an insignificant contribution from the mechanisms associated with plastic flow (K.-H. Zum Gahr, 1987). If a brittle surface is indented at a sufficiently high load by a blunt/dull (e.g. spherical) body and the contact stresses remain elastic, then a Hertzian cone crack will form. If the indenter slides over the surface a series of incomplete conical cracks forms, intersecting the surface in a row of circular arcs. Neither a complete conical crack nor a row of partial cone cracks leads readily to material removal.

If the sliding object is a hard, angular and abrasive particle then local plastic deformation can occur at the point of contact. This leads to the formation of cracks with different geometry which can cause immediate wear.

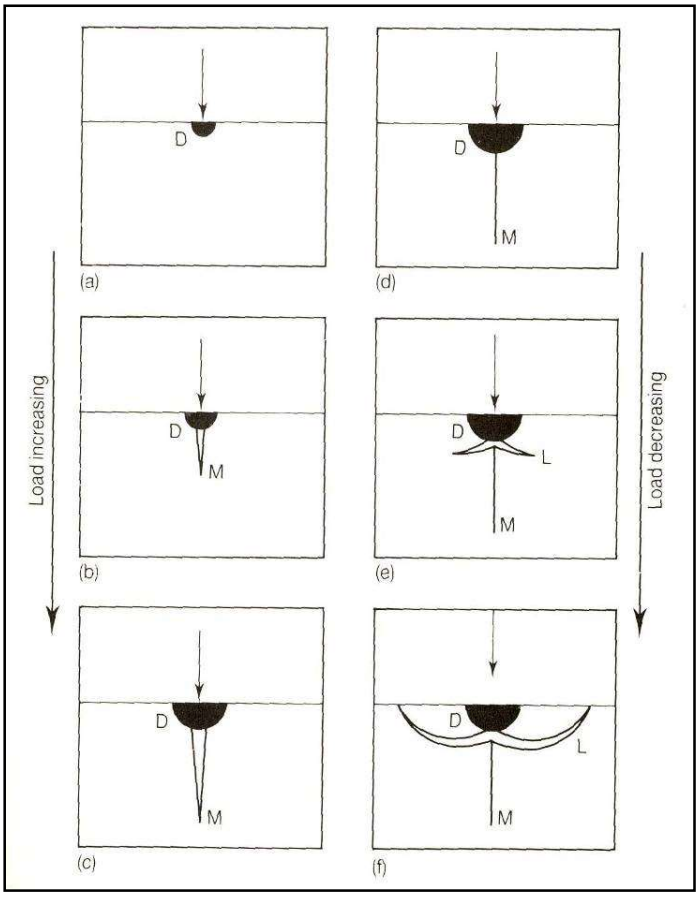


Figure 2.15 Diagram showing crack formation in a brittle material due to point indentation. The normal load increases from (a) to (c), and is then progressively reduced from (d) to (f) (Lawn & Swain, 1975)

The figure above shows how cracks can form in a brittle solid material subjected to a point contact load. These types of cracks grow beneath the sharp point of the rigid indenter (i.e. a cone or pyramid) which generates an elastic-plastic stress field. They differ greatly from the types of Hertzian cracks which form in elastic stress field under a blunt indenter (e.g. spherical) (K.-H. Zum Gahr, 1987).

2.6.2 Types of physical interactions that occur during abrasive wear

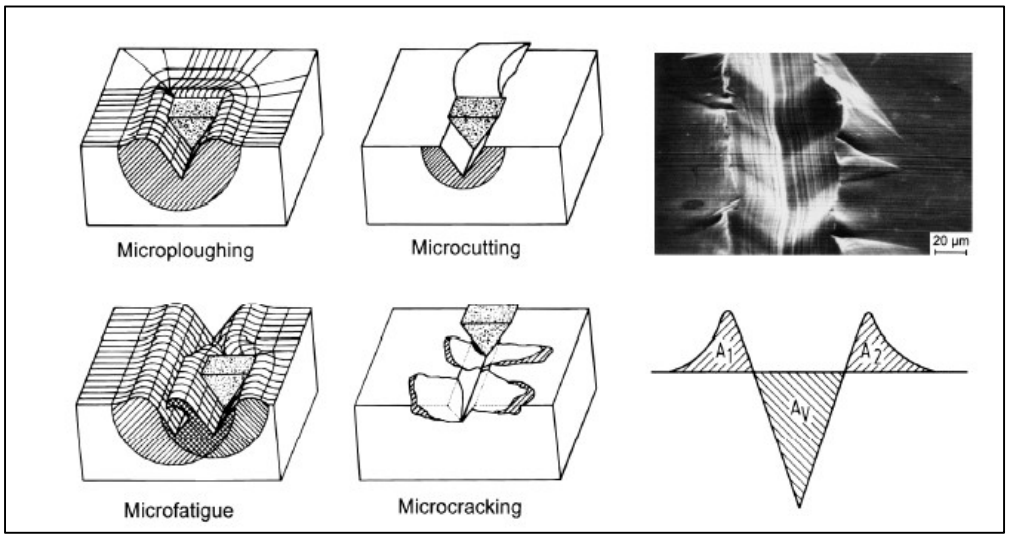


Figure 2.16 Schematic representation of different interactions between sliding abrasive particles and the surface of materials, scanning electron micrograph of a wear groove on an austenitic steel and a draft of a taper section through the wear groove (K.-H. Z. Gahr, 1998)**.**

2.6.2.1 Microploughing

In the model situation, microploughing due to an individual pass of one abrading particle does not cause any detachment of material from an abraded surface. A prow is formed ahead of the abrading particle and material is continuously displaced along each side to form ridges adjacent to the groove produced (‘Microstructure and Wear of Materials’, 1987a) (‘Microstructure and Wear of Materials’, 1987b).

2.6.2.2 Microfatigue

During microploughing material loss can occur due to the combined action of many abrasive particles acting simultaneously or successively. The repeated ploughing action of passing particles may result in a type of low cycle fatigue which would cause material to break off this is known as microfatigue (K.-H. Zum Gahr, 1987).

2.6.2.3 Microcutting

Pure microcutting results in a loss of material equivalent to the volume of the wear groove produced by the abrasive particle.

2.6.2.4 Microcracking

Microcracking occurs when highly concentrated stresses are exerted by abrasive particles. It occurs most commonly on brittle material, where large pieces of wear debris are detached from the surface due to crack formation and propagation.

Microploughing and microcutting are more prevalent in more ductile material. The ratio of microploughing to microcutting depends on the attack angle of the abrasive hard particles.

2.6.3 Factors that affect abrasive wear

2.6.3.1 Critical attack angle α

The orientation angle of the abrasive particle to the base material determines the types of physical interactions that occur. The critical value of this angle determines whether microcutting or microploughing occurs. Critical attack angle αc is a function of the wearing material and the test conditions (Sedriks & Mulhearn, 1964).

Theoretically, α_c describes a sharp transition between microploughing and microcutting. In experimental results it is shown that the transition from microploughing to microcutting is more gradual as the attack angle increases. Material is detached from a surface by microcutting when the attack angle of the abrasive hard particles is greater than a critical value (Sedriks & Mulhearn, 1964).

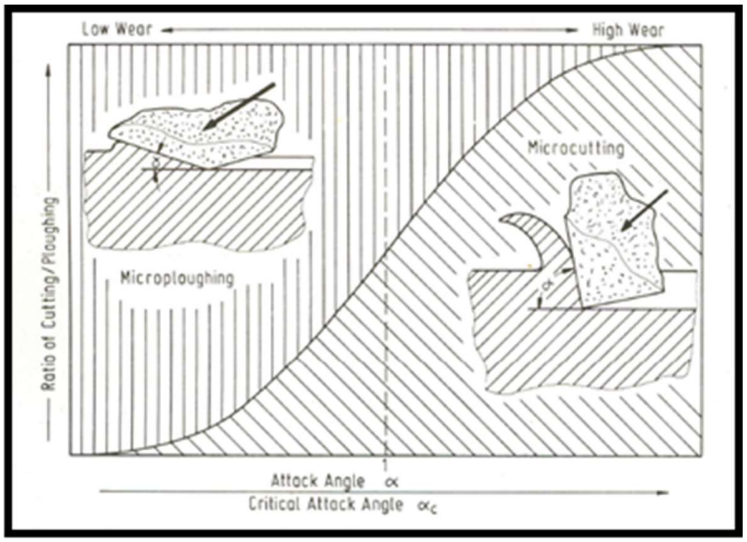


Figure 2.17 Ratio of microcutting to microploughing as a function of the ratio of the attack angle to the critical attack angle (K.-H. Zum Gahr, 1987)**.**

The attack angle is defined as the angle between the leading face of a contacting abrasive particles and the wearing surface. The critical attack angle is determined primarily by the co-efficient of friction between the contacting surfaces (Sedriks & Mulhearn, 1964).

Work hardening of the material results in an increase of the critical attack angle, as established by the research of Challen et al. 1983 (Tabor, 2000). The coefficient of wear includes a probability factor that allows for distribution of the attack angles during abrasion by multiple contacting abrasive particles. Therefore, only a small percentage of all the abrasive particles can form chips. Larsen-Badse (1968) had recorded that approximately 50% of the grains of SiC abrasive papers contacting a surface removed material in the form of tiny chips. In addition to the angle of attack, the distribution, size and shapes of the abrasive particles was also found.

2.6.3.2 Lubrication and environmental factors

Both lubrication type and the nature of the surrounding environment (e.g. humidity) have an overwhelming influence on wear by abrasion. The effect of lubrication on abrasive wear differs greatly to that of sliding wear.

Lubrication in sliding wear tends to reduce wear by decreasing the tangential stresses on the surface and by decreasing the frequency and impact of asperity contact. Between comparatively smooth surfaces, protective lubricant films are easily formed.

Abrasive particles however tend to be significantly larger than the hydrodynamic/ elasto-hydrodynamic film thickness and thus the film is unable to prevent direct contact between the particle and the counter face.

Therefore, in abrasive wear, lubrication would not cause a great reduction in wear rate seen in the absence of hard particles but is known to increase the wear rate. The abrasive wear rates of metal under two-body circumstances might be tripled when lubricating oil is applied. The predominant cause of this effect is that the lubricant lessens the friction between the abrasive particles and the metal surface, henceforth increasing the range of attack angles for which the cutting mode of deformation would occur thus leading to an amplified effectiveness in material removal (Axén et al., 2001). Numerous mechanisms can be attributed for a progressive decline in abrasiveness; fracture of particles, leading to a decrease in the number of cutting points; removal of whole particles from the binder resin (shelling); rounding of contact areas of particles by chemical, mechanical or thermal mechanisms (attrition); adhesion of wear debris to the tips of particles (capping); and the collection of wear debris in the spaces between particles so that it carries part of the applied load (clogging). The rates and relative importance of these mechanisms vary with specimen material (Axén et al., 2001).

Lubrication may also have the secondary effect of reducing adhesion of wear debris to the abrasive particles. This results in the slowing of the reduction in abrasiveness under multiple-pass/run situations by capping or clogging. Due to these factors the wear rate is increased due to lubrication whenever a plastic abrasion mechanism is dominant. The consequences of lubrication in brittle materials is less constant. The reduction in the tangential force by lubrication may lower the inclination to cracking but lubricants may also lead to greater crack growth rates through localised chemical effects at the crack tip (Axén et al., 2001).

Environmental factors can also encourage a change under previously constant abrasion conditions from fracture dominated wear to plastic wear modes. Atmospheric conditions can also influence abrasive wear rates, with Oxygen content and moisture/humidity being highly important factors. The effect of the gaseous atmosphere is often very complex. Even in high ductility metals the effect can fluctuate in size and directionality.

Generally, Oxygen offers a lubricating action in the abrading of metals. Rapid oxidation of the newly exposed metal surface at the tip of the abrasive particle produces a thin oxide layer/film with low shear strength that reduces adhesion between the particle and the metal. A similar effect is observed in conventional metal cutting, where volatile smaller scale molecules such as Oxygen, Chlorine or Carbon tetrachloride can react rapidly with clean metal surfaces both on the work specimen and on the cutting tool itself and lower the frictional force on the tool. The abrasive wear of metals in the absence of Oxygen is commonly less acute than in its presence, cutting is less efficient but in two-body wear, increased adhesion between metallic debris and the abrasive articles also leads to an advanced lowering in wear rate, due to capping and clogging (Axén et al., 2001).

2.6.4 Testing methods for abrasive wear

The most used abrasive wear tests use either a pin shaped specimen sliding against a fixed abrasive or a rotating wheel sliding against a planar specimen with loose abrasive particles being constantly delivered in between the two objects. Pin on abrasive disc, pin on abrasive wheel and pin on abrasive drum are three standard variations of the method in which a specimen pin slides against fixed abrasive particles, giving a two-body wear situation. Commercially adhered abrasive paper/cloth is commonly used for the counter face. Thus, conveying grit particles of a narrow size distribution which are evenly spread out and bonded to the counter face by a strong resin. The wear rate due to a fixed abrasive particle decreases with subsequent passes of a specimen along the previous track.

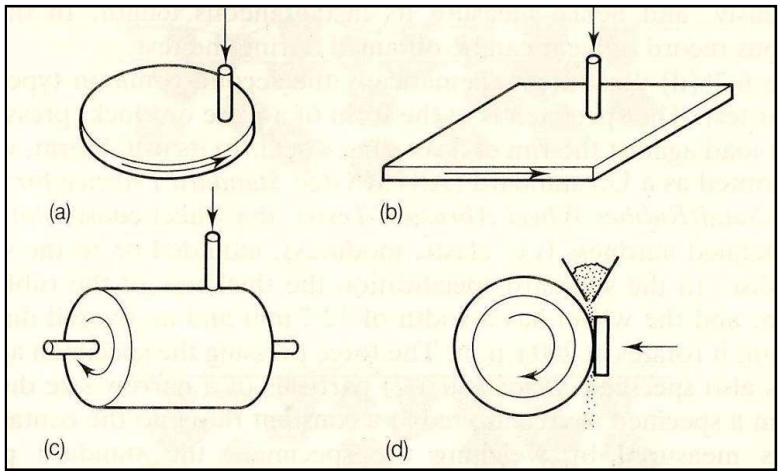


Figure 2.18 Schematic illustrations of four common methods used to measure abrasive wear rates of materials: (a) Pin on abrasive disc; (b) pin on abrasive plate; (c) pin on abrasive drum; (d) rubber wheel abrasion test (Axén et al., 2001)

In order to negate the detrimental effects caused by degradation of the abrasive, it is usually guaranteed that the specimen always slides against fresh/new abrasive. In the pin on disc geometry, this can be achieved by moving the pin radially on the disc during testing (producing a spiral wear track). Other geometries require rectilinear sliding over a rectangular sheet of abrasive paper or moving the pin axially along a rotating cylinder covered with abrasive particles (pin on abrasive drum). In each case a consistent load/force is loaded on to the pin, most often by a dead weight. The wear rate is generally determined by weighing the pin before and after the test. The rubber wheel abrasion test is an alternative type of abrasion test in which the specimen, in plate or block form, is pressed under constant load against the edge of a rotating wheel. The wheel consists of a rubber edge of known hardness and elastic modulus, moulded onto the surface of a steel disc. Silica (Quartz) particles with a limited size distribution, from a specific source are fed at a consistent rate into the contact area.The two testing variants described above subject the specimen to two different conditions. The rubber wheel test involves loose abrasive particles, which creates indentations the contrasting wheel during abrasion. The particles rotate drastically and therefore will tend to drift away from “cutting” orientations in order to minimise friction. This test generates three-body abrasive wear. The tests which focus on pin specimens sliding along fixed abrasives, produce two-body abrasion conditions. Alumina and Silicon Carbide papers are readily available.

The size, shape and hardness properties of the abrasive particles will hence directly affect the wear rate (Axén et al., 2001).

2.6.5 Effect of secondary phases on abrasive wear

Composites can offer a means to achieve enhanced hardness and adequate fracture toughness to circumvent brittle fracture. A secondary phase e.g. hard ceramic particles and/or fibres can be integrated into a softer and more ductile matrix material. The abrasive wear resistance of this type of composites depends on microstructural factors such as size, shape, hardness, volume fraction and distribution of the reinforcing phases. The properties of the matrix and the interfacial bonding between the second phases and the matrix are also relevant. Hard abrasive particles can dig out smaller phases with ease and cut/crack bigger ones. Soft abrasive particles can dig out small phases and generate large pits. The indentation depth of the soft abrasive particles is considerably lowered by hard reinforcing phases if its average free path between them is smaller than the size of the abrasive particles. Large phases can be ineffectively bonded to the matrix and can be pulled out. Nevertheless, large phases that are effectively bonded to the matrix can dull or fracture soft abrasive particles (K.-H. Z. Gahr, 1998). For brittle materials for example ceramics, the resistance to extreme abrasive wear is affected by the fracture toughness of the wearing material. Fracture toughness of brittle materials can commonly be improved by mechanisms of energy dissipation. Hence the advent of such toughening mechanisms such as stress-induced phase transformation, stress-induced microcracking, crack pinning with crack deflection, crack bridging or pull out of the reinforcing phases. Nonetheless, all tribologically linked interactions between abrasive particles are focused on a relatively thin surface zone. Hence a few of the toughening mechanisms would be unsuccessful under tribological contact because they act predominantly in greater volumes.

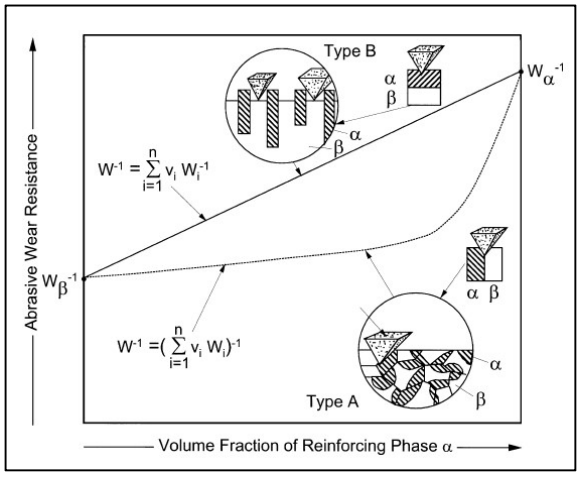


Figure 2.19 Schematic representation of abrasive wear resistance of two-phase structures as a function of volume fraction of a reinforcing phase (K.-H. Z. Gahr, 1998)**.**

A simple methodology for a calculating a best or first estimation of wear resistance of multiple phase structure or composites would be the Rule of Mixtures: if the reinforcement materials were strongly bonded to the matrix and were not pulled out or carved out by abrasive behaviour of particles (K.-H. Z. Gahr, 1998).

3. METHODOLOGY

3.1 Experimental Approach

The experimental approach that was followed for this research project consisted of several main stages.

Stage 1- Evaluating and determining the optimum processing conditions for the various compositions of TiC matrices without any reinforcements based on sintering density, phase composition determined by XRD analysis, microstructure, hardness and fracture toughness.

Stage 2 – Evaluating the processing conditions of various compositions of TiC matrices with the addition SiC whiskers and cBN particles as reinforcements based on sintering density, XRD phase analysis, microstructure, hardness testing and fracture toughness results.

Stage 3 – Evaluating the mechanical and fracture behavior determined via Biaxial Flexural Strength Testing (Ball on 3 Ball Testing) of a selection of TiC based CMC's. The TiC based CMC's chosen for testing were those with the best combination of physical properties as determined by stage 1 and 2.

Stage 4 – Investigating the tribological behaviour using Sliding Wear Testing (Ball on Disc Testing) for the same selection of TiC based CMC's as Stage 3

The work plan for the experimental approach are detailed in the diagram below. (Figure 3.1).

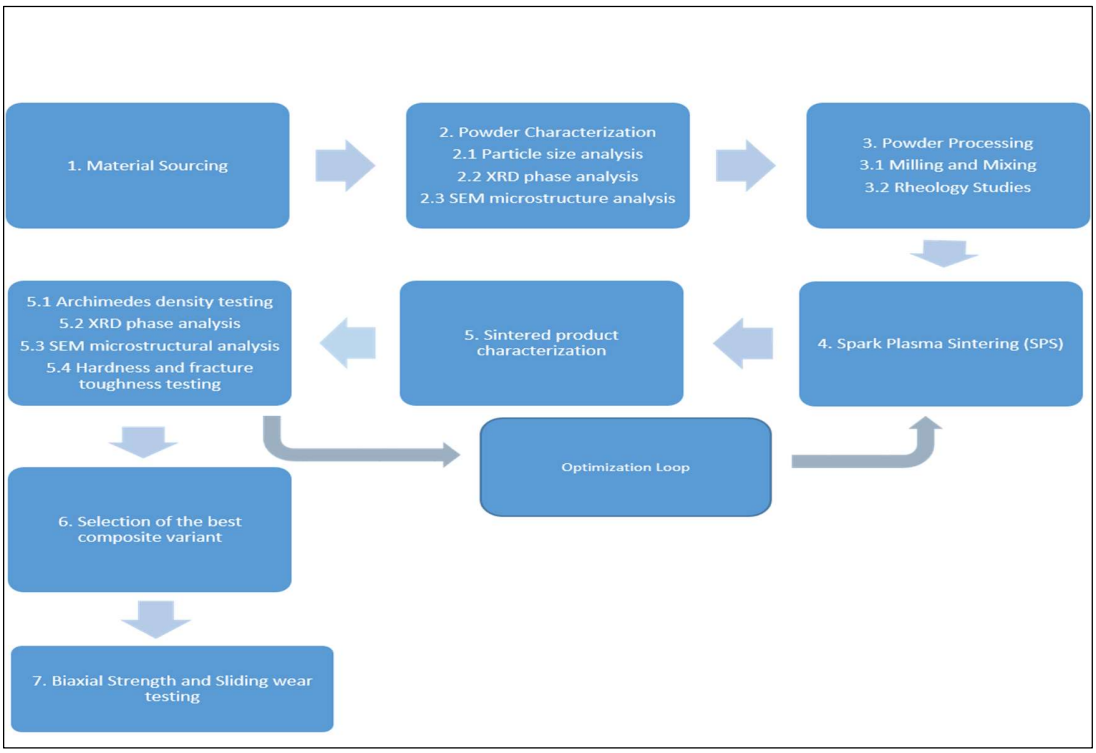


Figure 3.1 A brief outline of the work plan for the experimental approach

3.2 Materials used and their characterization

The table 3 contains the details of all chemicals (powders and solvents) used.

Table 3.1: Materials used for processing

Material Grade	Average Particle size (μm)	Company
TiC (Std 120) (matrix material)	2.0 μm	HC Starck
Y_2O_3 (liquid phase sintering aid)	1.6 μm	Sigma Aldrich
Al_2O_3 (AKP-50) (liquid phase sintering aid	0.3 μm	Sumitomo Chemical
SiO_2 (liquid phase sintering aid)	6.3 μm	Alfa Aesar
cBN (crush grade 6) (reinforcement material)	8.1 μm	Element 6
SiC whiskers (reinforcement material)	1.5 μm diameter x 18 μm length	Industrial Analytical
Hexane (solvent)	-	Sigma Aldrich 99%
H_2O (cleaning/solvent)	-	Distilled and deionized

(Average particle sizes listed above were taken from the Material Data Sheets for each material as supplied by the induvidual material manufacturers)

3.2.1 Scanning Electron Microscopy of Reinforcement Materials

For the characterization of the individual particle shape SEM image analysis was used. Figure 3.2 shows the SiC whiskers had a range of lengths and diameters present. There were also small amounts of particulate material present. Figure 3.3 shows the whiskers had a hexagonal cross-section. Figure 3.4 shows that the cBN grains had an overall cubic shape and the average particle size was less than 10μm. There were no extremely large or extremely small particles. Figure 3.5 shows a more detailed image of the individual cBN grains. The surfaces of the grains had signs of cleavage which was expected from crushed material.

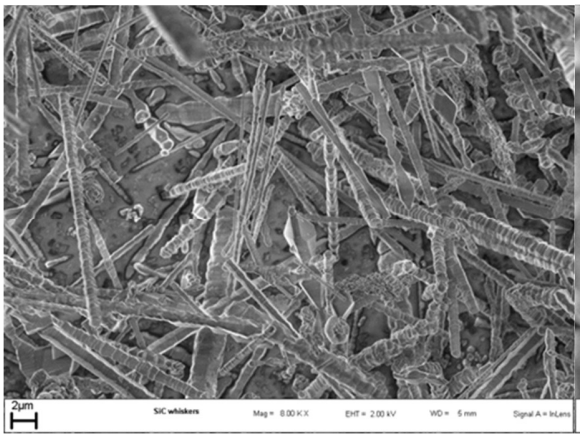


Figure 3.2 SEM image of SiC whiskers

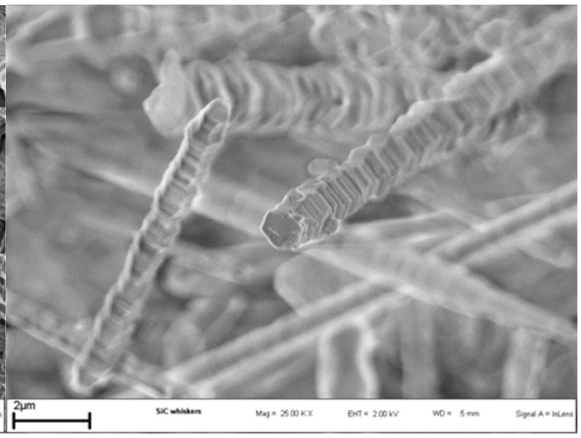


Figure 3.3 SEM images of SiC whiskers (higher magnification)

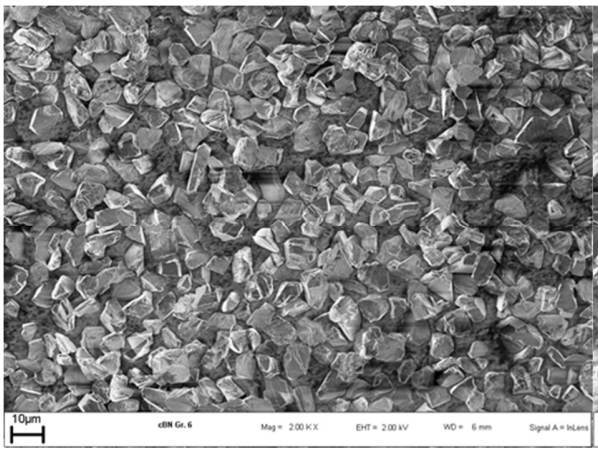


Figure 3.4 A SEM image of cBN crush grade 6

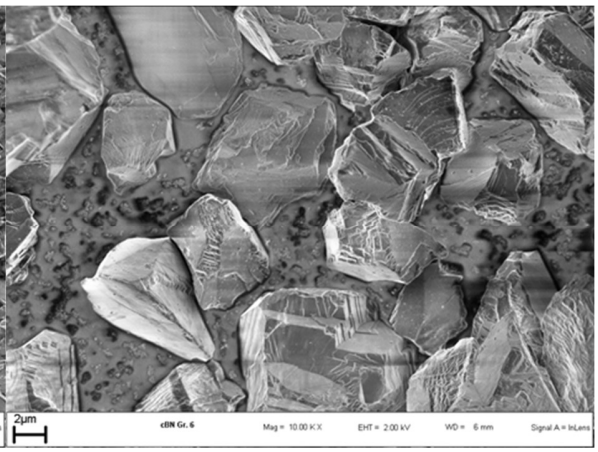


Figure 3.5 SEM image of cBN crush grade 6 (higher magnification)

3.3 Experimental Apparatus

In the process of creating the TiC base matrices and CMC's a wide variety of milling methods were used to process the powders prior to sintering. Ball milling was used to blend TiC powder with the liquid phase sintering aids during the making of the TiC matrices powders. Attrition milling was used to incorporate SiC whiskers into the previously made TiC matrices powders and Turbula mixing was used to incorporate cBN particles into the previously made TiC matrices powders. The milled powders were then consolidated and densified using a SPS Machine. Metallographic sample preparation equipment was then used to prepare the sintered samples for Light and Scanning Electron microscopy for analysis of microstructures. XRD phase analysis was performed on both the powder mixes and the sintered materials. Hardness and fracture toughness testing was done on the sintered materials. B3B testing was used to analyse the mechanical and fracture behaviour of selected sintered materials and Ball on disc sliding wear testing was performed to determine the tribological properties of selected sintered materials.

3.3.1 Planetary ball mill

A Fritsch Pulverisette 6 planetary ball mill as seen in figure 3.6 was used in order to ensure an even distribution of all the constituents in each mix. The powder mixtures were weighed out on an electronic balance and added to ~100g of 2 mm diameter alumina milling balls in a 250ml tungsten carbide milling bowl. The mixtures were milled at 150 rpm for 5 hours with hexane as a solvent. The slow milling speed was used to prevent tungsten carbide pick-up during the milling procedure.



Figure 3.6 Fritsch Pulverisette 6 planetary ball mill

The resultant slurry was poured into a round bottomed flask and rotary evaporated until dry. The dry powder and milling balls were then sieved through a 155µm sieve to remove the milling balls and the powder mixture was set aside till needed.

3.3.2 Attritor mill

The Attritor mill was used as a means to incorporate SiC whiskers into the matrix powder. The SiC whiskers and the matrix powders were mixed with Hexane and placed in an ultrasonic bath to disperse the whiskers in the solvent and breakdown any agglomerates in the powders. The dispersed slurry was then poured into the Attritor mill and stirred for 5 hours at 500 rpm to produce a homogenous mixture. Milling balls were not added to the bowl of the attritor mill during milling to prevent breaking of the SiC whiskers and any additional contamination from the wearing of the milling media. Extra care needed to be taken to ensure the stirrer did not make contact with the sides or bottom of the milling bowl. A lid was also needed to be used to lessen the evaporation of the solvent (hexane) during the milling time. The resultant slurry was poured into a round bottomed flask with a small amount of alumina milling balls. Any residual powder left in the milling bowl was rinsed with additional hexane and poured into the flask and was then dried in the rotary evaporator. The dry powder and milling balls were then sieved through a 155µm sieve to remove the milling balls and the powder mixture is set aside till needed. The SiC whisker and TiC matrix powder mixture was handled while wearing a respirator due to the dispersed SiC whiskers being a breathing hazard.

3.3.3 Turbula mixer

A Turbula mixer was used to incorporate cBN into to the TiC matrix powders that were previously milled in the planetary ball mill, dried in the rotary evaporator and sieved. The TiC matrix powders and cBN powders were weighed out and poured into a plastic container along with 3 large (10 mm diameter) alumina balls. The plastic container was then tightly sealed, secured inside the Turbula mixer and mixed vigorously for 5 hours. The Turbula mixer was used instead of the other available milling equipment due to the high hardness of the cBN which would cause significant wear of the milling bowls and hence cause contamination if incorporated using wet milling techniques.

3.3.4 Spark plasma sintering (SPS) machine

SPS sintering was used to produce samples of high density. The HPD-5 FCT group Systeme GmbH Spark Plasma Sintering machine as seen in figure 10 was used. The TiC matrix powders were weighed out to approximately 5g and carefully poured into the graphite die which was lined with graphite foil. The foils that covered the graphite dies were coated with a fine layer of hexagonal boron nitride (hBN). Samples were sintered at temperatures between 1450°C and 1650°C, pressures of 50MPa and 70MPa in a vacuum atmosphere. The heating rate used was 100°C/min and the cooling rate was 200°C/min to ambient temperature. The samples were sintered in a vacuum environment with holding times of 5 and 10 min at the selected temperature. After sintering the samples are sandblasted and the surfaces of the samples were cleaned by grinding on a SiC metal grinding disc (MD-Piano 220, Struers) to remove the hBN and graphite that were still on the samples.



Figure 3.7 FCT group Systeme GmbH Spark Plasma Sintering Machine

3.3.5 Materialography (Sample preparation) equipment

Samples were prepared for scanning electron microscopy (SEM), hardness and fracture toughness determination. The samples were cut in half using a diamond cutting blade. The samples were then hot mounted in Polyfast conductive resin, ground and polished. Polyfast resin was used specifically for its ability to be used for SEM analysis due to its conductive nature.

Table 3.2: Preparation method for grinding sintered TiC matrices samples

Step	Polishing pad	Abrasive	Lubricant	Speed	Force	Time
Plane grinding	220 Piano	SiC	Water	300 rpm	20 N	30 min
Fine grinding	1200 Piano	SiC	Water	300 rpm	20 N	45 min
Fine grinding	MD-Largo	9µm diamond	DP-Blue	300 rpm	20 N	30 min

Table 3.3: Preparation method for polishing sintered TiC matrices samples

Step	Polishing pad	Abrasive	Lubricant	Speed	Force	Time
Polishing	MD-Dac	3µm diamond	DP-Blue	150 rpm	20 N	30 min
Polishing	MD-Nap	1µm diamond	DP-Blue	150 rpm	20 N	15 min
Polishing	MD-Chem	Alumina	OP-solution	150 rpm	20 N	1.5 min

3.3.6 X-ray Diffractometry (XRD)

The phases present were determined by X-ray diffraction (XRD) using a Bruker AXS D2 phaser desktop powder diffractometer with a monochromatic Co Kα radiation produced at 30 kV and 10 mA, with a step size of 0.03°2θ. Each sample was scanned using a Cobalt source from 2Θ, 20-100° whilst spinning the sample to prevent preferred orientation. The powder mixtures and sintered products were each analysed and compared to determine which reaction products have formed during sintering.

3.3.7 Scanning Electron miscroscopy (SEM) and Energy Dispersive Spectroscopy (EDX)

The microstructures were characterized by scanning electron microscopy (SEM) using a Philips XL 30 ESEM-FEG series, with EDX detector. Scanning electron microscopy was used to take images of the polished mounted samples. The degree of sintering, porosity, grain size and homogeneity of the samples can be determined by the SEM images at various magnifications. EDX scanning results were used to compare and confirm results obtained by XRD analyses. A low accelerating voltage of 5 KeV was used to analyze the surface of the samples and a higher accelerating voltage of 20 KeV was used for EDX analysis due to the presence of heavier elements like Yttrium.

3.4 Powder processing

3.4.1 Preparation of matrix powders

TiC powder was milled with liquid phase sintering aids (Alumina, Yttria and Silica) in order to improve densification during sintering at lower temperatures. In section 2.1.6 of the literature review it was stated that Kolitsch et al. had studied isothermal sections of the Al_2O_3-Y_2O_3-SiO_2 system at 1573K (1300°C), 1673K (1400°C) and 1873K (1600°C). They found that the YAM phase ($Y_4Al_2O_9$) forms solid solutions with SiO_2 content up to 18-19 mol.%. The resultant solid solution has the chemical formula of $Y_4Al_{2(1-x)}Si_{2x}O_{9+x}$ ($0<x<0.31$) (Kolitsch et al., 1999).

3.4.2 Preparation of reinforced matrix powders

In section 2.1.8 of the literature review it was noted that in samples containing only Al_2O_3-Y_2O_3 liquid phase the ratio was 4:1 in weight % and in the samples containing Al_2O_3-Y_2O_3-SiO_2 as the liquid phase the ratio was 5:8:7 in weight % respectively. The weight % were then converted to volume % as seen in Table 3.4 below. These ratios had been described as having the lowest ternary eutectic temperature of 1371 ± 5°C as determined by high-temperature differential scanning calorimetry (DSC). At this temperature the system of Mullite (3 Al_2O_3-2SiO_2) + SiO_2 + $Y_2Si_2O_7$ ↔ Liquid has the lowest eutectic point. (Kolitsch et al., 1999). This would ensure that the liquid phase sintering aids would indeed be in the liquid state over sintering temperature range that was used.

Table 3.4: Components TiC matrices

TiC Mix names	Titanium Carbide (TiC)	Alumina (Al_2O_3)	Yttria (Y_2O_3)	Silica (SiO_2)
90 wt.% TiC	88.3 vol.%	9.8 vol.%	1.9 vol.%	-
90 wt. % TiC(+SiO_2)	86.9 vol.%	3.01 vol.%	3.8 vol.%	6.3 vol.%
85% TiC	82.6 vol.%	14.6 vol.%	2.9 vol.%	-
85 wt. % TiC(+SiO_2)	80.7 vol.%	4.4 vol.%	5.6 vol. %	9.3 vol.%

Reinforcements were added to the prepared TiC matrix powders via the various milling methods described previously. Tables 3.4-3.6 list the compositions of each TiC matrix composites as well as the composition of each reinforced material that was made. The TiC Mix names were based on wt. % and vol. % and were used as colloquial terms for each composition.

Table 3.5: Components TiC matrices with SiC whisker (SiCw) reinforcements

TiC Mix names	Titanium Carbide (TiC)	Alumina (Al_2O_3)	Yttria (Y_2O_3)	Silica (SiO_2)	SiC whiskers (SiCw)
90 wt.% TiC + 10 vol.% SiCw	79.4 vol.%	8.8 vol.%	1.7 vol.%	-	10.0 vol.%
90 wt.% TiC + 20 vol.% SiCw	70.7 vol.%	7.8 vol.%	1.5 vol.%	-	20.0 vol.%
90 wt.% TiC(+SiO_2) + 10 vol.% SiCw	78.2 vol.%	2.7 vol.%	3.4 vol.%	5.7 vol.%	20 vol.%
90 wt.% TiC(+SiO_2) + 20 vol.% SiCw	69.5 vol.%	2.4 vol.%	3.0 vol.%	5.0 vol.%	20.0 vol.%
85% TiC+ 10 vol.% SiCw	74.6 vol.%	13.1 vol.%	2.6 vol.%	-	9.7 vol.%
85% TiC+ 20 vol.% SiCw	66.1 vol.%	11.6 vol.%	2.3 vol.%	-	20.0 vol.%
85 wt. %TiC(+SiO_2) + 10 vol.% SiCw	72.6 vol.%	4.0 vol.%	5.0 vol. %	5.0 vol.%	10.0 vol.%
85 wt. %TiC(+SiO_2) + 20 vol.% SiCw	64.5 vol.%	3.6 vol.%	4.5 vol.%	7.4 vol.%	20 vol.%

Table 3.6: Components TiC matrices with Cubic boron nitride (cBN) reinforcements

TiC Mix names	Titanium Carbide (TiC)	Alumina (Al_2O_3)	Yttria (Y_2O_3)	Silica (SiO_2)	Cubic BN (cBN)
90 wt.% TiC + 7 vol.% cBN	82.1 vol.%	9.1 vol.%	1.8 vol.%	-	7.0 vol.%
90 wt.% TiC + 10 vol.% cBN	79.5 vol.%	8.8 vol.%	1.7 vol.%	-	10 vol.%
90 wt. % TiC(+SiO_2) + 7 vol.% cBN	80.8 vol.%	2.8 vol.%	3.5 vol.%	5.8 vol.%	7.0 vol.%
90 wt. % TiC(+SiO_2) + 10 vol.% cBN	78.2 vol.%	2.7 vol.%	3.4 vol.%	5.7 vol.%	10.0 vol.%
85% TiC+ 7 vol.% cBN	76.7 vol.%	13.5 vol.%	2.7 vol.%	-	7.1 vol.%
85% TiC+ 10 vol.% cBN	74.3 vol.%	13.1 vol.%	2.6 vol.%	-	10.0 vol.%
85 wt. % TiC(+SiO_2) + 7 vol.% cBN	75.0 vol.%	4.1 vol.%	5.2 vol.%	8.6 vol.%	7.0 vol.%
85% TiC(+SiO_2) + 10 vol.% cBN	72.7 vol.%	4.0 vol.%	5.0 vol.%	8.3 vol.%	10.0 vol.%

3.5 Analysis of sintered samples

3.5.1 Density Measurements

The bulk densities of the sintered samples were determined by the Archimedes' density determination method. The sintered samples were boiled for 3hrs in distilled water and allowed to cool in the water. The samples were then weighed; suspended in water, wet (after removing any visible water on its surface) and dry (after drying in an oven overnight and allowing to cool to room temperature). The density of the sintered sample was determined using the following formula:

$$\rho_{ceramic} = \frac{(Dry\ Mass)(\rho_{water})}{(Wet\ Mass) - (Suspended\ mass)}$$

The density of water at 25°C is 0.997 g.cm^{-3}. To determine the volume fraction of open porosity the following formula was used:

$$V_f of\ Porosity = \left(\frac{Wet\ mass - Dry\ mass}{Wet\ mass - Suspende\ \ mas}\right)$$

The determination of open porosity was relevant when there was a possibility of unsealed surface porosity which could absorb water (during the cleaning process) and cause the calculated densities to be higher than the true value.

('ASTM B962 - 15 Standard Test Methods for Density of Compacted or Sintered Powder Metallurgy (PM) Products Using Archimedes' Principle', 2015)

3.5.2 Vickers Hardness Testing

3.5.2.1 Hardness Testing

Hardness testing of the TiC matrices materials was done using a Microhardness testing machine. A diamond tip indenter was used to make 5 indentations in each sample with 2000gforce. The diagonal distance of each indentation was measured and the hardness is determined in Vickers hardness (Hv).

For the sintered reinforced TiC matrices material bulk hardness testing was done as it gives a better approximation of the bulk properties of the material as the indentation covers a larger area. The bulk hardness and fracture toughness of the sintered material was measured using a Vickers indentation machine (Future Tech Hardness Tester FV-800) at an indentation load of 5 kg. For toughness estimation, the radial crack length around the Vickers indentation was measured and the Evans and Charles formula was applied:

$$K_{IC}0.16 = (c/a)^{-1.5}.\left(Ha^{1/2}\right)$$

Where *a* – half length of the indentation diagonal and *H* – hardness (MPa) (Evans & Charles, 1976). At least five indentations were taken and the reported values were the average of the measured values.

3.5.2.2 Indentation based calculation of Fracture Toughness

The fracture toughness was calculated using the indents made during hardness testing together with the Evans and Charles Equation:

$$K_{IC} = 0.16\left(\frac{1}{2}C_{av}\Big/\frac{1}{2}D_{av}\right)^{-1.5}\left(H_v \times \frac{1}{2}D_{av}^{0.5}\right)$$

Where HV is the Vickers Hardness and C_{av} is the average of the crack lengths and D_{av} is the average diameter of the indentation (Evans & Charles, 1976).

3.5.2.3 SEM analysis of crack paths and toughening mechanism determination

Observations in whisker toughening in whisker reinforced CMC's suggest the possibility of five toughening mechanisms to be operative. These mechanisms are crack deflection, crack bowing, microcracking, whisker pull-out and crack bridging (Evans & Faber, 1984). The crack path gave information on the effect of the reinforcement on the bulk properties of the material. The crack path was observed using SEM at various magnifications.

3.5.3 B3B Biaxial strength testing

Spark plasma sintered samples were produced in the various compositions described previously with a diameter of 20 mm. The sintered samples were ground down to a thickness of approximately 2 mm and polished to 1µm surface quality on both sides. The testing rig was assembled as shown in figure 11 with the polished sample seated between the three top ball and single bottom ball. A testing rig was placed inside a mechanical testing machine that had been setup for compression testing. A preload of 10 N was applied and the block removed. This resulted in the sample being in contact with the balls only free from contact with the guide. The punch was then lowered with an approach speed of 0.017 mm/min. The samples are then broken and the load at fracture plus the pre-load recorded (Harrer et al., 2012).

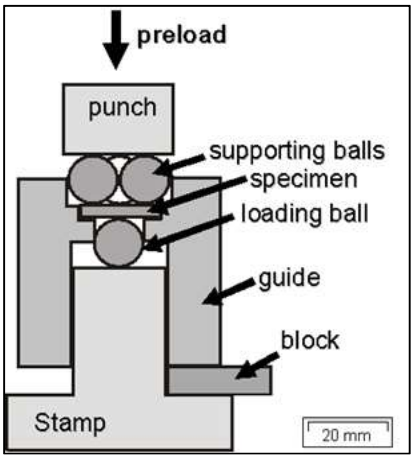


Figure 3.8 Sketch of the B3B experimental setup (Harrer et al., 2012)

The stress field in the sample had a cloverleaf symmetry and can only be determined numerically. The maximum tensile stress appears in the center of the disc on the opposite side of the loading ball where the biaxial stress state exists (Harrer et al., 2012).

Kirstein and Woolley specified that the maximum tensile stress σ_{max} could be calculated by the following equation:

$$\sigma_{max} = -\frac{3.F}{4.\pi.t^2}(\xi - \lambda)$$

Where:

$$\xi = (1+v).\ln\left(\frac{b}{R}\right)^2 + \frac{(1-v)}{2}.\left(\frac{b}{R}\right)^2 \quad \text{b = t/3 for } \zeta \geq 0$$

$$\lambda = (1+v)\left[1+\ln\left(\frac{Ra}{R}\right)^2\right] + (1-v).\left(\frac{Ra}{R}\right)^2$$

F- Applied load, t – sample thickness, v – Poisson's ratio of the disc material, b- radius of the loaded area (contact radius of a loading ball), R-radius of the disc, Ra – support radius and Rb – radius of the ball.

$$Ra = \frac{2\sqrt{3}}{3} Rb$$

$$\zeta = \left(\frac{3.F.Rb}{4.E'}\right)^{\frac{1}{3}} = \left(\frac{3.FRb.}{4} . \frac{1}{E'}\right)^{\frac{1}{3}}$$

$$\frac{1}{E'} = \frac{\left(1 - v_b^2\right)}{E_b} + \frac{(1 - v^2)}{E}$$

V_b – Poisson's ratio for the ball material, E_b – Young's modulus for ball material and E – Young's modulus for disc material (Börger et al., 2002).

Weibull statistics was used to relate a series of bending strength measurements σ to the probability of failure P_f [P_f being defined as *n/ (q+1)*], where n is the number of samples with the strength σ or less and *q* is the total number of samples tested] by the function:

$$\ln \ln\left[1/\left(1 - P_f\right)\right] = m \ln[(\sigma - \sigma_u)/\sigma_0] + const,$$

Where σ_u is the stress and where P_f is zero; σ_0 is a normalizing stress and *m* is the Weibull modulus. Taking σ_u to be zero as there is always some risk of failure even a low stresses the equation becomes:

$$\ln \ln\left[1/\left(1 - P_f\right)\right] = m \ln \sigma - m \ln \sigma_0 + const.$$ (Kendall et al., 1986)

The Weibull modulus was then compared for the different materials both with and without reinforcement as toughening from fibrous crack bridging behavior was shown to give an increase in Weibull modulus (Kendall et al., 1986).

The fracture surface of each sample was analyzed via SEM to identify the various modes of fracture that took place during the biaxial strength testing.

3.5.4 Sliding wear testing

Spark plasma sintered samples were prepared for ball on disc sliding wear testing by grinding and polishing the samples to a surface quality of 1μm. The samples created by SPS were round discs which were required for this method of testing. AISI 52100 100Cr6 Chrome steel balls with 6 mm diameter were used as the static partner.

Clean, dry specimens were secured inside the sample mandrel on the rotating disc inside the tribometer which was connected to the PC. The ball was secured inside the ball bolder and 10N of load was added on top of the ball holder. A spirit level was used to that the sample was flat inside the holder. The linear speed was set to 0.21m/s and the distance to stop was set at 300 m. The tribometer measured the frictional force, penetration depth, time and sliding distance over the duration of each test. These measurements were then used to plot the frictional force and penetration depth vs time and distance. SEM analysis and measurments were also done on the wear tracts left on both the sample surfaces and the ball to examine the degree of material removal by the sliding wear testing.



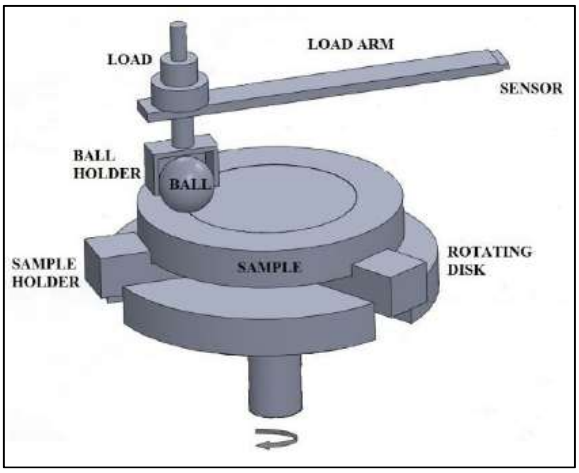


Figure 3.9 Ball on disc sliding wear testing rig. Figure 3.10 Diagram of the positioning of the sample disc and wear ball in a ball on disc sliding wear testing rig (ALEMDAĞ1* et al., 2015)**.**

Mass lost on ball bearing during wear testing

When there is a significant difference in hardness between the disc materials and steel balls. The mass lost during wear testing on the softer ball bearing material (in comparison to the TiC ceramic disc with/without reinforcements added) was calculated by determining the spherical cap volume and using the known density of the ball bearings (AISI 52100 steel: 7.81g/cm^3) (Weisstein, n.d.).

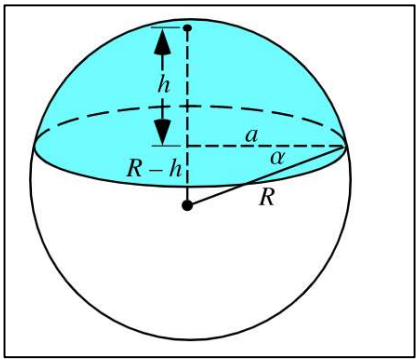


Figure 3.11 Diagram of a spherical cap region of a sphere (Weisstein, n.d.).

The volume of the spherical cap is given by: $V_{cap} = \frac{1}{3}\pi h^2(3R-h)$

Where *R* is the radius of the sphere (ball bearing) and *h* is the spherical cap height.

The area of the base of the spherical cap is given by: $A_{cap} = 2\pi Rh$

Cap height is given by: $h_{cap} = \frac{A_{cap}}{2\pi}$

The specific wear rate is calculated by the formula: $W_s = \frac{Volume\ loss\ (mm^3)}{Normal\ load\ (N) \times Sliding\ distance\ (m)}$

4. ANALYSIS OF UNREINFORCED TIC WITH AL_2O_3, Y_2O_3 AND SIO_2 SINTERING AIDS

TiC powder was combined with liquid phase sintering aids at various ratios and then sintered to determined optimal processing conditions. Prior to sintering XRD phase analysis was performed to confirm the phases present and check for possible contamination introduced during the milling process. The sintered samples were then analysed for density and phase changes caused by sintering. The TiC powder mixes and sintered material were analysed by SEM for analysis of the microstructure. Hardness testing of the sintered samples was also completed and the results allowed for the determination of the fracture toughness.

4.1 Particle size analysis of TiC, liquid phase sintering aids and reinforcement material

The particle size was analyzed using a Malvern Mastersizer 2000 particle size analyzer. Distilled water was used as a solvent to suspend and disperse the powders being analyzed. The Mastersizer 2000 operates on the principle of Laser diffraction size analysis. Due to the nature of the SiC whiskers particle size could not be accurately determined PSA. The results are given in Table 4.1 below.

Table 4.1 Results of the Particle size analysis of the starting powders

Starting Powder	d_{10} (µm)	d_{50} (µm)	d_{90} (µm)
TiC	0.6	2.0	4.4
SiO_2	2.6	6.4	8.6
Al_2O_3	0.3	0.3	0.4
Y_2O_3	1.4	1.6	2.0
PcBN grade 6 crush	5.5	8.1	11.4

4.2 Analysis of the TiC Matrix powders

4.2.1 XRD results of Milled TiC matrix powders with/without SiO_2

The XRD phase analysis was performed on the milled TiC powder mixes with liquid sintering aids to confirm the phases present prior to sintering and determine whether any contamination has occurred during the milling process.

4.2.1.1 Examples of typical XRD patterns for milled powders

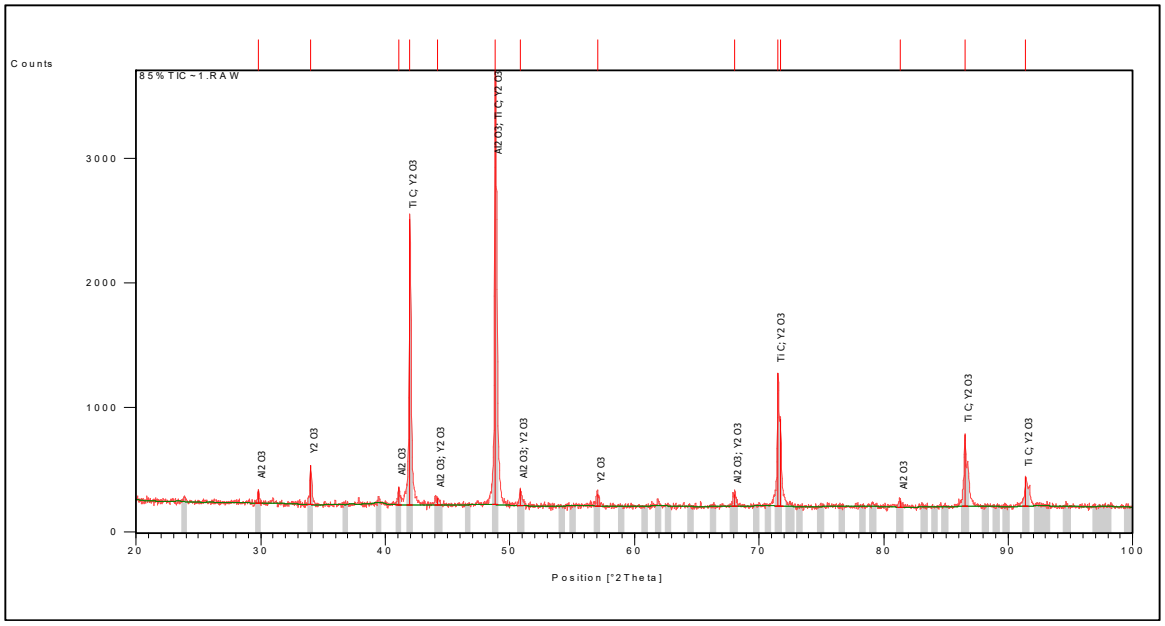


Figure 4.2a) 85 wt. % TiC +12 wt. % Al_2O_3 + 3 wt. % Y_2O_3 powder

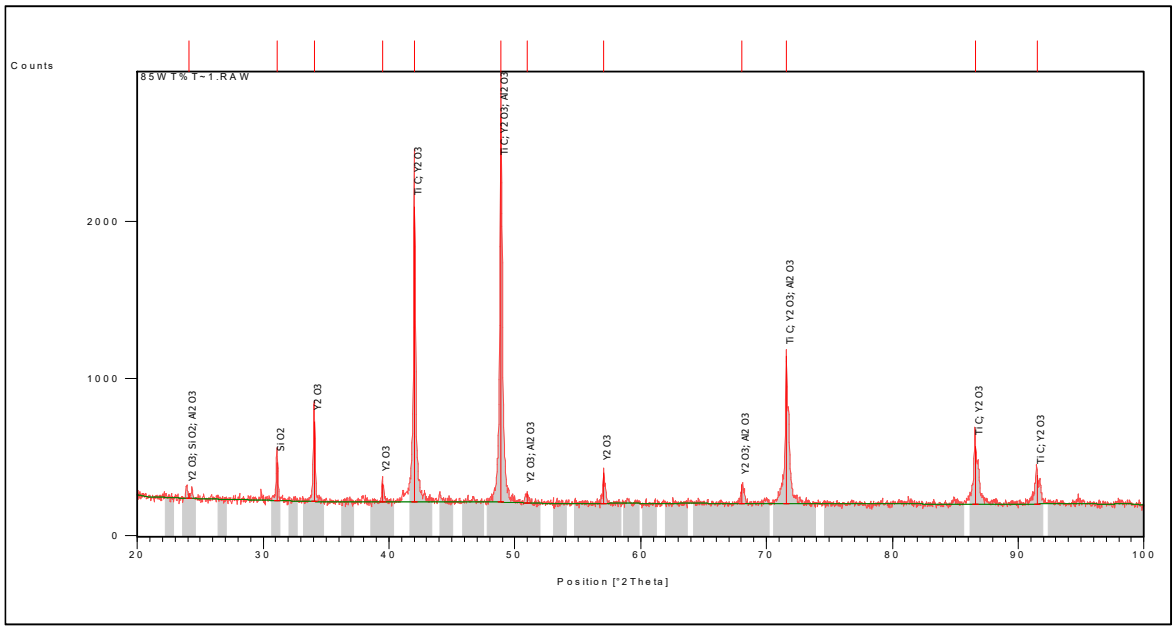


Figure 4.2b)85 wt. % TiC-3.75 wt. % Al_2O_3-6wt. % Y_2O_3-5.25 wt. % SiO_2 powder

4.2.1.2 Table 4.2 Results for XRD patterns for milled TiC matrix powders

Sample matrix name	Sample composition, Wt. %	Sample composition, Vol %	TiC	Al_2O_3	Y_2O_3	SiO2
90 wt.% TiC	90TiC-8Al_2O_3-2Y_2O_3	88.3TiC-9.8Al_2O_3-1.9Y_2O_3	X	X	X	-
85 wt.% TiC	85TiC-12Al_2O_3-3Y_2O_3	82.6TiC-14.6Al_2O_3-2.9Y_2O_3	X	X	X	-
90 wt. % TiC(+SiO_2)	90TiC-2.5Al_2O_3-4Y_2O_3-3.5SiO_2	86.9TiC-3.0Al_2O_3-3.8Y_2O_3-6.3SiO_2	X	X	X	X
85 wt.% TiC (+SiO_2)	85TiC-3.75Al_2O_3-6Y_2O_3-5.25SiO_2	80.7TiC-4.4Al_2O_3-5.6Y_2O_3-9.3SiO_2	X	X	X	X

The figures below (Fig. 4.3 A to D) are general examples of the SEM images of the TiC matrix powders. From visual analysis it can be seen that no contamination from Tunsten Carbide (WC) occurred during the milling process of TiC matrix powder plus liquid phase sintering aids. WC would have appeared as bright white areas if present under SEM analysis.

4.2.2 SEM analysis of the TiC Matrix powders

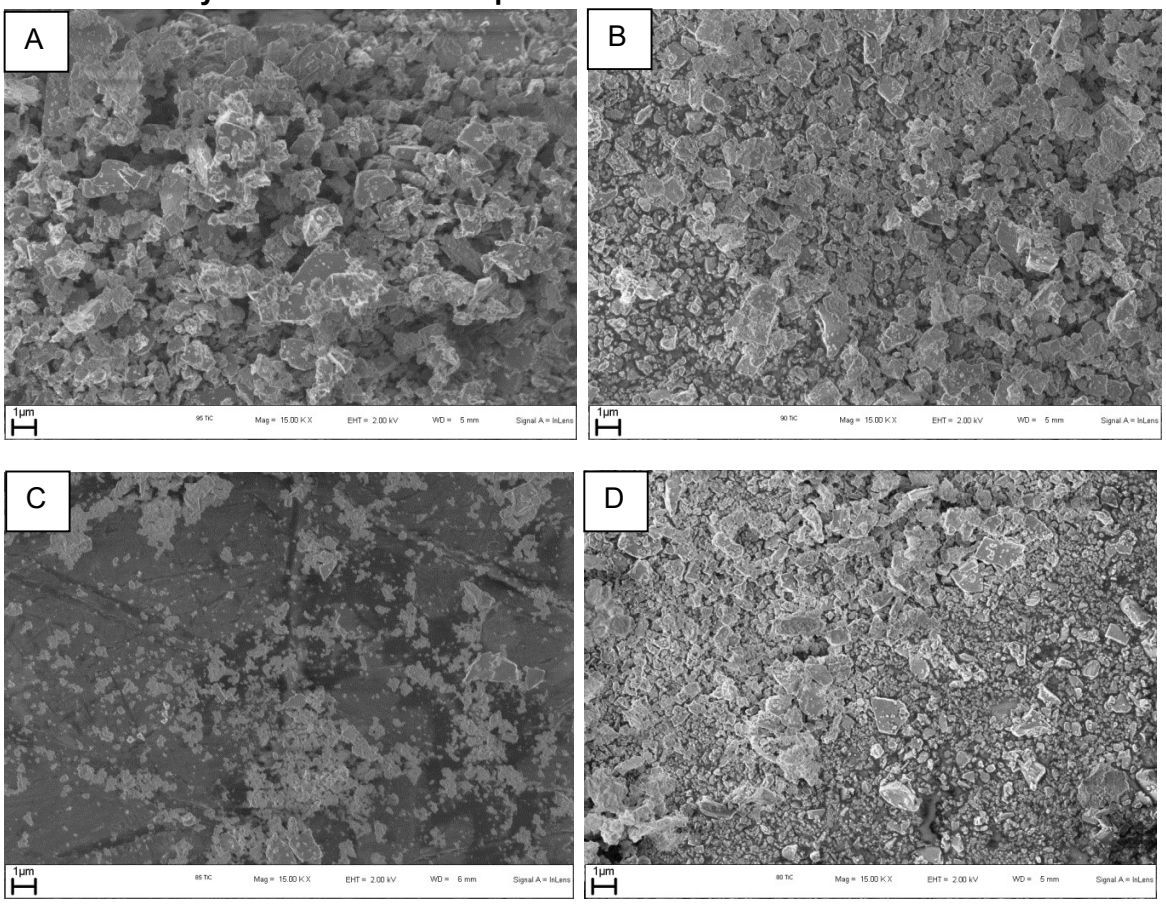


Figure 4.3A Micrograph of 95% TiC mix, Figure 4.3B Micrograph of 90% TiC mix, Figure 4.3C Micrograph of 85% TiC mix and Figure 4.3D Micrograph of 80% TiC mix

The addition of higher fractions of liquid phase sintering aids which overall have a smaller particle size is clearly visible from analysis of the SEM images. Figure 4.3D has the highest fraction of liquid phase sintering aids but it can be seen that there isn't a large amount of agglomeration in the powder after the milling and drying process.

4.3 SPS Sintering of TiC matrix powders

4.3.1 Theoretical densities of TiC powder mixes without SiO_2

Theoretical density values are calculated prior to the sample being sintered based on what the density of a 100% dense sample with the exact composition regardless of sintering parameters. See Appendix A for theoretical density calculations.

Table 4.3: Theoretical densities of TiC mixes with Al_2O_3, Y_2O_3

Sample matrix name	Sample composition, Wt. %	Sample composition, Vol %	Density (g/cm³)
95 wt.% TiC	95TiC-4Al_2O_3-1Y_2O_3	94.1TiC-4.9Al_2O_3-1.0Y_2O_3	4.88
90 wt.% TiC	90TiC-8Al_2O_3-2Y_2O_3	88.3TiC-9.8Al_2O_3-1.9Y_2O_3	4.84
85 wt.% TiC	85TiC-12Al_2O_3-3Y_2O_3	82.6TiC-14.6Al_2O_3-2.9Y_2O_3	4.79
80 wt.% TiC	80TiC-16Al_2O_3-4Y_2O_3	77TiC-19.2Al_2O_3-3.8Y_2O_3	4.74

After the initial sintering trials, the resulting densification data would then be analyzed and the two matrix compositions (TiC mixes) with the best densities at the specified sintering parameters would then be selected for the addition of SiO_2 and reinforcing materials. (See Table 4.7)

4.3.2 Theoretical densities of TiC powder mixes with the addition of Al_2O_3, Y_2O_3 and SiO_2

Table 4.4: Theoretical densities of TiC mixes with the addition of Al_2O_3, Y_2O_3 and SiO_2

Sample matrix name	Sample composition, Wt. %	Sample composition, Vol %	Density (g/cm³)
90 wt. % TiC(+SiO_2)	90TiC-2.5Al_2O_3-4Y_2O_3-3.5SiO_2	86.9TiC-3.0Al_2O_3-3.8Y_2O_3-6.3SiO_2	4.76
85 wt.% TiC (+SiO_2)	85TiC-3.75Al_2O_3-6Y_2O_3-5.25SiO_2	80.7TiC-4.4Al_2O_3-5.6Y_2O_3-9.3SiO_2	4.68

4.3.3 SPS sintering parameters for TiC mixes without SiO_2

95 wt.% TiC, 90 wt.% TiC, 85 wt.% TiC and 80 wt.% TiC matrix mixes are SPS sintered at a rate of 100°C/min to a temperature of 1450- 1650°C, 50MPa and 10 min hold at the selected temperature. See Appendix B for Sintering graphs (Piston position and Densification)

4.3.3.1 Preliminary Densification results of Sintered TiC mixes with Al_2O_3 and Y_2O_3

Values are the average values of 3 samples and the % values include the standard deviation. See Appendix C for values used for the calculation of % of full density and % of open porosity.

Table 4.5: Average density measurements for samples of TiC mixes with Al_2O_3 and Y_2O_3 sintered at 1450°C

Mix name	Theoretical Density (g/cm³)	% of Full density	% of open porosity
95% TiC	4.88	86.30±0.28	5.92±0.19
90% TiC	4.84	96.73±0.04	1.07±0.09
85% TiC	4.79	98.58±0.49	0.75±0.14
80% TiC	4.74	99.26±0.06	0.03±0.10

Table 4.6: Average density measurements for samples of TiC mixes with Al_2O_3 and Y_2O_3 sintered at 1550°C

Mix name	Theoretical Density (g/cm³)	% of Full density	% of open porosity
95% TiC	4.88	99.05±0.22	0.33±0.07
90% TiC	4.84	98.95±0.04	0.56±0.08
85% TiC	4.79	99.10±0.04	0.43±0.03
80% TiC	4.74	99.08±0.33	0.70±0.16

Table 4.7: Average density measurements for samples of TiC mixes with Al_2O_3 and Y_2O_3 sintered at 1650°C

Mix name	Theoretical Density (g/cm³)	% of Full density	% of open porosity
95% TiC	4.88	99.21±0.24	0.26±0.10
90% TiC	4.84	99.13±0.11	0.28±0.07
85% TiC	4.79	99.14±0.05	0.36±0.01
80% TiC	4.74	98.75±0.11	0.47±0.09

When considering the preliminary sintering results for the densification of the TiC mixes with Al_2O_3 and Y_2O_3 it was noted that some TiC mixes did not sinter as well as others under the specified conditions. The TiC mixes which sintered poorly would not be used as matrices for the production of the ceramic matrix composites.

The 95 wt.% TiC + 4 wt.% Al_2O_3 + 1 wt.% Y_2O_3 composition was rejected due to the poor densification and high percentage of open porosity of the sample at the lower sintering temperature (1450°C). 80 wt.% TiC + 16 wt.% Al_2O_3 + 4 wt.% Y_2O_3 composition was rejected as well due to the poor densification and high percentage of open porosity at the higher sintering temperature (1650°C). It was observed that the high percentage of liquid phase had resulted in some of it leaking out during the sintering process. This could be due to porosity caused by gas generating reactions occuring during sintering as referenced in the literature review Chapter 2.1.6.

4.3.4 SPS sintering parameters for TiC mixes with the addition of SiO_2

TiC matrix powders with the addition of SiO_2 are SPS sintered at a rate of 100°C/min to a temperature of 1550-1625°C, 50MPa and 10 min hold at the selected temperature. See Appendix D for Sintering graphs (Piston position and Densification)

4.3.5 Percentage of theoretical density of TiC mix sintered samples with/without SiO_2

Table 4.8 shows the density of samples comprising of 85 wt. % TiC, the balance being liquid phase sintering aids (with and without SiO_2) under differing sintering conditions (temperature, pressure and sintering hold time). The error bars represent the standard deviation of each point on the graph as they represent an average value of 3 sintered samples. The 85 wt. % TiC samples with Al_2O_3 and Y_2O_3 as liquid phase sintering aids have densities between 97.19-99.31 percent of theoretical density. The density of the samples with the higher sintering pressures and higher temperatures is the closest to full density. The samples that have higher sintering pressures also have a lower percentage of open porosity than those sintered at the lower pressure.

Table 4.8 Density of SPS sintered samples with 85 wt. % TiC and liquid phase sintering aids

Sample composition, wt. %	Temperature (°C)	Sintering hold time (min)	Sintering pressure (MPa)	Sample Density (g/cm^3)	% theoretical density	% open porosity
85TiC-12Al_2O_3-3Y_2O_3	1550	10	50	4.66	97.19	0.20
	1550	10	70	4.70	98.14	0.07
	1575	10	50	4.67	98.25	0.22
	1610	10	70	4.76	99.31	0.09
	1625	10	50	4.73	98.75	0.19
85TiC-3.75Al_2O_3-6Y_2O_3-5.25SiO_2	1550	10	50	4.68	99.91	0.13
	1550	10	70	4.68	99.40	0.31
	1575	10	50	4.67	99.90	0.24
	1575	10	70	4.68	99.44	1.98
	1610	10	70	4.68	99.93	1.43
	1625	10	70	4.68	99.83	4.97

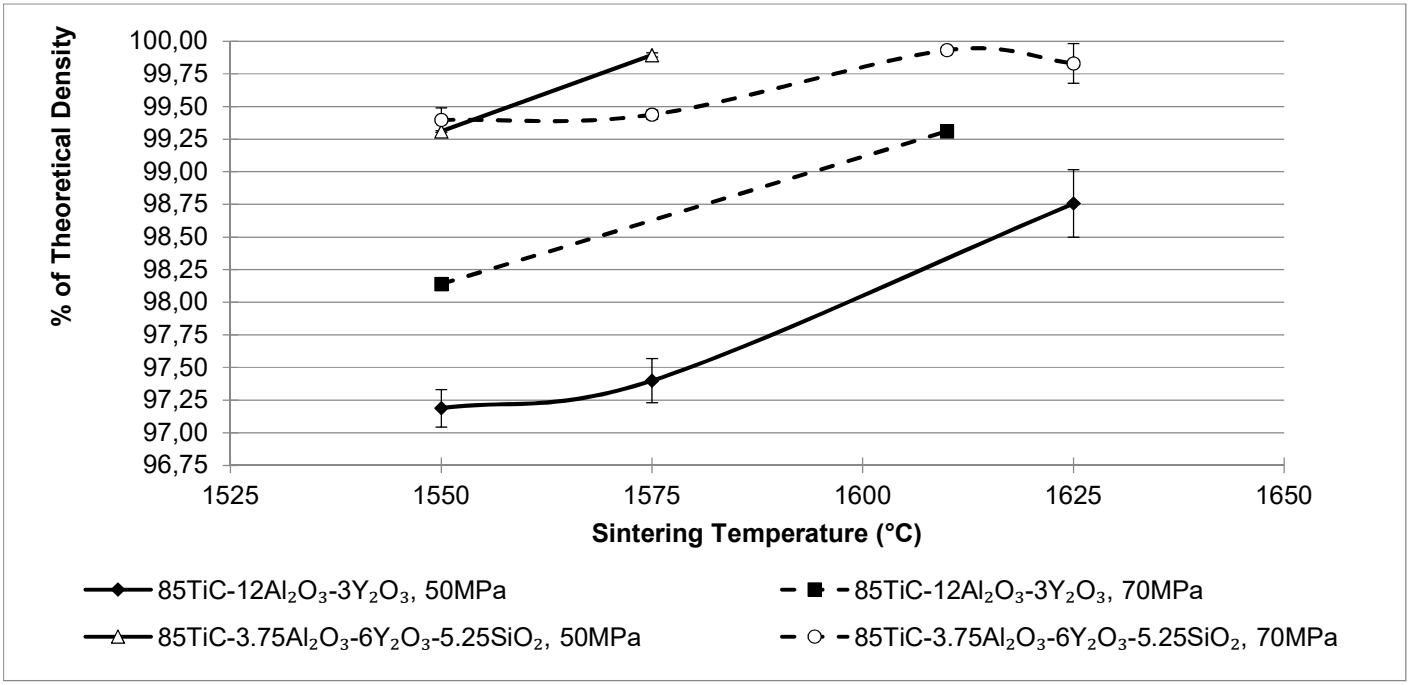


Figure 4.4 Graph of the trends in the density of SPS sintered samples with 85 wt. % TiC and liquid phase sintering aids

The samples that comprise 85 wt. % TiC and SiO_2 along with the other liquid phase sintering aids show a different pattern of behaviours from those previously mentioned. All the samples are close to full density. The addition of SiO_2 reduced the density from 4.79g/cm³ to 4.68 g/cm³ but increased the percentage of theoretical density of sintered samples even at the lowest temperature tested (1550°C). Densities of the sintered samples are within the range 99.40 - 99.93 as a percentage of theoretical density. Theoretical density values are calculated prior to the sample being sintered based on what the density of a 100% dense sample with the exact composition regardless of sintering parameters. The error bars represent the standard deviation of each point on the graph as they represent an average value of 3 sintered samples.

Generally, there was a slight increase in density with the increase in sintering temperature but a slight decrease in density with an increase in pressure. The increase in pressure also increases the percentage of open porosity. This is due to the interaction of SiO_2 with the other liquid phase sintering aids.

For sample compositions the samples with a sintering temperature of 1625°C showed a deviation from the trend of increasing density with increasing temperature by having a lower percentage of theoretical density of the samples sintered at 1610°C. At 1625°C there was a significant increase in the percentage of open porosity.

The decrease in the percentage theoretical density and increase in open porosity was most likely due to the evaporation of the liquid phase or the evolution of gases produced by the various gas-generating reactions. Closed pores formed under vacuum were expected to shrink easily during sintering but in liquid phase sintering of in the presence of oxides (SiO_2) trapped gases have been proved detrimental to densification (Chae et al., 1995).

The increased pressure conditions (70MPa) and sintering temperatures above 1610°C can further hinder the closing of pores by facilitating the leaking of liquid phase out of the samples during sintering. Table 4.9 shows the density of samples consisting of 90 wt. % TiC and liquid phase sintering aids (with and without SiO_2) under differing sintering conditions (temperature, pressure and sintering hold time).

The 90 wt. % TiC samples with Al_2O_3 and Y_2O_3 as liquid phase sintering aids had densities between 95.65-99.35 percent of theoretic density. The density of the samples with the higher sintering pressures and higher temperatures are the closest to full density. The samples that were sintered at higher pressures also have a lower percentage of open porosity than those sintered at the lower pressure.

Table 4.9 Density of SPS sintered samples with 90 wt. % TiC and liquid phase sintering aids

Sample composition, wt. %	Temperature (°C)	Sintering hold time (min)	Sintering pressure (MPa)	Sample Density (g/cm^3)	% theoretical density	% open porosity
90TiC-8Al_2O_3-2Y_2O_3	1550	10	50	4.63	95.65	1.37
	1550	10	70	4.77	98.71	0.03
	1575	10	50	4.70	97.25	0.27
	1575	10	70	4.73	97.84	0.28
	1625	10	50	4.77	98.75	0.22
	1625	10	70	4.80	99.35	0.05
90TiC-2.5Al_2O_3-4Y_2O_3-3.5SiO_2	1550	10	50	4.53	95.12	1.58
	1550	10	70	4.59	96.45	1.18
	1575	10	50	4.60	96.63	0.65
	1575	10	70	4.61	96.92	1.27
	1625	10	50	4.41	92.65	3.54
	1625	10	70	4.76	99.32	1.39

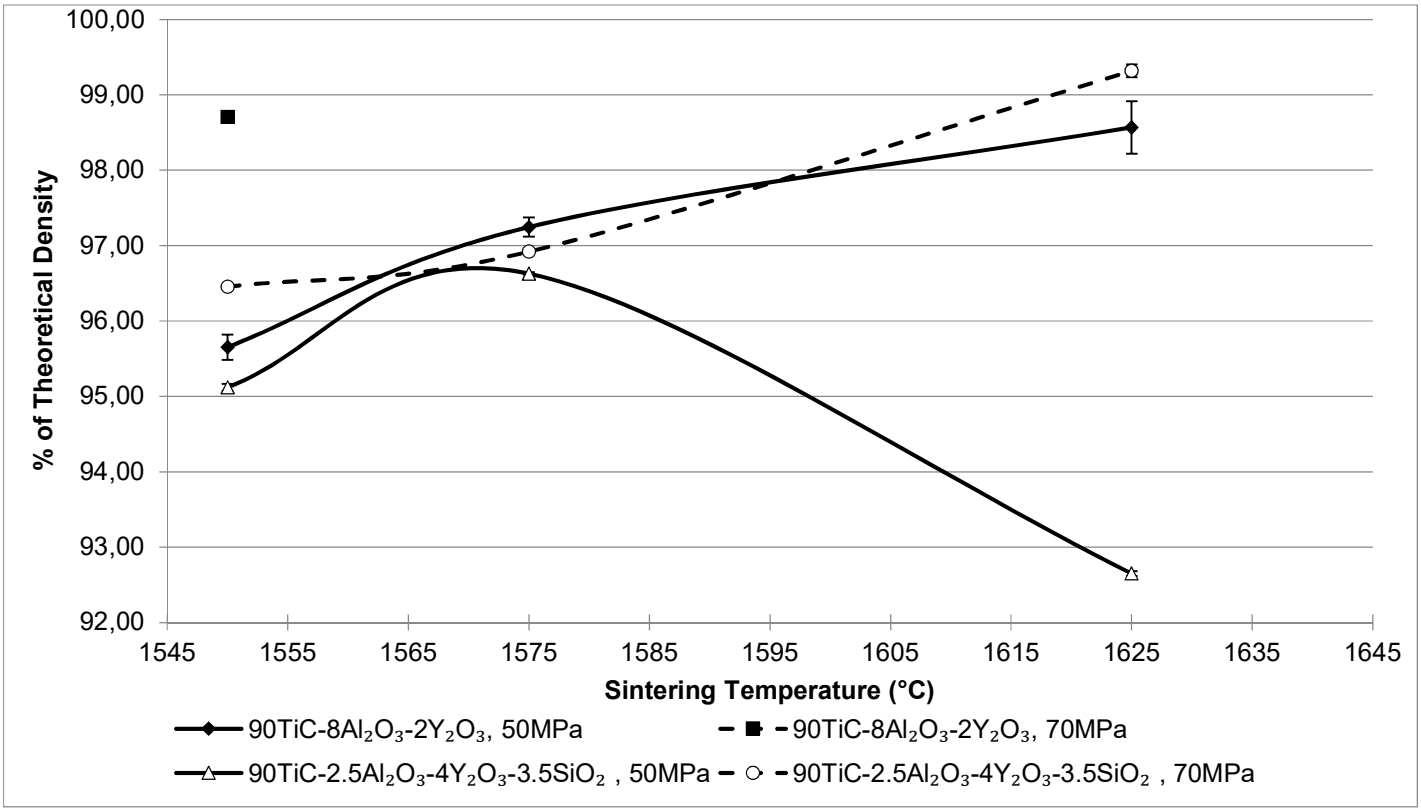


Figure 4.5 Graph of the trends in the density of SPS sintered samples with 90 wt. % TiC and liquid phase sintering aids

The addition of SiO_2 caused a slight reduction in the percentage theoretical density and slight increase in percentage open porosity. The addition of SiO_2 also reduced the theoretical density from 4.84g/cm³ to 4.76 g/cm³ and decreased the percentage of theoretical density of sintered samples in comparison to samples sintered without SiO_2 under the same sintering conditions. The increase in sintering pressure caused a slight increase in percentage theoretical density. The percentage of open porosity also decreased when sintering pressure was increased. At a sintering temperature of 1625°C and pressure of 70 MPa there is a 6.67% increase in percentage theoretical density from samples sintered at the same sintering temperature but the lower pressure condition (50MPa). At 1625°C and 50 MPa there is a significant decrease in the percentage theoretical density and increase percentage of open porosity in comparison with samples sintered at the lower temperature conditions.

The decrease in the percentage theoretical density and increase in open porosity at 1625°C and 50 MPa sintering conditions was most likely due to the evaporation of the liquid phase or the evolution of gases produced by the various gas-generating reactions as seen in the 85TiC-3.75Al_2O_3-6Y_2O_3-5.25SiO_2 composition. The experimental results show however that with the higher pressure condition (70MPa) the 90TiC-2.5Al_2O_3-4Y_2O_3-3.5SiO_2 composition which had less liquid phase sintering aids added was able to overcome the effects of the gas generating reactions and achieve higher percentage of theoretical density. The lower quantity of liquid phase sintering aids also prevented the leaking out of liquid phase at sintering temperatures above 1610°C as seen in the 85TiC-3.75Al_2O_3-6Y_2O_3-5.25SiO_2 composition samples.

4.4 Phases identified by XRD measurements of SPS sintered samples

Only the samples with the SPS sintering parameters that yielded the highest percentage of theoretical density were considered for XRD analysis. The XRD and EDS results were compared to each other and the results are compiled in the table below.

Table 4.10 Phases identified by XRD analysis of SPS's samples with the highest percentage theoretical density. (YAG-$Y_3Al_5O_{12}$, YAP- $YAlO_3$ and $Y_2Si_2O_7$)

Sample composition, Wt. %	Sample composition, Mol %	Sintering Pressure (MPa)	Sintering Temp (°C)	TiC	Al_2O_3	Y_2O_3	YAG	YAP	$Y_2Si_2O_7$
90TiC-8Al_2O_3-2Y_2O_3	94.51TiC-4.93Al_2O_3-0.56Y_2O_3	50	1625	X	X	X	-	-	-
90TiC-8Al_2O_3-2Y_2O_3	94.51TiC-4.93Al_2O_3-0.56Y_2O_3	70	1625	X	-	X	X	-	-
85TiC-12Al_2O_3-3Y_2O_3	91.55TiC-7.59Al_2O_3-0.86Y_2O_3	50	1625	X	X	-	-	X	-
85TiC-12Al_2O_3-3Y_2O_3	91.55TiC-7.59Al_2O_3-0.86Y_2O_3	70	1610	X	X	-	-	X	-
90TiC-2.5Al_2O_3-4Y_2O_3-3.5SiO_2	93.73TiC-1.53Al_2O_3-1.11Y_2O_3-3.63SiO_2	50	1575	X	X	-	X	-	X
90TiC-2.5Al_2O_3-4Y_2O_3-3.5SiO_2	93.73TiC-1.53Al_2O_3-1.11Y_2O_3-3.63SiO_2	70	1625	X	X	-	X	-	X
85TiC-3.75Al_2O_3-6Y_2O_3-5.25SiO_2	90.40TiC-2.34Al_2O_3-1.69Y_2O_3-5.57SiO_2	50	1575	X	X	X	X	-	X
85TiC-3.75Al_2O_3-6Y_2O_3-5.25SiO_2	90.40TiC-2.34Al_2O_3-1.69Y_2O_3-5.57SiO_2	70	1610	X	X	X	X	-	X

The results displayed in Table 4.10 above showed that the composition 90TiC-8Al_2O_3-2Y_2O_3 did not have any products of the Al_2O_3-Y_2O_3 system after sintering at the lower pressure condition (50MPa) as the only signals detected are those for the original reactants. At the higher sintering pressure condition, the signal for the Y_2O_3 reactant is no longer present but that of the YAG compound was found. A comparison of the mole % of the of Al_2O_3-Y_2O_3 in the 90wt. % TiC-8wt. % Al_2O_3-2wt. % Y_2O_3 equates to 94.51 mol % TiC-4.93 mol % Al_2O_3-0.56 mol % Y_2O_3 which has a mol ratio of liquid phase sintering aids of approximately 9:1.

When compared with the phase diagram in Figure 4.12 we expect there to be no reaction products formed at the sintering temperature of 1625°C. The results of the 50MPa sintering pressure condition agreed with the literature but the 70 MPa sintering pressure sample did not. This implies that for this particular composition the reaction is strongly dependant on the sintering pressure and hence the densification rate (Cheng et al., 2012). For the samples with the composition 85TiC-12Al_2O_3-3Y_2O_3 produced at the sintering conditions of 1625°C and 50 MPa, the results in Table 4.7 show that only TiC and Al_2O_3 are detected from the initial reactants.

The reaction product YAP is detected as well. The samples with the same composition but produced at the sintering conditions of 1610°C and 70 MPa show the same results. A comparison of the mole % of the of Al_2O_3-Y_2O_3 in the 85wt. % TiC-12wt. % Al_2O_3-3wt. % Y_2O_3 equates to 91.55mol % TiC-7.59 mol % Al_2O_3-0.86 mol % Y_2O_3 which has a ratio of matrix to liquid phase sintering aids of approximately 9:1. When compared with the phase diagram in Figure 4.6, we expect that no reaction products should be present but our results show that YAP is formed which is only expected to form at around 50 mol % Y_2O_3. The difference between the results could be due to the difference in sintering conditions such as sintering pressure, hold time, heating and cooling rates.

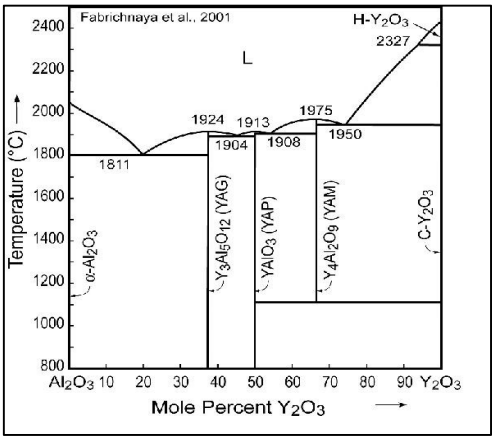


Figure 4.6 Y_2O_3-Al_2O_3 phase diagram (Fabrichnaya & Seifert, 2001)

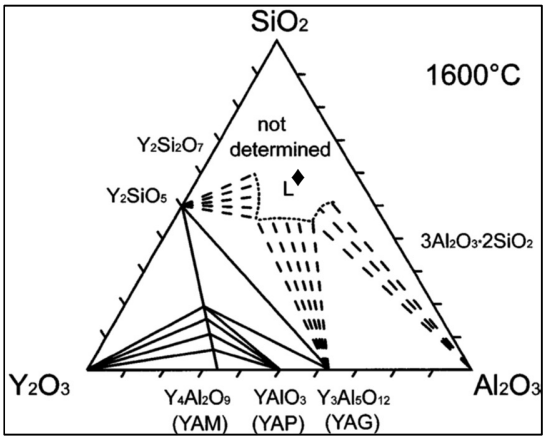


Figure 4.7 Isothermal section of the system Y_2O_3-Al_2O_3-SiO_2 at 1600°C in air (in mol %). (Kolitsch et al., 1999) ♦ - Represents liquid phase sintering aid composition used.

Table 4.11 lists results for compositions which have the addition of SiO_2 to the other liquid sintering aids. Samples analysed with the composition of 90TiC-2.5Al_2O_3-4Y_2O_3-3.5SiO_2 sintered at 1575°C and 50 MPa showed that TiC and Al_2O_3 was detected but the Y_2O_3 reactant was no longer present and the YAG compound along with $Y_2Si_2O_7$ was found. The composition above sintered at 1625°C and 70 MPa yielded the same result. The mole % of the of Al_2O_3-Y_2O_3-SiO_2 system in the 90wt. % TiC-2.5 wt. % Al_2O_3-4wt. % Y_2O_3-3.5wt. % SiO_2 composition equates to 93.73mol % TiC-1.53 mol % Al_2O_3-1.11 mol % Y_2O_3-3.63 mol % SiO_2. It had a ratio of liquid phase sintering aids of approximately 3:2:7, respectively. When compared with the isothermal phase diagram in Figure 4.7, we find that our results agreed with the results predicted by the phase diagram. The final composition analysed in Table 4.11 was 85TiC-3.75Al_2O_3-6Y_2O_3-5.25SiO_2. Samples sintered under the lower pressure condition of 50 MPa and a temperature of 1575°C and 70 MPa and 1625°C showed that TiC, Al_2O_3, Y_2O_3, YAG and $Y_2Si_2O_7$ were detected. The larger weight % of liquid phase sintering aids explains the presence of Y_2O_3 in the sintered sample for this composition but not in the previous composition (90TiC-2.5Al_2O_3-4Y_2O_3-3.5SiO_2). The mole % of the of Al_2O_3-Y_2O_3-SiO_2 system in the 85wt. % TiC-3.75 wt. % Al_2O_3-6wt. % Y_2O_3-5.25wt. % SiO_2 composition equates to 90.40mol % TiC-2.34 mol % Al_2O_3-1.69 mol % Y_2O_3-5.57 mol % SiO_2. The sintered samples had a mol ratio of liquid phase sintering aids of approximately 3:2:7 respectively. As with the previous composition the phase diagram in Figure 4.7 agrees with the experimental results.

4.5 Microstructural Analysis

4.5.1 Scanning Electron Microscopy TiC mix sintered samples with/without SiO_2

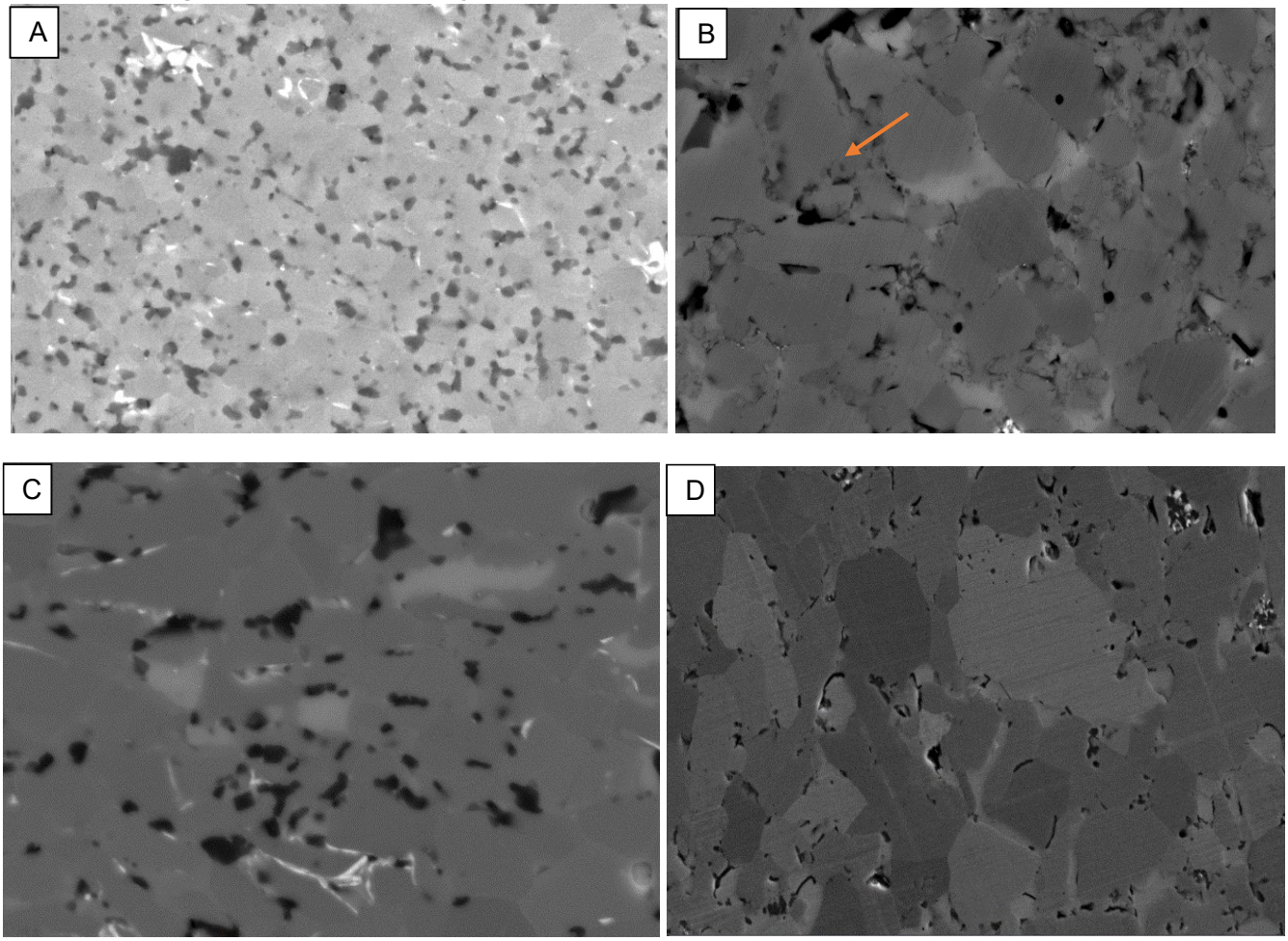


Figure 4.8A: SEM image of the microstructure of 85TiC-12Al_2O_3-3Y_2O_3 SPS'd at 1550 °C, 50MPa and 10 min hold. 4.8B: SEM image of 85TiC-3.75Al_2O_3-6Y_2O_3-5.25SiO_2 SPS'd at 1610°C, 70MPa and 10 min hold. 4.8C: SEM image of 90TiC-8Al_2O_3-2Y_2O_3 SPS'd at 1550°C, 50MPa and 10 min hold. 4.8D: SEM image of 90TiC-2.5Al_2O_3-4Y_2O_3-3.5SiO_2 SPS'd at 1625°C, 70MPa and 10 min hold

Figure 4.8A above show the microstructure of the 85TiC-12Al_2O_3-3Y_2O_3 composition which has been SP sintered at a temperature of 1550°C and a sintering pressure of 50 MPa. The porosity is difficult to distinguish from the Al_2O_3 as both appear as the darkest phases on the micrograph. The percentage of theoretical density of the sample being 97.19% indicates that not all the dark areas are porosity.

4.5.2 Energy-dispersive X-ray spectroscopy on TiC mix sintered samples with/without SiO_2

4.5.2.1 Energy-dispersive X-ray spectroscopy on TiC mix sintered samples without the addition of SiO_2

Energy-dispersive X-ray spectroscopy (EDS) was done to confirm the composition of the differently coloured regions as seen in the SEM analysis. The large dark grains were found to be mostly Al_2O_3 as confirmed by EDS in Figures 4.9A and B below.

The brightest phase in the micrograph was confirmed to be a small amount of tungsten carbide (WC) contamination from the milling bowl during the milling process as seen in Figures 4.10A and B. The grains with paler shade of grey shows the Y_2O_3 containing regions while the darker regions contained more Al_2O_3 as seen in Figures 4.11A and B.

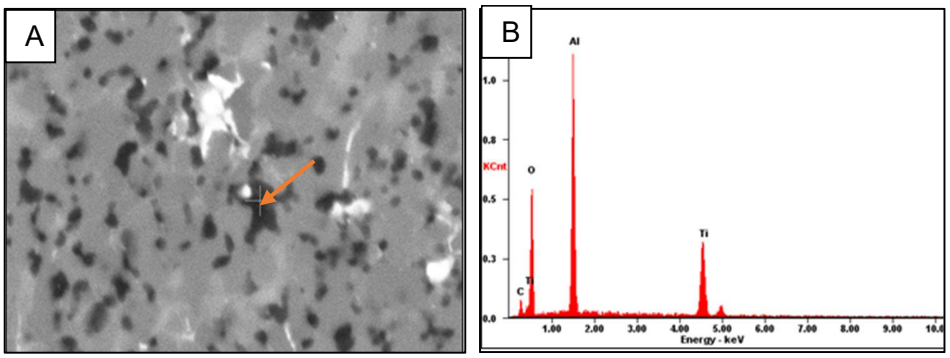


Figure 4.9 A: Image of the area of sintered 85TiC-12Al_2O_3-3Y_2O_3 SPS'd at 1550 °C, 50MPa and 10 min hold scanned by EDS for composition B: Results of EDS qualitative analysis on the area highlighted in Fig. 4.9 A.

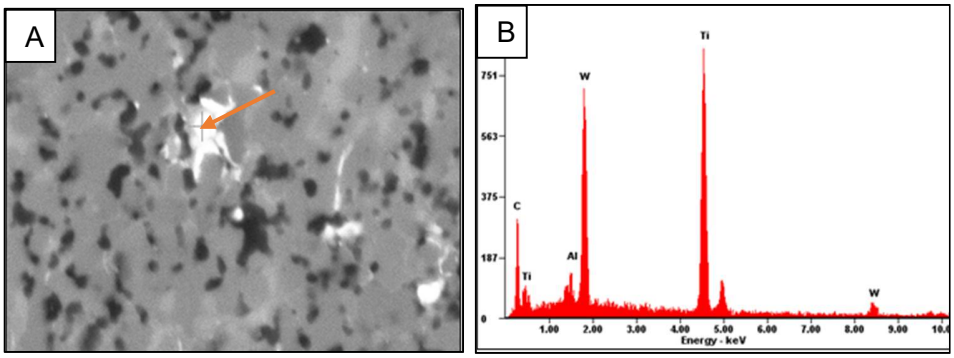


Figure 4.10 A: Image of the area of sintered 85TiC-12Al_2O_3-3Y_2O_3 SPS'd at 1550 °C, 50MPa and 10 min hold scanned by EDS for composition B: Results of EDS qualitative analysis on the area highlighted in Fig. 4.10 A.

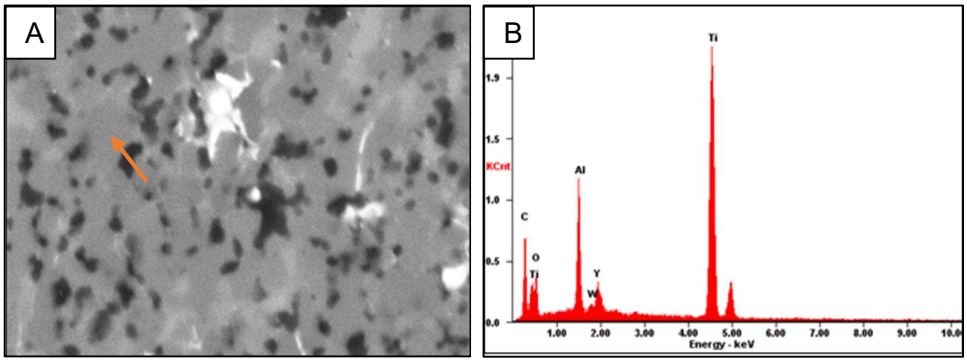


Figure 4.11 A: Image of the area of sintered 85TiC-12Al_2O_3-3Y_2O_3 SPS'd at 1550 °C, 50MPa and 10 min hold scanned by EDS for composition B: Results of EDS qualitative analysis on the area highlighted in Fig. 4.11 A.

The contamination was eliminated in subsequent batches by reducing the milling speed. The predominant phase present was TiC grains which vary in shades of grey depending on the content to Al_2O_3 and Y_2O_3 present.

Figure 4.8B above showed the microstructure of 85TiC-3.75Al_2O_3-6Y_2O_3-5.25SiO_2, the larger grey grains were predominantly TiC and the lighter phase between the larger grains is a combination of the liquid phase sintering aids. The darkest phase present were pores, some of which were present in the material after sintering (small round pores) and some were resultant of material removal during the polishing process (thin irregular pores).

The liquid phase sintering aids that were found between the TiC grains were significantly softer than the TiC grains and were worn away selectively during sample preparation. Figure 4.8C was very similar to Figure 4.8A but the higher magnification showed the porosity and Al_2O_3 grains more clearly. The grains with paler shade of grey showed the Y_2O_3 containing regions while the darker regions contain more Al_2O_3. The brightest phase is Tungsten carbide contamination from the milling process. Figure 4.8D showed large grains of YAG (large light grey grains) which were visible along with small amounts of liquid phase along the grain boundaries. There was less liquid phase visible in Figure 4.8D than in Figure 4.8B. The TiC grains appear to have experienced grain growth. At the higher sintering temperature coarsening may have taken place at the grain level as well as grain boundary diffusion which usually dominates the final stage of sintering (Cheng et al., 2012).

4.5.2.2 Energy-dispersive X-ray spectroscopy on TiC mix sintered samples with the addition of SiO_2

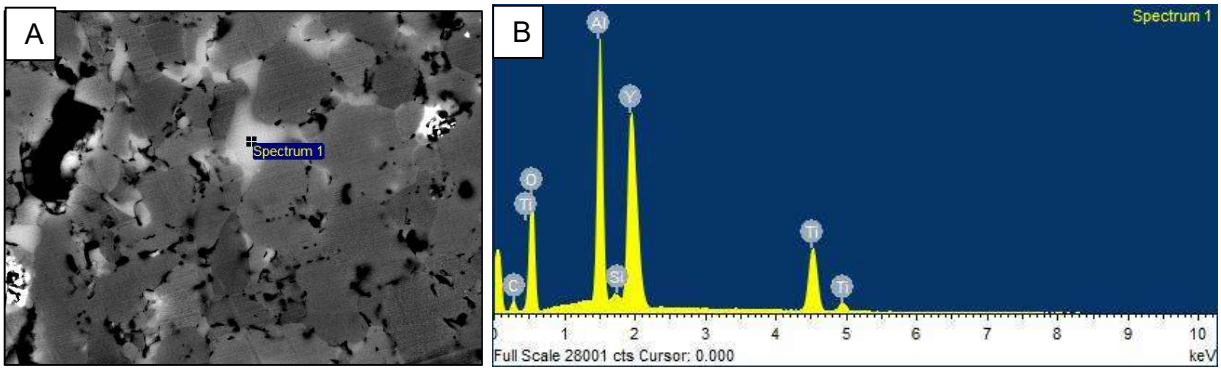


Figure 4.12 A: Image of the area of sintered 90TiC-2.5Al_2O_3-4Y_2O_3-3.5SiO_2 SPS'd at 1625°C, 70MPa and 10 min hold scanned by EDS for composition B: Results of EDS qualitative analysis on the area highlighted in Fig. 4.12 A.

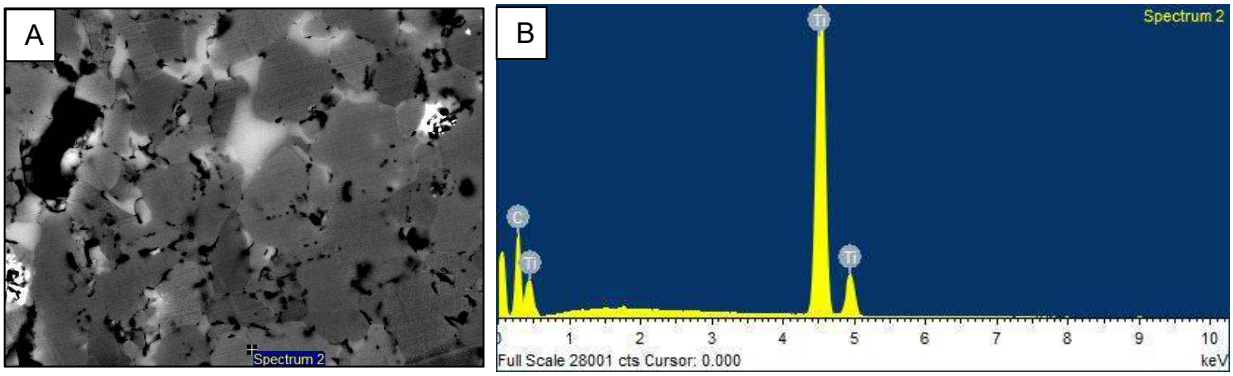


Figure 4.13 A: Image of the area of sintered 90TiC-2.5Al_2O_3-4Y_2O_3-3.5SiO_2 SPS'd at 1625°C, 70MPa and 10 min hold scanned by EDS for composition B: Results of EDS qualitative analysis on the area highlighted in Fig. 4.13 A.

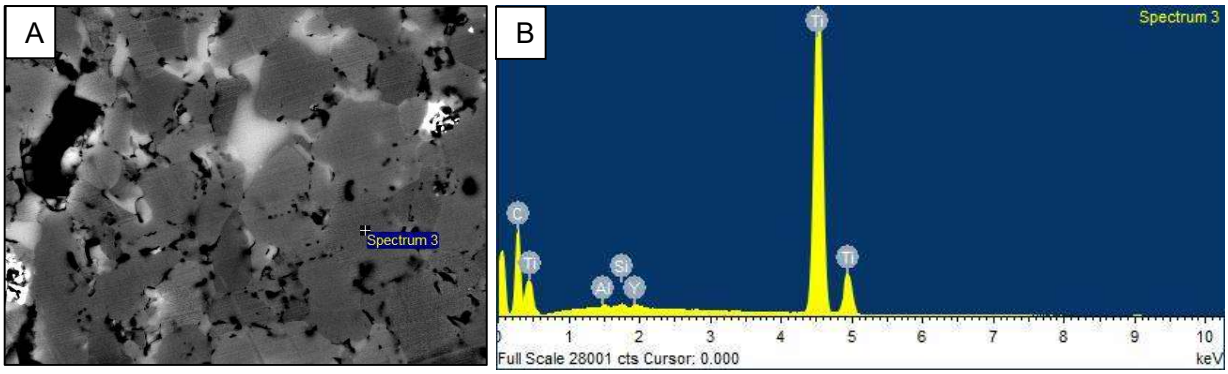


Figure 4.14 A: Image of the area of sintered 90TiC-2.5Al_2O_3-4Y_2O_3-3.5SiO_2 SPS'd at 1625°C, 70MPa and 10 min hold scanned by EDS for composition B: Results of EDS qualitative analysis on the area highlighted in Fig. 4.14 A.

The large pale grey grains were found to be mostly liquid phase sintering aids and possibly YAG as the largest peaks were Al_2O_3 and Y_2O_3 as confirmed by EDS in Figures 4.12A and B above. The medium grey phase in the micrograph was confirmed to be almost entirely comprised of TiC as seen in Figures 4.13A and B. The grains with darker shade of grey show the ones with mostly TiC with small quantities of Y, Al and Si as seen in Figures 4.14A and B.

4.6 Hardness and fracture toughness of sintered samples

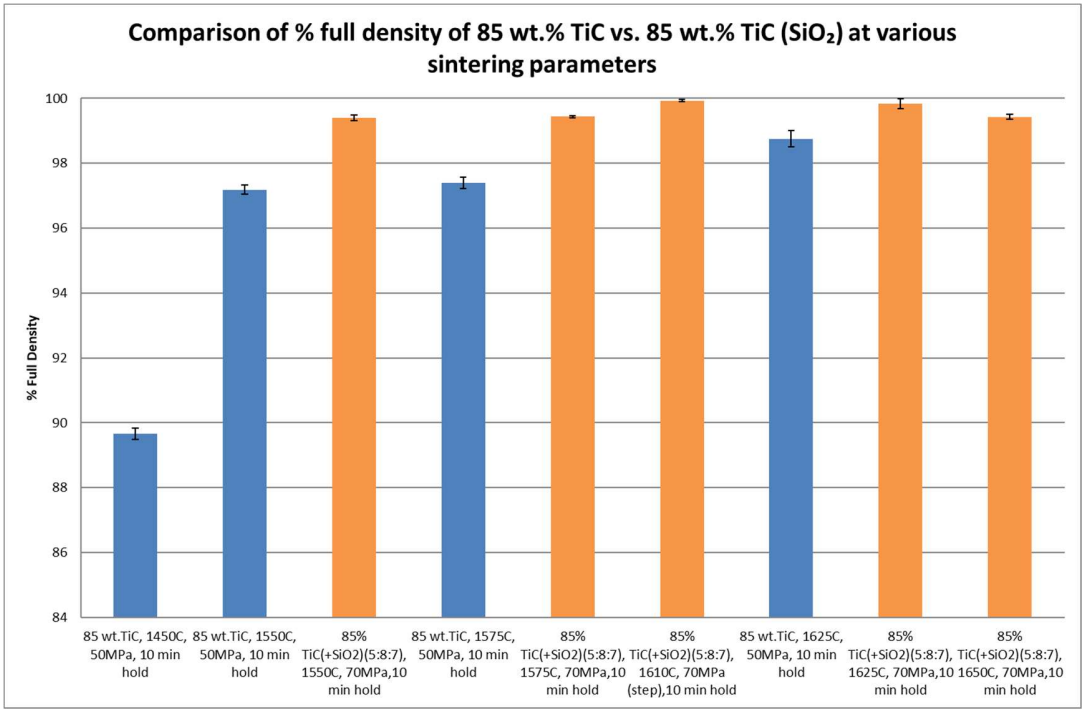


Figure 4.15 Comparison of % of full density of 85 wt.% TiC vs. 85 wt.% TiC(SiO_2) at various sintering parameters

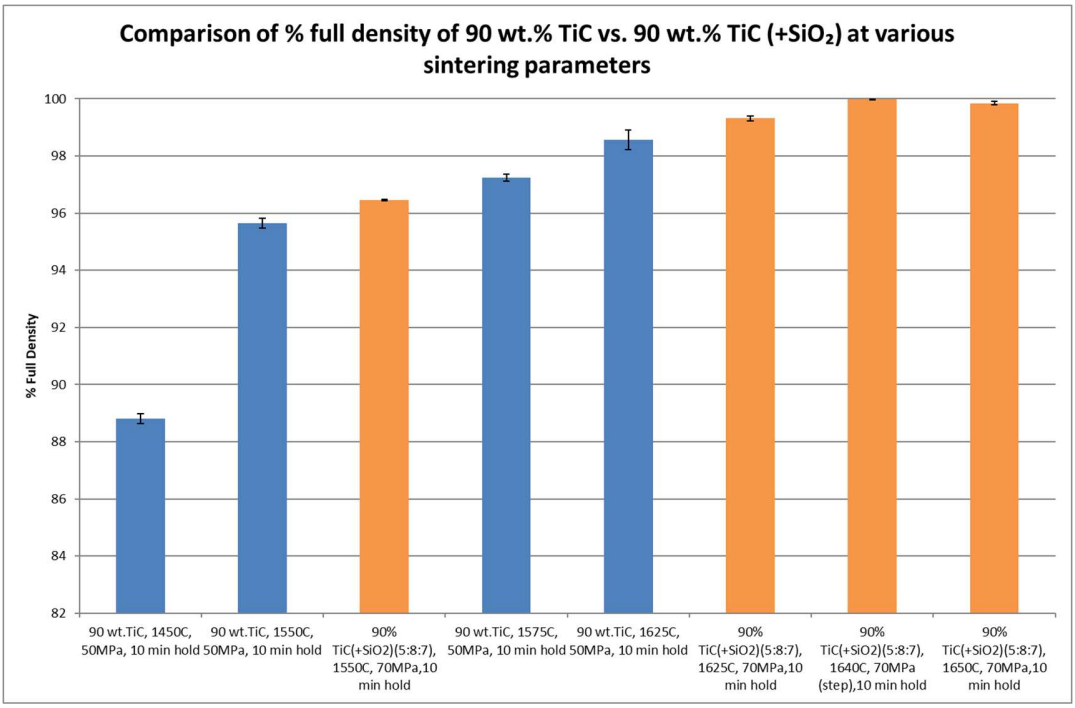


Figure 4.16 Comparison of % of full density of 90 wt.% TiC vs. 90 wt.% TiC(SiO_2) at various sintering parameters

Table 4.11 Hardness and Fracture Toughness of SPS samples with highest density

Sample composition Wt. %	Sintering Pressure MPa)	Sintering Temperature (°C)	Hardness (GPa)	Fracture Toughness– K_{1c} (MPa.$m^{½}$)
90TiC-8Al_2O_3-2Y_2O_3,	50	1625	19.64±0.47	4.48±0.17
90TiC-8Al_2O_3-2Y_2O_3,	70	1625	21.15±0.97	3.98±0.15
85TiC-12Al_2O_3-3Y_2O_3	50	1625	19.23±0.38	5.48±0.26
85TiC-12Al_2O_3-3Y_2O_3	70	1610	20.73±0.27	3.77±0.16
90TiC-2.5Al_2O_3-4Y_2O_3-3.5SiO_2	50	1575	15.15±0.09	3.64±0.25
90TiC-2.5Al_2O_3-4Y_2O_3-3.5SiO_2	70	1625	17.59±1.12	3.74±0.29
85TiC-3.75Al_2O_3-6Y_2O_3-5.25SiO_2	50	1575	16.44±0.09	3.95±0.20
85TiC-3.75Al_2O_3-6Y_2O_3-5.25SiO_2	70	1610	16.10±0.88	3.56±0.53

It was expected that materials with higher hardness values would have lower fracture toughness values as is the case with most polycrystalline ceramic materials. The mechanical properties of the 85 and 90 wt. % TiC compositions without SiO_2 added to their liquid phase agree with this statement. The sintered sample with the highest Vickers hardness was found to be 90TiC-8Al_2O_3-2Y_2O_3 SPS sintered at 1625°C, 70MPa and the sintered sample with the highest fracture toughness was determined to be 85TiC-12Al_2O_3-3Y_2O_3 SPS sintered at 1625°C, 50MPa. From the XRD results it can be observed that the sintered material with the highest fracture toughness had formed YAP instead of YAG during SPS sintering.

The addition of SiO_2 to the liquid phase of the 85-90 wt. % TiC reduced the hardness significantly and fracture toughness in both compositions to which it has been added regardless of the sintering parameters. This could be the result of the formation of large YAG grains which are weaker than the TiC grains and lower the mechanical properties of the sintered material.

Also the presence of yttrium-aluminosillicate glass ($Y_2Si_2O_7$) which acts as a path of least resistance for cracks paths in the sintered material would also lower the fracture toughness of the material.(Kolitsch et al., 1999) All the samples that had SiO_2 added to the liquid phase sintering aids had fracture toughness values that were in agreement with each other and hardness values that has very little difference between then despite the difference in the sintering parameters. The sintered sample with the lowest Vickers hardness and fracture toughness was 90TiC-2.5Al_2O_3-4Y_2O_3-3.5SiO_2 SPS sintered at 1575°C and 50MPa.

5. ANALYSIS OF TIC BASED CMC'S WITH SIC WHISKER OR CBN PARTICLE REINFORCEMENT

5.1 Analysis of the TiC Matrix powders with/without SiO_2 and the addition of SiC whiskers and cBN respectively

Th analysis of XRD patterns were used to confirm the phases of the TiC matrix powders with the addition of liquid phase sintering aids and various reinforcement materials prior to sintering. Knowing which phases were present help to determine which phases were products and which phases were reactants of the chemical reactions that occurred during the sintering process. XRD was also used to check for contamination in the TiC matrix powders after the incorporation of the reinforcement materials.

5.1.1 Examples of typical XRD patterns XRD of milled TiC matrix powders with/without SiO_2 and the addition of SiC whiskers and cBN respectively

The phases present were determined by X-ray diffraction (XRD) using a Bruker AXS D2 phaser desktop powder diffractometer with a monochromatic Co Kα radiation produced at 30 kV and 10 mA, with a step size of 0.03°2θ.

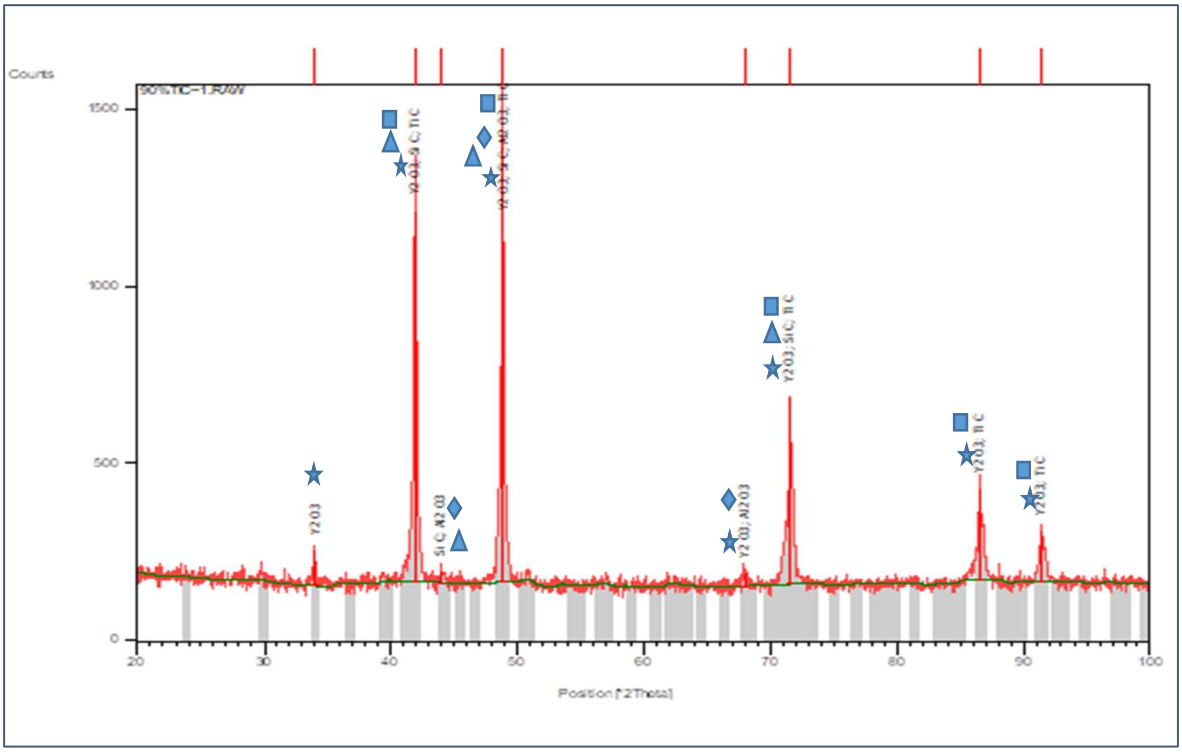


Figure 5.1 a) 90 wt.% TiC (2µm) + 10 vol.% SiCw powder (■TiC, ♦ Al_2O_3, ▲SiC, ★Y_2O_3)

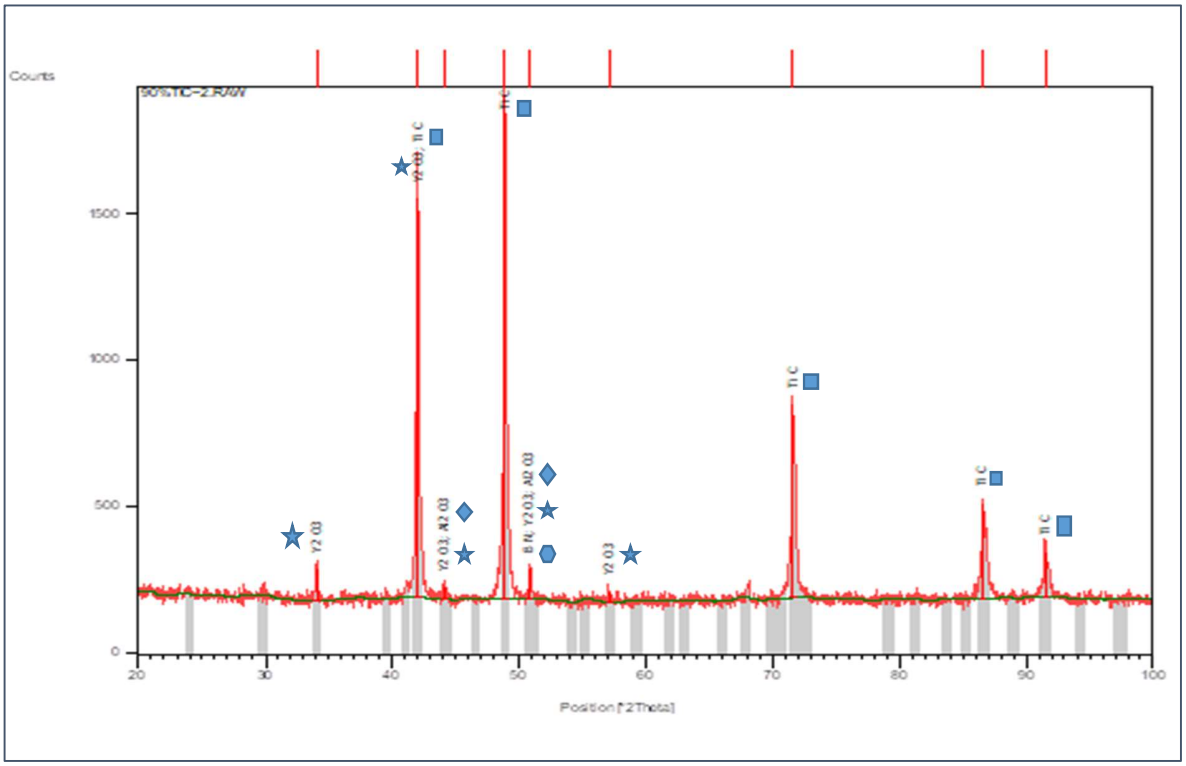


Figure 5.1 b) 90 wt.% TiC (2µm) + 7 vol.% cBN powder (■TiC, ♦ Al_2O_3,⬣ BN , ★Y_2O_3)

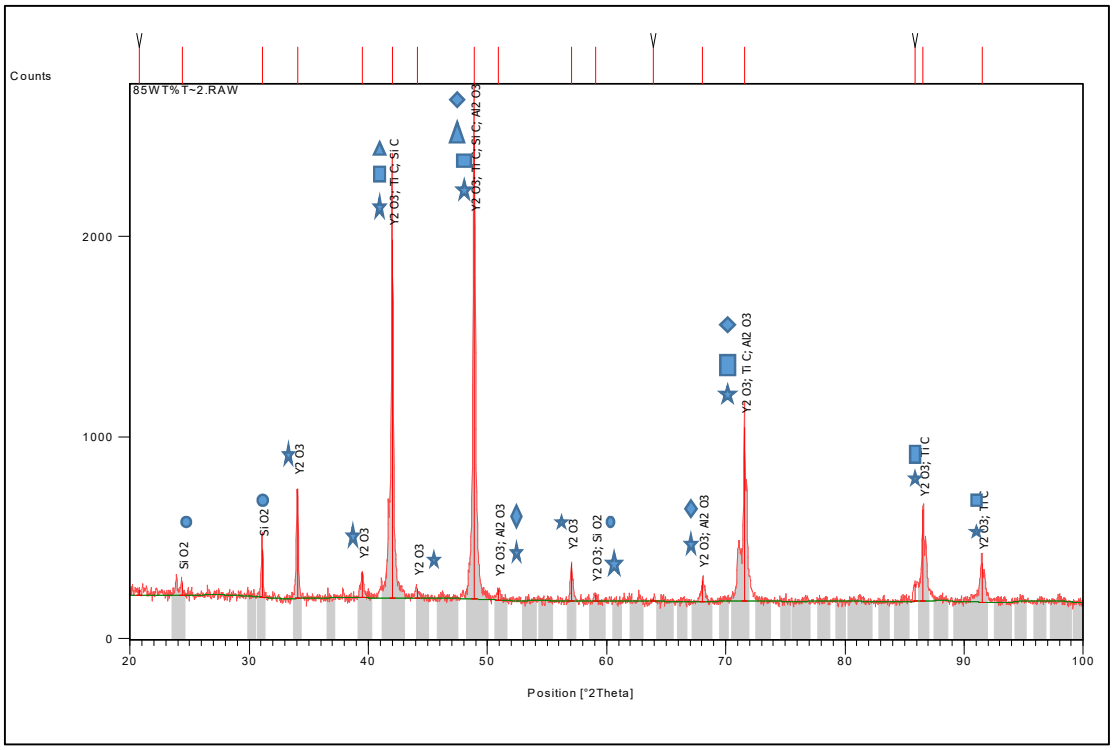


Figure 5.1 c) 85 wt.% TiC (+SiO_2) (5:8:7) + 20 vol.% SiCw powder (■TiC, ♦ Al_2O_3, ▲SiC, ●SiO_2, ★Y_2O_3)

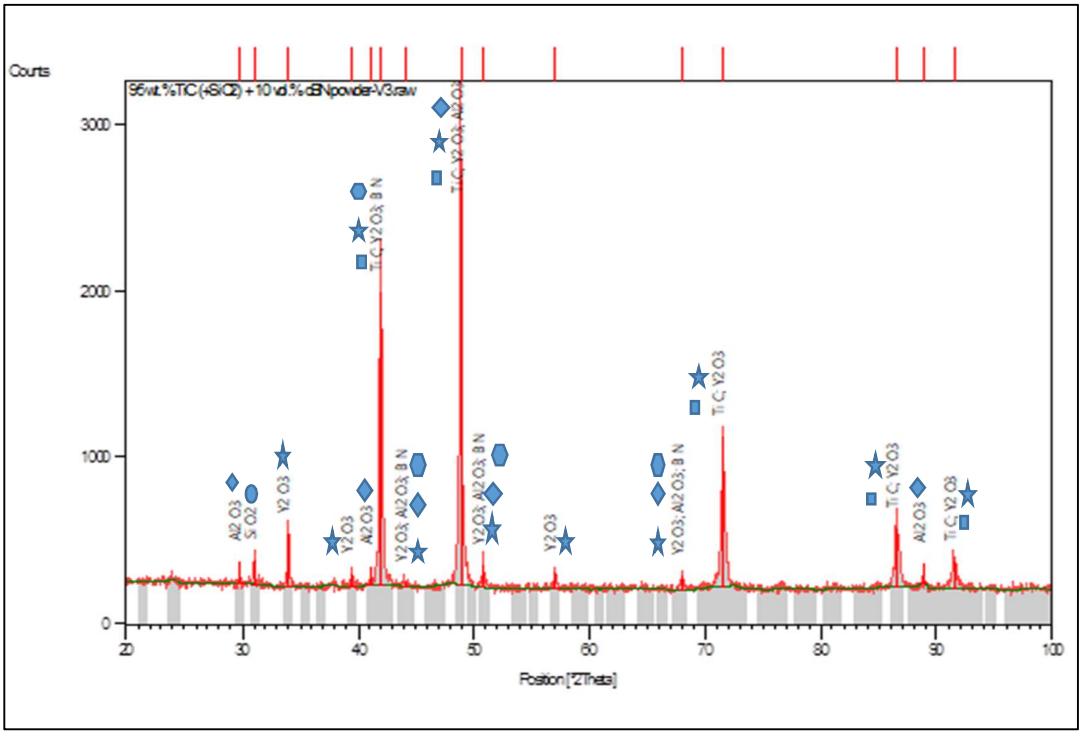


Figure 5.1 d) 90 wt.% TiC (+SiO_2) (5:8:7) + 10 vol.% cBN powder (■TiC, ♦ Al_2O_3, ⬣ BN , ●SiO_2, ★Y_2O_3)

5.1.1.1 Table 5.1 Results of XRD patterns for milled 90 wt.% TiC matrix powders with/without SiO_2 and the addition of SiC whiskers and cBN respectively

Number	Sample name (matrices + reinforcement)	Sample composition, Wt. %	Sample composition, Mol %	TiC	Al_2O_3	Y_2O_3	SiO_2	SiC	cBN
1	90wt.% TiC + 10vol.% SiC_w	83.8TiC-7.45Al_2O_3-1.86Y_2O_3-6.89 (10 vol.%) SiC_w	84.69TiC-4.42Al_2O_3-0.48Y_2O_3-10.41 (10 vol.%) SiC_w	X	X	X	-	X	-
2	90wt.% TiC + 20vol.% SiC_w	77.79TiC-6.86Al_2O_3-1.72Y_2O_3-14.24 (20 vol.%) SiC_w	74.99TiC-3.9Al_2O_3-0.47Y_2O_3-20.65 (20 vol.%) SiC_w	X	X	X	-	X	-
3	90wt.% TiC + 7vol.% cBN	85.41TiC-7.59Al_2O_3-1.9Y_2O_3-5.1 (7 vol.%) cBN	83.24TiC-4.32Al_2O_3-0.47Y_2O_3-11.96 (7 vol.%) cBN	X	X	X	-	-	X
4	90wt.% TiC + 10vol.% cBN	83.41TiC-7.41Al_2O_3-1.85Y_2O_3-7.32 (10 vol.%) cBN	78.75TiC-4.13Al_2O_3-0.45Y_2O_3-16.68 (10 vol.%) cBN	X	X	X	-	-	X
5	90wt.% TiC(+SiO_2) + 10vol.% SiC_w	83.72TiC-2.33Al_2O_3-3.72Y_2O_3-3.26SiO_2-6.98 (10 vol.%) SiC_w	83.98TiC-1.38Al_2O_3-0.96Y_2O_3-3.24SiO_2-10.44 (10 vol.%) SiC_w	X	X	X	X	X	-
6	90wt.% TiC(+SiO_2) + 20vol.% SiC_w	76.99TiC-2.14Al_2O_3-3.42Y_2O_3-2.99SiO_2-14.46 (20 vol.%) SiC_w	74.21TiC-1.21Al_2O_3-0.87Y_2O_3-2.89SiO_2-20.83 (20 vol.%) SiC_w	X	X	X	X	X	-
7	90wt.% TiC(+SiO_2) + 7vol.% cBN	85.35TiC-2.37Al_2O_3-3.78Y_2O_3-3.32SiO_2-5.17 (7 vol.%) cBN	82.47TiC-1.33Al_2O_3-0.98Y_2O_3-3.18SiO_2-12.04 (7 vol.%) cBN	X	X	X	X	-	X
8	90wt.% TiC(+SiO_2) + 10vol.% CBN	83.29TiC-2.31Al_2O_3-3.7Y_2O_3-3.24SiO_2-7.45 (10 vol.%) cBN	77.97TiC-1.29Al_2O_3-0.9Y_2O_3-3.03SiO_2-16.82 (10 vol.%) cBN	X	X	X	X	-	X

5.1.1.2 Table 5.2 Results of XRD patterns for milled 85 wt.% TiC matrix powders with/without SiO_2 and the addition of SiC whiskers and cBN respectively

Number	Sample name (matrices + reinforcement)	Sample composition, Wt. %	Sample composition, Mol %	TiC	Al_2O_3	Y_2O_3	SiO_2	SiC	cBN
9	85wt.% TiC + 10vol.% SiC_w	79.29TiC-11.19Al_2O_3-2.80Y_2O_3-6.72(10 vol.%) SiC_w	82.03TiC-6.82Al_2O_3-0.74Y_2O_3-10.41 (10 vol.%) SiC_w	X	X	X	-	X	-
10	85wt.% TiC + 20vol.% SiC_w	72.77TiC-10.27Al_2O_3-2.57Y_2O_3- 14.38(20 vol.%) SiC_w	72.15TiC-6.0Al_2O_3-0.65Y_2O_3-21.20 (20 vol.%) SiC_w	X	X	X	-	X	-
11	85wt.% TiC + 7vol.% cBN	80.57TiC-11.37Al_2O_3-2.84Y_2O_3-5.21(7 vol.%) cBN	80.06TiC-6.67Al_2O_3-0.77Y_2O_3-12.5 (7 vol.%) cBN	X	X	X	-	-	X
12	85wt.% TiC + 10vol.% cBN	78.701TiC-11.11Al_2O_3-2.79Y_2O_3-7.41(10 vol.%) cBN	75.731TiC-6.34Al_2O_3-0.69Y_2O_3-17.23 (10 vol.%) cBN	X	X	X	-	-	X
13	85wt.% TiC(+SiO_2) + 10vol.% SiC_w	78.96.72TiC-3.48Al_2O_3-5.57Y_2O_3-4.88SiO_2-7.11(10 vol.%) SiC_w	80.62TiC-2.08Al_2O_3-1.53Y_2O_3-4.95SiO_2-10.82 (10 vol.%) SiC_w	X	X	X	X	X	-
14	85wt.% TiC(+SiO_2) + 20vol.% SiC_w	72.53TiC-3.20Al_2O_3-5.12Y_2O_3-4.48SiO_2-14.68 (20 vol.%) SiC_w	70.98TiC-1.82Al_2O_3-1.35Y_2O_3-4.4SiO_2-21.45 (20 vol.%) SiC_w	X	X	X	X	X	-
15	85wt.% TiC(+SiO_2) + 7vol.% cBN	80.53TiC-3.55Al_2O_3-5.68Y_2O_3-4.97SiO_2-5.26 (7 vol.%) cBN	79.13TiC-2.06Al_2O_3-1.47Y_2O_3-4.87SiO_2-12.47 (7 vol.%) cBN	X	X	X	X	-	X
16	85wt.% TiC(+SiO_2) + 10vol.% CBN	78.59TiC-3.47Al_2O_3-5.55Y_2O_3-4.85SiO_2-7.54 (10 vol.%) cBN	74.75TiC-1.94Al_2O_3-1.42Y_2O_3-4.61SiO_2-17.30 (10 vol.%) cBN	X	X	X	X	-	X

5.2 SPS Sintering of TiC matrix powders with/without SiO_2 and the addition of SiC whiskers and cBN

5.2.1 Theoretical density of TiC matrices with/without SiO_2 and the addition of SiC whiskers and cBN respectively

Theoretical density is determined by calculating the average density based on the ratio of components in each composition assuming that all components are at full density.

5.2.1.1 Table 5.3 Compositions of TiC matrix samples without SiO_2 and with the addition of SiC whiskers and cBN respectively

Sample name (matrices + reinforcement) (wt.%)	Theoretical density (g/cm^3)
85TiC-12Al_2O_3-3Y_2O_3	4.79
79.29TiC-11.19Al_2O_3-2.80Y_2O_3-6.72 (10 vol.%) SiC_w	4.64
72.77TiC-10.27Al_2O_3-2.57Y_2O_3-14.38 (20 vol.%) SiC_w	4.48
80.57TiC-11.37Al_2O_3-2.84Y_2O_3-5.21 (7 vol.%) cBN	4.69
78.701TiC-11.11Al_2O_3-2.79Y_2O_3-7.41 (10 vol.%) cBN	4.66
90TiC-8Al_2O_3-2Y_2O_3	4.84
83.8TiC-7.45Al_2O_3-1.86Y_2O_3-6.89 (10 vol.%) SiC_w	4.67
77.79TiC-6.86Al_2O_3-1.72Y_2O_3-14.24 (20 vol.%) SiC_w	4.51
85.41TiC-7.59Al_2O_3-1.9Y_2O_3-5.1 (7 vol.%) cBN	4.74
83.41TiC-7.41Al_2O_3-1.85Y_2O_3-7.32 (10 vol.%) cBN	4.70

5.2.1.2 Table 5.4 Compositions of 85 wt.% TiC matrix samples with SiO_2 and with the addition of SiC whiskers and cBN respectively

Sample composition (Wt. %)	Theoretical density (g/cm^3)
85TiC-3.75Al_2O_3-6Y_2O_3-5.25SiO_2	4.68
78.96.72TiC-3.48Al_2O_3-5.57Y_2O_3-4.88SiO_2-7.11 (10 vol.%) SiCw	4.53
72.53TiC-3.20Al_2O_3-5.12Y_2O_3-4.48SiO_2-14.68 (20 vol.%) SiCw	4.39
80.53TiC-3.55Al_2O_3-5.68Y_2O_3-4.97SiO_2-5.26 (7 vol.%) cBN	4.59
78.59TiC-3.47Al_2O_3-5.55Y_2O_3-4.85SiO_2-7.54 (10 vol.%) cBN	4.56

5.2.1.3 Table 5.5 Composition of 90 wt.% TiC matrix samples with SiO_2 and with the addition of SiC whiskers and cBN respectively

Sample composition (Wt. %)	Theoretical density (g/cm^3)
90TiC-2.5Al_2O_3-4Y_2O_3-3.5SiO_2	4.76
83.72TiC-2.33Al_2O_3-3.72Y_2O_3-3.26SiO_2-6.98 (10 vol.%) SiCw	4.61
76.99TiC-2.14Al_2O_3-3.42Y_2O_3-2.99SiO_2-14.46 (20 vol.%) SiCw	4.47
85.35TiC-2.37Al_2O_3-3.78Y_2O_3-3.32SiO_2-5.17 (7 vol.%) cBN	4.67
83.29TiC-2.31Al_2O_3-3.7Y_2O_3-3.24SiO_2-7.45 (10 vol.%) cBN	4.63

5.2.2 SEM analysis of TiC matrix powder samples with the addition of reinforcing materials

5.2.2.1 Examples of SEM images of TiC matrix powder mixes after the addition of reinforcing material (SiC whiskers) prior to SPS sintering

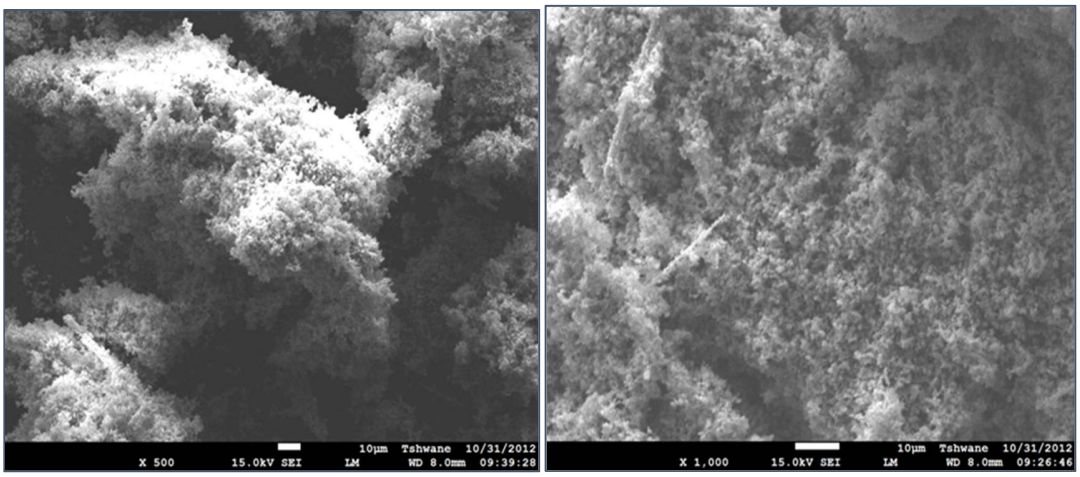


Figure 5.2 SEM images of 83.8 wt.% TiC-7.45 wt.% Al_2O_3-1.86 wt. %Y_2O_3 matrix powder after the addition of 6.89 wt.% (10 vol.%) SiC whiskers

When compared to the SEM images of Figure 4.3 A-D it can be seen that there is far more agglomeration of the TiC matrix powders after attrition milling than prior to it. The SiC whiskers appeared to have survived the attrition milling without having the whiskers broken into shorter lengths. They also appear to be well incorporated into the TiC matrix powders and not gathered into bundles.

SEM images of the TiC matrix powders with the addition of cBN was not required as there was no risk of agglomeration or damage to the reinforcement material during the Turbula mixing process.

5.2.3 SPS sintering parameters for TiC mixes using TiC powder without SiO_2 and with the addition of cBN

TiC matrix mixes are SPS sintered at a rate of 100°C/min to a temperature of 1450- 1625°C, 50-70MPa and 10 min hold at the selected temperature. See Appendix E for Sintering graphs (Piston position and Densification)

5.2.4 SPS sintering parameters for TiC mixes using TiC powder with SiO_2 and with the addition of cBN

TiC matrix mixes are SPS sintered at a rate of 100°C/min to a temperature of 1450- 1625°C, 70MPa and 5/10 min hold at the selected temperature. See Appendix F for Sintering graphs (Piston position and Densification)

5.2.5 SPS sintering parameters for TiC mixes using 2µm TiC powder without SiO_2 and with the addition of SiC whiskers

TiC matrix mixes are SPS sintered at a rate of 100°C/min to a temperature of 1450- 1625°C, 70MPa and 10 min hold at the selected temperature. The graphs below show examples of the densification curves produced during the SPS sintering process. See Appendix G for Sintering graphs (Piston position and Densification)

5.2.6 SPS sintering parameters for TiC mixes using TiC powder with SiO_2 and with the addition of SiC whiskers

TiC matrix mixes are SPS sintered at a rate of 100°C/min to a temperature of 1450- 1625°C, 70MPa and 10 min hold at the selected temperature. The graphs below show examples of the densification curves produced during the SPS sintering process. See Appendix H for Sintering graphs (Piston position and Densification)

5.3 Density of SPS sintered samples

5.3.1 Densities of TiC powder mixes without SiO_2 and with the addition of SiC whiskers

Theoretical density values are calculated prior to the sample being sintered based on what the density of a 100% dense sample with the exact chemical composition regardless of sintering parameters.

Table 5.6: Density of SPS sintered samples with 85 wt. % TiC, liquid phase sintering aids (Al_2O_3-Y_2O_3), SiC whiskers and cBN respectively of various compositions and sintering parameters

Sample composition, Wt. %	Temperature (°C)	Sintering hold time (min)	Sintering pressure (MPa)	Sample Density (g/cm^3)	% theoretical density	% open porosity
85TiC-12Al_2O_3-3Y_2O_3	1550	10	50	4.66	97.19	0.20
	1575	10	50	4.67	97.25	0.22
	1625	10	50	4.73	98.75	0.19
	1550	10	70	4.70	98.14	0.07
	1610	10	70	4.76	99.31	0.09
79TiC+11Al_2O_3-3Y_2O_3-7 (10 vol.%) SiCw	1550	10	50	4.35	93.86	3.68
	1575	10	50	4.40	94.93	2.24
	1600	10	50	4.51	97.32	0.19
	1625	10	50	4.55	98.20	0.64
	1550	10	70	4.45	95.98	1.27
	1600	10	70	4.61	99.35	0.04
73TiC-10Al_2O_3-3Y_2O_3-14 (20 vol.%) SiCw	1550	10	70	3.89	86.02	12.71
	1575	10	70	4.13	92.18	5.97
	1625	10	70	4.36	97.39	0.97
	1550	20	70	4.21	94.00	4.03
	1575	20	70	4.17	93.07	4.53
	1600	20	70	4.33	96.77	1.22
	1625	20	70	4.34	95.99	0.41
80.57TiC-11.37Al_2O_3-2.84Y_2O_3-5.21 (7 vol.%) cBN	1450	5	70	3.83	81.62	17.78
	1550	5	70	3.99	85.07	13.15
	1575	5	70	4.06	86.51	10.30
	1625	5	70	4.20	89.45	8.11
78.7TiC-11.11Al_2O_3-2.79Y_2O_3-7.41 (10 vol.) cBN	1575	10	70	4.00	85.92	12.30
	1625	10	70	4.08	87.53	9.38

Table 5.7: Density of SPS sintered samples with 90 wt. % TiC, liquid phase sintering aids (Al_2O_3-Y_2O_3), SiC whiskers and cBN respectively of various compositions and sintering parameters

Sample composition, Wt. %	Temperature (°C)	Sintering hold time (min)	Sintering pressure (MPa)	Sample Density (g/cm^3)	% theoretical density	% open porosity
90TiC-8Al_2O_3-2Y_2O_3	1450	10	50	4.29	88.81	8.86
	1550	10	50	4.63	95.65	1.37
	1575	10	50	4.84	97.25	0.27
	1625	10	50	4.77	98.57	0.22
83.8TiC-7.45Al_2O_3-1.86Y_2O_3-6.89 (10 vol.%) SiCw	1450	10	50	3.95	84.41	13.78
	1550	10	50	4.33	95.61	3.57
	1575	10	50	4.36	93.41	2.36
	1625	10	50	4.52	96.77	0.05
	1550	10	70	3.97	84.91	10.70
77.79TiC-6.86Al_2O_3-1.72Y_2O_3-14.24 (20 vol.%) SiCw	1550	10	70	3.73	82.65	16.58
	1575	10	70	4.07	90.09	3.16
	1625	20	70	4.20	92.97	5.09
	1550	20	70	4.17	92.48	5.73
85.41TiC-7.59Al_2O_3-1.9Y_2O_3-5.1 (7 vol.%) cBN	1450	10	50	3.62	76.34	21.43
	1550	10	50	3.76	79.43	17.07
	1575	10	50	3.78	79.83	15.40
	1625	10	50	3.90	82.31	11.78
	1450	5	70	3.76	79.38	19.45
	1550	5	70	0.89	82.18	15.90
	1575	5	70	3.94	83.28	14.37
	1625	5	70	4.05	85.45	11.04
83.41TiC-7.41Al_2O_3-1.85Y_2O_3-7.32 (10 vol.%) cBN	1575	10	70	3.91	83.24	14.29
	1625	10	70	4.02	85.53	10.65

Table 5.6 shows the density of samples comprising of 85 wt. % TiC, the balance being liquid phase sintering aids (Al_2O_3-Y_2O_3) under different sintering conditions (temperature, pressure and sintering hold time). The 85 wt. % TiC samples with Al_2O_3 and Y_2O_3 as liquid phase sintering aids have densities between 97.19-99.31 percent of theoretical density. The density of the samples with the higher sintering pressures and higher temperatures are the closest to full density. The samples that have higher sintering pressures also have a lower percentage of open porosity than those sintered at the lower pressure.

There was a marked decrease in the density of the samples with the addition of 10 vol. % (7 wt. %) SiCw when compared with samples without the SiCw when sintered at the same sintering temperature pressure and hold time. At 1550°C, 50 MPa and 10 min holding condition the percentage of theoretical density decreased from 97.19% to 93.86% and the percentage of open porosity increased from 0.20% to 3.86%.

The decrease in density is due to the whiskers preventing the close packing of the matrix particles during the sintering process, inhibiting particle rearrangement before the melting of the liquid phase sintering aids as well as after such melting, when they inhibit the liquid phase to act as lubricant for such densification. Shen et al. 2002 considered sintering pressure condition to be related to densification when higher pressure was applied. This could be mainly attributed to higher packing density of the particles. This is especially the case when the powder contains agglomerates which have a higher probability of being broken down with applying a higher pressure. That process would accelerate densification during sintering (Shen et al., 2002). The sintering pressure was then increased to 70MPa which increased the percentage of theoretical density of the SiCw reinforced samples from 93.86% to 95.98% and decreased the open porosity from 3.86% to 1.27%.

At the higher sintering temperature (1610°C and 1600°C for the unreinforced and reinforced sintered samples respectively) and pressure of 70MPa resulted in the percentage of theoretical density that were very similar; 99.31±0.04% for the unreinforced sintered material and 99.35±0.03% for the SiCw reinforced sintered materials.

At 1610°C the SiCw reinforced sample leaked liquid phase during the sintering process and did not give reliable results for its density hence a slightly lower sintering temperature of 1600°C was used. By increasing the sintering temperature and pressure, the negative effects of the SiCw on the densification of the sample during sintering had been eliminated. The next composition to be sintered included the addition of 20 vol. % SiCw (14 wt. %). The TiC powder mix with the addition of a higher volume of SiCw was sintered at 1550°C, 70 MPa and 10 min hold time resulted in a sintered sample with a dramatic drop in percentage of theoretical density. The percentage of theoretical density dropped from 95.98% for the 7 wt. % SiCw reinforced sintered samples to 86.02% for 14 wt. % SiCw reinforced sintered samples. The percentage open porosity also increased from 1.27% to 12.71% respectively.

With an increase in sintering temperature to 1625°C and with a sintering pressure of 70MPa and 10 min hold the percentage theoretical density increased to 97.39% and the percentage of open porosity decreased to 0.97%. Although this significantly increased the percentage of theoretical density, full theoretical density was not yet achieved. Samples with the 14 wt. % SiCw reinforcement were then sintered for longer hold times in order to increase the densification by allowing more time for the sintering process to reach completion. At 1625°C, 70MPa and 20 min hold there is a slight decrease in the percentage of full density and slight increase in the percentage open porosity of the sintered samples. The extension of the sintering time resulted in a decrease of the relative density probably due to the evaporation of the liquid phase or the evolution of gases produced by various gas producing reactions. This could be due to prolonged sintering under vacuum which leads to deterioration (Chae et al., 1995). Table 5.7 shows the density of samples comprising 90 wt. % TiC, the balance being liquid phase sintering aids (Al_2O_3-Y_2O_3) under differing sintering conditions (temperature, pressure and sintering hold time). The 90 wt. % TiC samples with Al_2O_3 and Y_2O_3 as liquid phase sintering aids have densities between 88.81-98.57 percent of theoretical density. The density of the samples with the higher sintering pressures and higher temperatures are the closest to full density.

The samples that have higher sintering pressures also have a lower percentage of open porosity than those sintered at the lower pressure. There is a noticeable decrease in the density of the samples with the addition of 10 vol.% (7 wt.%) SiCw when compared with the sample without the SiCw when sintered under the same sintering pressure, temperature and hold time. Similarly, with an increase in SiCw content from 10 vol.% (7 wt.%) to 20 vol.% (14 wt.%), the percentage of theoretical density decreased from 84.91 to 82.65 % and the percentage of open porosity increased from 10.70 to 16.50%. To further increase the percentage of theoretical density of the 20 vol.% (14 wt.%) SiCw; the sintering hold time was increased from 10 min to 20 min resulting in an increase in the percentage theoretical density from 82.65% to 92.43% and a decrease in open porosity from 16.50% to 5.73%. Increasing the hold time during sintering had the equivalent effect to sintering at a higher temperature (1625°C) at the same pressure (70MPa).

5.3.2 Densities of TiC powder mixes with SiO_2 and with the addition of SiC whiskers

Table 5.8: Density of SPS sintered samples with 85 wt. % TiC, liquid phase sintering aids (Al_2O_3-Y_2O_3-SiO_2) and SiC whiskers of various compositions and sintering parameters

Sample composition, Wt. %	Temperature (°C)	Sintering hold time (min)	Sintering pressure (MPa)	Sample Density (g/cm^3)	% theoretical density	% open porosity
85TiC-3.75Al_2O_3-6Y_2O_3-5.25SiO_2	1550	10	50	4.68	99.91	0.13
	1575	10	50	4.67	99.90	0.24
	1625	10	50	4.68	99.83	4.97
	1550	10	70	4.68	99.40	0.31
	1575	10	70	4.68	99.44	1.98
	1610	10	70	4.68	99.93	1.43
78.96TiC-3.48Al_2O_3-5.57Y_2O_3-4.48SiO_2-7.11 (10 vol.%) SiC_w	1600	10	70	4.53	99.96	0.40
72.53TiC-3.20Al_2O_3-5.12Y_2O_3-4.48SiO_2-14.68 (20 vol.%) SiC_w	1550	10	70	4.09	93.29	2.93
	1625	10	70	4.36	99.46	0.54

Table 5.9: Density of SPS sintered samples with 90 wt. % TiC, liquid phase sintering aids (Al_2O_3-Y_2O_3-SiO_2) and SiC whiskers of various compositions and sintering parameters

Sample composition, Wt. %	Temperature (°C)	Sintering hold time (min)	Sintering pressure (MPa)	Sample Density (g/cm^3)	% theoretical density	% open porosity
90TiC-2.5Al_2O_3-4Y_2O_3-3.5SiO_2	1550	10	50	4.53	95.12	1.58
	1575	10	50	4.60	96.63	0.65
	1625	10	50	4.73	97.84	0.28
	1550	10	70	4.59	96.45	1.18
	1575	10	70	4.61	96.92	1.27
	1625	10	70	4.73	99.85	1.39
	1650	10	70	4.75	98.85	1.13
76.99TiC-2.14Al_2O_3-3.42Y_2O_3-2.99SiO_2-14.46 (20 vol.%) SiC_w	1550	10	70	3.87	86.84	12.61
	1625	10	70	4.22	94.80	3.06
	1640	10	70	4.15	93.13	4.42
	1650	10	70	4.22	94.88	4.35

Table 5.8 shows the density of sintered samples that comprise 85 wt. % TiC and SiO_2 along with the other liquid phase sintering aids. All the samples are close to full density. The addition of SiO_2 reduced the theoretical density from 4.79g/cm³ to 4.68 g/cm³ but increased the percentage of theoretical density of sintered samples even at the lowest temperature tested (1550°C). Densities of the sintered samples are within the range 99.40% - 99.93% as a percentage of theoretical density. Generally, there was a slight increase in density with the increase in sintering temperature but a slight decrease in density with an increase in pressure due the liquid phase leaking out during sintering. The increase in pressure also increases the percentage of open porosity. The samples with a sintering temperature of 1625°C showed a deviation from the trend of increasing density with increasing temperature by having a lower percentage theoretical density of the samples sintered at 1610°C. At 1625°C there was a significant increase in the percentage of open porosity.

There is a marked decrease in the density of the samples with the addition of 20 vol. % (15 wt. %) SiCw when compared with samples without the SiCw when sintered under the equivalent sintering temperature pressure and hold time. At the 1550°C, 70 MPa and 10 min hold condition the percentage of theoretical density decreased from 99.40% to 93.29% and the percentage of open porosity increased from 0.31% to 2.93%. The decrease in density is due to the whiskers preventing the close packing of the matrix materials. There is a decrease in the percentage of theoretical density and increase in open porosity of the SiCw reinforced samples at 1550°C and 70 MPa sintering conditions when compared to the matrix only samples. This was most likely due to the evaporation of the liquid phase or the evolution of gases produced by the various gas-generating reactions as seen in the 85TiC-3.75Al_2O_3-6Y_2O_3-5.25SiO_2 composition. With an increase in sintering temperature to 1625°C and with a sintering pressure of 70MPa and 10 min hold the percentage theoretical density of the SiCw reinforced sintered samples increased to 99.46% and the percentage of open porosity decreased to 0.54%.

Table 5.9 shows the density of sintered samples that comprise 90 wt. % TiC and SiO_2 along with the other liquid phase sintering aids. All the samples are close to full density. The addition of SiO_2 reduced the theoretical density from 4.84/cm³ to 4.76 g/cm^3 but increased the percentage of theoretical density of sintered samples even at the lowest temperature tested (1550°C). There is an increase in theoretical density with increase in temperature as well as a slight increase when the sintering pressure is increased from 50MPa to 70MPa. The percentage of open porosity however increased with the increase in sintering pressure. At temperature above 1625°C there is a 1% decrease in the percentage of theoretical density at the same sintering pressure and sintering hold time even though the percentage of open porosity had decreased from 1.39% to 1.13%. This could be due to the flow of liquid sintering aids from the center of the sample towards the edges during sintering at the higher temperatures creating a potential density gradient within the sample. However, this effect is negligible at best due to the sample being very close to full density.

5.3.3 Densities of TiC powder mixes with/without SiO_2 and with the addition of cBN

The aim during sintering was to prevent hexagonalization from cBN to hBN during sintering and still obtain a reasonable percentage of theoretical density. Carefully balancing the desire to maintain the cBN and still densify the sample to a high enough density that can be treated as a technical ceramic was a challenge when trying to create sintering profiles for this material. cBN itself can be difficult to sinter at lower pressures and higher volume ratios due to the formation of an incompressible lattice-like substructure within the sample leading to large pores that cannot be closed during the sintering process. hBN is analogous to the graphite phase of carbon and hinders sintering and densification by preventing wetting of the surface grains during the sintering process regardless of the liquid phase sintering additives added (Zhang et al., 2014).

Table 5.10: Density of SPS sintered samples with 85 wt. % TiC, liquid phase sintering aids (Al_2O_3-Y_2O_3-SiO_2) and cBN of various compositions and sintering parameters

Sample composition, Wt. %	Temperature (°C)	Sintering hold time (min)	Sintering pressure (MPa)	Sample Density (g/cm^3)	% theoretical density	% open porosity
80.57TiC-11.37Al_2O_3-2.84Y_2O_3-5.21 (7 vol.%) cBN	1450	5	70	3.83	81.62	17.78
	1550	5	70	3.99	85.07	13.15
	1575	5	70	4.06	86.51	10.30
	1625	5	70	4.20	89.45	8.11
78.70TiC-11.11Al_2O_3-2.79Y_2O_3-7.41 (10 vol.%) cBN	1575	10	70	4.00	85.92	12.30
	1625	10	70	4.08	87.53	9.38
78.59TiC-3.47Al_2O_3-5.55Y_2O_3-4.85SiO_2-7.54 (10 vol.%) cBN	1575	10	70	3.89	85.43	0.03
	1575	5	70	4.40	96.45	0.34

Table 5.10 shows the theoretical density and percentage of theoretical density in SPS'd samples that contain 85 wt. % TiC with the addition of liquid phase sintering additives.

The addition of 7 vol.% (5 wt.%) cBN to the 85 wt.% TiC matrices caused a significant decrease in the percentage of theoretical density at the same sintering pressure and temperature. Shorter hold times were used to prevent the conversion of cBN to hBN although this may have also contributed to the decrease in the theoretical density.

In the sample sintered at 1550°C, 70MPa the density decreased from 98.14% to 85.07% and increased the percentage of open porosity from 0.07% to 13.15%. Increasing the cBN content from 7 vol.% (5 wt.%) to 10 vol. % (7.4 wt.%) resulted in a drastic decrease in the percentage of theoretical density in the 85 wt.% TiC matrices. At temperatures below 1575°C, pressures below 70 MPa and a hold time of less than 10 min sintering was incomplete. The addition of cBN to a matrix containing 15 wt.% liquid phase sintering aids of which 11 wt.% was Al_2O_3 could cause a lowering in the densification rate as cBN has a suppressive effect on the grain growth of Al_2O_3 during sintering (Hotta & Goto, 2008).

The addition of SiO_2 of 85 wt. % TiC matrix changes the rate of densification as seen in Figure 5.3 below. The addition of cBN in SPS sintered ceramic matrix composites usually decreased the relative density at equivalent pressures; but the addition of SiO_2 to the Al_2O_3-Y_2O_3 liquid phase sintering aids in the 85wt.% TiC matrix had increased the densification rate possibly due to the formation of SiAlON which reacts with the cBN (Ye et al., 2010). The samples containing SiO_2 have very similar percentage of theoretical density to those of samples without SiO_2 from 85.92% to 85.43% for the same sintering conditions (1575°C, 70 MPa and 10 min hold). The percentage of open porosity decreased substantially from 12.30% to 0.03%. When the hold time was reduced from 10 min to 5 min keeping the other sintering parameters the same (1575°C, 70 MPa) there was a large jump in the percentage of theoretical density for 85.43% to 96.45% and a slight increase in the percentage of open porosity from 0.03% to 0.34%. It would be hypothesized that the longer hold time and high percentage of liquid phase additives could have resulted the squeezing out of the liquid phase preventing or reducing the samples ability to densify or maintain densification during sintering.

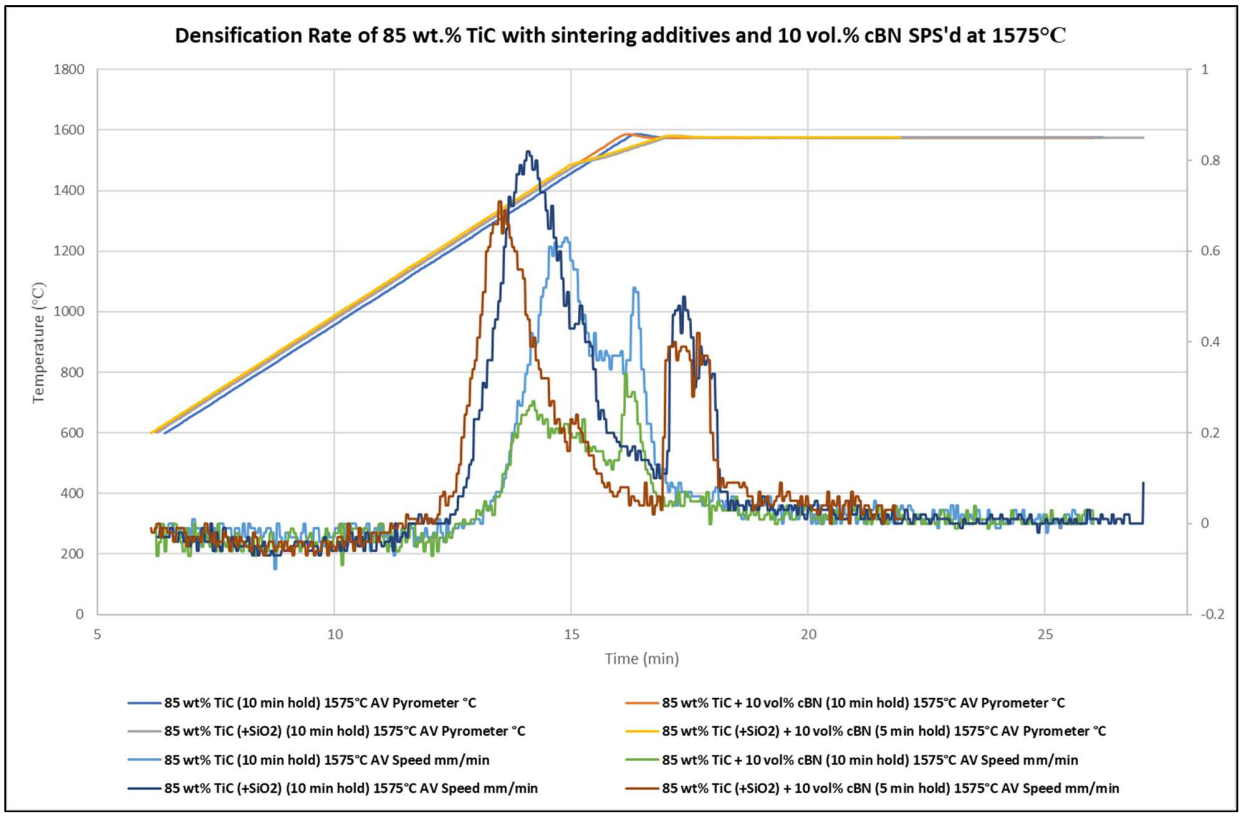


Figure 5.3 Densification rate of 85 wt.% TiC matrices with/without SiO_2 and 10 vol.% cBN SPS'd at 1575°C

Table 5.11: Density of SPS sintered samples with 90 wt. % TiC, liquid phase sintering aids (Al_2O_3-Y_2O_3-SiO_2) and cBN of various compositions and sintering parameters

Sample composition, Wt. %	Temperature (°C)	Sintering hold time (min)	Sintering pressure (MPa)	Sample Density (g/cm^3)	% theoretical density	% open porosity
85.41TiC-7.59Al_2O_3-1.9Y_2O_3-5.1 (7 vol.%) cBN	1450	10	50	3.62	76.34	21.43
	1550	10	50	3.76	79.43	17.07
	1575	10	50	3.78	79.83	15.40
	1625	10	50	3.90	82.31	11.78
	1450	5	70	3.76	79.38	19.45
	1550	5	70	0.89	82.18	15.90
	1575	5	70	3.94	83.28	14.37
	1625	5	70	4.05	85.45	11.04
83.41TiC-7.41Al_2O_3-1.85Y_2O_3-7.32 (10 vol.%) cBN	1575	10	70	3.91	83.24	14.29
	1625	10	70	4.02	85.53	10.65
83.29TiC-2.31Al_2O_3-3.7Y_2O_3-3.24SiO_2-7.45 (10 vol.%) cBN	1575	10	70	4.24	91.50	4.81
	1575	5	70	4.14	89.46	7.46

Table 5.11 shows the theoretical density and percentage of theoretical density in SPS'd samples that contain 90 wt. % TiC with the addition of liquid phase sintering additives but without SiO_2. The addition of 7 vol.% (5 wt.%) cBN to the 90 wt.% TiC matrices caused a significant decrease in the percentage of theoretical density at the same sintering pressure and temperature. Shorter hold times were used to prevent the conversion of cBN to hBN. In Table 5.10, the sample sintered at 1550°C, 50MPa the density decreased from 95.65% to 79.43% and increased the percentage of open porosity from 1.37% to 17.07 %. In an attempt to increase the density of the samples containing cBN sintering parameters are adjusted to increase the pressure from 50 to 70MPa and reduce the hold time from 10 min to 5 min. This adjustment resulted in an increase in percentage of theoretical density from 79.83% to 83.28% and percentage of open porosity of 15.40% to 14.37%.

Increasing the cBN content from 7 vol.% (5 wt.%) to 10 vol. % (7.4 wt.%) resulted in a substantial decrease in the percentage of theoretical density in the 90 wt.% TiC matrix**.** At temperatures below 1575°C, pressures below 70 MPa and a hold time of less than 10 min during sintering was considered to be incomplete.

The addition of SiO_2 in the ceramic made with 90 wt. % TiC matrix changes the rate of densification. The addition of cBN in SPS sintered ceramic matrix composites usually decreased the relative density at equivalent pressures; but the addition of SiO_2 to the Al_2O_3-Y_2O_3 liquid phase sintering aids in the 90wt.% TiC matrix had increased the densification rate. The samples containing SiO_2 have a higher percentage of theoretical density compared with those of samples without SiO_2 from 83.24% to 91.50% for the same sintering conditions (1575°C, 70 MPa and 10 min hold). The percentage of open porosity decreased substantially from 14.29% to 4.81%. When the hold time was reduced from 10 min to 5 min keeping the other sintering parameters the same (1575°C, 70 MPa) there was a decrease in the percentage of theoretical density from 91.50% to 89.46% and an increase in the percentage of open porosity from 4.81% to 7.46%. The difference in the sintering behavior between the 85 wt.% TiC matrices and the 90 wt.% TiC matrices after the addition of the cBN reinforcement directly correlate to the volume and composition of the liquid phase sintering aids and their interaction with the cBN.

5.4 Phases identified by XRD measurements of SPS sintered samples

5.4.1 Phases identified by XRD analysis of SPS'd samples of TiC + SiCw with the highest percentage theoretical density

Table 5.12 Phases identified by XRD analysis of SPS'd samples of 85 wt. % TiC + SiCw with the highest percentage theoretical density. (YAG-$Y_3Al_5O_{12}$, YAP- $YAlO_3$)

Sample composition, Wt. %	Sample composition, Mol %	% of Theoretical Density	Sintering Pressure (MPa)	Sintering Temp (°C)	TiC	Al_2O_3	Y_2O_3	YAG	YAP	SiC	Al_2OC	$Y_2Si_2O_7$
85TiC-12Al_2O_3-3Y_2O_3	91.55TiC-7.59Al_2O_3-0.86Y_2O_3	99.31	70	1610	X	X	X	-	X	-	-	-
79TiC-11Al_2O_3-3Y_2O_3-7 (10 vol.%) SiCw	81.69TiC-6.68Al_2O_3-0.82Y_2O_3-10.81SiCw	99.35	70	1600	X	X	-	X	-	X	-	-
73TiC-10Al_2O_3-3Y_2O_3-14 (20 vol.%) SiCw	72.58TiC-5.84Al_2O_3-0.79Y_2O_3-20.79SiCw	97.39	70	1625	X	X	-	X	-	X	-	-
85TiC-3.75Al_2O_3-6Y_2O_3-5.25SiO_2	90.40TiC-2.34Al_2O_3-1.69Y_2O_3-5.57SiO_2	99.93	70	1610	X	X	-	X	-	-	-	X
73TiC-3Al_2O_3-5Y_2O_3-4SiO_2-15 (20 vol.%) SiCw	71.23TiC-1.72Al_2O_3-12.94Y_2O_3-3.89SiO_2-21.86SiCw	99.46	70	1625	X	X	X	X	-	X	X	X

The results in Table 5.12 above show the sample composition in both weight % and mole % of the reactants prior to sintering. For the sample with the composition 85 wt. % TiC-12 wt. % Al_2O_3-3 wt. % Y_2O_3 the results of the XRD analysis show that YAP is detected as a reaction product during the sintering process as well as the original reactants TiC, Al_2O_3 and Y_2O_3. A comparison of the mole % of the of Al_2O_3-Y_2O_3 in the 85wt. % TiC-12wt. % Al_2O_3-3wt. % Y_2O_3 equates to 91.55mol % TiC-7.59 mol % Al_2O_3-0.86 mol % Y_2O_3 which has a ratio of liquid phase sintering aids of approximately 9:1 moles.

When compared with the Al_2O_3-Y_2O_3 phase diagram described by Fabrichnaya and Seifert (Figure 5.4) we expect that no reaction products should be present but our results show that YAP is formed which is only expected to form at around 50 mol % Y_2O_3 (Fabrichnaya & Seifert, 2001). The difference between the results could be due to the difference in sintering conditions such as sintering pressure, hold time, heating and cooling rates. The sample with the composition 79 wt. % TiC-11 wt. % Al_2O_3-3 wt. % Y_2O_3-7wt. % SiCw equates to 81.69 mol. %TiC-6.68 mol. % Al_2O_3-0.82 mol. % Y_2O_3-10.81 mol. % SiCw. The ratio of SiC: Al_2O_3: Y_2O_3 was ~ 13:8:1 mole, respectively.

The analysis shows the presence of the TiC, YAG, Al_2O_3 and SiC in the sintered material which is in agreement with the phase diagram in Figure 5.5 even though the sample was sintered at the higher temperature of 1600°C. Y_2O_3 is not present after sintering which is possibly due to the formation of YAG during sintering. Following that the sample with the composition 73 wt. % TiC-10 wt. % Al_2O_3-3 wt. % Y_2O_3-14 wt. % SiCw equating to 72.58 mol. % TiC-5.84 mol. % Al_2O_3-0.79 mol. % Y_2O_3-20.79 mol. % SiCw was analysed. The ratio of SiC: Al_2O_3: Y_2O_3 was ~ 53:15:2 mole, respectively. The analysis of the results showed similar results as the sample containing 7 wt. % SiCw. They showed the presence of the TiC, YAG, Al_2O_3 and SiC in the sintered material which agrees with the phase diagram in Figure 5.6. Neher et al. found through careful EDX analysis of the microstructure of SPS and heat treated samples did not result in the formation of some SiO_2 containing glasses or crystalline phases. This was to be expected as the SiO_2 content introduced by the surface oxidation of the SiCw was not sufficient to react with the liquid phase sintering aids (Neher et al., 2011).

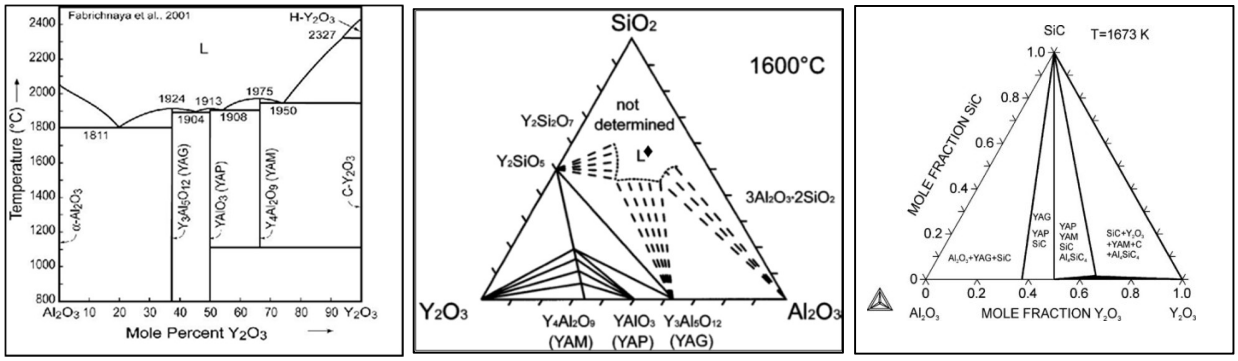


Figure 5.4 Y_2O_3-Al_2O_3 phase diagram (Fabrichnaya & Seifert, 2001)**, Figure 5.5 Isothermal section of the system Y_2O_3-Al_2O_3-SiO_2 at 1600°C in air (in mol %)** (Kolitsch et al., 1999) **♦ - Represents liquid phase sintering aid composition used and Figure 5.6 Phase relation in the ternary system SiC- Al_2O_3-Y_2O_3 at 1400°C** (Neher et al., 2011)

The next composition analysed was 85TiC-3.75Al_2O_3-6Y_2O_3-5.25SiO_2. Samples sintered under the 70 MPa and 1610°C condition showed that TiC, Al_2O_3, Y_2O_3, YAG and $Y_2Si_2O_7$ were detected. The mole % of the of Al_2O_3-Y_2O_3-SiO_2 system in the 85 wt. % TiC-3.75 wt. % Al_2O_3-6 wt. % Y_2O_3-5.25 wt. % SiO_2 composition equates to 90.40 mol. % TiC-2.34 mol. % Al_2O_3-1.69 mol. % Y_2O_3-5.57 mol. % SiO_2. The sintered samples had a ratio of liquid phase sintering aids of approximately 3:2:7 mole, respectively. The phase diagram in Figure 5.4 is in agreement with the experimental results.

The final composition analysed was 73 wt. % TiC-3 wt. % Al_2O_3-5 wt. % Y_2O_3-4 wt. % SiO_2-15 wt. % SiCw which equates 71.23 mol. % TiC-1.72 mol. % Al_2O_3-12.94 mol. % Y_2O_3-3.89 mol. % SiO_2-21.86 mol.% SiCw. Samples sintered at a temperature of 1625°C, 70 MPa and 10 min hold were analysed and the following components were detected: TiC, Al_2O_3, Y_2O_3, YAG, Y_2SiO_7 and Al_2OC. The presence of YAG and Y_2SiO_7 was in agreement with the phase diagram in Figure 5.5. Al_2OC can be an interfacial phase in composites that contain SiC and Al_2O_3 most notably when SiC is sintered with Al, B and/or C additives. Al_2OC are usually present as nanometre-thick grain boundary films that are weaker than the surrounding matrix (Yu & Zhang, 2007).

Table 5.13 Phases identified by XRD analysis of SPS'd samples of 90 wt. % TiC + SiCw with the highest percentage theoretical density. (YAG-$Y_3Al_5O_{12}$, YAP- $YAlO_3$)

Sample composition, Wt. %	Sample composition, Mol %	% of Theoretical Density	Sintering Pressure (MPa)	Sintering Temp (°C)	TiC	Al_2O_3	Y_2O_3	YAG	YAP	SiC	$Y_2Si_2O_7$	Y_5Si_3C
90TiC-8Al_2O_3-2Y_2O_3	94.51TiC-4.93Al_2O_3-0.56Y_2O_3	98.57	70	1625	X	-	X	X	-	-	-	-
83.8TiC-7.45Al_2O_3-1.86Y_2O_3-6.89 (10 vol.%) SiCw	84.69TiC-4.42Al_2O_3-0.48Y_2O_3-10.41SiCw	96.77	50	1625	X	X	-	-	-	X	-	X
77.79TiC-6.86Al_2O_3-1.72Y_2O_3-14.24 (20 vol.%) SiCw	74.99TiC-3.90Al_2O_3-0.47Y_2O_3-20.65SiCw	92.97	50	1625	X	-	X	X	-	X	-	-
90TiC-2.5Al_2O_3-4Y_2O_3-3.5SiO_2	93.73TiC-1.53Al_2O_3-1.11Y_2O_3-3.63SiO_2	99.85	70	1625	X	X	-	X	-	-	X	-
76.99TiC-2.14Al_2O_3-3.42Y_2O_3-2.99SiO_2-14.46 (20 vol.%) SiCw	74.21TiC-1.21Al_2O_3-0.87Y_2O_3-2.89SiO_2-20.83SiCw	94.88	70	1650	X	-	X	X	-	X	X	-

The results in Table 5.13 show the sample composition in both weight % and mole % of the reactants prior to sintering. For the sample with the composition 90 wt.% (88.3 vol.%) TiC-8 wt.% (9.8 vol.%) Al_2O_3-2 wt.% (1.9 vol.%) Y_2O_3 the results of the XRD analysis show that all the reactants besides Al_2O_3 were present in detectable amounts as well as YAG as a reaction product.

A comparison of the mole % of the of Al_2O_3-Y_2O_3 in the 90wt.% (88.3 vol.%) TiC-8wt.% (9.8 vol.%) Al_2O_3-2wt.% (1.9 vol.%) Y_2O_3 equates to 94.51mol % TiC-4.93 mol % Al_2O_3-0.56 mol % Y_2O_3 which has a ratio of liquid phase sintering aids of approximately 17:1 mole.

The sample with the composition 83.8wt.% (79.4 vol.%) TiC-7.45wt.% (8.8 vol.%) Al_2O_3-1.86wt.% (1.7 vol.%) Y_2O_3-6.89wt.% (10 vol.%) SiCw equates to 84.69 mol. %TiC-4.42 mol. % Al_2O_3-0.48 mol. % Y_2O_3-10.41 mol. % SiCw. The mol ratio of SiC: Al_2O_3: Y_2O_3 was ~ 22:9:1 respectively. The analysis shows the presence of the TiC, YAG, Al_2O_3 and SiC in the sintered material which is in agreement with the phase diagram in Figure 5.4 even though the sample was sintered at the higher temperature of 1625°C. Y_2O_3 is not present after sintering which is possibly due to the formation of Y_5Si_3C during sintering as seen in Table 5.12.

The sample with the composition 77.79wt.% (70.7 vol.%) TiC-6.86wt.% (7.8 vol.%) Al_2O_3-1.72 wt.% (1.5 vol.%) Y_2O_3-14.24wt.% (20 vol.%) SiCw equating to 74.99 mol. % TiC-3.90 mol. % Al_2O_3-0.47 mol. % Y_2O_3-20.65 mol. % SiCw was analysed. The ratio of SiC: Al_2O_3: Y_2O_3 was ~ 44:8:1 mole, respectively. The analysis of the results showed similar results as the sample containing 7 wt. % SiCw. They showed the presence of the TiC, YAG, Y_2O_3 and SiC in the sintered material which is in agreement with the phase diagram in Figure 5.6.

Neher et al. found through careful EDX analysis of the microstructure of SPS and heat treated samples did not result in the formation of some SiO_2 containing glasses or crystalline phases. This was to be expected as the SiO_2 content introduced by the surface oxidation of the SiCw was not sufficient to react with the liquid phase sintering aids (Neher et al., 2011).

The next composition analysed was 90wt.% (86.9 vol.%) TiC-2.5wt.% (3.0 vol.%) Al_2O_3-4wt.% (3.8 vol.%) Y_2O_3-3.5wt.% (6.3 vol.%) SiO_2. Samples sintered under the 70 MPa and 1625°C condition showed that TiC, Al_2O_3, Y_2O_3, YAG and $Y_2Si_2O_7$ were detected. The mole % of the of Al_2O_3-Y_2O_3-SiO_2 system in the 90 wt. % TiC-2.5 wt. % Al_2O_3-4 wt. % Y_2O_3-3.5 wt. % SiO_2 composition equates to 93.73 mol. % TiC-1.53 mol. % Al_2O_3-1.11 mol. % Y_2O_3-3.63 mol. % SiO_2. The sintered samples had a ratio of liquid phase sintering aids of approximately 3:2:7 mole, respectively. The phase diagram in Figure 5.5 is in agreement with the experimental results.

The final composition analysed in the set with SiCw reinforced ceramics was 76.99wt.% (69.5 vol.%) TiC-2.14 wt.% (2.4 vol.%) Al_2O_3-3.42wt.% (3.0 vol.%) Y_2O_3-2.99 wt.% (5.0 vol.%) SiO_2-14.46wt.% (20 vol.%) SiCw which equates 74.21 mol. % TiC-1.21 mol. % Al_2O_3-0.87 mol. % Y_2O_3-2.89 mol. % SiO_2-20.83 mol.% SiCw. Samples sintered at a temperature of 1625°C, 70 MPa and 10 min hold were analysed and the following components were detected: TiC, Y_2O_3, YAG, Y_2SiO_7. The presence of YAG and Y_2SiO_7 was in agreement with the phase diagram in Figure 5.11 (Yu & Zhang, 2007).

5.4.2 Phases identified by XRD analysis of SPS'd samples of TiC + cBN with the highest percentage theoretical density

Table 5.14 Phases identified by XRD analysis of SPS'd samples of 85 wt. % TiC + cBN with the highest percentage theoretical density. (YAG-$Y_3Al_5O_{12}$, YAP- $YAlO_3$)

Sample composition, Wt. %	Sample composition, Mol %	% of Theoretical Density	Sintering Pressure and time (MPa)	Sintering Temp (°C)	TiC	TiB_2	Al_2O_3	Y_2O_3	YAG	YAP	cBN	hBN	$Y_2Si_2O_7$	$Y_2Al_3Si_2$
80.57TiC-11.37Al_2O_3-2.84Y_2O_3-5.21 (7 vol.%) cBN	80.06TiC-6.67Al_2O_3-0.77Y_2O_3-12.5cBN	86.51	70–5min	1575	X	-	X	X	-	X	X	-	-	-
80.57TiC-11.37Al_2O_3-2.84Y_2O_3-5.21 (7 vol.%) cBN	80.06TiC-6.67Al_2O_3-0.77Y_2O_3-12.5cBN	89.45	70-5 min	1625	X	-	X	-	-	X	-	X	-	-
78.7TiC-11.11Al_2O_3-2.79Y_2O_3-7.41 (10 vol.%) cBN	75.73TiC-6.34Al_2O_3-0.69Y_2O_3-17.23 cBN	85.92	70-10 min	1575	X	X	X	-	X	-	X	-	-	-
78.7TiC-11.11Al_2O_3-2.79Y_2O_3-7.41(10 vol.%) cBN	75.73TiC-6.34Al_2O_3-0.69Y_2O_3-17.23 cBN	87.53	70-10 min	1625	X	X	X	X	X	-	-	-	-	-
78.59TiC-3.47Al_2O_3-5.55Y_2O_3-4.85SiO_2-7.54 (10 vol.%) cBN	74.75TiC-1.94Al_2O_3-1.42Y_2O_3-4.61SiO_2-17.30cBN	85.43	70-10 min	1575	X	X	X	-	-	-	X	-	X	X
78.59TiC-3.47Al_2O_3-5.55Y_2O_3-4.85SiO_2-7.54 (10 vol.%) cBN	74.75TiC-1.94Al_2O_3-1.42Y_2O_3-4.61SiO_2-17.30cBN	96.45	70-5 min	1575	X	-	-	X	X	X	X	-	X	-

The results in Table 5.14 show the sample composition in both weight % and mole % of the reactants prior to sintering. For the sample with the composition 80.57 wt. % TiC-11.37 wt. % Al_2O_3-2.84 wt. % Y_2O_3 -5.21 wt. % cBN the results of the XRD analysis show that all the reactants were present in detectable amounts as well as YAP as a reaction product in the sample sintered at 1575°C, 70MPa and 5 min hold.

A comparison of the volume % of the of Al_2O_3-Y_2O_3 in the 80.57 wt. % TiC-11.37wt. % Al_2O_3-2.84wt. % Y_2O_3 -5.21 wt. % cBN equates to 82.1 vol. % TiC-9.1 vol. % Al_2O_3-1.8 vol. % Y_2O_3- 7.0 vol. % cBN which has a ratio of liquid phase sintering aids to TiC of approximately 8:1. The ratio of cBN: Al_2O_3: Y_2O_3 was ~ 4:5:1 respectively.

For the same composition sintered at 1625°C, 70MPa and 5 min hold the results of the XRD analysis show that most of the reactants except for the Y_2O_3 which may have been used up during the reaction to form YAP as a product. The sample with the composition 78.7 wt. % TiC-11.11 wt. % Al_2O_3-2.79 wt. % Y_2O_3-7.41 wt. % cBN equates to 79.5 vol. %TiC-8.8 vol. % Al_2O_3-1.7 vol. % Y_2O_3-10.0 vol. % cBN. The ratio of cBN: Al_2O_3: Y_2O_3 was ~ 6:5:1 respectively.

The analysis shows the presence of the TiC, TiB_2 YAG, Al_2O_3 and cBN. Y_2O_3 is not present after sintering which is possibly due to the formation of YAG during sintering at 1575°C, 70MPa and 10 min hold. For the same composition sintered at 1625°C, 70MPa and 10 min hold the results of the XRD analysis show the presence of the Y_2O_3 which should have been used up during the reaction to form YAG as a product.

Which was unexpected as it was not found in the samples sintered at a lower temperature. The next composition analysed was 78.59 wt. %TiC-3.47 wt. %Al_2O_3-5.55 wt. % Y_2O_3-4.85 wt. % SiO_2-7.54 wt. % cBN. Samples sintered under the 70 MPa, 1575°C and 10 min condition showed that TiC, TiB_2 Al_2O_3, Y_2O_3, $Y_2Al_3Si_2$ and $Y_2Si_2O_7$ were detected. Surprisingly YAG was not detected in the sintered sample.

The volume % of the of Al_2O_3-Y_2O_3-SiO_2 system in the 78.59 wt. % TiC-3.47 wt. % Al_2O_3-5.55 wt. % Y_2O_3-4.85 wt. % SiO_2 -7.54 wt.% cBN composition equates to 72.7 vol. % TiC-4.0 vol. % Al_2O_3-5.0 vol. % Y_2O_3-8.3 vol. % SiO_2-10.0 vol.% cBN. The sintered samples had a ratio of liquid phase sintering aids to cBN (cBN: Al_2O_3: Y_2O_3: SiO_2) of approximately 3:1:1:2 respectively. For the same composition sintered at 1575°C, 70MPa and 5 min hold the results of the XRD analysis show the presence of the TiC, Y_2O_3, YAG, YAP, BN, SiO_2, $Y_2Si_2O_7$. The reduced sintering time appears to affect the formation of TiB_2.

Table 5.15 Phases identified by XRD analysis of SPS'd samples of 90 wt. % TiC + cBN with the highest percentage theoretical density. (YAG-$Y_3Al_5O_{12}$, YAP- $YAlO_3$)

Sample composition, Wt. %	Sample composition, Mol %	% of Theoretical Density	Sintering Pressure and time (MPa)	Sintering Temp (°C)	TiC	TiB_2	Al_2O_3	Y_2O_3	YAG	YAP	cBN	hBN	$Y_2Si_2O_7$	$Y_2Al_3Si_2$
85.4TiC-7.59Al_2O_3-1.9Y_2O_3-5.1 (7 vol.%) cBN	83.24TiC-4.32Al_2O_3-0.47Y_2O_3-11.96cBN	83.28	70-5 min	1575	X	-	X	-	-	X	X	-	-	-
85.4TiC-7.59Al_2O_3-1.9Y_2O_3-5.1(7 vol.%) cBN	83.24TiC-4.32Al_2O_3-0.47Y_2O_3-11.96cBN	85.45	70-5 min	1625	X	-	X	-	-	X	-	X	-	-
83.41TiC-7.41Al_2O_3-1.85Y_2O_3-7.32 (10 vol.%) cBN	78.75TiC-4.13Al_2O_3-0.45Y_2O_3-16.68cBN	83.24	70-10min	1575	X	X	X	-	-	X	X	X	-	-
83.41TiC-7.41Al_2O_3-1.85Y_2O_3-7.32 (10 vol.%) cBN	78.75TiC-4.13Al_2O_3-0.45Y_2O_3-16.68cBN	85.53	70-10min	1625	X	X	X	-	-	X	-	X	-	-
83.29TiC-2.31Al_2O_3-3.7Y_2O_3-3.24SiO_2-7.45 (10 vol.%) cBN	82.47TiC-1.33Al_2O_3-0.98Y_2O_3-3.18SiO_2-12.04cBN	91.50	70-10min	1575	X	X	-	-	X	X	X	X	-	-
83.29TiC-2.31Al_2O_3-3.7Y_2O_3-3.24SiO_2-7.45 (10 vol.%) cBN	82.47TiC-1.33Al_2O_3-0.98Y_2O_3-3.18SiO_2-12.04cBN	89.46	70-5 min	1575	X	X	-	-	X	X	X	-	-	-

In Table 5.15 the results show the sample composition in both weight % and mole % of the reactants prior to sintering. For the sample with the starting composition 85.4 wt. % TiC-7.59 wt. % Al_2O_3-1.9 wt. % Y_2O_3 -5.1 wt. % cBN the results of the XRD analysis show that some of the reactants were present in detectable amounts namely TiC, Al_2O_3, and BN as well as YAP as a reaction product in the sample sintered at 1575°C, 70MPa and 5 min hold. A comparison of the volume % of the of Al_2O_3-Y_2O_3 in the 85.4wt. % TiC-7.59wt. % Al_2O_3-1.9wt. % Y_2O_3 - 5.1 wt. % cBN equates to 76.7 vol. % TiC-13.5 vol. % Al_2O_3-2.7 vol. % Y_2O_3- 7.1 vol. % cBN which has a ratio of TiC to liquid phase sintering aids of approximately 5:1. The ratio of cBN: Al_2O_3: Y_2O_3 was ~ 3:5:1 respectively. For the same composition sintered at 1625°C, 70MPa and 5 min hold the results of the XRD analysis show the presence most of the reactants except for the Y_2O_3 which may have been used up during the reaction to form YAP as a product.

The sample with the composition 83.41 wt. % TiC-7.41 wt. % Al_2O_3-1.85 wt. % Y_2O_3-7.32 wt. % cBN equates to 74.3 vol. %TiC-13.1 vol. % Al_2O_3-2.6 mol. % Y_2O_3-10.0 mol. % cBN. The ratio of cBN: Al_2O_3: Y_2O_3 was ~ 4:5:1 respectively. The analysis shows the presence of the TiC, TiB_2 YAP, Al_2O_3 and cBN. Y_2O_3 is not present after sintering which is possibly due to the formation of YAP during sintering at 1575°C, 70MPa and 10 min hold. For the same composition sintered at 1625°C, 70MPa and 10 min hold the results of the XRD analysis shows no presence of the Y_2O_3 reactant which would have been used up during the reaction to form YAP as a product. The next composition analysed was 83.29 wt.% TiC-2.31 wt.% Al_2O_3-3.7 wt.% Y_2O_3-3.24 wt.% SiO_2-7.45 wt.% cBN. Samples sintered under the 70 MPa, 1575°C and 10 min condition showed that TiC, TiB_2, YAG, YAP and cBN were detected. The volume % of the of Al_2O_3-Y_2O_3-SiO_2 system in the 83.29 wt. % TiC-2.31 wt. % Al_2O_3-3.7 wt. % Y_2O_3-3.24 wt. % SiO_2 -7.45 wt.% cBN composition equates to 78.2 vol. % TiC-2.7 vol. % Al_2O_3-3.4 vol. % Y_2O_3-5.7 vol. % SiO_2-10.0 vol.% cBN. The sintered samples had a ratio of liquid phase sintering aids to cBN (cBN: Al_2O_3: Y_2O_3: SiO_2) of approximately 4:1:1:2 respectively. For the same composition sintered at 1575°C, 70MPa and 5 min hold the results of the XRD analysis show the presence of the TiC, TiB_2, YAG, YAP and BN similar to samples sintered with a longer holding time.

5.5 Microstructural Analysis by SEM

5.5.1 SEM analysis of SPS sintered samples with 85 wt. % TiC, liquid phase sintering aids (Al_2O_3-Y_2O_3) and SiC whiskers of various compositions and sintering parameters

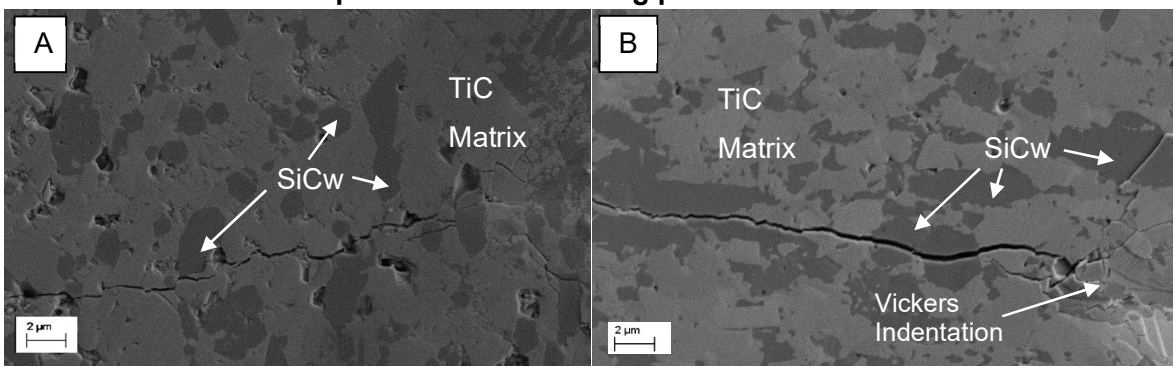


Figure 5.7 SEM micrographs of A - crack path from Vickers Hardness indentation in a sample with the composition 79TiC-11Al_2O_3-3Y_2O_3-7 (10 vol.%) SiCw SPS'd at 1600°C, 70MPa and 10 min hold time and B - crack path from Vickers Hardness indentation in a sample with the composition 73TiC-10Al_2O_3-3Y_2O_3-14 (20 vol.%) SiCw SPS'd at 1625°C, 70MPa and 10 min hold.

Figure 5.7A displayed the crack path from Vickers Hardness indentation in a sample with the composition 79TiC-11Al_2O_3-3Y_2O_3-7(10 vol.%) SiCw SPS'd at 1600°C, 70MPa and 10 min hold time. The sample has a high percentage of theoretical density but whisker-matrix interface is still weak enough to allow crack deflection around the whiskers. There is also evidence of crack bridging along the crack path. It also shows large grains of YAG (large light grey grains) which are visible along with small amounts of liquid phase along the grain boundaries. There is less liquid phase visible. The TiC grains appear to have experienced grain growth. At the higher sintering temperature coarsening may take place at the grain level as well as grain boundary diffusion which usually dominates the final stage of sintering (Cheng et al., 2012).

Figure 5.7B displayed the crack path from Vickers Hardness indentation in a sample with the composition 73TiC-10Al_2O_3-3Y_2O_3-14 (20 vol.%) SiCw SPS'd at 1625°C, 70MPa and 10 min hold. The whisker-matrix interface is so strong that it behaves like one material. There is no deflection as the crack path is straight through the whiskers.

5.5.2 SEM analysis of SPS sintered samples with 85 wt. % TiC, liquid phase sintering aids (Al_2O_3-Y_2O_3-SiO_2) and SiC whiskers of various compositions and sintering parameters

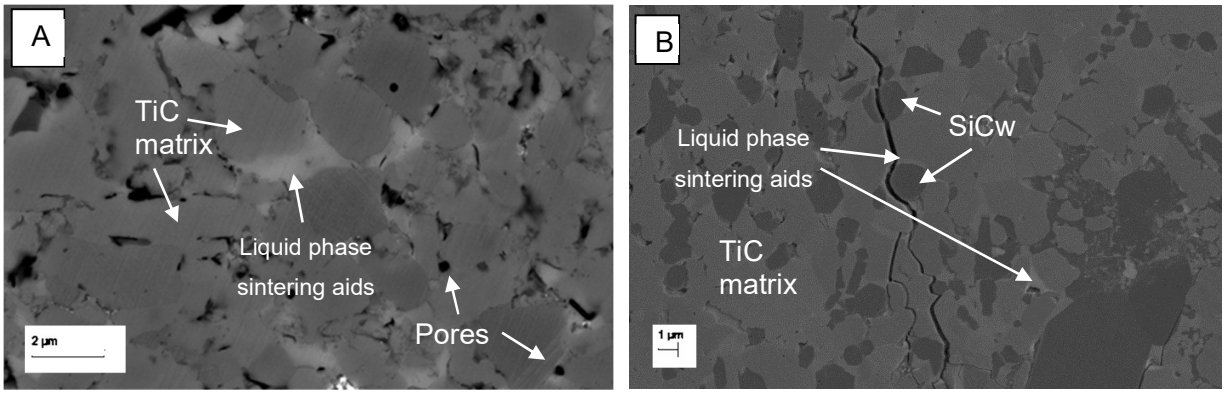


Figure 5.8 SEM micrographs of A - 85TiC-3.75Al_2O_3-6Y_2O_3-5.25SiO_2 SPS'd at 1610°C, 70MPa and 10 min hold time and B - crack path from Vickers Hardness indentation in 73TiC-3Al_2O_3-5Y_2O_3-4SiO_2-15 (20 vol.%) SiCw SPS'd at 1625°C, 70MPa and 10 min hold.

Figure 5.8A above showed the microstructure of 85TiC-3.75Al_2O_3-6Y_2O_3-5.25SiO_2 the larger grey grains are predominantly TiC and the lighter phase between the larger grains is a combination of the liquid phase sintering aids. The darkest phase present are pores, some of which are present in the material after sintering (small round pores) and some are resultant of material removal during the polishing process (thin irregular pores). The liquid phase sintering aids that are found between the TiC grains are significantly softer than the TiC grains and are worn away selectively during sample preparation.

Figure 5.8B showed a crack path caused by a Vickers indentation in a sample with the composition of 73TiC-3Al_2O_3-5Y_2O_3-4SiO_2-15 (20 vol.%) SiCw SPS'd at 1625°C, 70 MPa, 10 min hold. The material is very close to full density and the SEM images show distinct phases within the matrix which comprise various compositions of the matrix components. The crack is deflected slightly as it moves through the different phases of the matrix. The bond between the whiskers is strong in some areas and weaker in others which is why the whiskers deflect the crack in some places and allow the crack to run though in others. SiCw, Al_2O_3 and SiO_2 may react to form mullite producing a strong interface.

This strong interface minimizes the usual reinforcement mechanisms such as crack deflection along the interface, whisker pull-out and resistance to crack opening (Garnier et al., 2005). The whisker deflection could be increased in some areas due to the possible presence of Al_2OC as an interfacial phase at the grain boundary that are weaker than the surrounding matrix (Yu & Zhang, 2007).

5.5.3 SEM analysis of SPS sintered samples with 90 wt. % TiC, liquid phase sintering aids (Al_2O_3-Y_2O_3) and SiC whiskers of various compositions and sintering parameters

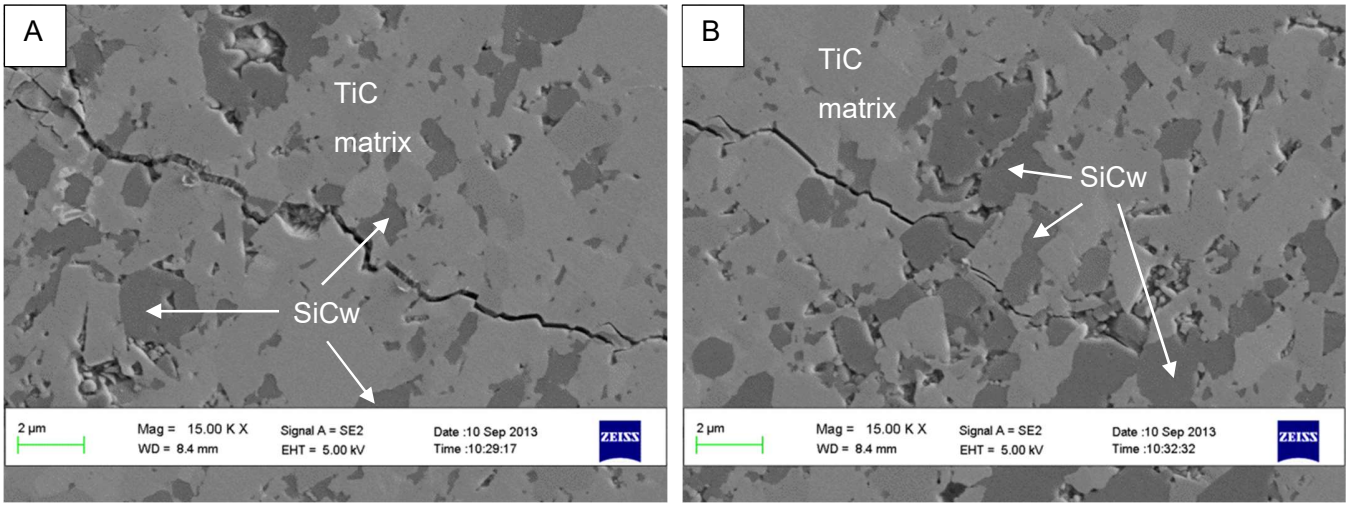


Figure 5.9 SEM micrographs of A – 77.2TiC-6.9Al_2O_3-1.7Y_2O_3-14.2 (20 vol.%) SiCw SPS'd at 1625°C, 70MPa and 20 min hold time and B - crack path from Vickers Hardness indentation in 77.2TiC-6.9Al_2O_3-1.7Y_2O_3-14.2 (20 vol.%) SiCw SPS'd at 1625°C, 70MPa and 20 min hold time magnified by 15 K X.

Figure 5.9 shows a sample with the composition of 85 wt. % TiC (2µm) + 20 vol. % SiC whiskers SPS'd at 1625°C, 70 MPa, 20 min hold. The whisker-matrix interface is so strong that it behaves like one material. There is no deflection as the crack path is straight through the whiskers. In all the 85wt.% TiC + 20 vol.% SiCw samples the crack always runs through the whisker irrespective of the sintering temp. This could be an effect of the longer hold time during sintering increasing the strength of the bonds between the whiskers and the matrix.

5.5.4 SEM analysis of SPS sintered samples with 90 wt. % TiC, liquid phase sintering aids (Al_2O_3-Y_2O_3-SiO_2) and SiC whiskers of various compositions and sintering

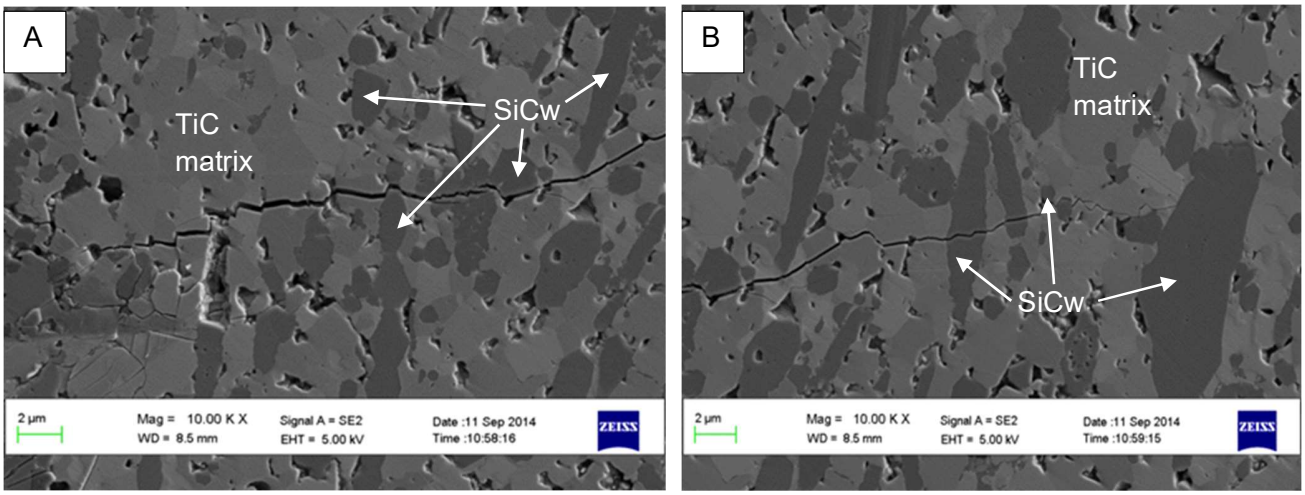


Figure 5.10 SEM micrographs of A – 77TiC-2.1Al_2O_3-3.4Y_2O_3-3SiO_2-14.5 (20 vol.%) SiCw SPS'd at 1640°C, 70MPa and 10 min hold time and B - crack path from Vickers Hardness indentation in 77TiC-2.1Al_2O_3-3.4Y_2O_3-3SiO_2-14.5 (20 vol.%) SiCw SPS'd at 1640°C, 70MPa and 10 min hold time magnified by 10 K X.

90 wt. % TiC (+SiO_2) + 20 vol. % SiC whiskers SPS'd at 1640°C, 70 MPa, 10 min hold. The density is high, and the SEM images show distinct phases within the matrix which comprise various compositions of the matrix components. The crack is deflected slightly as it moves through the different phases of the matrix. Due to the high temperature the bond between the whiskers and matrix is very strong. Thus the whisker bonding causes the crack to run through the whiskers, displaying no deflection.

5.5.5 SEM analysis of SPS sintered samples with 85 wt. % TiC, liquid phase sintering aids (Al_2O_3-Y_2O_3-SiO_2) and cBN of various compositions and sintering parameters

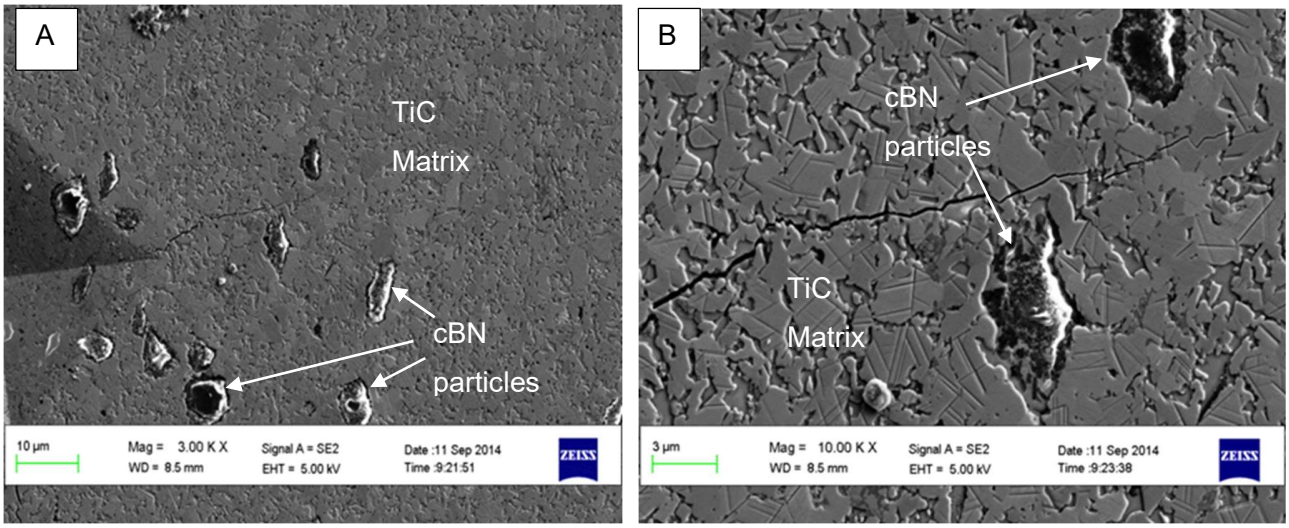


Figure 5.11 SEM micrographs of A – 78.6TiC-3.5Al_2O_3-5.6Y_2O_3-4.9SiO_2-7.5 (10 vol.%) cBN SPS'd at 1625°C, 70MPa and 10 min hold time and B - crack path from Vickers Hardness indentation in 78.6TiC-3.5Al_2O_3-5.6Y_2O_3-4.9SiO_2-7.5 (10 vol.%) cBN SPS'd at 1625°C, 70MPa and 10 min hold time magnified by 10 K X.

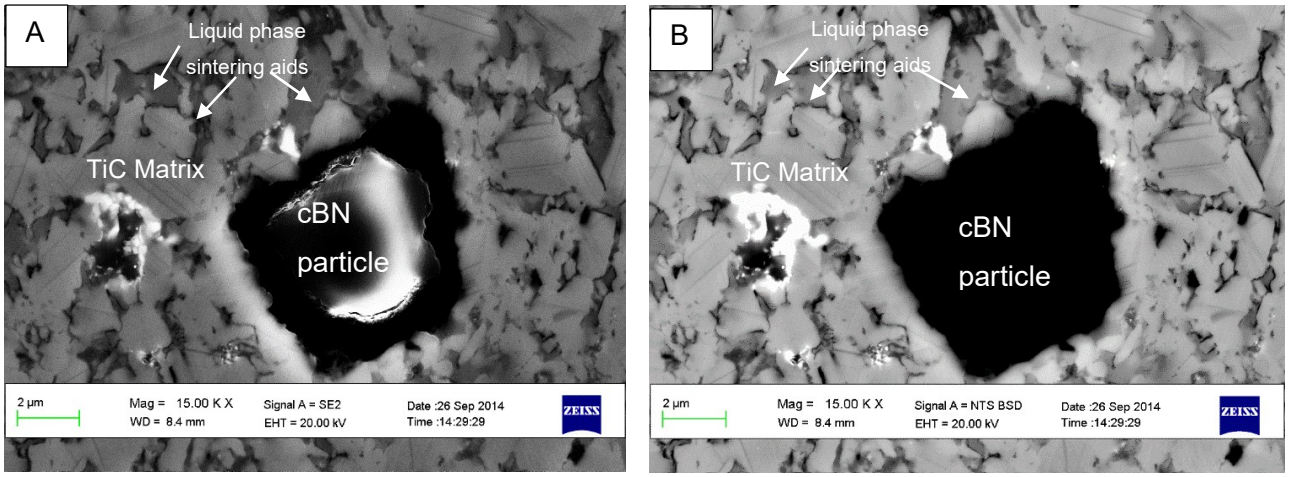


Figure 5.12 SEM micrographs of A – 78.6TiC-3.5Al_2O_3-5.6Y_2O_3-4.9SiO_2-7.5 (10 vol.%) cBN SPS'd at 1575°C, 70MPa and 10 min hold time viewed with the Secondary detector magnified by 15 K X and B - 78.6TiC-3.5Al_2O_3-5.6Y_2O_3-4.9SiO_2-7.5 (10 vol.%) cBN SPS'd at 1575°C, 70MPa and 10 min hold time viewed via Backscatter detector magnified by 15 K X.

85 wt. % TiC (+SiO_2) + 10 vol. % cBN SPS'd at 1625°C, 70 MPa, 10 min hold. The SEM images show the path of the crack through the material but due to the low volume % of the cBN grains they do not always come in contact with the crack. There is however a slight deflection of the crack path from the matrix. A gap between the cBN grains and the matrix can clearly be seen around some of the cBN grains.

The gap formation and the porous microstructure of the BN grains could be attributed to the difference in thermal expansion co-efficient between TiC and BN particles. Another cause could be the hexagonalization of cBN to hBN which has a significantly lower hardness. (Hotta & Goto, 2008). In Figure 5.12 A and B: 78.6TiC-3.5Al_2O_3-5.6Y_2O_3-4.9SiO_2-7.5 (10 vol.%) cBN SPS'd at 1575°C, 70MPa and 10 min; it is possible to differentiate between the TiC matrix and the areas of liquid phase sintering aids which was not visible in Figure 11 A and B due to the higher beam energy used (5KV vs. 20 KV). In Figure 5.18 B the cBN particle appears only as a dark shadow due to its composition of lighter elements (Boron and Nitrogen) than the heavier element in the TiC Matrix and liquid phase sintering aids.

5.5.6 SEM analysis of SPS sintered samples with 90 wt. % TiC, liquid phase sintering aids (Al_2O_3-Y_2O_3-SiO_2) and cBN of various compositions and sintering

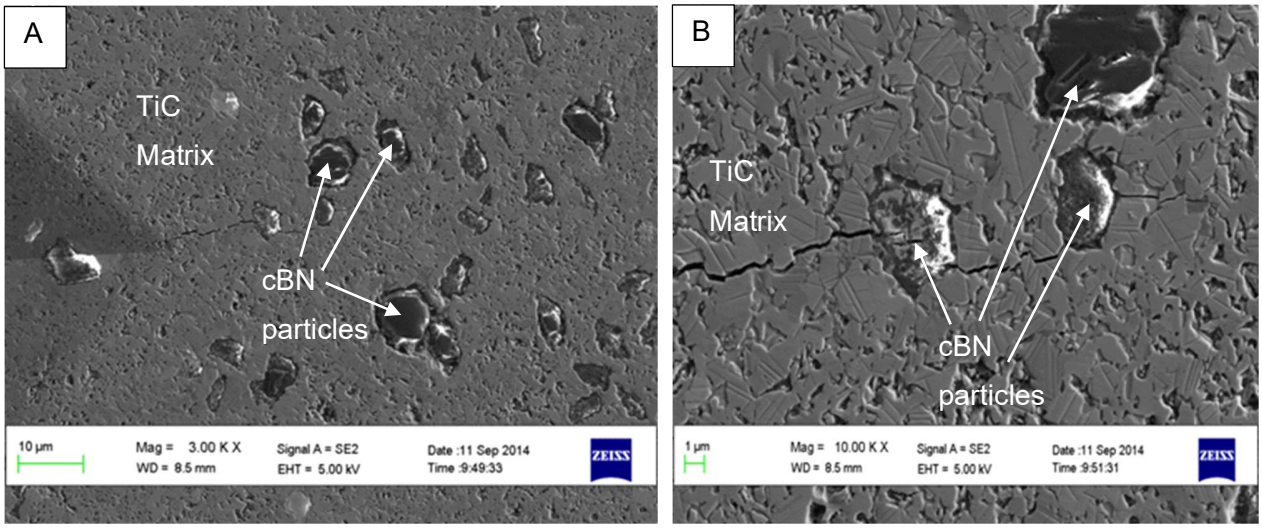


Figure 5.13 SEM micrographs of A – 83.3TiC-2.3Al_2O_3-3.7Y_2O_3-3.2SiO_2-7.5 (10 vol.%) cBN SPS'd at 1575°C, 70MPa and 10 min hold time and B - crack path from Vickers Hardness indentation in 83.3TiC-2.3Al_2O_3-3.7Y_2O_3-3.2SiO_2-7.5

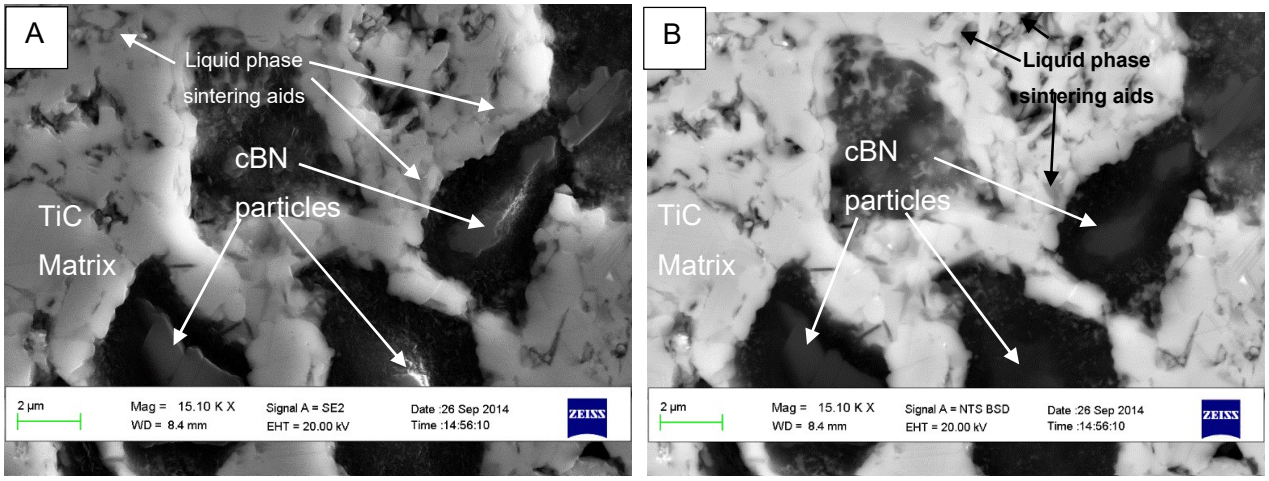


Figure 5.14 SEM micrographs of A – 83.3TiC-2.3Al_2O_3-3.7Y_2O_3-3.2SiO_2-7.5 (10 vol.%) cBN SPS'd at 1575°C, 70MPa and 10 min hold time viewed with the Secondary electron detector magnified at 15.1 K X and B - 83.3TiC-2.3Al_2O_3-3.7Y_2O_3-3.2SiO_2-7.5 (10 vol.%) cBN SPS'd at 1575°C, 70MPa and 10 min hold time viewed via Backscatter electron detector magnified by 15.1 K X.

Figure 5.13 Shows a sintered sample with the composition of 90 wt. % TiC (+SiO_2) + 10 vol. % cBN SPS'd at 1575°C, 70 MPa, 10 min hold. Analysis of the SEM images shows that the reinforcement-matrix interface is mostly weak as it appears that the cBN grains have a gap between themselves and the matrix possibly due to the formation of hBN on the surface of the cBN grain during sintering as detected in XRD results (Table 5.15). The SEM images show that the cBN grains that have a stronger interface with the matrix do not deflect the crack but allow it to pass through whereas the cBN grains with the weaker interface have the crack deflected around them. The crack path is also slightly deflected by the matrix itself.

In Figure 5.14 A and B: 83.3TiC-2.3Al_2O_3-3.7Y_2O_3-3.2SiO_2-7.5 (10 vol.%) cBN SPS'd at 1575°C, 70MPa and 10 min hold time; it is possible to differentiate between the TiC matrix and the areas of liquid phase sintering aids which was not visible in Figure 19 A and B due to the higher beam energy used (5KV vs. 20 KV). In Figure 5.12 B the cBN particles appears only as dark shadows due its composition of lighter elements (Boron and Nitrogen) than the heavier element in the TiC Matrix and liquid phase sintering aids. There is significantly less liquid phase sintering aid visible than in Figure 5.12 as the matrix contains a lesser amount and also possibly due to the comparatively softer liquid phase sintering aid rich areas being softer than the surrounding areas and wearing away differentially during the polishing process.

5.6 Hardness and fracture toughness

Mechanical behaviour/properties of reinforced composites can be anisotropic especially when the longitudinal axes of the reinforcing fibers or whiskers are preferentially oriented within the sintered body. Anisotropy can be reduced by prolonged ball milling during powder processing but the milling procedure may also breakdown the whiskers themselves. Thus extensive ball milling was avoided during the processing of the powder mixtures for Spark Plasma sintering. In hot pressed SiC-whisker reinforced composites, the whiskers exhibit a preferred orientation as the longitudinal axes of the whiskers attempt to align perpendicularly to the hot pressing axis. Becher et al. found through microscopy observations that the longitudinal axes of most of the whiskers lie at angles within 70-105° to the hot pressing axis (P. F. Becher et al., 1995).

From the analysis of the microstructures of the SPS'd samples it can be noted that a similar preferred orientation has occurred in the whisker reinforced TiC composites. The anisotropy was taken into consideration when analyzing the fracture toughness by giving values for the cracks caused by the Vickers indentations that run both parallel and perpendicular to the pressing direction. Fracture Toughness values were calculated via Vickers hardness indentation as detailed in Chapter 3.5.2.2.

5.6.1 Hardness and fracture toughness of SPS sintered samples with 85 wt.% TiC, liquid phase sintering aids and SiC whiskers with the highest density

Table 5.16: Hardness and fracture toughness of SPS sintered samples with 85 wt. % TiC, liquid phase sintering aids (Al_2O_3-Y_2O_3) and SiC whiskers with the highest density

Sample composition, Wt. %	Temperature (°C)	Sintering hold time (min)	Sintering pressure (MPa)	Vickers Hardness (GPa)	Fracture Toughness – K_{1C} (MPa.m^{½})
85TiC-12Al_2O_3-3Y_2O_3	1610	10	70	20.73±0.27	3.77±0.16
79TiC+11Al_2O_3-3Y_2O_3-7 (10 vol.%) SiCw	1600	10	70	21.27±0.19	3.50±0.07 (parallel) 4.51±0.10 (perpendicular)
73TiC-10Al_2O_3-3Y_2O_3-14 (20 vol.%) SiCw	1625	10	70	18.97±0.47	6.01±0.40 (parallel) 4.36±0.15 (perpendicular)

Table 5.16 above shows the Vickers hardness and fracture toughness of 85TiC-12Al_2O_3-3Y_2O_3 on its own, with 7 wt. % and 14 wt. % SiCw added as reinforcement prior to sintering. The addition of the 7 wt. % SiCw does not cause a significant difference in the hardness, which increased marginally from 20.73±0.27 GPa to 21.27±0.19 GPa. Which was expected as there is no significant difference in the percentage theoretical density between the two, with density being 99.31% and 99.35% respectively. There was however a noticeable difference in the fracture toughness. Parallel to the pressing direction there was a very slight decrease in the fracture toughness from 3.77±0.16 MPa.m^{½} to 3.50±0.07 MPa.m^{½} and perpendicular to the pressing direction the increase in fracture toughness was larger from 3.77±0.16 MPa.m^{½} to 4.51±0.10 MPa.m^{½}.

From the XRD analysis we can see that the addition of the SiCw facilitates the formation of YAG over the formation of YAP which occurred in the un-reinforced sintered material as predicted in Figure 5.4 and Figure 5.6. The addition of 14 wt. % SiCw to the TiC matrix prior to sintering resulted in a large decrease in hardness from 20.73±0.27 GPa to 18.97±0.47 GPa. The decrease in the hardness is most likely due to the difference in the percentage theoretical density which was lower in the 73TiC-10Al_2O_3-3Y_2O_3-14SiCw samples at 97.39% than that of the 85TiC-12Al_2O_3-3Y_2O_3 composition on its own which was 99.31%. There was also a significant increase in the fracture toughness overall. Parallel to the pressing direction there is a substantial increase in the fracture toughness from 3.77±0.16 MPa.m^{½} to 6.01±0.40 MPa.m^{½} and perpendicular to the pressing direction the increase in fracture toughness is large as well from 3.77±0.16 MPa.m^{½} to 4.36±0.15 MPa.m^{½}. As expected, the SiC whisker reinforced materials had better fracture toughness as a result of the addition of the SiC whiskers. Another potential factor in the increase in the fracture toughness is the crack deflection by the porosity itself.

Table 5.17: Hardness and fracture toughness of SPS sintered samples with 85 wt. % TiC, liquid phase sintering aids (Al_2O_3-Y_2O_3-SiO_2) and SiC whiskers with the highest density.

Sample composition, Wt. %	Temperature (°C)	Sintering hold time (min)	Sintering pressure (MPa)	Vickers Hardness (GPa)	Fracture Toughness – K_{1C} (MPa.m^{½})
85TiC-3.75Al_2O_3-6Y_2O_3-5.25SiO_2	1610	10	70	16.10±0.88	3.56±0.53
79TiC-3Al_2O_3-6Y_2O_3-5SiO_2-7 (10 vol.%) SiCw	1600	10	70	15.43±0.92	4.47±0.38 (parallel) 3.51±0.32 (perpendicular)
73TiC-3Al_2O_3-5Y_2O_3-4SiO_2-15 (20 vol.%) SiCw	1625	10	70	18.82±0.49	4.21±0.12 (parallel) 4.44±0.15 (perpendicular)

Table 5.17 above showed the Vickers hardness and fracture toughness of 85TiC-3.75Al_2O_3-6Y_2O_3-5.25SiO_2 on its own and with 15 wt. % SiCw added as reinforcement prior to sintering. The addition of the 15 wt. % SiCw does cause a small difference in the Vickers hardness from 16.10±0.88 GPa to 18.82±0.49 GPa which is expected as there is a minor difference in the percentage theoretical density between the two, with density being 99.93% and 99.42% respectively. There was however a noticeable difference in the fracture toughness. Parallel to the pressing direction the was no significant change in the fracture toughness from 3.56±0.53 MPa.m^{½} to 4.21±0.12 MPa.m^{½} and perpendicular to the pressing direction the increase in fracture toughness was larger from 3.56±0.53 MPa.m^{½} to 4.44±0.15 MPa.m^{½}. From the XRD analysis we can see that the addition of the SiCw produced the same reaction products as 85TiC-3.75Al_2O_3-6Y_2O_3-5.25SiO_2 with the exception of Al_2OC. The addition of SiO_2 to the liquid phase of the 85 wt. % TiC matrices significantly reduced the hardness and fracture toughness in compositions with and without SiCw to which it had been added regardless of the sintering parameters. This could be the result of the formation of large YAG grains which are weaker than the TiC grains and lower the mechanical properties of the sintered material.

Also the presence of yttrium aluminosilicate glass ($Y_2Si_2O_7$) which acts as a path of least resistance for crack paths in the sintered material would also lower the fracture toughness of the material (Kolitsch et al., 1999).

5.6.2 Hardness and fracture toughness of SPS sintered samples with 85 wt.% TiC, liquid phase sintering aids and cBN with the highest density

Table 5.18: Hardness and fracture toughness of SPS sintered samples with 85 wt.% TiC, liquid phase sintering aids (Al_2O_3-Y_2O_3-SiO_2) and cBN with the highest density.

Sample composition, Wt. %	Temperature (°C)	Sintering hold time (min)	Sintering pressure (MPa)	Vickers Hardness (GPa)	Fracture Toughness – K_{1C} (MPa.m^{½})
78.59TiC-3.47Al_2O_3-5.55Y_2O_3-4.85 SiO_2-7.54 (10 vol.%) cBN	1575	5	70	12.13±0.46	3.17±0.07 (parallel) 4.69±041 (perpendicular)
78.59TiC-3.47Al_2O_3-5.55Y_2O_3-4.85 SiO_2-7.54 (10 vol.%) cBN	1575	10	70	12.80±0.38	3.16±0.11 (parallel) 4.64±0.23 (perpendicular)

Table 5.18 above showed the Vickers hardness and fracture toughness of 79.59TiC-3.47Al_2O_3-5.55Y_2O_3-4.85SiO_2-7.54cBN sintered at 1575°C, 70MPa and a hold time of either 5 min or 10 min hold. The temperature was set at 1575°C as any temperature above this would have resulted in the conversion of cBN to hBN at this sintering pressure (Will et al., 2000). The change in hold time does cause a negligible difference in the Vickers hardness from 12.13±0.48 GPa to 12.80±0.38 GPa which is unexpected as there is a significant difference in the percentage of theoretical density between the two, with density being 96.45% (5 min hold) and 85.43% (10 min hold) respectively. The decrease in the percentage of theoretical density was most likely due to the longer hold time giving more time for the liquid phase to escape. There was however a negligible difference in the fracture toughness. Parallel to the pressing direction the was no significant change in the fracture toughness from 3.17±0.07 MPa.m^{½} to 3.16±0.11 MPa.m^{½} and perpendicular to the pressing direction there was no real change in fracture toughness from 4.69±0.41 MPa.m^{½} to 4.64±0.23 MPa.m^{½}. From the XRD analysis we can see that the shorter hold time had resulted in the production of YAG and YAP which are not present in the samples sintered with the longer hold time which has TiB_2 and $Y_2Al_3Si_2$ as reaction products instead.

5.6.3 Hardness and fracture toughness of SPS sintered samples with 90 wt.% TiC, liquid phase sintering aids and SiC whiskers with the highest density

Table 5.19: Hardness and fracture toughness of SPS sintered samples with 90 wt. % TiC, liquid phase sintering aids (Al_2O_3-Y_2O_3) and SiC whiskers with the highest density

Sample composition, Wt. %	Temperature (°C)	Sintering hold time (min)	Sintering pressure (MPa)	Vickers Hardness (GPa)	Fracture Toughness – K_{1C} (MPa.m^{½})
90TiC-8Al_2O_3-2Y_2O_3	1625	10	50	19.64±0.47	4.48±0.17
83.8TiC-7.45Al_2O_3-1.86Y_2O_3-6.89 (10 vol.%) SiCw	1625	10	50	17.91±0.70	5.27±0.59 (parallel) 4.00±0.67 (perpendicular)
77.79TiC-6.86Al_2O_3-1.72Y_2O_3-14.24 (20 vol.%) SiCw	1625	20	70	14.41±0.32	5.17±0.35 (parallel) 5.03±0.45 (perpendicular)

Table 5.19 above shows the Vickers hardness and fracture toughness of 90TiC-8Al_2O_3-2Y_2O_3 on its own, with 7 wt. % and 14 wt. % SiCw added as reinforcement prior to sintering. The addition of the 7 wt. % SiCw does cause a slight decrease in the Vickers hardness from 19.64±0.47 GPa to 17.91±0.70 GPa which is expected as there is a slight decrease in the percentage theoretical density between the two, with density being 98.57% and 96.77% respectively. There was however a noticeable difference in the fracture toughness. Parallel to the pressing direction there was a very slight increase in the fracture toughness from 4.48±0.17 MPa.m^{½} to 5.27±0.59 MPa.m^{½} and perpendicular to the pressing direction the decrease in fracture toughness was negligible from 4.48±0.17 MPa.m^{½} to 4.00±0.67 MPa.m^{½}. From the XRD analysis we can see that the addition of the SiCw facilitates the formation of Y_5Si_3C over the formation of YAG which occurred in the un-reinforced sintered material. The addition of 14 wt. % SiCw to the TiC matrix prior to sintering resulted in a significant decrease in hardness from 19.64±0.47 GPa to 14.41±0.32 GPa. The decrease in the hardness is most likely due to the difference in the percentage theoretical density which was lower in the 83.8TiC-7.45Al_2O_3-1.86Y_2O_3-14.24SiCw samples at 92.97% than that of the 90TiC-8Al_2O_3-2Y_2O_3 composition on its own which was 98.57%. There was also a small increase in the fracture toughness in the parallel direction and the perpendicular direction.

Parallel to the pressing direction there is an increase in the fracture toughness from 4.48±0.17 MPa.m^{½} to 5.17±0.35 MPa.m^{½} and perpendicular to the pressing direction the slight increase in fracture toughness is from 4.48±0.17 MPa.m^{½} to 5.03±0.45 MPa.m^{½}. As expected the SiC whisker reinforced materials had better fracture toughness properties which improved with the addition of the SiC whiskers parallel to the pressing direction. The fracture toughness perpendicular to the pressing direction was lower than that of those parallel to the pressing direction due to the anisotropy and preferred orientation of the SiC whiskers during Spark plasma sintering. The expression of this effect seems highly dependent of the amount of liquid phase sintering aids present in the TiC matrix during sintering.

Table 5.20: Hardness and fracture toughness of SPS sintered samples with 90 wt. % TiC, liquid phase sintering aids (Al_2O_3-Y_2O_3-SiO_2) and SiC whiskers with the highest density.

Sample composition, Wt. %	Temperature (°C)	Sintering hold time (min)	Sintering pressure (MPa)	Vickers Hardness (GPa)	Fracture Toughness – K_{1C} (MPa.m^{½})
90TiC-2.5Al_2O_3-4Y_2O_3-3.5SiO_2	1625	10	70	17.59±1.12	3.54±0.13
76.99TiC-2.14Al_2O_3-3.42Y_2O_3-2.99SiO_2-14.46 (20 vol.%) SiCw	1640	10	70	15.60±0.51	3.84±0.78 (parallel) 4.20±0.34 (perpendicular)

Table 5.20 above showed the Vickers hardness and fracture toughness of 90TiC-2.5Al_2O_3-4Y_2O_3-3.5SiO_2 on its own and with ±14 wt. % SiCw added as reinforcement prior to sintering. The addition of the ±14 wt. % SiCw does cause a large decrease in the Vickers hardness from 17.59±1.12 GPa to 15.60±0.51 GPa which is expected as there is a significant difference in the percentage theoretical density between the two, with density being 99.85% and 93.13% respectively. There was however a noticeable difference in the fracture toughness.

Parallel to the pressing direction the was a slight change in the fracture toughness from 3.54±0.13 MPa.m^{½} to 3.84±0.78 MPa.m^{½} and perpendicular to the pressing direction the increase in fracture toughness was larger from 3.54±0.13 MPa.m^{½} to 4.20±0.34 MPa.m^{½}. From the XRD analysis we can see that the addition of the SiCw produced the same reaction products as 85TiC-3.75Al_2O_3-6Y_2O_3-5.25SiO_2 with the exception of $Y_2Si_2O_7$.

Similarly, to the 80 wt.% TiC matrices the addition of SiO_2 to the liquid phase of the 90 wt. % TiC matrices reduced the hardness and fracture toughness significantly in compositions with and without SiCw to which it had been added regardless of the sintering parameters. This could be the result of the formation of large YAG grains which are weaker than the TiC grains and lower the mechanical properties of the sintered material. Also the presence of yttrium aluminosilicate glass ($Y_2Si_2O_7$) which acts as a path of least resistance for crack paths in the sintered material would also lower the fracture toughness of the material (Kolitsch et al., 1999).

5.6.4 Hardness and fracture toughness of SPS sintered samples with 90 wt.% TiC, liquid phase sintering aids and cBN with the highest density

Table 5.21: Hardness and fracture toughness of SPS sintered samples with 90 wt.% TiC, liquid phase sintering aids (Al_2O_3-Y_2O_3-SiO_2) and cBN with the highest density.

Sample composition, Wt. %	Temperature (°C)	Sintering hold time (min)	Sintering pressure (MPa)	Vickers Hardness (GPa)	Fracture Toughness – K_{1C} (MPa.m^{½})
83.29TiC-2.31Al_2O_3-3.7Y_2O_3-3.24 SiO_2-7.45 (10 vol.%) cBN	1575	5	70	9.28±0.03	3.25±0.16 (parallel) 4.02±0.13 (perpendicular)
83.29TiC-2.31Al_2O_3-3.7Y_2O_3-3.24 SiO_2-7.45 (10 vol.%) cBN	1575	10	70	10.46±0.10	3.20±0.05 (parallel) 4.23±0.16 (perpendicular)

Table 5.21 above showed the Vickers hardness and fracture toughness of 83.29TiC-2.31Al_2O_3-3.7Y_2O_3-3.24SiO_2-7.45cBN sintered at 1575°C, 70MPa and a hold time of either 5 min or 10 min hold.

The temperature was set at 1575°C as any temperature above this would have resulted in the conversion of cBN to hBN at this sintering pressure. (Will et al., 2000) The change in hold time causes a large difference in the Vickers hardness from 9.28±0.03 GPa to 10.46±0.10 GPa with increasing hold time during sintering which is expected as there are a slight differences in the percentage theoretical density between the two, with density being 89.46% (5 min hold) and 91.50% (10 min hold) respectively. There was however a negligible difference in the fracture toughness. Parallel to the pressing direction there was no significant change in the fracture toughness from 3.25±0.16 MPa.m^{½} to 3.20±0.05 MPa.m^{½} and perpendicular to the pressing direction there was also no real change in fracture toughness from 4.02±0.13 MPa.m^{½} to 4.23±0.16 MPa.m^{½}. From the XRD analysis in Table 5.15 we can see that both hold times had resulted in the production of TiB_2, YAG and YAP. Neither $Y_2Si_2O_7$ nor $Y_2Al_3Si_2$ were detected in sample of either sintering hold condition.

From the analysis of the micrographs 5.18-A: 78.6TiC-3.5Al_2O_3-5.6Y_2O_3-4.9SiO_2-7.5 (10 vol.%) cBN SPS'd at 1575°C, 70MPa and 10 min hold time and 5.20-A: 83.3 TiC- 2.3 Al_2O_3- 3.7 Y_2O_3-3.2SiO_2-7.5 (10 vol.%) cBN SPS'd at 1575°C, 70 MPa and 10 min hold time it can be observed that there is a gap between the cBN particles and TiC matrix. The hexagonalization that occurred on of the surface of the cBN during sintering resulted in it being converted to hBN. This was confirmed by XRD analysis results from Table 5.15.

The gap was most likely the result of the layer of hBN which would be present between the cBN and the matrix. The hBN layer was probably removed during the grinding and/or polishing process and would prevent the cBN from providing any reinforcement to the matrix as it was not adhered directly to the matrix.

The coefficient of thermal expansion of TiC is between 4.1-7.7 X e^{-6} K^{-1} (*Titanium Carbide / TiC Chemical, Mechanical, Physical and Environmental Properties of Materials*, n.d.) and is larger than that of cBN -1.26 X 10^{-6} K^{-1} (*Boron Nitride (BN) - Properties and Information on Boron Nitride*, 2001).

During sintering the matrix should have expanded during heating and then contracted during cooling around the cBN particles eliminating any gaps. The gaps that can be seen therefore indicates that another phase must have been present there prior to being removed by the polishing process. The reason the hBN was not always detected by the XRD analysis could be due to two factors, those being: a. The amount present was too low to be detected and b. The phase produced was amorphous and unable to be detected by the XRD.

6. BIAXIAL STRENGTH TESTING USING BALL ON 3 BALL TESTING

6.1 Analysis of the flexural strength tests of sintered TiC samples with the best combination of density and fracture toughness.

The sintered TiC sample compositions (matrices with reinforcement materials) and sintering conditions that resulted in the best combinations of high density and high fracture toughness had been selected to undergo B3B testing. The maximum tensile stress σ_{max} was calculated using the formulae outlined in Chapter 3.5.3. For our experiment R_b = 6.5 mm (measured) and R_a = 7.506 mm (calculated)

Table 6.1. Table of sintering parameters, sintered density and fracture toughness for selected sample compositions

Sample name	Sintering Parameters (Temperature, Sintering Pressure and Hold Time)	Sintered Density (g/cm^3)	% of Theoretical Density	Vickers Hardness (GPa)	Fracture Toughness – K_{1C} ($MPa.m^{½}$)
85TiC-12Al_2O_3-3Y_2O_3	1610°C, 70MPa and 10 min hold	4.76	99.31	20.73 ± 0.27	3.77 ± 0.16
79TiC-11Al_2O_3-3Y_2O_3-7(10 vol.%) SiCw	1600°C, 70MPa and 10 min hold	4.61	99.35	21.27 ± 0.19	3.50 ± 0.07 parallel 4.57 ± 0.10 perpendicular
73TiC-10Al_2O_3-3Y_2O_3-14(20 vol.%) SiCw	1625°C, 70MPa and 10 min hold	4.34	95.99	18.97 ± 0.47	6.01 ± 0.40 parallel 4.36 ± 0.15 perpendicular
79TiC-4.5Al_2O_3-5.6Y_2O_3-4.9SiO_2-7.1(10 vol.%) SiCw	1600°C, 70MPa and 10 min hold	4.53	99.96	15.43 ± 0.92	4.47 ± 0.38 parallel 3.51 ± 0.32 perpendicular
78.6TiC-3.5Al_2O_3-5.6Y_2O_3-4.9SiO_2-7.5 (10 vol.%) cBN	1575°C, 70MPa and 5 min hold	4.40	96.45	9.28 ± 0.03	3.25 ± 0.16 parallel 4.02 ± 0.13 perpendicular
77.8TiC-6.9Al_2O_3-1.7Y_2O_3-14(20 vol.%) SiCw	1625°C, 70MPa and 20 min hold	4.20	92.97	14.41 ± 0.32	5.17 ± 0.35 parallel 5.03 ± 0.45 perpendicular

Table 6.2. Table of results for the force at the moment of fracture for samples of various compositions

Sample name	Sintering Parameters (Temperature, Sintering Pressure and Hold Time)	Diameter (mm)	Thickness (mm)	Force at fracture (N)	Force + 10N Preload
85TiC-12Al_2O_3-3Y_2O_3	1610°C, 70MPa and 10 min hold	20.32±0.03	2.02±0.03	1435.28±357.41	1445.28±357.41
79TiC-11Al_2O_3-3Y_2O_3-7(10 vol.%) SiCw	1600°C, 70MPa and 10 min hold	20.31±0.02	2.03±0.03	1784.72±286.77	1794.72±286.77
73TiC-10Al_2O_3-3Y_2O_3-14(20 vol.%) SiCw	1625°C, 70MPa and 10 min hold	20.33±0.03	2.09±0.02	1689.33±259.17	1699.33±259.17
79TiC-4.5Al_2O_3-5.6Y_2O_3-4.9SiO_2-7.1(10 vol.%) SiCw	1600°C, 70MPa and 10 min hold	20.31±0.02	2.02±0.03	1480.00±251.02	1490.00±251.02
78.6TiC-3.5Al_2O_3-5.6Y_2O_3-4.9SiO_2-7.5 (10 vol.%) cBN	1575°C, 70MPa and 5 min hold	20.29±0.02	2.08±0.03	1614.43±174.40	1624.43±174.40
77.8TiC-6.9Al_2O_3-1.7Y_2O_3-14(20 vol.%) SiCw	1625°C, 70MPa and 20 min hold	20.39±0.02	2.05±0.00	1874.15±81.78	1884.15±81.78

The Young's modulus and Poisson's Ratio for each composition of the disc material was calculated using the Rule of Mixtures for the matrix and the reinforcement material:

$$E_c = E_f V_f + E_m V_m$$

$$\upsilon_{12} = \upsilon_f V_f + \upsilon_m V_m$$

Table 6.3. Table of Poisson's Ratios and Young's moduli for the constituents of the composite materials

Material	Poisson's Ratio	Young's Modulus (GPa)	Source (Webpage/reference)
99.5% Al_2O_3	0.220	375	(*Aluminum Oxide | Al2O3 Material Properties*, n.d.)
SiC	0.190	410	(*Property of Silicon Carbide (SiC)*, n.d.)
SiO_2	0.170	73	(*Fused Silica | SiO2 Material Properties*, n.d.)
TiC	0.187	439	(*Material: Titanium Carbide (TiC), Bulk*, n.d.)
Y_2O_3	0.299	179	(Yeheskel & Tevet, 1999)
cBN	0.150	710	(Bergs et al., 2020)

Table 6.4. Table of results for theoretical Poisson's Ratios and Young's moduli of various compositions based on Rule of Mixtures

Sample name	Composition in vol.%	Theoretical Poisson's Ratio	Theoretical Young's Modulus (GPa)
85TiC-12Al_2O_3-3Y_2O_3	82.6 vol.% TiC + 14.6 vol.% Al_2O_3 + 2.9 vol.% Y_2O_3	0.195	422.91
79TiC-11Al_2O_3-3Y_2O_3-7(10 vol.%) SiCw	74.6 vol.% TiC + 13.1 vol.% Al_2O_3 + 2.6 vol.% Y_2O_3 + 10 vol.% SiCw	0.195	422.59
73TiC-10Al_2O_3-3Y_2O_3-14(20 vol.%) SiCw	66.1 vol.% TiC + 11.6 vol.% Al_2O_3 + 2.3 vol.% Y_2O_3 + 20 vol.% SiCw	0.194	420.08
79TiC-4.5Al_2O_3-5.6Y_2O_3-4.9SiO_2-7.1(10 vol.%) SiCw	76.0 vol.% TiC + 4.0 vol.% Al_2O_3 + 5.0 vol.% Y_2O_3 + 5.0 vol. % SiO_2 + 10 vol.% SiCw	0.193	402.57
78.6TiC-3.5Al_2O_3-5.6Y_2O_3-4.9SiO_2-7.5 (10 vol.%) cBN	72.7 vol.% TiC + 4.0 vol.% Al_2O_3 + 5.0 vol.% Y_2O_3 + 8.3 vol. % SiO_2 + 10 vol.% cBN	0.189	420.47
77.8TiC-6.9Al_2O_3-1.7Y_2O_3-14(20 vol.%) SiCw	70.7 vol.% TiC + 7.8 vol.% Al_2O_3 + 1.5 vol.% Y_2O_3 + 20 vol.% SiCw	0.192	424.61

If we combine the formulae specified by Kirstein and Woolley (Börger et al., 2002) with the experimental results in Table 6.2 and the calculated theoretical results in Table 6.4; we can calculate the maximum tensile stress σ_{max} for each composition as seen in the table below.

Table 6.5 Table of results for the calculation of Poisson's Ratio (υ), Young's Modulus (E) and maximum tensile stress (σ_{max}) for samples of various composition and sintering parameters

Sample name	υ (disc material)	E (disc material) GPa	1/E'	ζ	b	ξ	λ	$\sigma_{max\ (GPa)}$
85TiC-12Al_2O_3-3Y_2O_3	0.195	422.91	0.00694	3.656	0.672	-6.488	1.744	114.010
79TiC-11Al_2O_3-3Y_2O_3-7(10 vol.%) SiCw	0.195	422.59	0.00694	3.930	0.678	-6.463	1.744	143.481
73TiC-10Al_2O_3-3Y_2O_3-14(20 vol.%) SiCw	0.194	420.08	0.00695	3.862	0.697	-6.398	1.743	142.613
79TiC-4.5Al_2O_3-5.6Y_2O_3-4.9SiO_2-7.1(10 vol.%) SiCw	0.193	402.57	0.00705	3.714	0.672	-6.476	1.743	117.354
78.6TiC-3.5Al_2O_3-5.6Y_2O_3-4.9SiO_2-7.5 (10 vol.%) cBN	0.189	420.47	0.00695	3.804	0.694	-6.375	1.741	134.827
77.8TiC-6.9Al_2O_3-1.7Y_2O_3-14(20 vol.%) SiCw	0.192	424.61	0.00693	3.992	0.683	-6.441	1.742	152.669

Weibull statistics was used to relate a series of bending strength measurements σ to the probability of failure P_f as described in Chapter 3.5.3. The Weibull modulus is then compared for the different materials both with and without reinforcement as toughening from fibrous crack bridging behavior is shown to give an increase in Weibull modulus (Kendall et al., 1986).

6.1.1 85TiC-12Al_2O_3-3Y_2O_3 SPS'd at 1610°C, 70MPa and 10 min hold



Figure 6.1 Photograph of fractured sample of 85TiC-12Al_2O_3-3Y_2O_3

Visual analysis of the fractured sample show that the samples cracked from the central point where the contact load was applied. The number of fractured pieces indicate a low-medium internal residual stress present in the sample from the sintering process. Fractured samples are relatively even which could be due to the lack of large flaws within the sample prior to testing.

6.1.1.1 Fractography: analysis of fracture surfaces using SEM microscopy of 85TiC-12Al_2O_3-3Y_2O_3

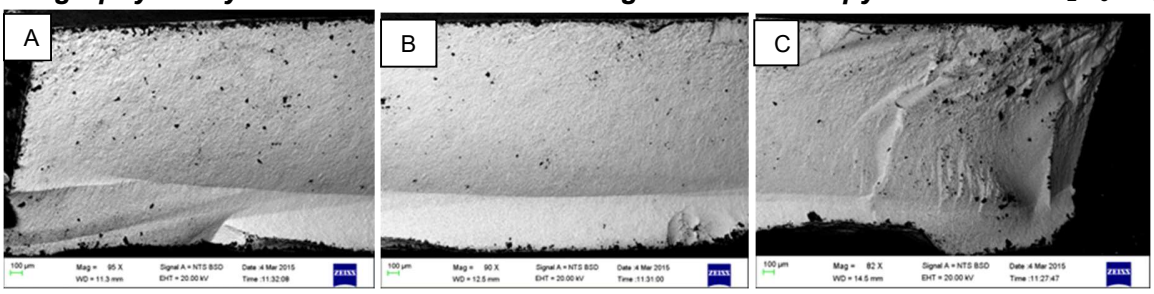


Figure 6.2 A- Outer limit of fractured edge (outside circumference of sample furthest from the site of loading), B- mid-length of fractured edge and C-inner edge of fracture of edge (centre of sample directly under the site of loading)

SEM micrographs on the macro scale show that surfaces have an almost smooth appearance with no signs of ductility. Figure 6.2C has the initiation site of the crack highlighted by regions of mirroring, misting and hackles as the crack energy radiated form the point of loading to the outer edges of the sample. In figure 6.2A-C a large fracture perpendicular to the applied load can be seen. This appears to be “cantilever/compression curl”. During flexural fracture, the stress in the un-cracked material in front of the crack rapidly changes from compression to tension. The orientation of the principle stress changes in such an unpredictable way that any asymmetry in the loading is amplified, causing the crack to wander out of its original plane (Mitchell et al., 2009).

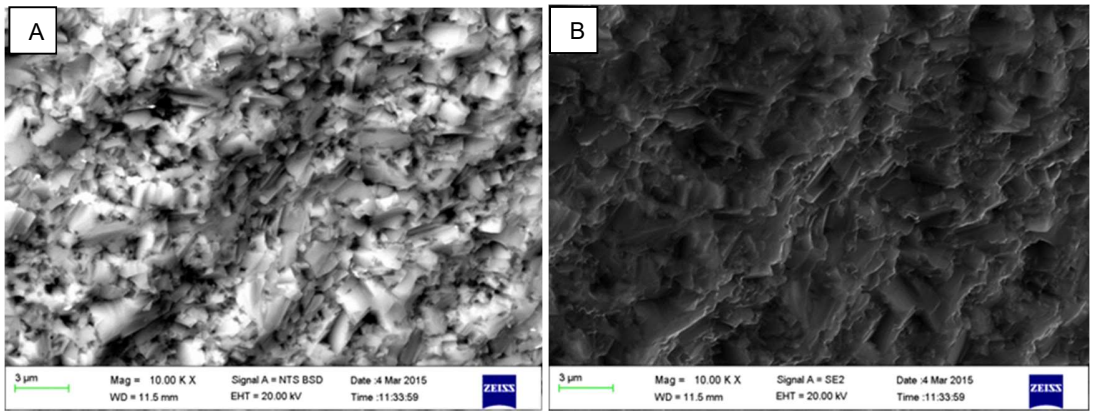


Figure 6.3 A - Fracture surface analysed under high magnification (10.0 K X) using Backscatter Detector and B- same surfaced analysed under high magnification using Secondary Electron Detector

SEM micrographs under higher magnification the fracture surfaces show cleavage and inter-granular fracture as the main modes of failure during loading which is common in ceramic materials exhibiting brittle behaviour. Inter-granular fracture might indicate weak grain boundary strength and it may also be a manifestation of between grain stresses due to elastic/thermal anisotropy especially in non-cubic ceramics (Quinn, 2016).

6.1.1.2 Calculations to determine Weibull Modulus of 85TiC-12Al_2O_3-3Y_2O_3

Table 6.6 Table of results for the calculation of the probability of fracture and Weibull modulus of 85TiC-12Al_2O_3-3Y_2O_3

85wt% TiC (2µm), 1610°C, 70MPa and 10 min hold	i	σf (MPa)	X= ln σf	Pf = (i-0.5)/n	ln [1/(1-Pf)]	Y = ln ln [1/(1-Pf)]
	1	81657.7	11.310	0.08	0.087	-2.442
	2	97667.4	11.489	0.25	0.288	-1.246
	3	98358.5	11.496	0.42	0.539	-0.618
	4	108547.8	11.595	0.58	0.875	-0.133
	5	138725.5	11.840	0.75	1.386	0.327
	6	159809.1	11.982	0.92	2.485	0.910

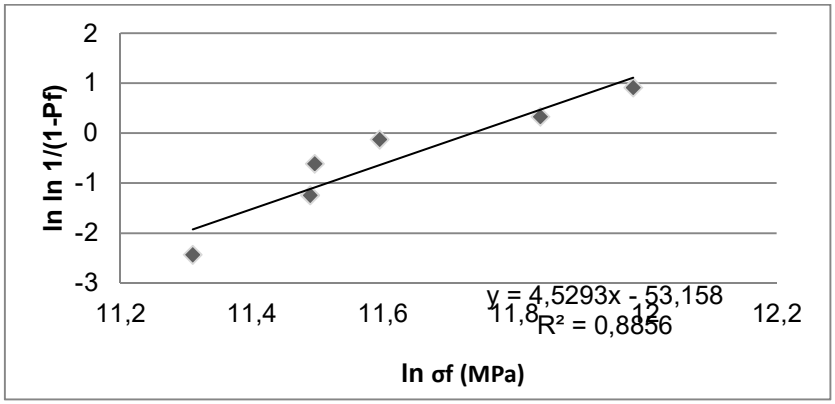


Figure 6.4 Graph of the regression line used to determine the Weibull modulus for 85TiC-12Al_2O_3-3Y_2O_3

6.1.2 79TiC-11Al_2O_3-3Y_2O_3-7(10 vol.%) SiCw SPS'd at 1600°C, 70MPa and 10 min hold



Figure 6.5 Photograph of fractured sample of 79TiC-11Al_2O_3-3Y_2O_3-7(10 vol.%) SiCw

Visual analysis of the fractured sample show that the samples cracked from the central point where the contact load was applied. The number of fractured pieces indicate a medium to high internal residual stress present in the sample on the left and a high to very high internal residual stress in the sample on the right from the sintering process.

Fractured pieces are relatively even in the sample on the left which could be due to the lack of large flaws within the sample prior to testing and more numerous and more fractured in the sample on the right which could be due to large flaws within the sample relatively close to the surface indicated by the chipping observed.

6.1.2.1 Fractography: analysis of fracture surfaces using SEM microscopy of 79TiC-11Al_2O_3-3Y_2O_3-7(10 vol.%) SiCw

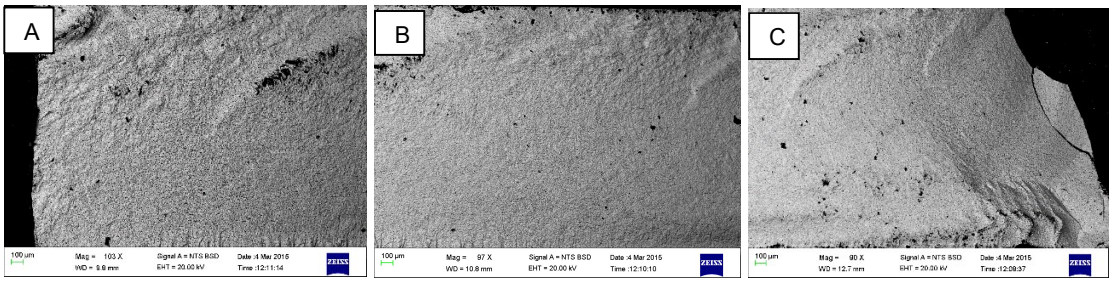


Figure 6.6 A- Outer limit of fractured edge (outside circumference of sample furthest from the site of loading), B- mid-length of fractured edge and C-inner edge of fracture of edge (centre of sample directly under the site of loading)

SEM micrographs on the macro scale show that surfaces have an almost smooth appearance with no signs of ductility. Figure 6.6C has the initiation site of the crack highlighted by regions of mirroring, misting and hackles as the crack energy radiated form the point of loading to the outer edges of the sample.

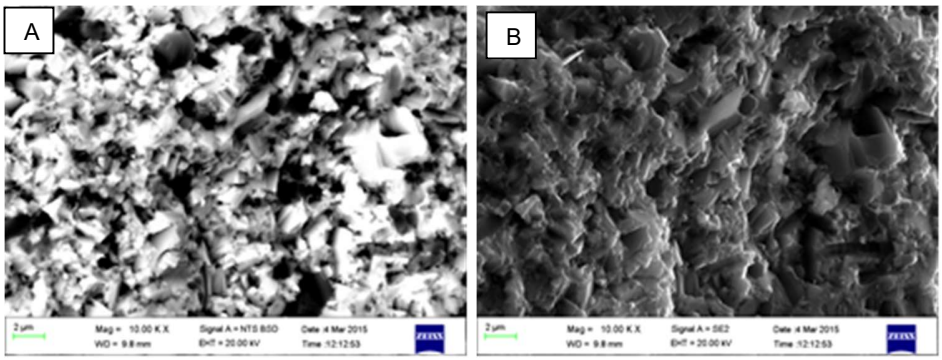


Figure 6.7 A - Fracture surface analysed under high magnification (10.0 K X) using Backscatter Detector and B- same surfaced analysed under high magnification using Secondary Electron Detector

SEM micrographs under higher magnification the fracture surfaces show cleavage, trans-granular and inter-granular fracture as the main modes of failure during loading which is common in ceramic materials exhibiting brittle behaviour. It can also be observed that the addition of SiC whiskers as fibre reinforcement has resulted in the whiskers effecting the fracture modes or the material. The whiskers appear to have suffered both pull-out and crack bridging which indicates and intermediate degree of interfacial bonding between the fibre-matrix interface.

6.1.2.2 Calculations to determine Weibull Modulus of 79TiC-11Al_2O_3-3Y_2O_3-7(10 vol.%) SiCw

Table 6.7 Table of results for the calculation of the probability of fracture and Weibull modulus of 79TiC-11Al_2O_3-3Y_2O_3-7(10 vol.%) SiCw

85wt% TiC + 10 vol% SiCw, 1600°C, 70MPa and 10 min hold	i	σf (MPa)	X= ln σf	Pf = (i-0.5)/n	ln [1/(1-Pf)]	Y = ln ln [1/(1-Pf)]
	1	114967.2	11.652	0.08	0.087	-2.442
	2	116804.6	11.668	0.25	0.288	-1.246
	3	148170.8	11.906	0.42	0.539	-0.618
	4	158008.9	11.970	0.58	0.875	-0.133
	5	158472.0	11.973	0.75	1.386	0.327
	6	163335.6	12.004	0.92	2.485	0.910

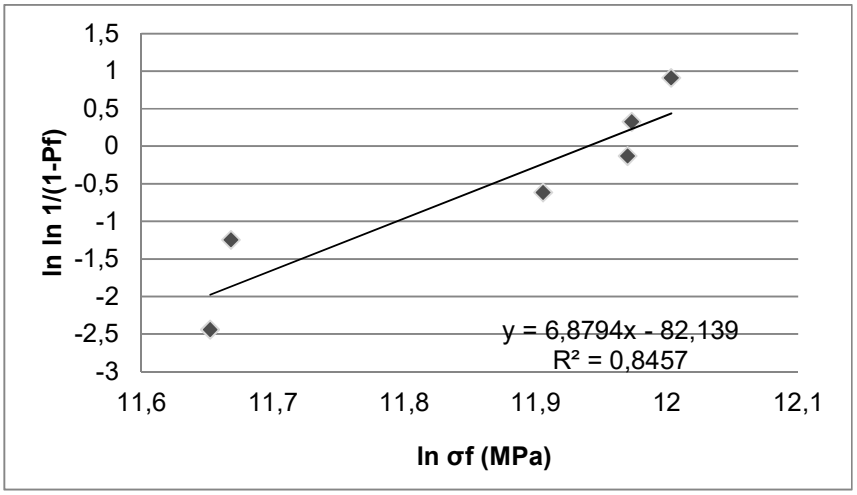


Figure 6.8 Graph of the regression line used to determine the Weibull modulus for 79TiC-11Al_2O_3-3Y_2O_3-7(10 vol.%) SiCw

6.1.3 73TiC-10Al_2O_3-3Y_2O_3-14(20 vol.%) SiCw SPS'd at 1625°C, 70MPa and 10 min hold



Figure 6.9 Photograph of fractured sample of 73TiC-10Al_2O_3-3Y_2O_3-14(20 vol.%) SiCw

Visual analysis of the fractured sample show that the samples cracked from the central point where the contact load was applied.

The number of fractured pieces indicate a medium internal residual stress present in the samples. Fractured pieces are relatively even in the sample on the right which could be due to the lack of large flaws within the sample prior to testing and more numerous and more fractured in the sample on the left.

This could be due to large flaws such as “whisker clumps/tangles” within the sample which cause the crack paths to diverge from the point of loading contact.

6.1.3.1 Fractography: analysis of fracture surfaces using SEM microscopy of 73TiC-10Al$_2$O$_3$-3Y$_2$O$_3$-14(20 vol.%) SiCw

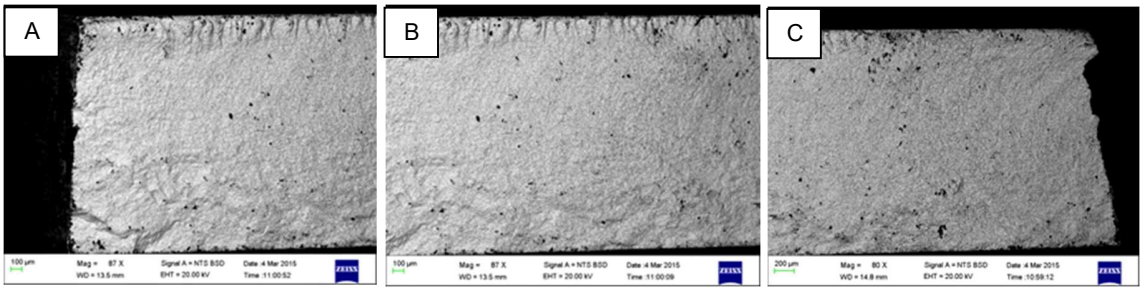


Figure 6.10 A- Outer limit of fractured edge (outside circumference of sample furthest from the site of loading), B- mid-length of fractured edge and C-inner edge of fracture of edge (centre of sample directly under the site of loading)

SEM micrographs on the macro scale show that surfaces have an almost smooth appearance with no signs of ductility. Figure 6.10C has the initiation site of the crack highlighted by regions of mirroring, misting and hackles as the crack energy radiated form the point of loading to the outer edges of the sample. Figure 6.10 A and B show minor cracks forming along the polished upper surface which may indicate micro-flaws on the surface acting as sites of crack propagation.

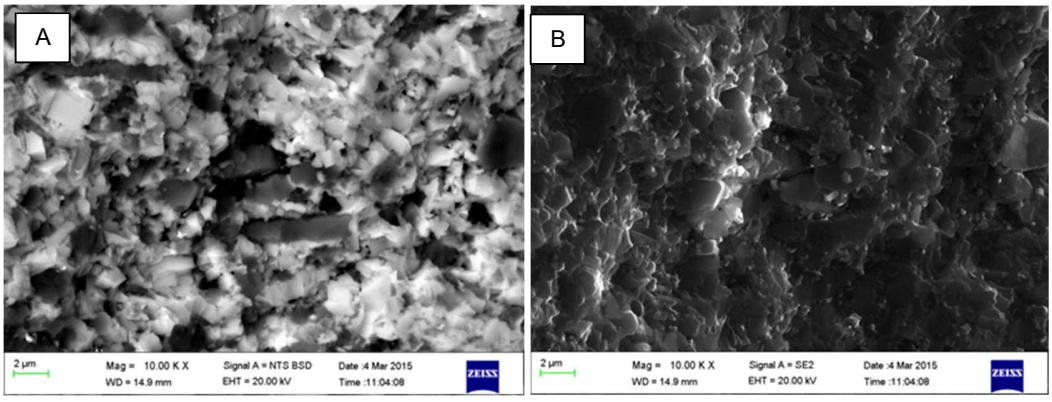


Figure 6.11 A - Fracture surface analysed under high magnification (10.0 K X) using Backscatter Detector and B- same surfaced analysed under high magnification using Secondary Electron Detector

SEM micrographs under higher magnification the fracture surfaces show cleavage, trans-granular and inter-granular fracture as the main modes of failure during loading which is common in ceramic materials exhibiting brittle behaviour. Crack bridging seems to be the dominant form of fibre fracture with little evidence of pull-out occurring.

6.1.3.2 Calculations to determine Weibull Modulus of 73TiC-10Al_2O_3-3Y_2O_3-14(20 vol.%) SiCw

Table 6.8 Table of results for the calculation of the probability of fracture and Weibull modulus of *73TiC-10Al_2O_3-3Y_2O_3-14(20 vol.%) SiCw*

85wt% TiC + 20 vol% SiCw, 1625°C, 70MPa and 10 min hold	i	σf (MPa)	X= ln σf	Pf = (i-0.5)/n	ln [1/(1-Pf)]	Y = ln ln [1/(1-Pf)]
	1	109444.4	11.603	0.08	0.087	-2.442
	2	131637.0	11.788	0.25	0.288	-1.246
	3	141463.6	11.860	0.42	0.539	-0.618
	4	142658.0	11.868	0.58	0.875	-0.133
	5	154554.2	11.948	0.75	1.386	0.327
	6	176209.7	12.079	0.92	2.485	0.910

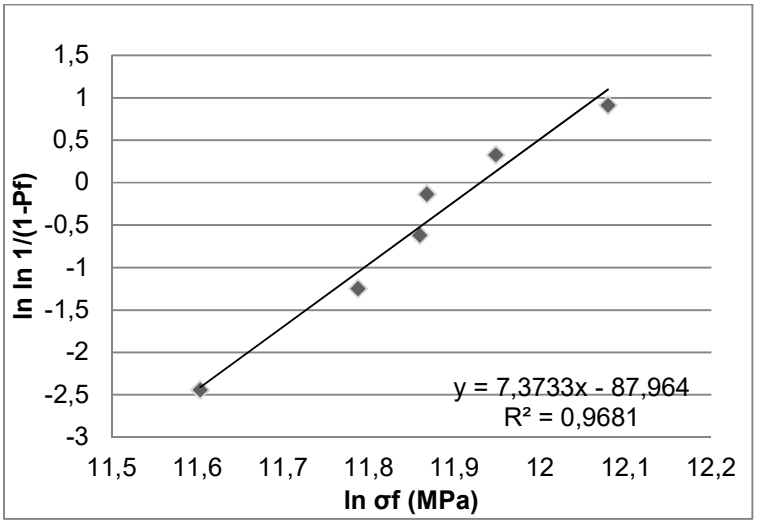


Figure 6.12 Graph of the regression line used to determine the Weibull modulus for 73TiC-10Al_2O_3-3Y_2O_3-14(20 vol.%) SiCw

6.1.4 79TiC-4.5Al_2O_3-5.6Y_2O_3-4.9SiO_2-7.1(10 vol.%) SiCw SPS'd at 1600°C, 70MPa and 10 min hold



Figure 6.13 Photograph of fractured sample of 79TiC-4.5Al_2O_3-5.6Y_2O_3-4.9SiO_2-7.1(10 vol.%) SiCw

Visual analysis of the fractured sample show that the samples cracked from the central point where the contact load was applied. The number of fractured pieces indicate a medium internal residual stress present in the sample from the sintering process. Fractured samples are relatively even which could be due to the lack of large flaws within the sample prior to testing.

6.1.4.1 Fractography: analysis of fracture surfaces using SEM microscopy of 79TiC-4.5Al_2O_3-5.6Y_2O_3-4.9SiO_2-7.1(10 vol.%) SiCw

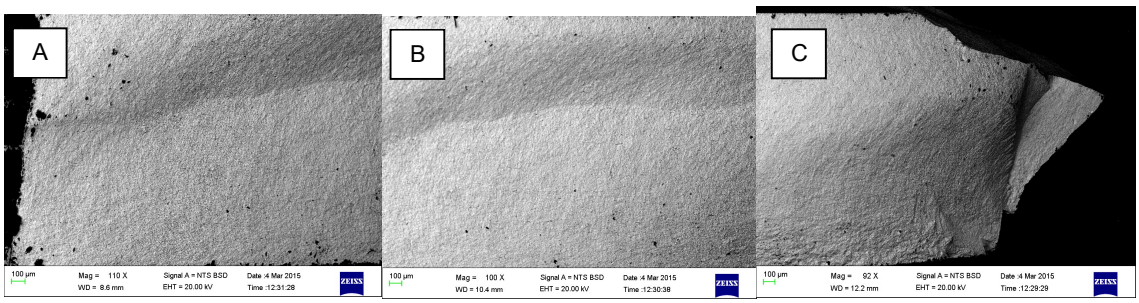


Figure 6.14 A- Outer limit of fractured edge (outside circumference of sample furthest from the site of loading), B- mid-length of fractured edge and C-inner edge of fracture of edge (centre of sample directly under the site of loading)

SEM micrographs on the macro scale show that surfaces have an almost smooth appearance with no signs of ductility. Figure 6.14C has the initiation site of the crack highlighted by regions of mirroring, misting and hackles as the crack energy radiated form the point of loading to the outer edges of the sample. In figure 6.14A-C a large fracture perpendicular to the applied load can be seen. This appears to be “cantilever/compression curl”

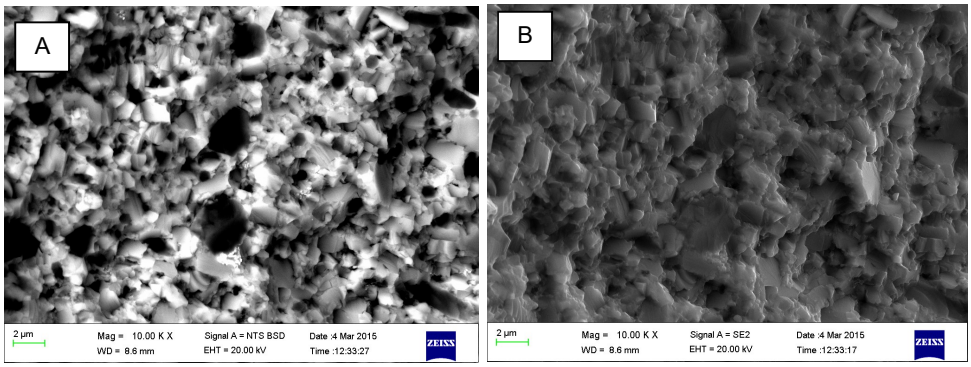


Figure 6.15 A - Fracture surface analysed under high magnification (10.0 K X) using Backscatter Detector and B- same surfaced analysed under high magnification using Secondary Electron Detector

SEM micrographs under higher magnification the fracture surfaces show cleavage, trans-granular and inter-granular fracture as the main modes of failure during loading which is common in ceramic materials exhibiting brittle behaviour. Crack bridging seems to be the dominant form of fibre fracture with no evidence of pull-out occurring.

6.1.4.2 Calculations to determine Weibull Modulus of 79TiC-4.5Al_2O_3-5.6Y_2O_3-4.9SiO_2-7.1(10 vol.%) SiCw

Table 6.9 Table of results for the calculation of the probability of fracture and Weibull modulus of 79TiC-4.5Al_2O_3-5.6Y_2O_3-4.9SiO_2-7.1(10 vol.%) SiCw

85wt% TiC (+SiO_2) + 10 vol% SiCw, 1600°C, 70MPa and 10 min hold	i	σf (MPa)	X= ln σf	Pf = (i-0.5)/n	ln [1/(1-Pf)]	Y = ln ln [1/(1-Pf)]
	1	97901.1	11.492	0.08	0.087	-2.442
	2	97996.2	11.493	0.25	0.288	-1.246
	3	114820.8	11.651	0.42	0.539	-0.618
	4	121987.9	11.712	0.58	0.875	-0.133
	5	123930.4	11.727	0.75	1.386	0.327
	6	146851.6	11.897	0.92	2.485	0.910

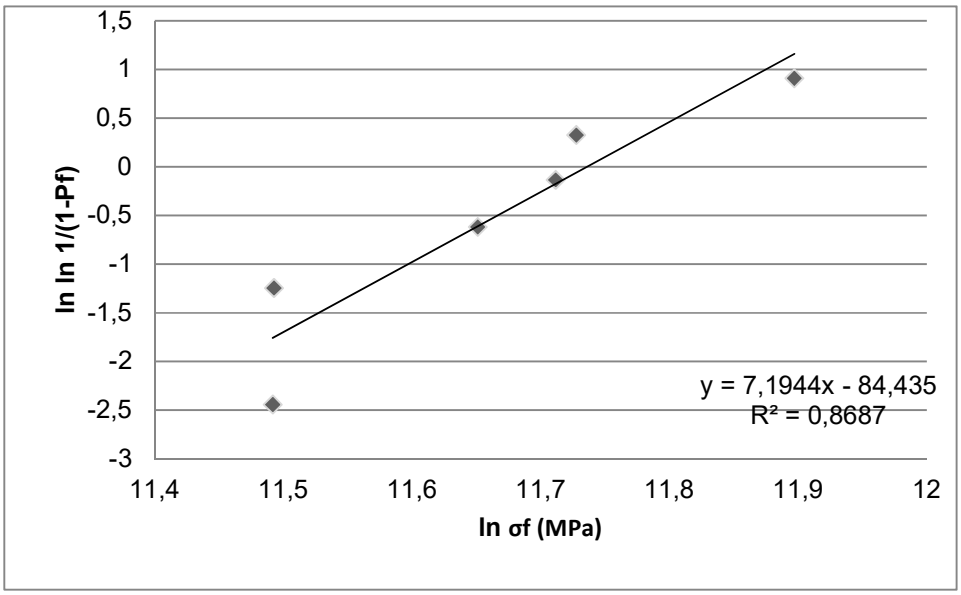


Figure 6.16 Graph of the regression line used to determine the Weibull modulus for 79TiC-4.5Al_2O_3-5.6Y_2O_3-4.9SiO_2-7.1(10 vol.%) SiCw

6.1.5 78.6TiC-3.5Al_2O_3-5.6Y_2O_3-4.9SiO_2-7.5 (10 vol.%) cBN SPS'd at 1575°C, 70MPa and 5 min hold



Figure 6.17 Photograph of fractured sample of78.6TiC-3.5Al_2O_3-5.6Y_2O_3-4.9SiO_2-7.5 (10 vol.%) cBN

Visual analysis of the fractured sample show that the samples cracked from the central point where the contact load was applied. The number of fractured pieces indicate a medium-high internal residual stress present in the samples. Fractured pieces are relatively even in both of the samples which could be due to the lack of large flaws within the sample prior to testing. There is however slight evidence of crack divergence. This could be due to the effects of local chemical interaction around cBN grains caused by minute quantities of hBN on the grains surface. The presence of hBN would inhibit local sintering causing pockets of porosity within the sample which cause the crack paths to diverge from the point of loading contact.

6.1.5.1 Fractography: analysis of fracture surfaces using SEM microscopy of 78.6TiC-3.5Al_2O_3-5.6Y_2O_3-4.9SiO_2-7.5 (10 vol.%) cBN

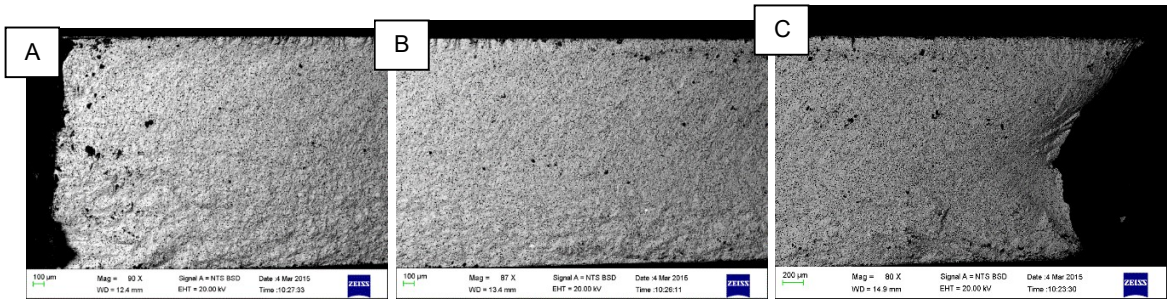


Figure 6.18 A- Outer limit of fractured edge (outside circumference of sample furthest from the site of loading), B- mid-length of fractured edge and C-inner edge of fracture of edge (centre of sample directly under the site of loading)

SEM micrographs on the macro scale show that surfaces have an almost smooth appearance with no signs of ductility. Figure 6.18C has the initiation site of the crack highlighted by regions of mirroring, misting and hackles as the crack energy radiated form the point of loading to the outer edges of the sample.

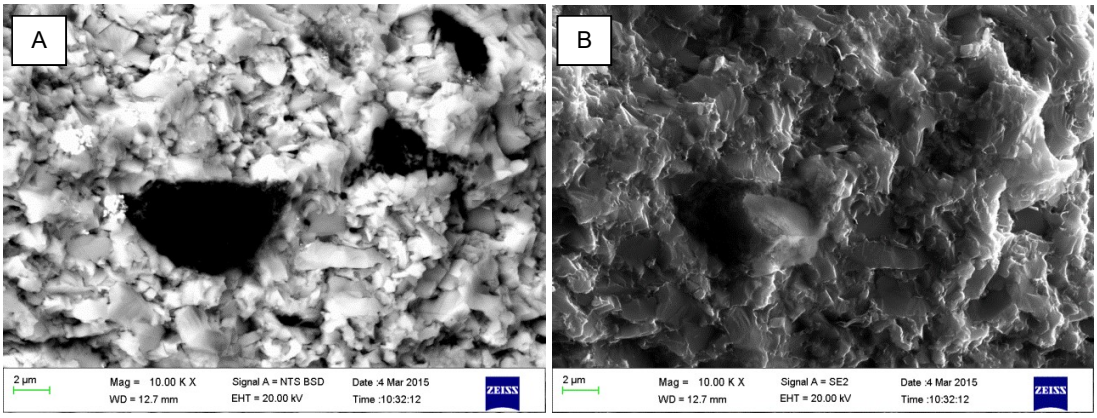


Figure 6.19 A - Fracture surface analysed under high magnification (10.0 K X) using Backscatter Detector and B- same surfaced analysed under high magnification using Secondary Electron Detector

SEM micrographs under higher magnification the fracture surfaces show cleavage, trans-granular fracture in the matrix material and inter-granular fracture around the cBN grains. Crack bridging seems to be the dominant form of fracture in the matrix but it appears that pull-out is occurring around the cBN grains which have signs of debonding. This could be the result of small amounts of hBN on the cBN surface preventing wetting and bonding between the matrix and the cBN; which was added as a secondary hard phase.

6.1.5.2 Calculations to determine Weibull Modulus of 78.6TiC-3.5Al_2O_3-5.6Y_2O_3-4.9SiO_2-7.5 (10 vol.%) cBN

Table 6.10 Table of results for the calculation of the probability of fracture and Weibull modulus of 78.6TiC-3.5Al_2O_3-5.6Y_2O_3-4.9SiO_2-7.5 (10 vol.%) cBN

85wt% TiC(+SiO_2) + 10 vol% cBN, 1575°C, 70MPa and 5 min hold	i	σf (MPa)	X= ln σf	Pf = (i-0.5)/n	ln [1/(1-Pf)]	Y = ln ln [1/(1-Pf)]
	1	119064.8	11.687	0.08	0.087	-2.442
	2	121784.9	11.710	0.25	0.288	-1.246
	3	126646.2	11.749	0.42	0.539	-0.618
	4	137144.2	11.829	0.58	0.875	-0.133
	5	150341.3	11.921	0.75	1.386	0.327
	6	153984.8	11.945	0.92	2.485	0.910

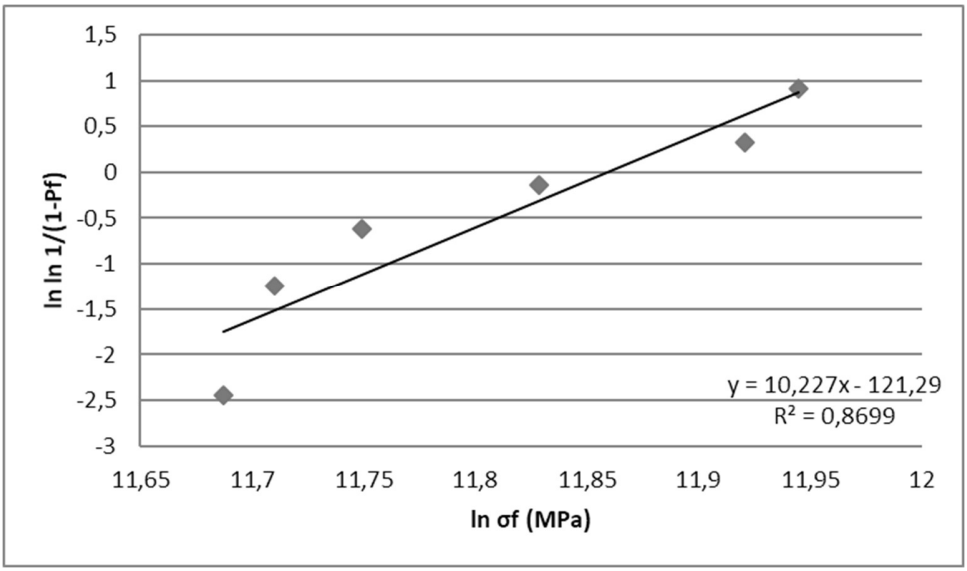


Figure 6.20 Graph of the regression line used to determine the Weibull modulus for 78.6TiC-3.5Al_2O_3-5.6Y_2O_3-4.9SiO_2-7.5 (10 vol.%) cBN

6.1.6 77.8TiC-6.9Al_2O_3-1.7Y_2O_3-14(20 vol.%) SiCw SPS'd at 1625°C, 70MPa and 20 min hold



Figure 6.21 Photograph of fractured sample of77.8TiC-6.9Al_2O_3-1.7Y_2O_3-14(20 vol.%) SiCw

Visual analysis of the fractured sample show that the samples cracked from the central point where the contact load was applied. The number of fractured pieces indicate a medium-high internal residual stress present in the samples. Fractured pieces are relatively even in both of the samples which could be due to the lack of large flaws within the sample prior to testing.

6.1.6.1 Fractography: analysis of fracture surfaces using SEM microscopy of 77.8TiC-6.9Al_2O_3-1.7Y_2O_3-14(20 vol.%) SiCw

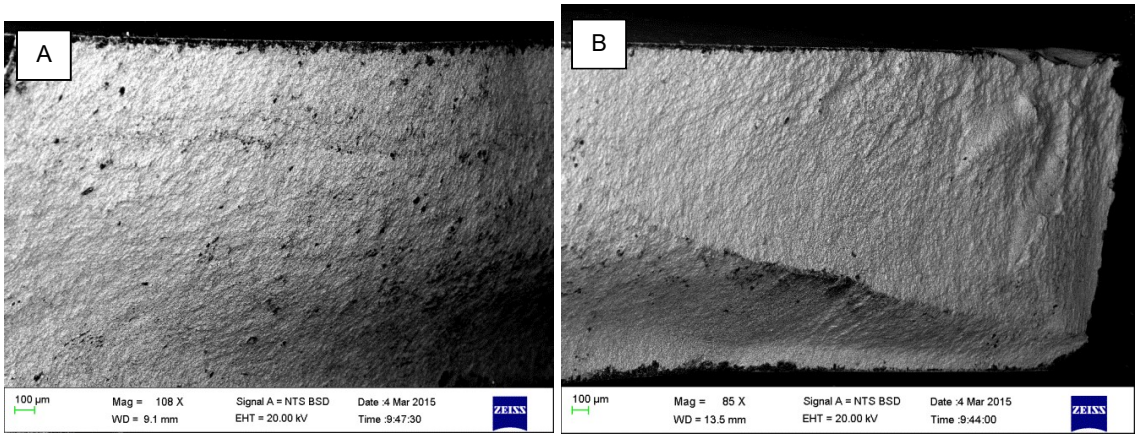


Figure 6.22 A- mid-length of fractured edge and B- inner edge of fracture of edge (centre of sample directly under the site of loading)

SEM micrographs on the macro scale show that surfaces have an almost smooth appearance with no signs of ductility. Figure 6.22B has the initiation site of the crack highlighted by regions of mirroring, misting and hackles as the crack energy radiated form the point of loading to the outer edges of the sample. In figure 6.22A-B a large fracture perpendicular to the applied load can be seen. This appears to be “cantilever/compression curl”. Figure 6.17B show minor cracks forming along the polished upper surface which may indicate micro-flaws on the surface acting as sites of crack propagation.

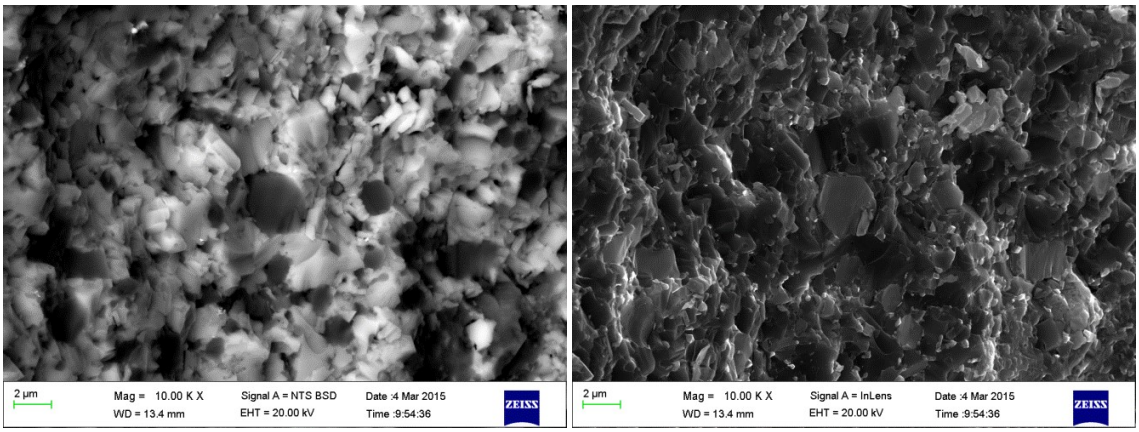


Figure 6.23 A - Fracture surface analysed under high magnification (10.0 K X) using Backscatter Detector and B- same surfaced analysed under high magnification using Secondary Electron Detector

SEM micrographs under higher magnification the fracture surfaces show cleavage, trans-granular and inter-granular fracture as the main modes of failure during loading which is common in ceramic materials exhibiting brittle behaviour. Crack bridging seems to be the dominant form of fibre fracture with no evidence of pull-out occurring.

6.1.6.2 Calculations to determine Weibull Modulus of 77.8TiC-6.9Al_2O_3-1.7Y_2O_3-14(20 vol.%) SiCw

Table 6.11 Table of results for the calculation of the probability of fracture and Weibull modulus of 77.8TiC-6.9Al_2O_3-1.7Y_2O_3-14(20 vol.%) SiCw

90wt% TiC + 20 vol.% SiCw, 1625°C, 70MPa and 20 min hold	i	σf (MPa)	X= ln σf	Pf = (i-0.5)/n	ln [1/(1-Pf)]	Y = ln ln [1/(1-Pf)]
	1	142220.4	11.865	0.08	0.087	-2.442
	2	149551.1	11.915	0.25	0.288	-1.246
	3	150996.8	11.925	0.42	0.539	-0.618
	4	154100.5	11.945	0.58	0.875	-0.133
	5	158833.1	11.976	0.75	1.386	0.327
	6	160316.0	11.985	0.92	2.485	0.910

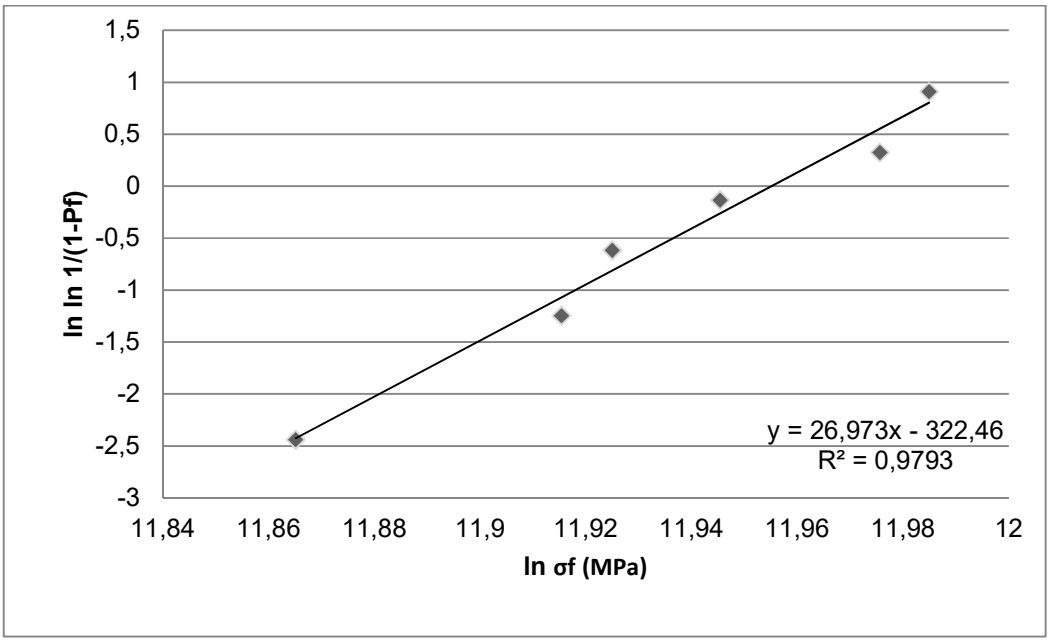


Figure 6.24 Graph of the regression line used to determine the Weibull modulus for 77.8TiC-6.9Al_2O_3-1.7Y_2O_3-14(20 vol.%) SiCw

6.1.7 Comparison of the Weibull moduli of sintered TiC with various liquid phase sintering aids and with/without the addition of reinforcement materials

In ceramics high toughness leads to greater flaw tolerances and higher Weibull Moduli, where by Weibull modulus *m* is a measure of reliability (Kendall et al., 1986).

Table 6.12: Typical values of the Weibull modulus m for some materials

Materials	*m*	Reference
Traditional ceramics: Brick, pottery, chalk	<3	(Chawla & Meyers, 1999)
Engineered ceramics: SiC, Si_3N_4, Al_2O_3	5-10	(Chawla & Meyers, 1999)
Metals: Aluminium, Steel	90-100	(Chawla & Meyers, 1999)
Extruded Mg Alloy	92.6	(Guo et al., 2017)
3D fibre reinforced C/SiC composite	23.3	(Xu et al., 2001)
CVD SiC fibres SiC/RB-Si_3N_4 composite @1550°C	31.5	(Gyekenyesi & Bansal, 2000)

Typically, Weibull moduli for traditional ceramics are quite low as the brittle nature and low strength of the material results in them being less reliable than metals. Metals have Weibull moduli of between 90-100 due to their ductility and toughness. Engineering ceramics are far tougher than traditional ceramics due to the special bonding configurations between the molecules. This increased fracture toughness also results in higher reliability (*m* = 5-10) but still much lower than that of metals. Hence the desire to increase fracture toughness by the addition of fibre reinforcement and secondary hard phases and herewith increase the Weibull moduli.

Table 6.13: Weibull moduli of sintered TiC with various liquid phase sintering aids and with/without the addition of reinforcement materials

Sample name	Sintering Parameters (Temperature, Sintering Pressure and Hold Time)	σ max (GPa)	Weibull modulus	R^2
85TiC-12Al_2O_3-3Y_2O_3	1610°C, 70MPa and 10 min hold	114.01	4.5293	0.8856
79TiC-11Al_2O_3-3Y_2O_3-7(10 vol.%) SiCw	1600°C, 70MPa and 10 min hold	143.56	6.8794	0.8457
73TiC-10Al_2O_3-3Y_2O_3-14(20 vol.%) SiCw	1625°C, 70MPa and 10 min hold	142.61	7.3733	0.9681
79TiC-4.5Al_2O_3-5.6Y_2O_3-4.9SiO_2-7.1(10 vol.%) SiCw	1600°C, 70MPa and 10 min hold	117.35	7.1944	0.8687
78.6TiC-3.5Al_2O_3-5.6Y_2O_3-4.9SiO_2-7.5 (10 vol.%) cBN	1575°C, 70MPa and 5 min hold	134.83	10.227	0.8699
77.8TiC-6.9Al_2O_3-1.7Y_2O_3-14(20 vol.%) SiCw	1625°C, 70MPa and 20 min hold	152.67	26.973	0.9793

The addition of 10 vol.% SiC whiskers to the unreinforced matrix samples with 85 wt.% TiC without the addition of SiO_2 to the liquid phase sintering aids have an increase in the ultimate stress at fracture from 114.01 to 143.56 GPa and Weibull modulus from 4.529 to 6.879. These values are significantly higher than without the SiC whisker reinforcement.

Further increase in the SiC whisker content to 20 vol.% results in only a slight decrease in ultimate fracture strength from 143.56 to 142.61 GPa and a slight increase in Weibull modulus possibly due to the more even distribution of whiskers throughout the matrix.

However, the addition of SiO_2 to the matrix in addition the presence of 10 vol.% SiC whiskers results in a decrease in the ultimate fracture stress from 143.56 to 117.35 while the Weibull modulus only underwent a slight increase from 6.879 to 7.194. This result could be due to the increased bonding strength at the interface between the fibres and the matrix as SiO_2 is known to form glassy phases at the interface.

Thus preventing fibre debonding or crack deflection which can slow crack propagation and absorb crack energy leading to fracture at lower stresses. Crack bridging can be seen in Figure 5.14B. The slight increase in reliability is due to the material behaving more homogeneously as the SiC whisker reinforcement behaves more like a part of the matrix and less like sites of potential flaws.

When 10 vol.% cBN is added to the 85 wt.% TiC matrix with the addition of SiO_2 there in a significant increase in the ultimate fracture strength from 114.01 to 134.83 GPa and Weibull moduli from 4.529 to 10.227. Even compare to the equivalent volume fraction of SiC whisker reinforcement the fracture strength is lower 134.83 GPa compared to 143.56 GPa but a large increase in Weibull modulus to 10.227 is obtained compared to 6.88. This could be due to local chemistry around the reinforcements as well as the shape of the reinforcements; long thin whiskers vs cubic crystalline shapes. The whisker shape leads to preferred orientation during sintering which is not a problem with cBN thus effecting the reliability of the material.

When comparing the 85 wt.% TiC matrix with 20 vol.% SiC whiskers (without the addition of SiO_2 as a liquid phase sintering aid) to the 90 wt.% TiC matrix with 20 vol.% SiC whiskers (without the addition of SiO_2 as a liquid phase sintering aid), we find that the 90 wt.% TiC matrix with 20 vol.% SiC whiskers (without the addition of SiO_2 as a liquid phase sintering aid) has the greatest ultimate fracture strength of 152.67 GPa and a Weibull modulus of 26.973 which is significantly higher than any unreinforced engineering ceramics but similar to other ceramic matrix composites especially those reinforced with ceramic fibres (Gyekenyesi & Bansal, 2000; Xu et al., 2001).

7. BALL ON DISC SLIDING WEAR TESTING

The test system was performed under well-defined conditions. The test system consists of a stationary ball (6 mm diameter) held against a horizontally rotating disc (20 mm outside diameter). The operating variables were continuous unidirectional sliding at a velocity of v = 0.1 ms^{-1}, a normal load of F_N = 10 N, an ambient temperature of 22°C and a sliding distance of s = 300 m. The 6 materials chosen to be tested as the disc material are the same as those used for biaxial strength testing as they have the best combination of density and fracture toughness. The stationary balls used for testing was made from AISI 52100 steel ball bearings. The test environment was specified to be laboratory air with a 60% relative humidity and no lubricant was used during testing (Czichos et al., 1989).

Six types of data were analysed:

1. The disc wear track width which was used to confirm the path travelled by the ball on the disc during the wear test and that the ball maintained contact over the duration of the test. It also defined the areas that would need to be analysed via SEM and EDS.
2. Energy dispersive X-ray spectroscopy (EDS) determines the composition of the material on the contacting surfaces. The surface which is removing material will have traces of the softer material on its surface allong the path marked out by the disc wear track.
3. The ball wear scar diameter indicates which disc material is better at wearing away the ball by determing which wear scar diameter is the largest. The diameter and area of the wear scar on the ball surface was used to determine the volume and hence the mass loss of the ball during the sliding wear test using the formulae provided in Chapter 3.5.4.
4. The linear wear rate of the system defined as the displacement of the test specimens, perpendicular to the sliding interface divided by the sliding distance difference. (This was a geometry dependant quantity)
5. Visual analysis of ball surface wear shows which types of physical interactions are occuring on the balls surface during the abrasive wear. This was further mentioned in Chapter 2.6.2.
6. The friction co-efficient determined after 300 m of sliding distance. The friction coefficient describes the resistance between the contacting face of the ball as they try to slide across the surface of the disc. The condition of the contacting surfaces can result in larger or smaller coefficients of friction as the surface roughness changes over the sliding distance. Rougher surfaces will result in larger coefficients of friction and vice versa. Reinforment materials in the sintered TiC based CMC's can act as secondary phases during abrasive wear. This concept was discussed in more detail in Chapter 2.6.5

7.1 85TiC-12Al_2O_3-3Y_2O_3 SPS'd at 1610°C, 70MPa and 10 min hold

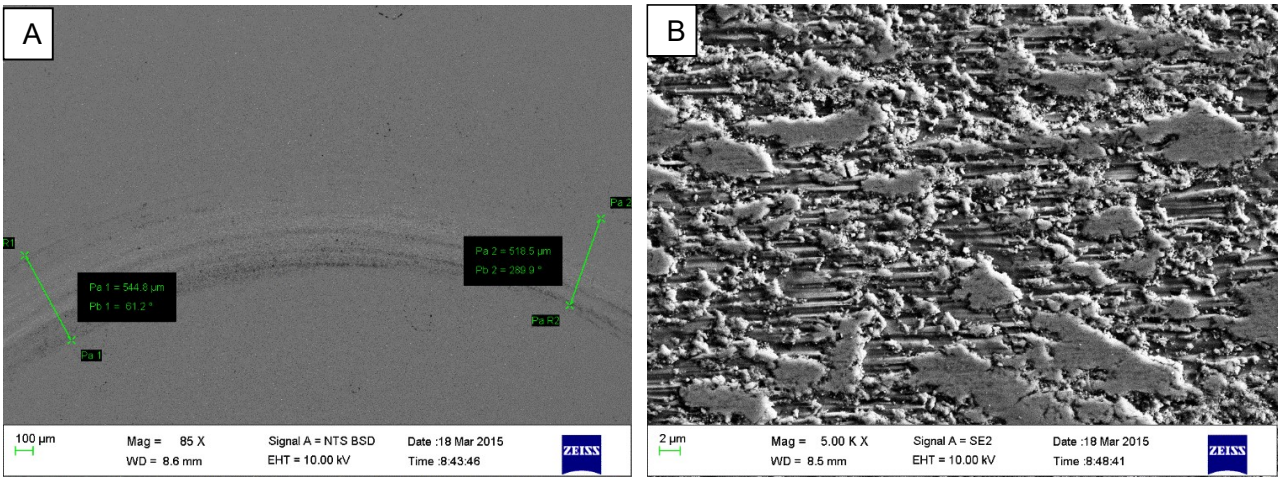


Figure 7.1 A: wear track on the surface of the 85TiC-12Al_2O_3-3Y_2O_3 matrix only sample disc. B: High magnification image of the wear track on the 85TiC-12Al_2O_3-3Y_2O_3 matrix only sample disc.

Figure 7.1A the image of the wear track at a lower magnification shows the wear track as well as the measurement of the track left by the ball on the disc.

The minimum thickness of the wear track measured is 518.5µm. Figure 7.1B showed a magnified view of the wear track. A significant difference can be seen between the surface of the the wear track and the unaffected surface. The wear track has a significantly rougher surface and it appears to be higher than the surrounding area. The presence of scuffing and smearing can also clearly be seen. This could be due to adhesive wear i.e. removal of material from the AISI 52100 steel ball and the removed material adhering on to the sintered TiC disc.

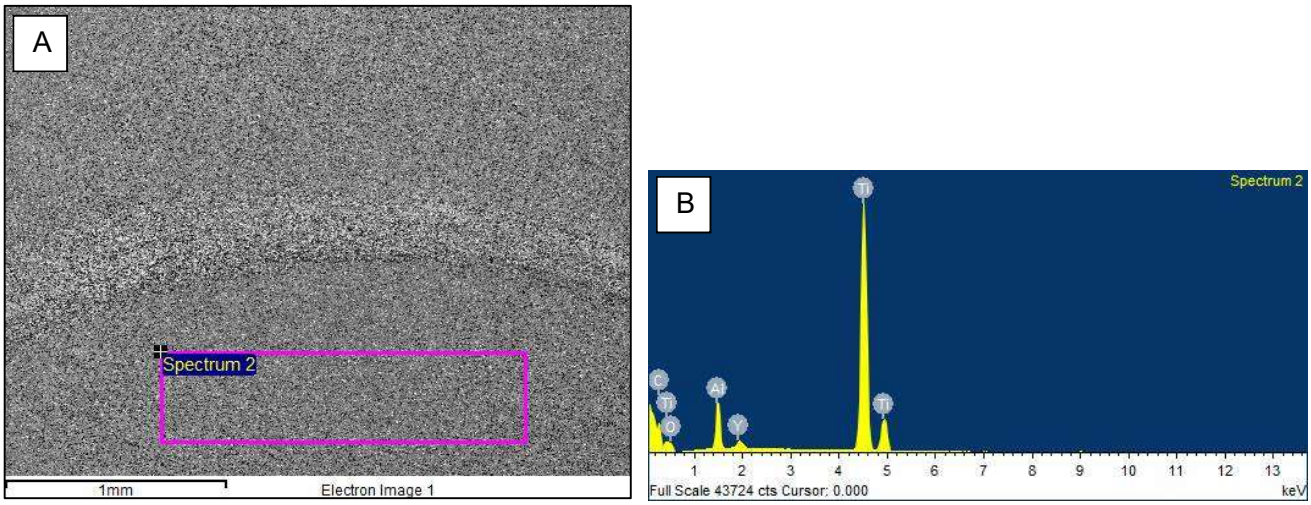


Figure 7.2 A: Spectrum 2 Area alongside the wear track scanned by EDS for composition B: Results of EDS qualitative analysis on Spectrum 2.

Figure 7.2A Spectrum 2 shows the area alongside the wear track which is unaffected by wear giving us a base area for comparison. The results of the scan are as expected with peaks present for Titanium, Carbon, Oxygen, Aluminium and Yttrium.

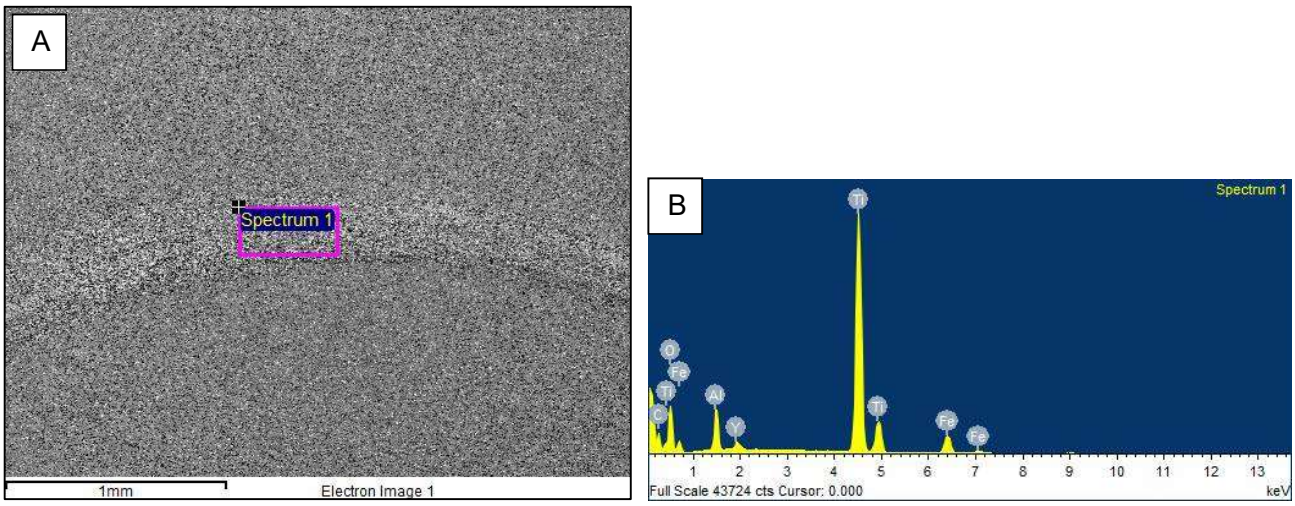


Figure 7.3 A: Spectrum 1 Area on the wear track scanned by EDS for composition B: Results of EDS qualitative analysis on Spectrum 1.

Figure 7.3A Spectrum 1 Area shows a scan area on the wear track. The results of a scan area showed the presence of Iron on the surface which is not present in the scan of the area alongside the wear track.

This could be attributed to material from the ball being transferred to the disc during the wear testing. This confirms the possibility that adhesion is the dominant mode of wear.

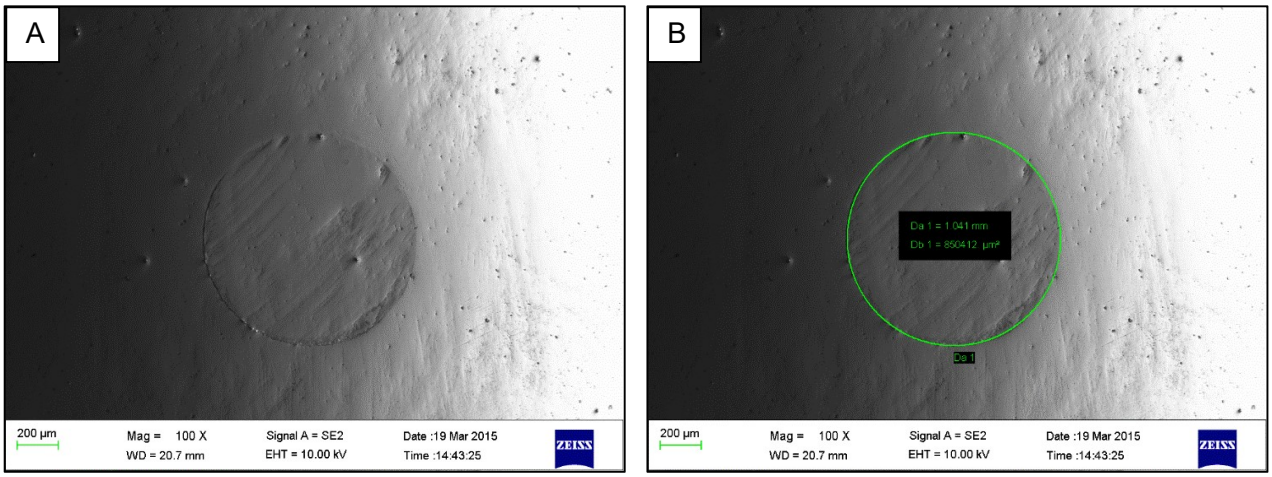


Figure 7.4 A: Wear scar on the surface of the worn AISI 52100 steel ball bearing. B: Diameter and area of the wear scar on the worn AISI 52100 steel ball bearing. (Diameter: 1.041mm and Area: 0.850mm^2)

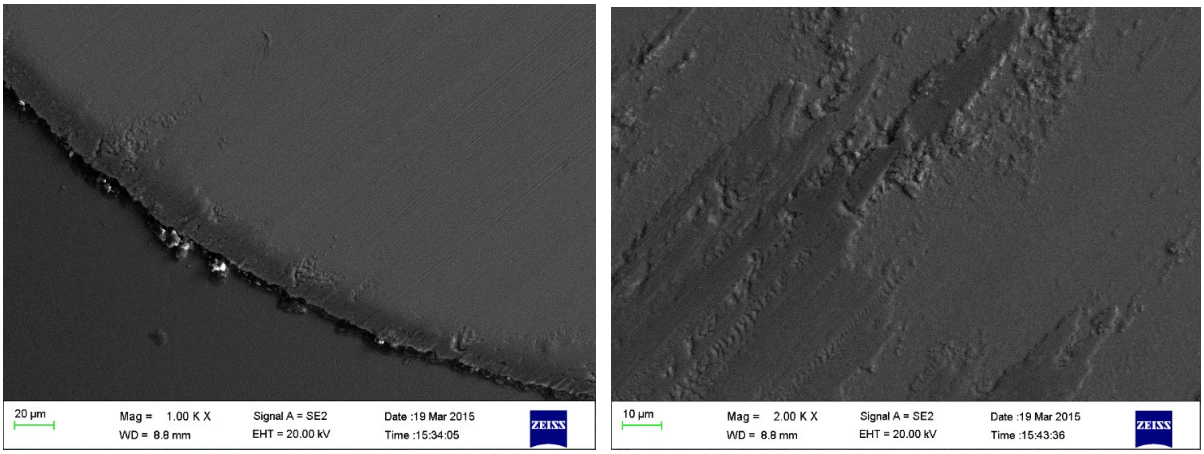


Figure 7.5 A: High magnification image of the edge of the wear scar on the worn AISI 52100 steel ball bearing. B: Higher magnification image of the centre of the wear scar on the worn AISI 52100 steel ball bearing.

Figure 7.5A showed severe plastic deformation in the direction of the sliding wear. Figure 7.5 B Showed the worn surface of the steel ball bearing. The wear scar shows signs of delamination and the presence of a mechanically mixed layer (Radhika et al., 2018).

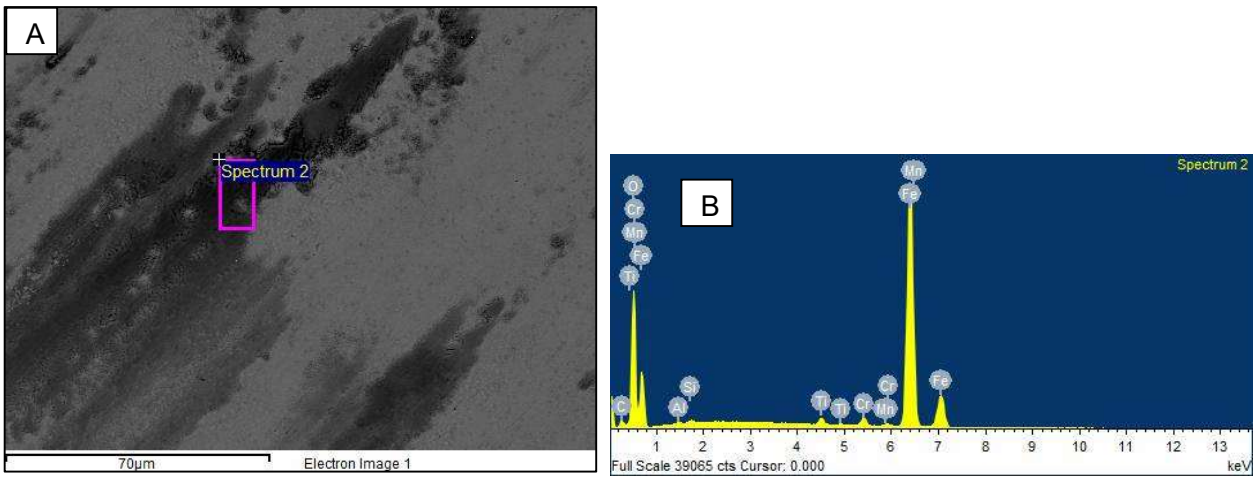


Figure 7.6 A: Spectrum 2 Area inside the wear scar on the worn AISI 52100 steel ball bearing scanned by EDS for composition B: Results of EDS qualitative analysis on Spectrum 2.

Figure 7.6 A shows the EDS scan area which include what is suspected to be a layer of mechanically mixed material. The EDS analysis confirmed both the ball bearing material and material from the sintered ceramic disc notably Titanium and Aluminium.

7.2 79TiC-11Al_2O_3-3Y_2O_3-7(10 vol.%) SiCw SPS'd at 1600°C, 70MPa and 10 min hold

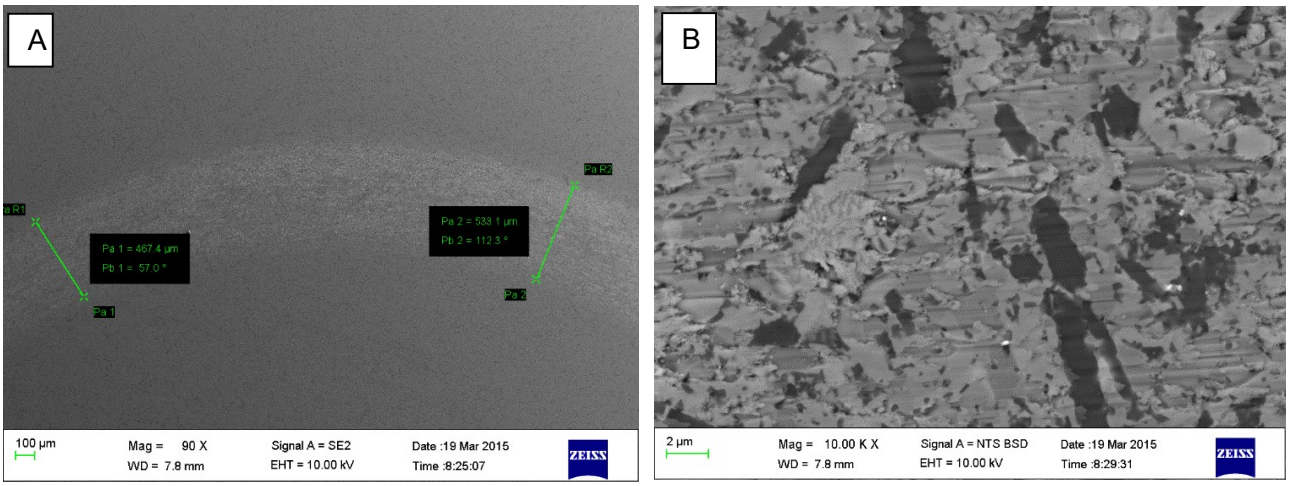


Figure 7.7 A: wear track on the surface of the 79TiC-11Al_2O_3-3Y_2O_3-7(10 vol.%) SiCw sample disc. B: High magnification image of the wear track on the79TiC-11Al_2O_3-3Y_2O_3-7(10 vol.%) SiCw sample disc.

Figure 7.7A the image of the wear track at a lower magnification shows the wear track as well as the measurement of the track left by the ball on the disc. The minimum thickness of the wear track measured is 467.4µm. Figure 7.7B showed a magnified view of the wear track. A significant difference can be seen between the surface of the the wear track and the unaffected surface. The presence of grooves and smearing can also clearly be seen. This could be due to adhesive wear i.e. removal of material from the AISI 52100 steel ball and the removed material adhering on to the sintered TiC + SiC whisker reinforced disc as well as abrasive wear which is the removal of material and responsible for the grooves on the surface.

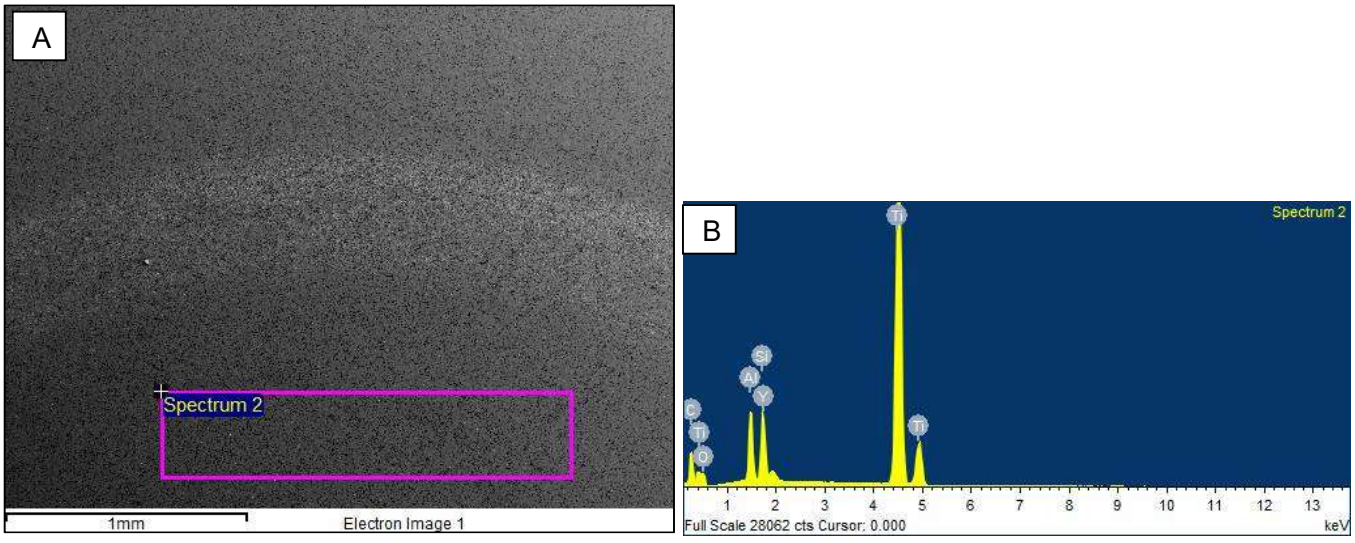


Figure 7.8 A: Spectrum 2 Area alongside the wear track scanned by EDS for composition B: Results of EDS qualitative analysis on Spectrum 2

Figure 7.8A Shows the scan area Spectrum 2 which shows the area alongside the wear track which is unaffected by wear giving us a base area for comparison. The results of the scan are as expected with peaks present for Titanium, Carbon, Oxygen, Aluminium, Silicon and Yttrium.

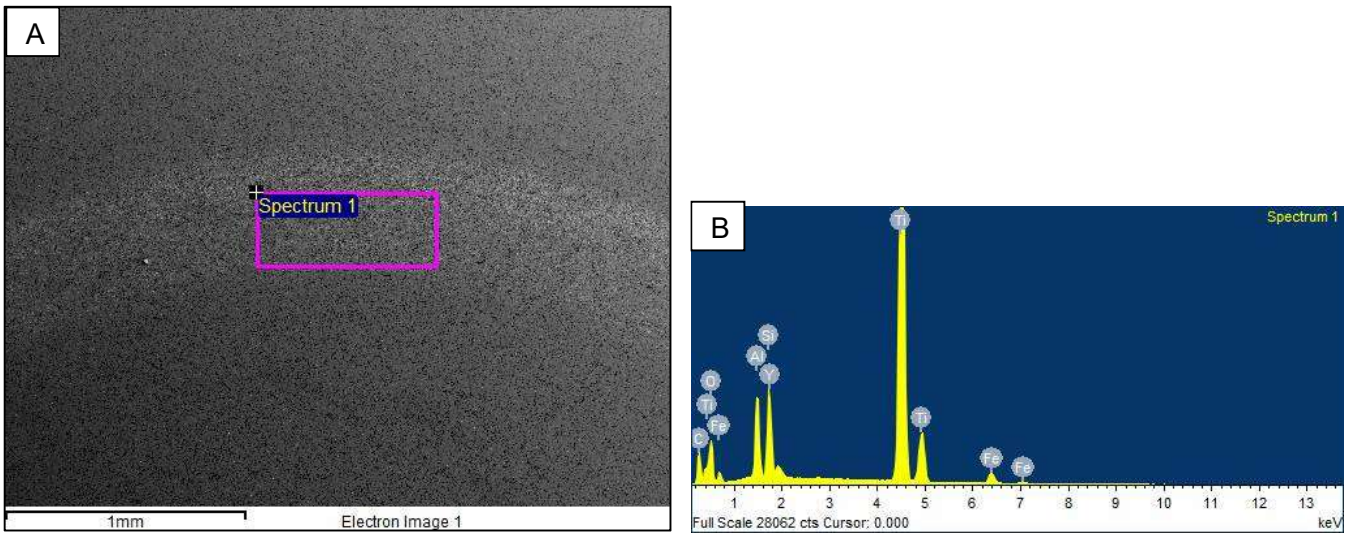


Figure 7.9 A: Spectrum 1 Area on the wear track scanned by EDS for composition B: Results of EDS qualitative analysis on Spectrum 1.

Figure 7.9A Spectrum 1 Area shows a scan area on the wear track. The results of a scan area showed the presence of Iron on the surface which is not present in the scan of the area alongside the wear track. This could be attributed to material from the ball being transferred to the disc during the wear testing.

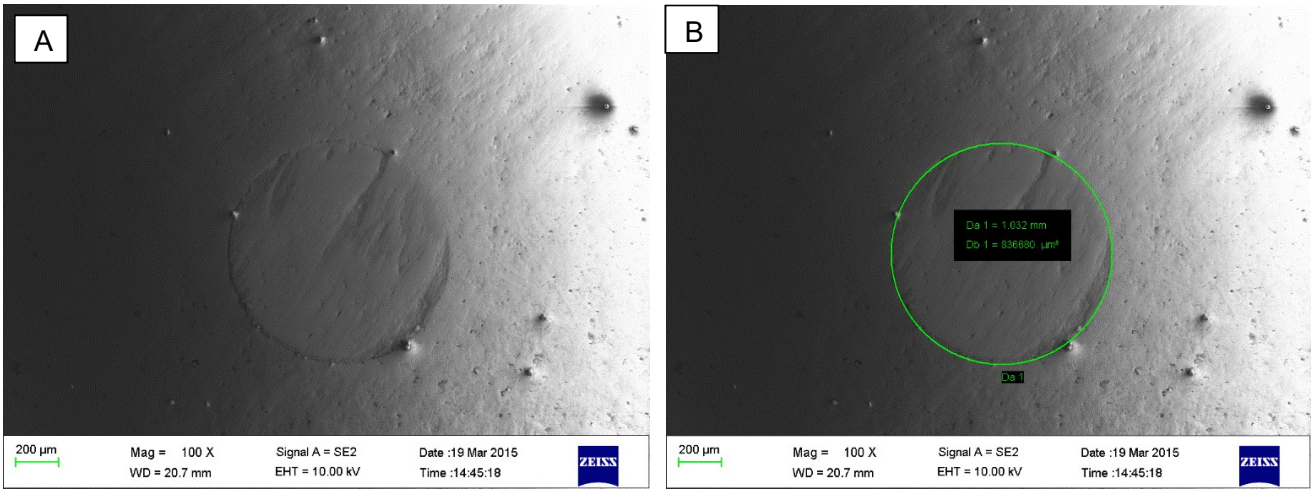


Figure 7.10 A: Wear scar on the surface of the worn AISI 52100 steel ball bearing. B: Diameter and area of the wear scar on the worn AISI 52100 steel ball bearing. (Diameter: 1.032mm and Area: 0.837mm^2)

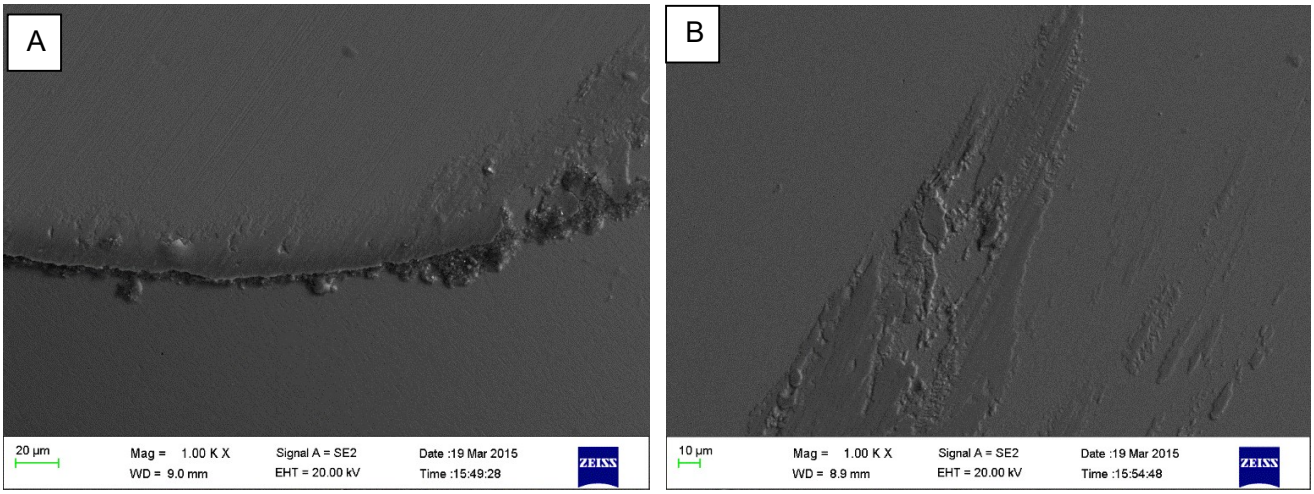


Figure 7.11 A: High magnification image of the edge of the wear scar on the worn AISI 52100 steel ball bearing. B: Higher magnification image of the centre of the wear scar on the worn AISI 52100 steel ball bearing.

Figure 7.11A showed severe plastic deformation in the direction of the sliding wear. Figure 7.11 B Showed the worn surface of the steel ball bearing. The wear scar shows signs of delamination and the presence of a mechanically mixed layer (Radhika et al., 2018).

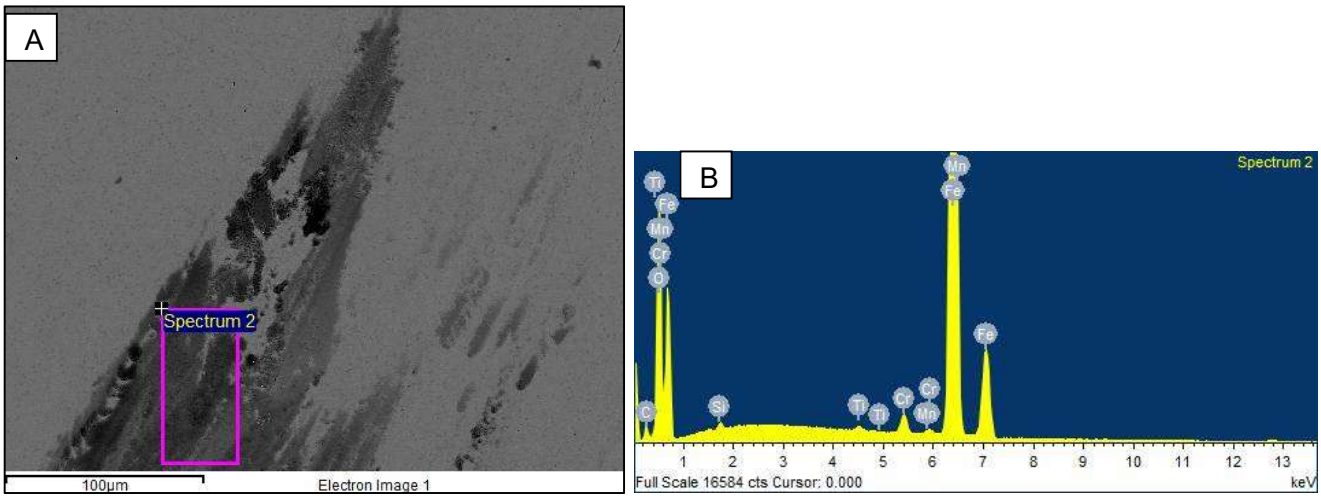


Figure 7.12 A: Spectrum 2 Area inside the wear scar on the worn AISI 52100 steel ball bearing scanned by EDS for composition B: Results of EDS qualitative analysis on Spectrum 2.

Figure 7.12 A shows the EDS scan area which include what is suspected to be a layer of mechanically mixed material. The EDS analysis confirmed both the ball bearing material and material from the sintered ceramic disc notably Titanium, Oxygen and Aluminium.

7.3 73TiC-10Al_2O_3-3Y_2O_3-14(20 vol.%) SiCw SPS'd at 1625°C, 70MPa and 10 min hold

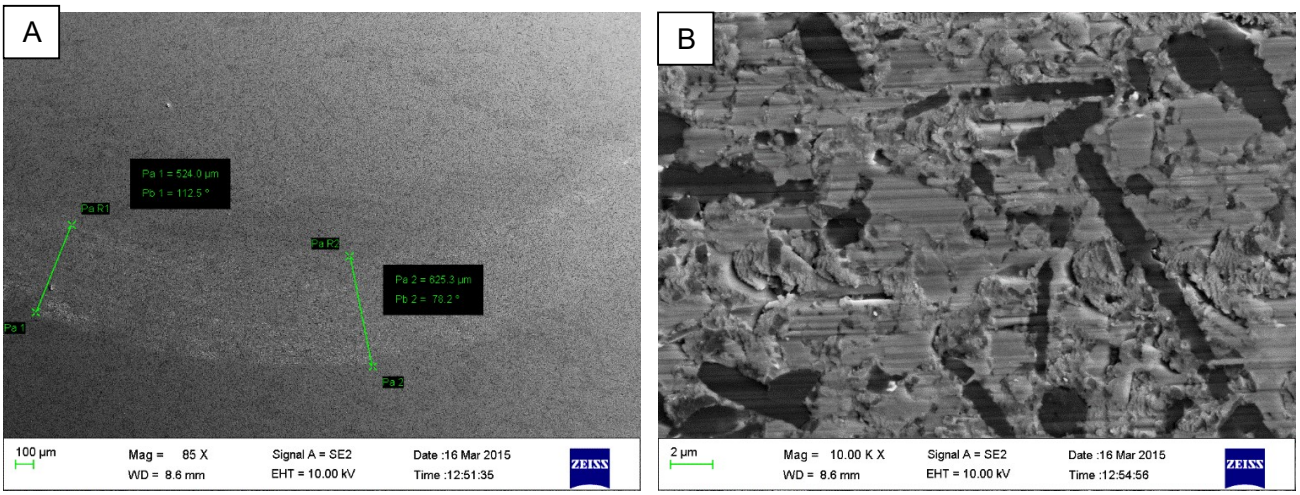


Figure 7.13 A: wear track on the surface of the 73TiC-10Al_2O_3-3Y_2O_3-14(20 vol.%) SiCw sample disc. B: High magnification image of the wear track on the 73TiC-10Al_2O_3-3Y_2O_3-14(20 vol.%) SiCw sample disc.

Figure 7.13 A the image of the wear track at a lower magnification shows the wear track as well as the measurement of the track left by the ball on the disc. The minimum thickness of the wear track measured is 524.0µm. Figure 7.13B showed a magnified view of the wear track. A significant difference can be seen between the surface of the the wear track and the unaffected surface.

The presence of grooves and delamination can also clearly be seen. This could be due to adhesive wear i.e. removal of material from the AISI 52100 steel ball and the removed material adhering on to the sintered TiC + SiC whisker reinforced disc as well as abrasive wear which is the removal of material and responsible for the grooves on the surface.

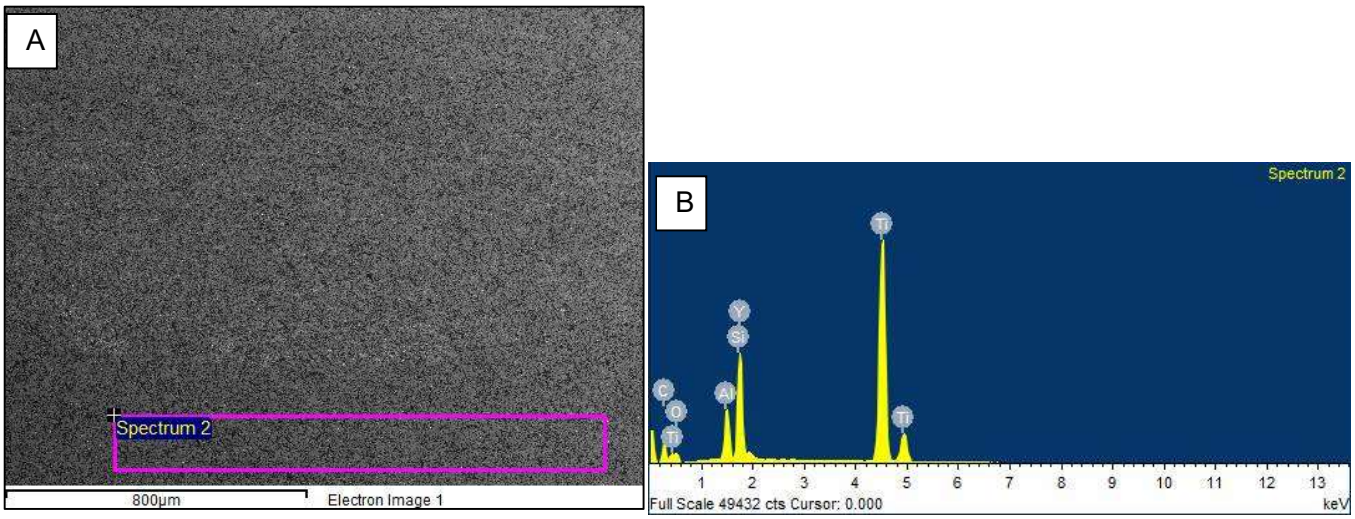


Figure 7.14 A: Spectrum 2 Area alongside the wear track scanned by EDS for composition B: Results of EDS qualitative analysis on Spectrum 2.

Figure 7.14 A Shows the scan area Spectrum 2 which shows the area alongside the wear track which is unaffected by wear giving us a base area for comparison. The results of the scan are as expected with peaks present for Titanium, Carbon, Oxygen, Aluminium, Silicon and Yttrium.

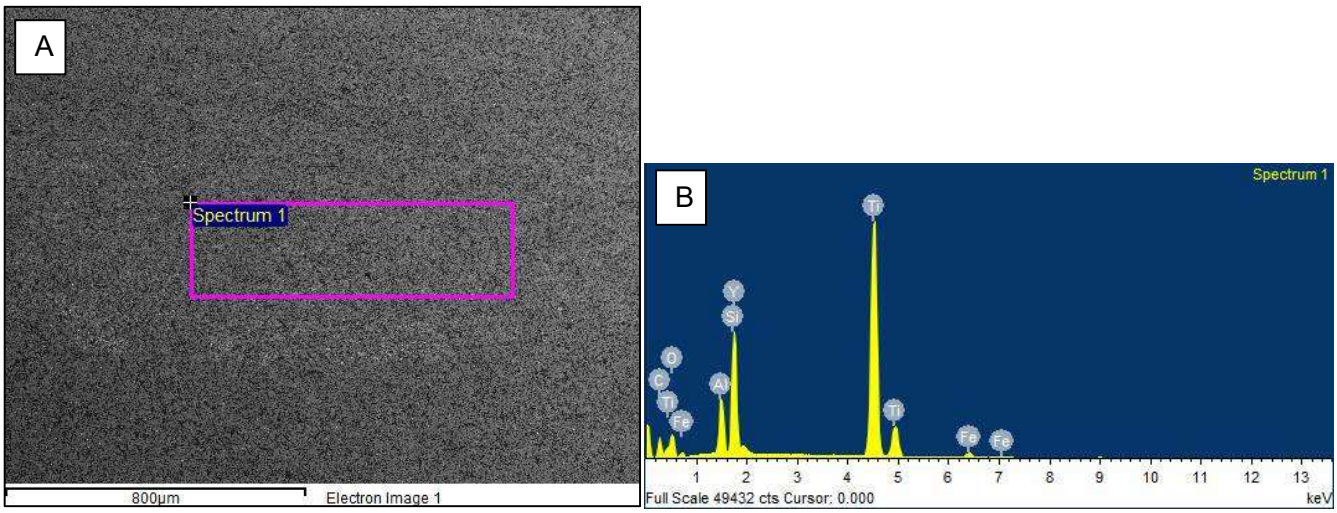


Figure 7.15 A: Spectrum 1 Area on the wear track scanned by EDS for composition B: Results of EDS qualitative analysis on Spectrum 1.

Figure 7.15A Spectrum 1 Area shows a scan area on the wear track. The results of a scan area showed the presence of Iron on the surface which is not present in the scan of the area alongside the wear track. This could be attributed to material from the ball being transferred to the disc during the wear testing.

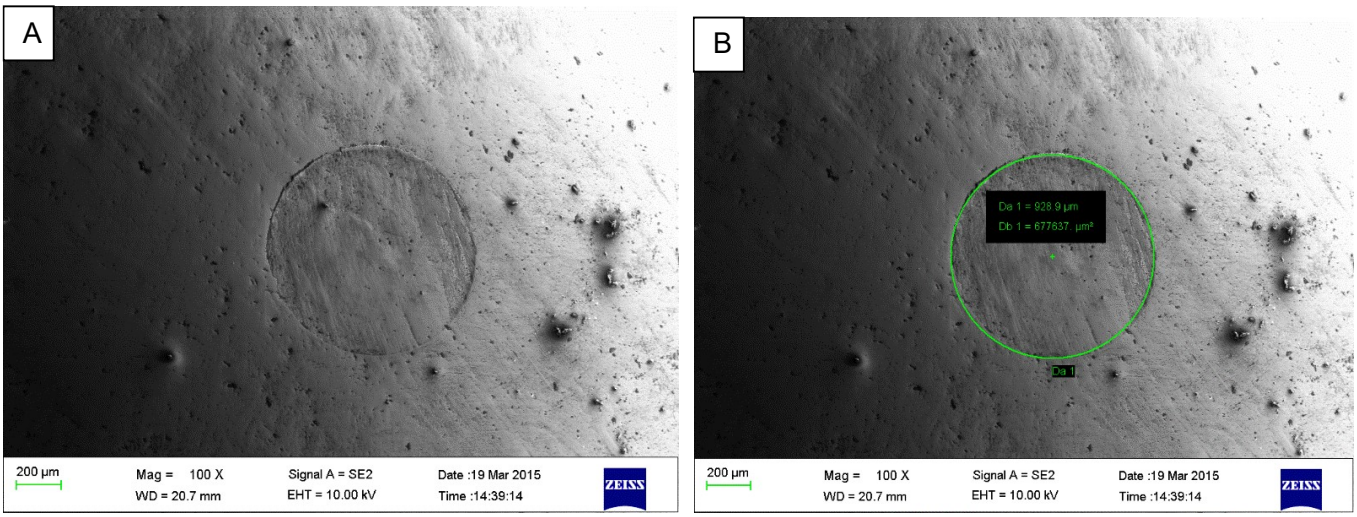


Figure 7.16 A: Wear scar on the surface of the worn AISI 52100 steel ball bearing. B: Diameter and area of the wear scar on the worn AISI 52100 steel ball bearing. (Diameter: 0.929mm and Area: 0.678mm^2)

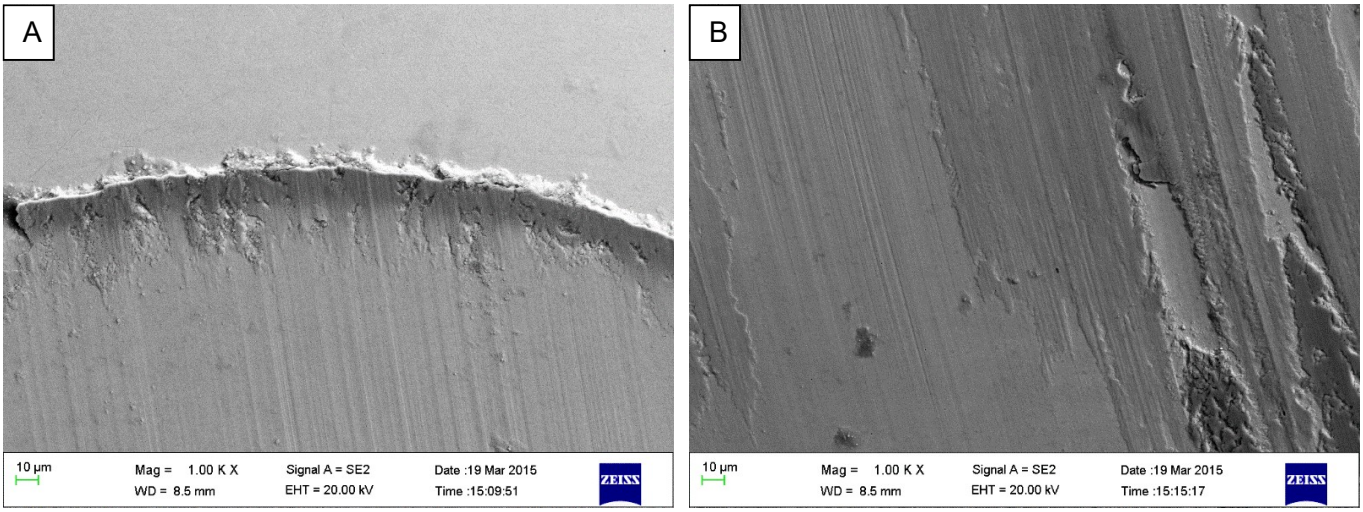


Figure 7.17 A: High magnification image of the edge of the wear scar on the worn AISI 52100 steel ball bearing. B: Higher magnification image of the centre of the wear scar on the worn AISI 52100 steel ball bearing.

Figure 7.17A showed severe plastic deformation in the direction of the sliding wear. Figure 7.17 B Showed the worn surface of the steel ball bearing. The wear scar shows signs of delamination and the presence of a mechanically mixed layer (Radhika et al., 2018).

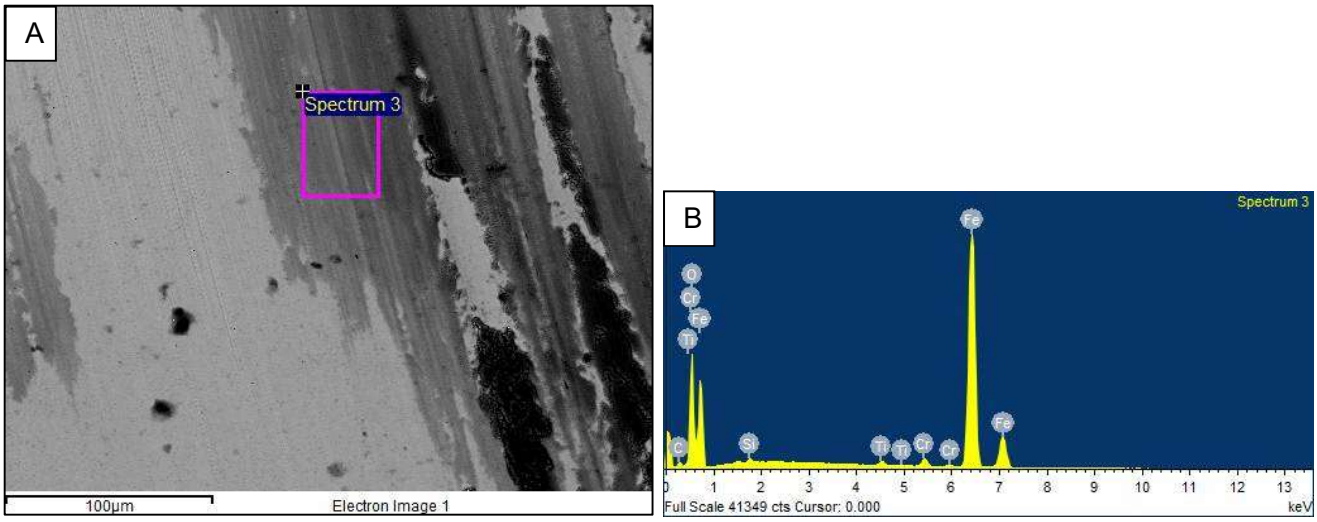


Figure 7.18 A: Spectrum 3 Area inside the wear scar on the worn AISI 52100 steel ball bearing scanned by EDS for composition B: Results of EDS qualitative analysis on Spectrum 3.

Figure 7.18 A shows the EDS scan area which include what is suspected to be smeared delaminated. The EDS analysis confirmed both the ball bearing material and material from the sintered ceramic disc notably Titanium, Oxygen and Silicon.

7.4 79TiC-4.5Al_2O_3-5.6Y_2O_3-4.9SiO_2-7.1(10 vol.%) SiCw SPS'd at 1600°C, 70MPa and 10 min hold

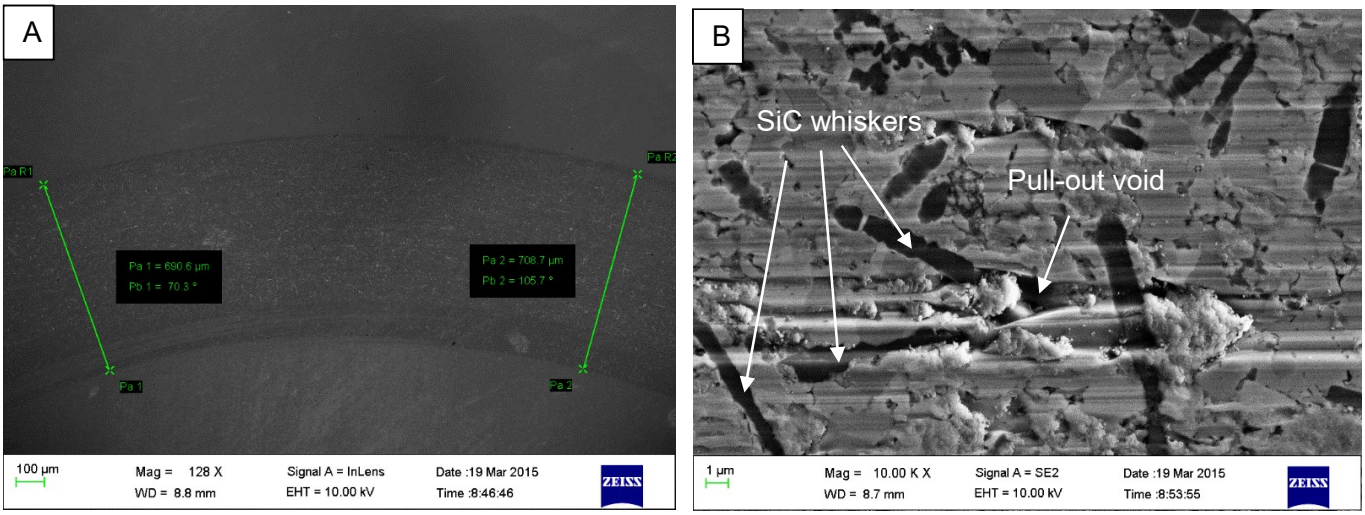


Figure 7.19 A: wear track on the surface of 79TiC-4.5Al_2O_3-5.6Y_2O_3-4.9SiO_2-7.1(10 vol.%) SiCw sample disc. B: High magnification image of the wear track on the 79TiC-4.5Al_2O_3-5.6Y_2O_3-4.9SiO_2-7.1(10 vol.%) SiCw sample disc.

Figure 7.19 A the image of the wear track at a lower magnification shows the wear track as well as the measurement of the track left by the ball on the disc. The minimum width of the wear track measured is 690.6µm. Figure 7.19B showed a magnified view of the wear track. A significant difference can be seen between the surface of the the wear track and the unaffected surface. The presence of grooves and mechanically mixed materials can also clearly be seen. This could be due to adhesive wear i.e. removal of material from the AISI 52100 steel ball and the removed material; which is now mechanically mixed, adhering on to the sintered TiC + SiC whisker reinforced disc. Abrasive wear which is the removal of material is also responsible for the grooves on the surface. Some pull out of the SiC whiskers can be seen on the surface as well.

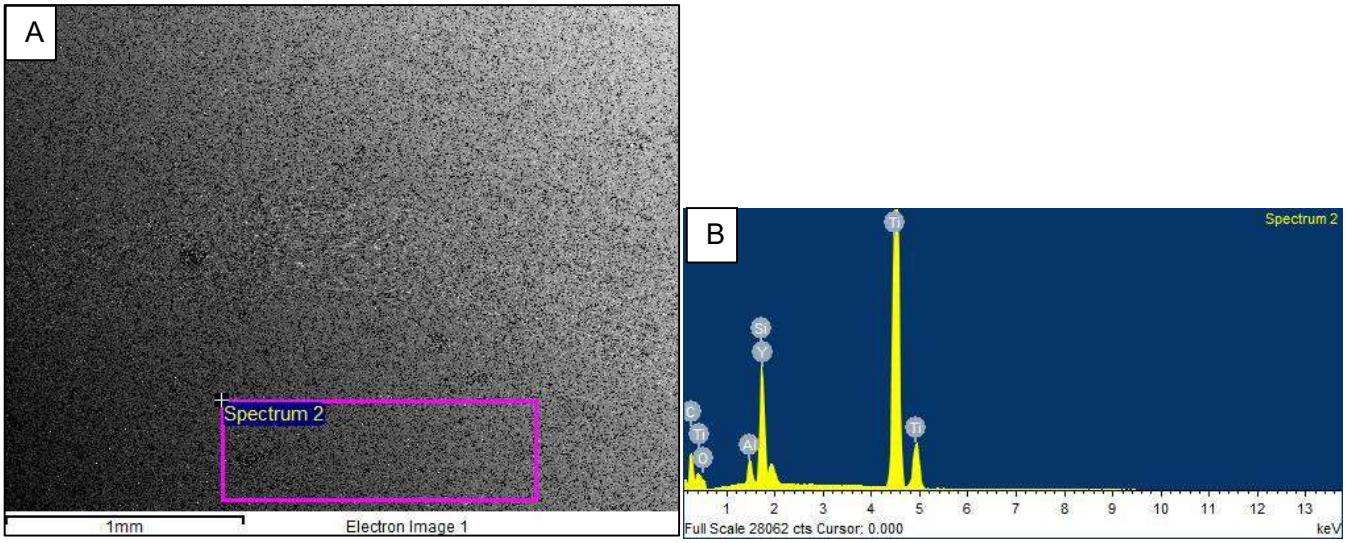


Figure 7.20 A: Spectrum 2 Area alongside the wear track scanned by EDS for composition B: Results of EDS qualitative analysis on Spectrum 2.

Figure 7.20 A Shows the scan area Spectrum 2 which shows the area alongside the wear track which is unaffected by wear giving us a base area for comparison. The results of the scan are as expected with peaks present for Titanium, Carbon, Oxygen, Aluminium, Silicon and Yttrium.

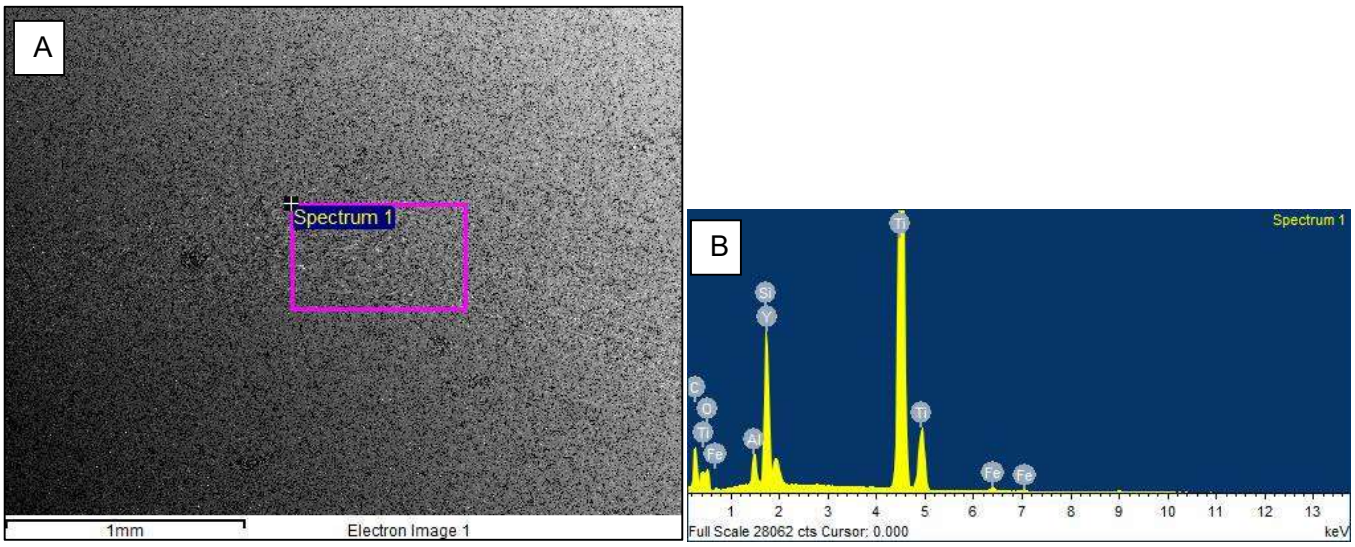


Figure 7.21 A: Spectrum 1 Area on the wear track scanned by EDS for composition B: Results of EDS qualitative analysis on Spectrum 1.

Figure 7.21A Spectrum 1 Area shows a scan area on the wear track. The results of a scan area showed the presence of Iron on the surface which is not present in the scan of the area alongside the wear track. This could be attributed to material from the ball being transferred to the disc during the wear testing.

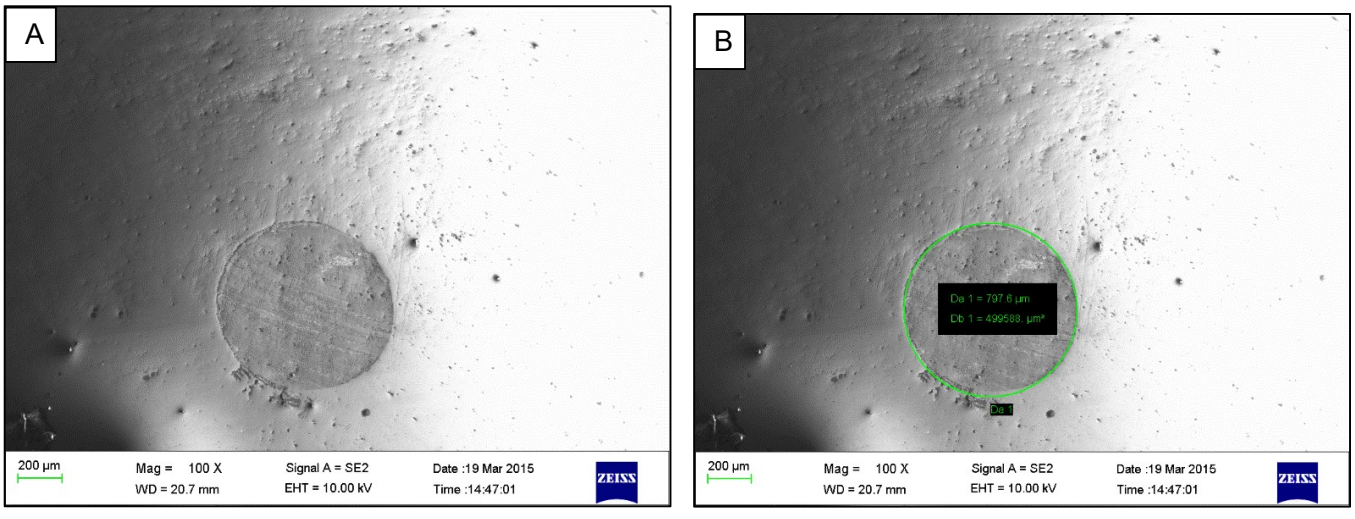


Figure 7.22 A: Wear scar on the surface of the worn AISI 52100 steel ball bearing. B: Diameter and area of the wear scar on the worn AISI 52100 steel ball bearing. (Diameter: 0.798mm and Area: 0.500mm^2)

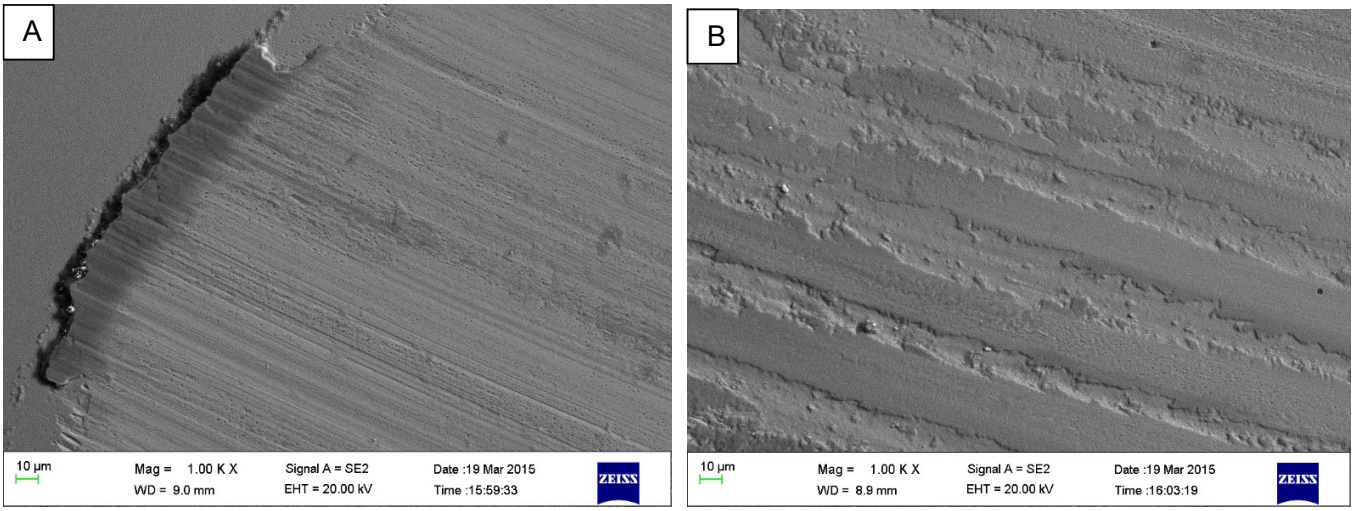


Figure 7.23 A: High magnification image of the edge of the wear scar on the worn AISI 52100 steel ball bearing. B: Higher magnification image of the centre of the wear scar on the worn AISI 52100 steel ball bearing.

Figure 7.23 A showed severe plastic deformation in the direction of the sliding wear. Figure 7.17 B Showed the worn surface of the steel ball bearing. The wear scar shows signs of delamination and to a much lesser degree than the other materials; the presence of a mechanically mixed layer.

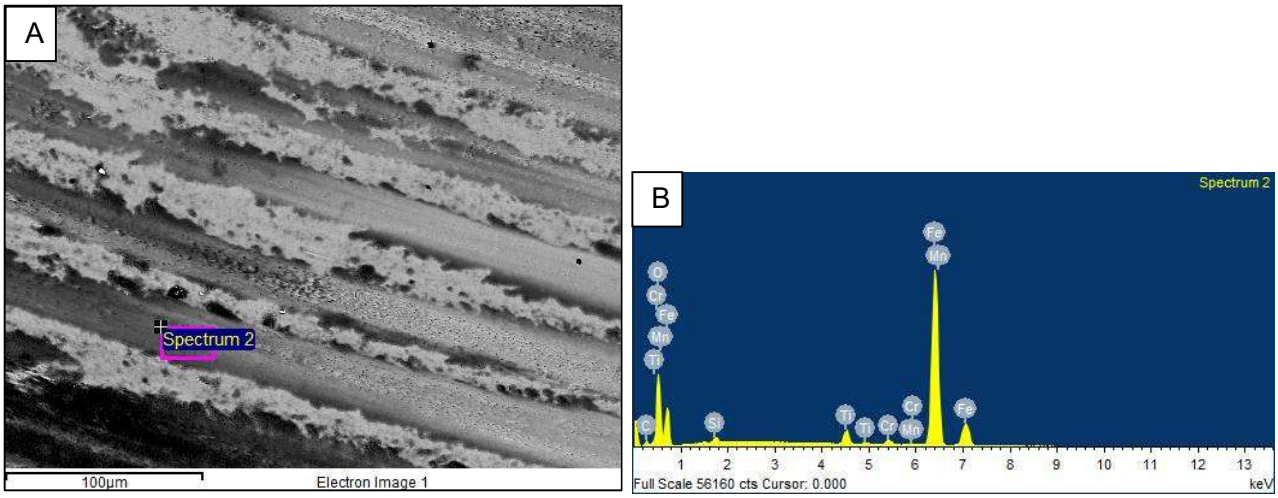


Figure 7.24 A: Spectrum 2 Area inside the wear scar on the worn AISI 52100 steel ball bearing scanned by EDS for composition B: Results of EDS qualitative analysis on Spectrum 2.

Figure 7.24 A shows the EDS scan area which include what is suspected to be smeared delaminated. The EDS analysis confirmed both the ball bearing material and material from the sintered ceramic disc notably Titanium, Oxygen and Silicon.

7.5 78.6TiC-3.5Al_2O_3-5.6Y_2O_3-4.9SiO_2-7.5 (10 vol.%) cBN SPS'd at 1575°C, 70MPa and 5 min hold

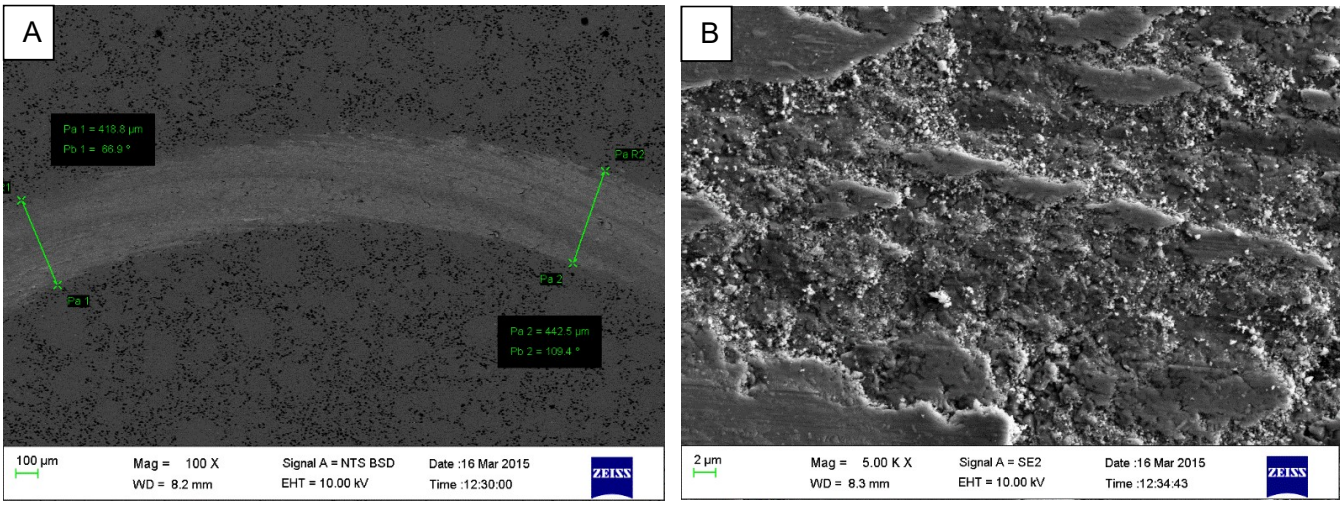


Figure 7.25 A: wear track on the surface of the 78.6TiC-3.5Al_2O_3-5.6Y_2O_3-4.9SiO_2-7.5 (10 vol.%) cBN sample disc SPS'd at 1575°C, 70MPa and 5 min hold . B: High magnification image of the wear track on the 78.6TiC-3.5Al_2O_3-5.6Y_2O_3-4.9SiO_2-7.5 (10 vol.%) cBN sample disc.

Figure 7.25 A the image of the wear track at a lower magnification shows the wear track as well as the measurement of the track left by the ball on the disc. The minimum width of the wear track measured is 418.8µm. Figure 7.25B showed a magnified view of the wear track. A significant difference can be seen between the surface of the the wear track and the unaffected surface. Large sections of delaminated and mechanically mixed materials can also clearly be seen. This could be due to adhesive wear i.e. removal of material from the AISI 52100 steel ball and the removed material; which is now mechanically mixed, adhering on to the sintered TiC + cBN particle reinforced disc.

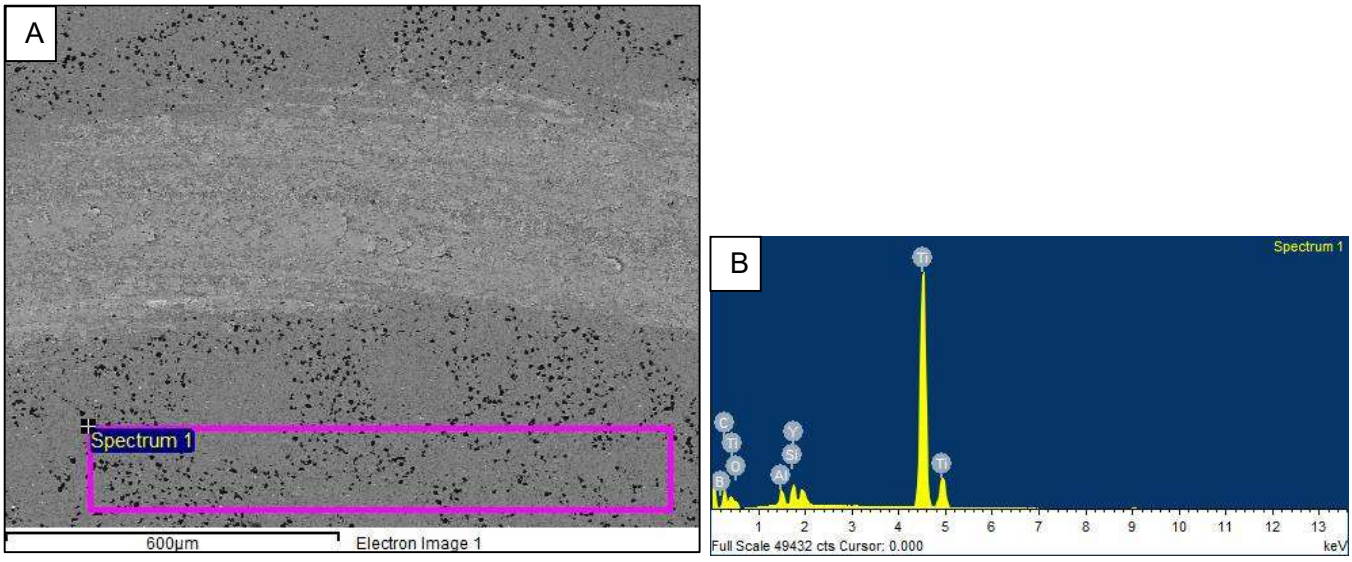


Figure 7.26 A: Spectrum 1 Area alongside the wear track scanned by EDS for composition B: Results of EDS qualitative analysis on Spectrum 1.

Figure 7.26 A Shows the scan area Spectrum 1 which shows the area alongside the wear track which is unaffected by wear giving us a base area for comparison. The results of the scan are as expected with peaks present for Titanium, Boron, Carbon, Oxygen, Aluminium, Silicon and Yttrium.

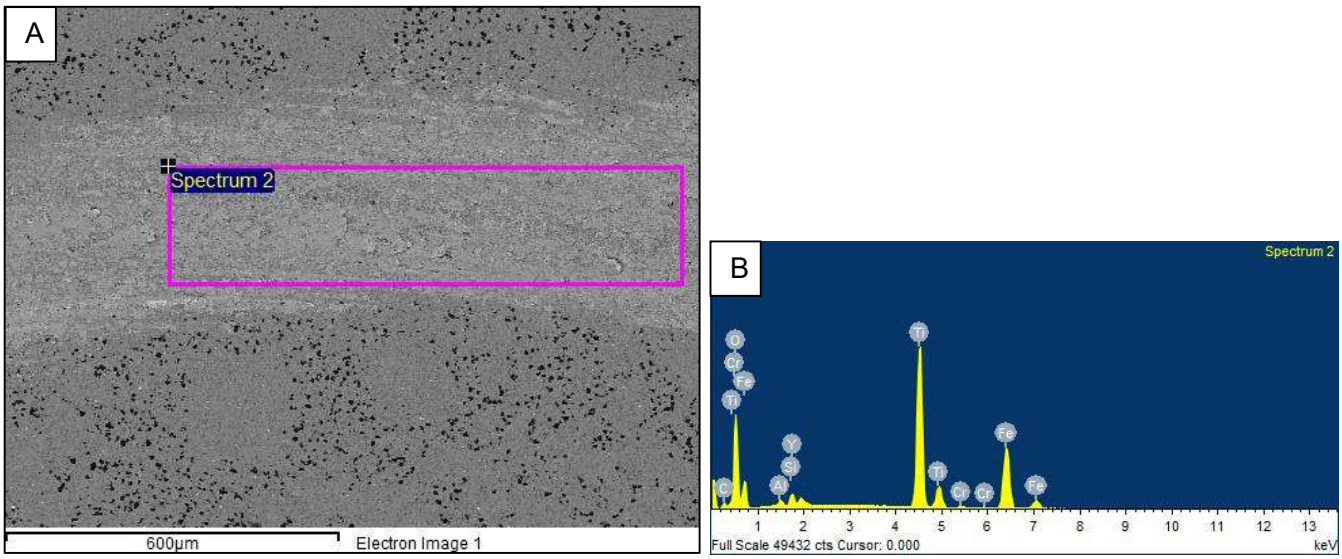


Figure 7.27 A: Spectrum 2 Area on the wear track scanned by EDS for composition B: Results of EDS qualitative analysis on Spectrum 2.

Figure 7.27A Spectrum 2 Area shows a scan area on the wear track. The results of a scan area showed the presence of Iron and Chromium on the surface which is not present in the scan of the area alongside the wear track. This could be attributed to material from the ball being transferred to the disc during the wear testing.

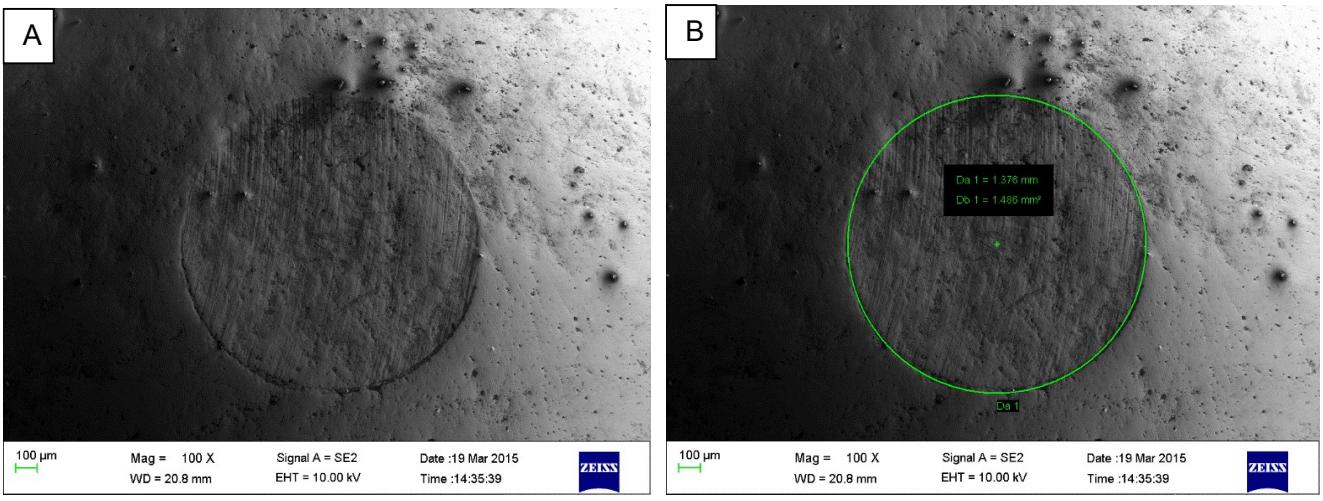


Figure 7.28 A: Wear scar on the surface of the worn AISI 52100 steel ball bearing. B: Diameter and area of the wear scar on the worn AISI 52100 steel ball bearing. (Diameter: 1.376mm and Area: 1.486mm^2)

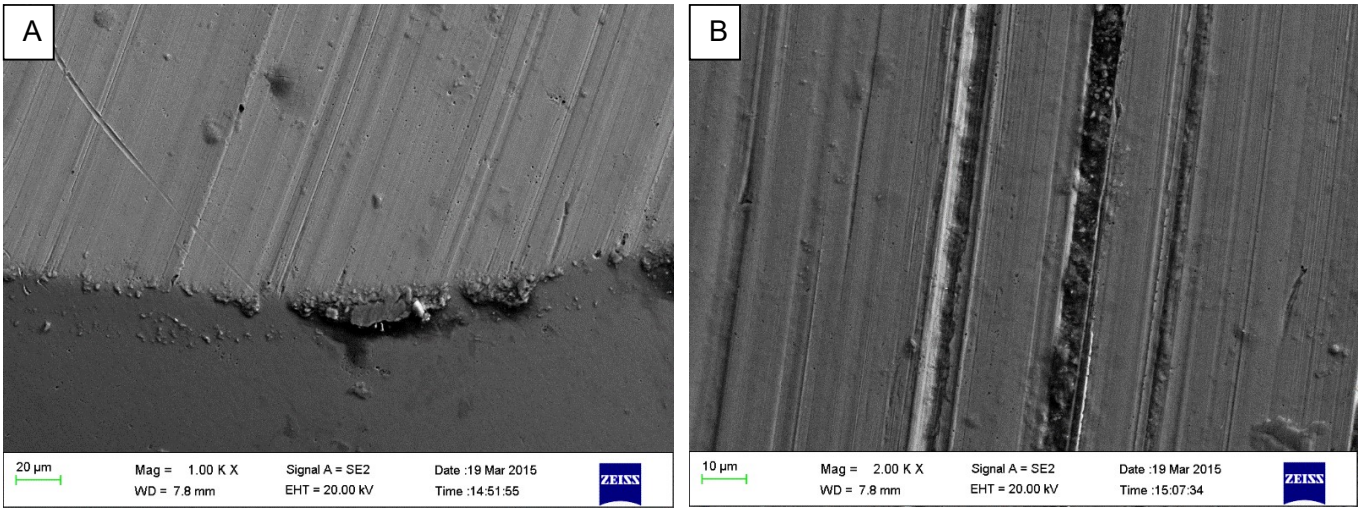


Figure 7.29 A: High magnification image of the edge of the wear scar on the worn AISI 52100 steel ball bearing. B: Higher magnification image of the centre of the wear scar on the worn AISI 52100 steel ball bearing.

Figure 7.29 A showed barely any plastic deformation in the direction of the sliding wear. Figure 7.29 B Showed the worn surface of the steel ball bearing. The wear scar shows signs of significant grooves which are a sign of abrasive wear and the presence of a mechanically mixed layer to a much lesser degree than the other sintered materials.

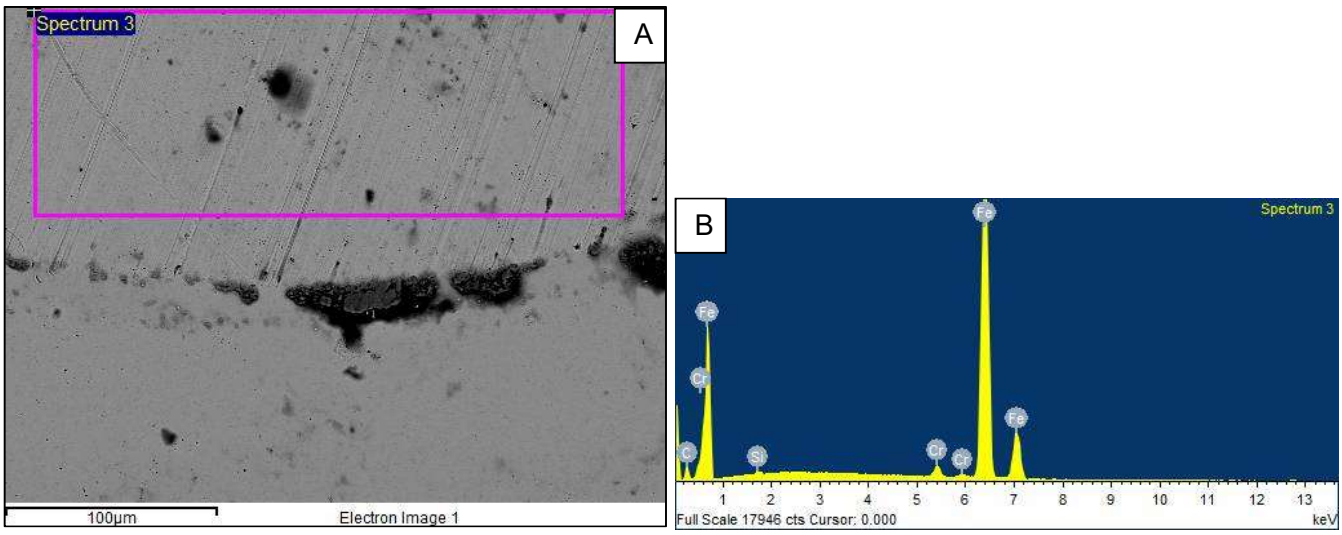


Figure 7.30 A: Spectrum 3 Area inside the wear scar on the worn AISI 52100 steel ball bearing scanned by EDS for composition B: Results of EDS qualitative analysis on Spectrum 3.

Figure 7.30 A shows the EDS scan area which includes the wear scar on the steel ball bearing material. The EDS analysis confirmed that only the ball bearing material and no material from the sintered ceramic disc was present. No Titanium or Boron was found in the scan area analysed.

7.6 77.8TiC-6.9Al_2O_3-1.7Y_2O_3-14 (20 vol.%) SiCw SPS'd at 1625°C, 70MPa and 20 min hold

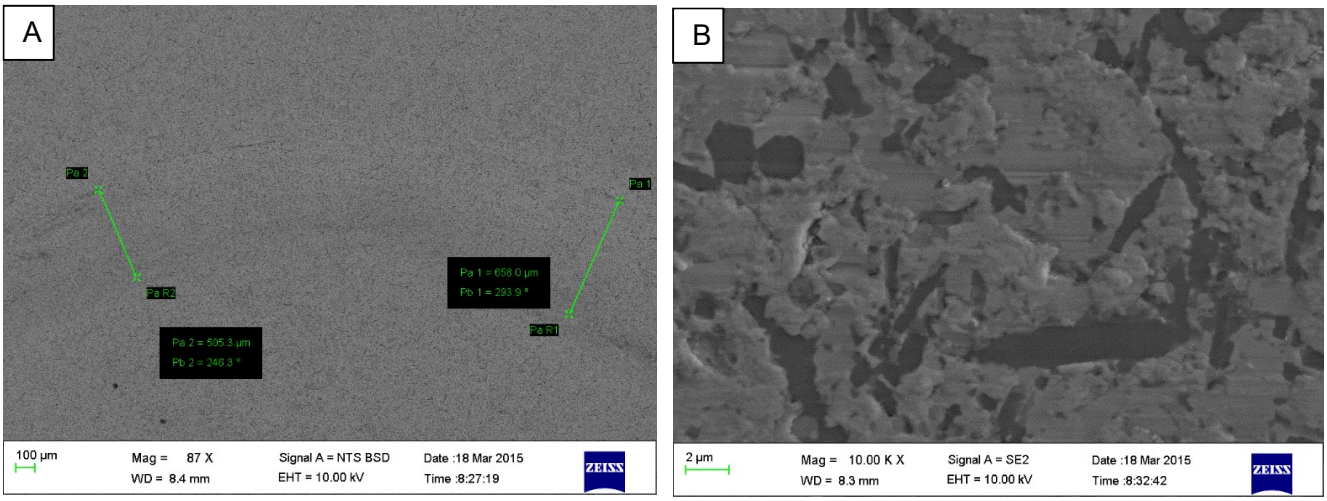


Figure 7.31 A: wear track on the surface of the 77.8TiC-6.9Al_2O_3-1.7Y_2O_3-14(20 vol.%) SiCw sample disc. B: High magnification image of the wear track on the 77.8TiC-6.9Al_2O_3-1.7Y_2O_3-14(20 vol.%) SiCw sample disc.

Figure 7.31 A the image of the wear track at a lower magnification shows the wear track as well as the measurement of the track left by the ball on the disc. The minimum width of the wear track, as measured, is 505.3µm. Figure 7.31 B showed a magnified view of the wear track. A significant difference can be seen between the surface of the the wear track and the unaffected surface.

The presence of grooves and mechanically mixed materials can also clearly be seen. This could be due to adhesive wear i.e. removal of material from the AISI 52100 steel ball and the removed material; which is now mechanically mixed, adhering on to the sintered TiC + SiC whisker reinforced disc. Abrasive wear which is the removal of material is also responsible for the grooves on the surface.

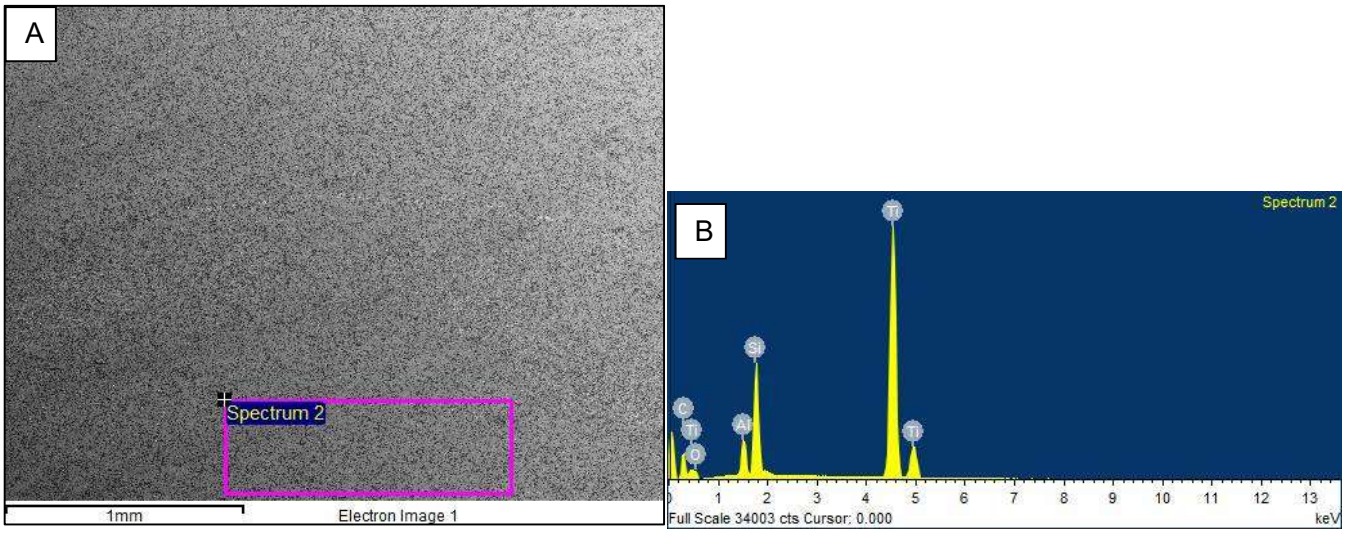


Figure 7.32 A: Spectrum 2 Area alongside the wear track scanned by EDS for composition B: Results of EDS qualitative analysis on Spectrum 2.

Figure 7.32 A Shows the scan area Spectrum 2 which shows the area alongside the wear track which is unaffected by wear giving us a base area for comparison. The results of the scan are as expected with peaks present for Titanium, Carbon, Oxygen, Aluminium and Silicon.

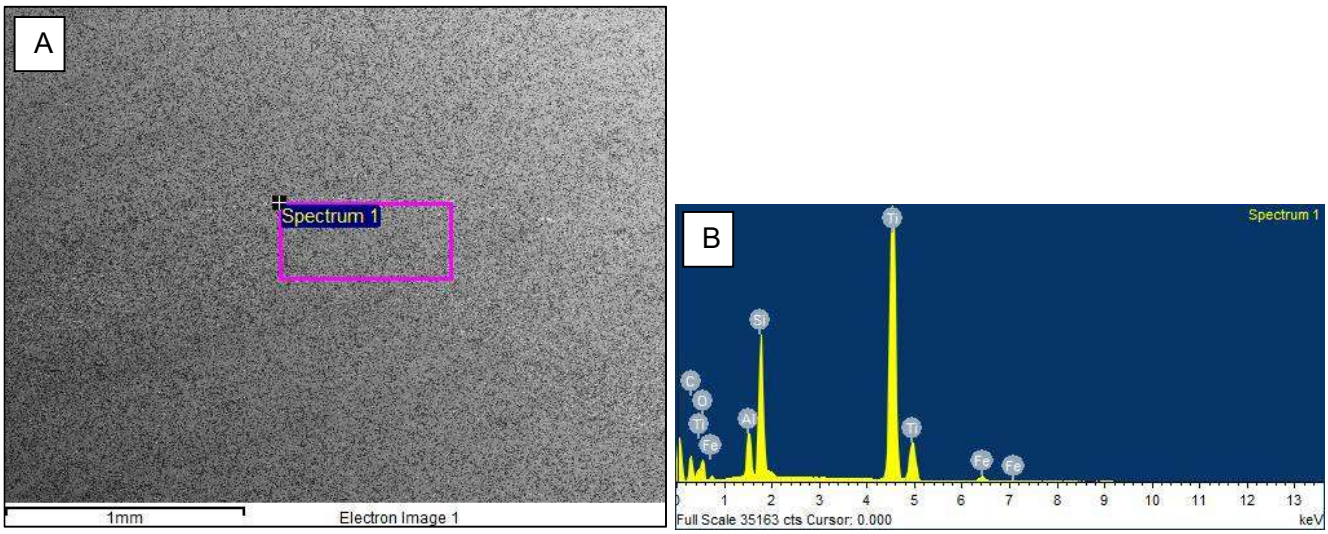


Figure 7.33 A: Spectrum 1 Area on the wear track scanned by EDS for composition B: Results of EDS qualitative analysis on Spectrum 1.

Figure 7.33 A Spectrum 1 Area shows a scan area on the wear track. The results of a scan area showed the presence of Iron on the surface which is not present in the scan of the area alongside the wear track. This could be attributed to material from the ball being transferred to the disc during the wear testing.

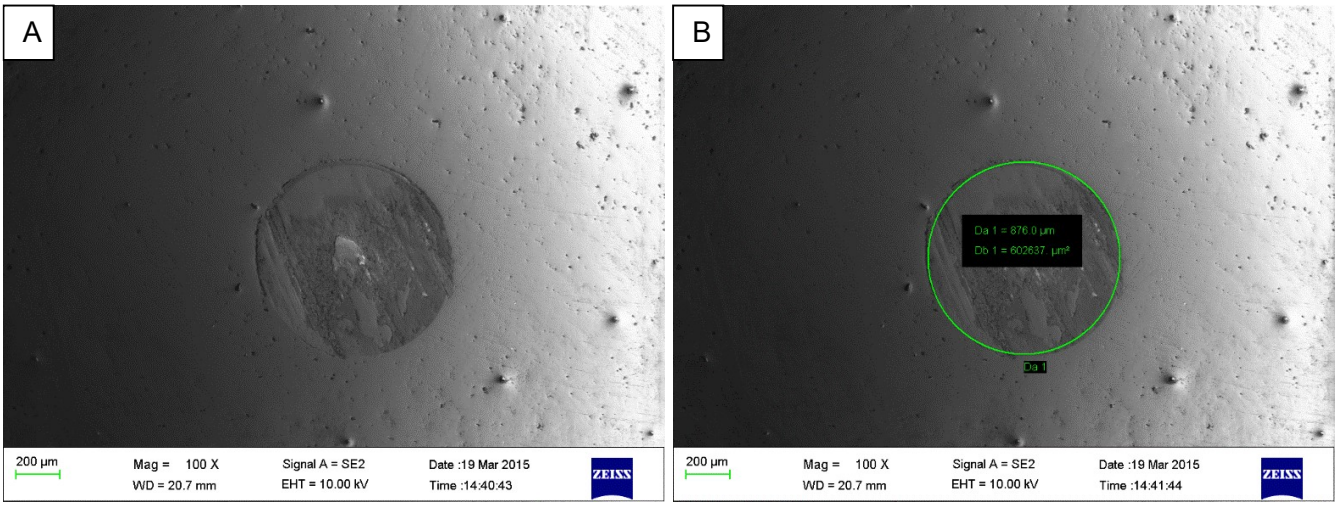


Figure 7.34 A: Wear scar on the surface of the worn AISI 52100 steel ball bearing. B: Diameter and area of the wear scar on the worn AISI 52100 steel ball bearing. (Diameter: 0.876mm and Area: 0.603mm^2)

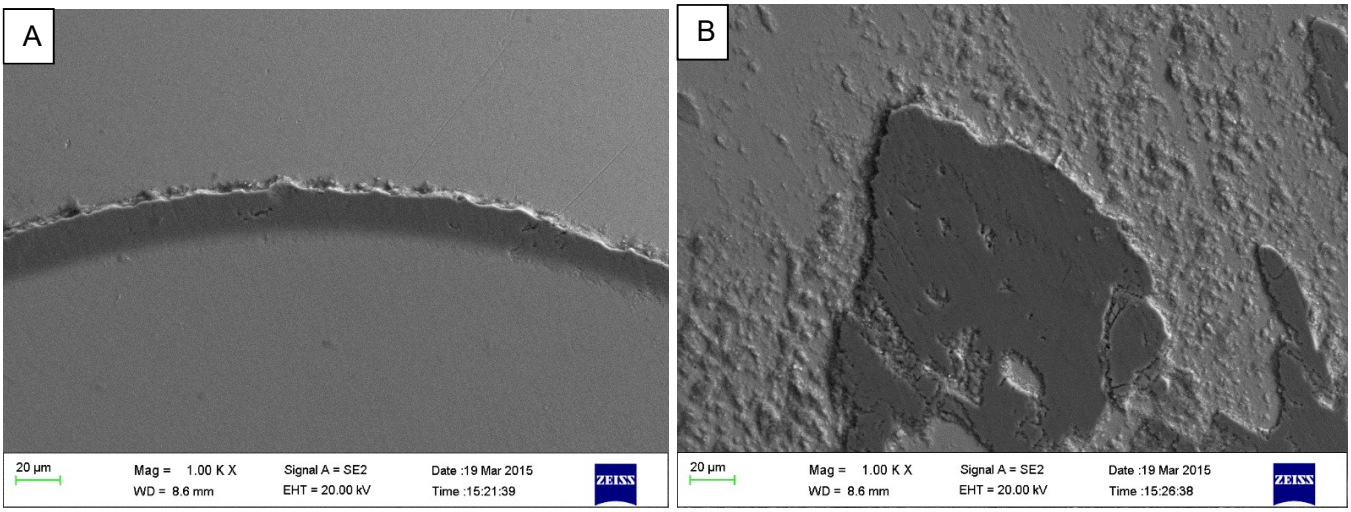


Figure 7.35 A: High magnification image of the edge of the wear scar on the worn AISI 52100 steel ball bearing. B: Higher magnification image of the centre of the wear scar on the worn AISI 52100 steel ball bearing.

Figure 7.35 A showed severe plastic deformation in the direction of the sliding wear. Figure 7.35 B Showed the worn surface of the steel ball bearing. The wear scar shows signs of delamination and the presence of a mechanically mixed layer (Radhika et al., 2018).

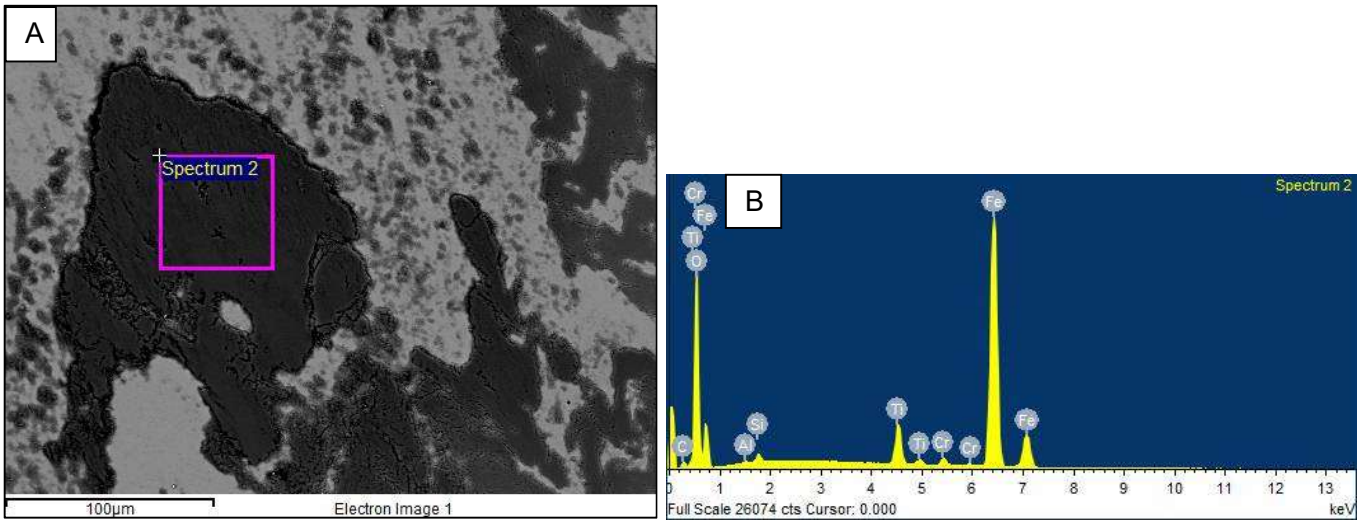


Figure 7.36 A: Spectrum 2 Area inside the wear scar on the worn AISI 52100 steel ball bearing scanned by EDS for composition B: Results of EDS qualitative analysis on Spectrum 2.

Figure 7.36 A shows the EDS scan area which include what is suspected to be a heavy layer of mechanically mixed material. The EDS analysis confirmed both the ball bearing material and material from the sintered ceramic disc notably Titanium, Oxygen, Aluminium and Silicon.

7.7 Mass lost on ball bearing during wear testing

There was a significant difference in hardness between the disc materials and steel balls. The mass lost during wear testing on the softer ball bearing material (in comparison to the TiC ceramic disc with/without reinforcements added) was calculated by determining the spherical cap volume and using the known density of the ball bearings (AISI 52100 steel: 7.81g/cm^3) (Weisstein, n.d.). Details of the formulae used for the calculations are described in Chapter 3.5.4.

Table 7.1 Mass lost on ball bearing during wear testing

Disc material	Spherical cap diameter (mm)	Spherical cap area (mm^2)	Spherical cap volume /volume loss (mm^3)	Mass of Spherical cap/mass loss (g)	Specific wear rate (mm^3/Nm)
85TiC-12Al_2O_3-3Y_2O_3	1.041	0.850	$1.909X10^{-2}$	$1.491X10^{-4}$	$6.363X10^{-6}$
79TiC-11Al_2O_3-3Y_2O_3-7(10 vol.%) SiCw	1.032	0.837	$1.848X10^{-2}$	$1.443X10^{-4}$	$6.160X10^{-6}$
73TiC-10Al_2O_3-3Y_2O_3-14(20 vol.%) SiCw	0.929	0.668	$1.119X10^{-2}$	$0.750X10^{-4}$	$3.730X10^{-6}$
79TiC-4.5Al_2O_3-5.6Y_2O_3-4.9SiO_2-7.1(10 vol.%) SiCw	0.798	0.500	$0.660X10^{-2}$	$0.516X10^{-4}$	$2.200X10^{-6}$
78.6TiC-3.5Al_2O_3-5.6Y_2O_3-4.9SiO_2-7.5 (10 vol.%) cBN	1.376	1.486	$5.800X10^{-2}$	$4.530X10^{-4}$	$19.333X10^{-6}$
77.8TiC-6.9Al_2O_3-1.7Y_2O_3-14(20 vol.%) SiCw	0.876	0.603	$0.960X10^{-2}$	$0.750X10^{-4}$	$3.200X10^{-6}$

Analysis of the mass loss and the specific wear rate of the steel ball bearing show that the composition of the mating surface i.e. the sintered disc material has a huge effect of these factors. The addition of 7 wt. % SiCw to the 85 wt.% TiC + additives matrix (79TiC-11Al_2O_3-3Y_2O_3-7(10 vol.%) SiCw) has a negligible effect on the mass loss and the specific wear rate of the steel ball bearing. Increasing the amount of SiCw from 7 wt.% to 14 wt.% in the 85 wt.% TiC + additives matrix (73TiC-10Al_2O_3-3Y_2O_3-14(20 vol.%) SiCw) reduces the mass loss from $1.443X10^{-4}$g to $0.750X10^{-4}$g. Which is a decrease of 52%. The specific wear rate also decreases drastically from $6.160X10^{-6}$ N.mm^{-3} to $3.730X10^{-6}$ N.mm^{-3}, which is a decrease of 61%.

The addition of SiO_2 to the matrix of the 85 wt.% TiC + additives and 7 wt.% SiCw (79TiC-4.5Al_2O_3-5.6Y_2O_3-4.9SiO_2-7.1(10 vol.%) SiCw) caused a decrease in mass loss from $1.443X10^{-4}$g to $0.516X10^{-4}$g which is a reduction of 36%. The specific wear rate decreased $6.160X10^{-6}$ N.mm^{-3} to $2.200X10^{-6}$ N.mm^{-3} which is a reduction of 36% as well.

The difference between the 85 wt.% + additives with 14 wt.% SiCw (73TiC-10Al_2O_3-3Y_2O_3-14(20 vol.%) SiCw) and 90 wt.% + additives with 14 wt.% SiCw (77.8TiC-6.9Al_2O_3-1.7Y_2O_3-14(20 vol.%) SiCw) has no discernable difference in mass loss and only a negligible decrease from $3.730X10^{-6}$ N.mm^{-3} to $3.200X10^{-6}$ N.mm^{-3} in specific wear rate.

The addition of 7.5 wt.% cBN particles to the 85 wt.% TiC + additives + SiO_2 matrix (78.6TiC-3.5Al_2O_3-5.6Y_2O_3-4.9SiO_2-7.5 (10 vol.%) cBN) has the largest mass loss of material from the steel ball bearing at 4.530X10^{-4}g and the highest specific wear rate at 19.333X10^{-6} N.mm^{-3}. This confirms the results of the SEM analyses on the worn surfaces. The addition of cBN particles changed the wear mode from adhesive to abrasive wear. Which is the more effective mode for material removal.

7.8 Friction and sliding wear results from CSM Tribometer

The friction co-efficient is measured as a function of the sliding distance registered during the wear test for the sintered materials when worn against the steel ball bearing. For most of the samples during the initial stage of testing from 0-100m, the friction coefficient increases steadily until approximately 180m where the co-efficient reaches a steady level. This behaviour could be attributed to a polishing process during the wear testing, where the surface asperities or roughness peaks are removed. This occurs to varying degrees for most of the samples except for sample of composition 66.1 vol.%TiC-11.6 vol.%Al_2O_3-2.3 vol.%Y_2O_3-20 vol.% SiCw and 70.7 vol.%TiC-7.8 vol.%Al_2O_3-1.5 vol.%Y_2O_3-20 vol.% SiCw which contains the highest quantity of SiC whiskers which can delaminate during testing and increase surface roughness.

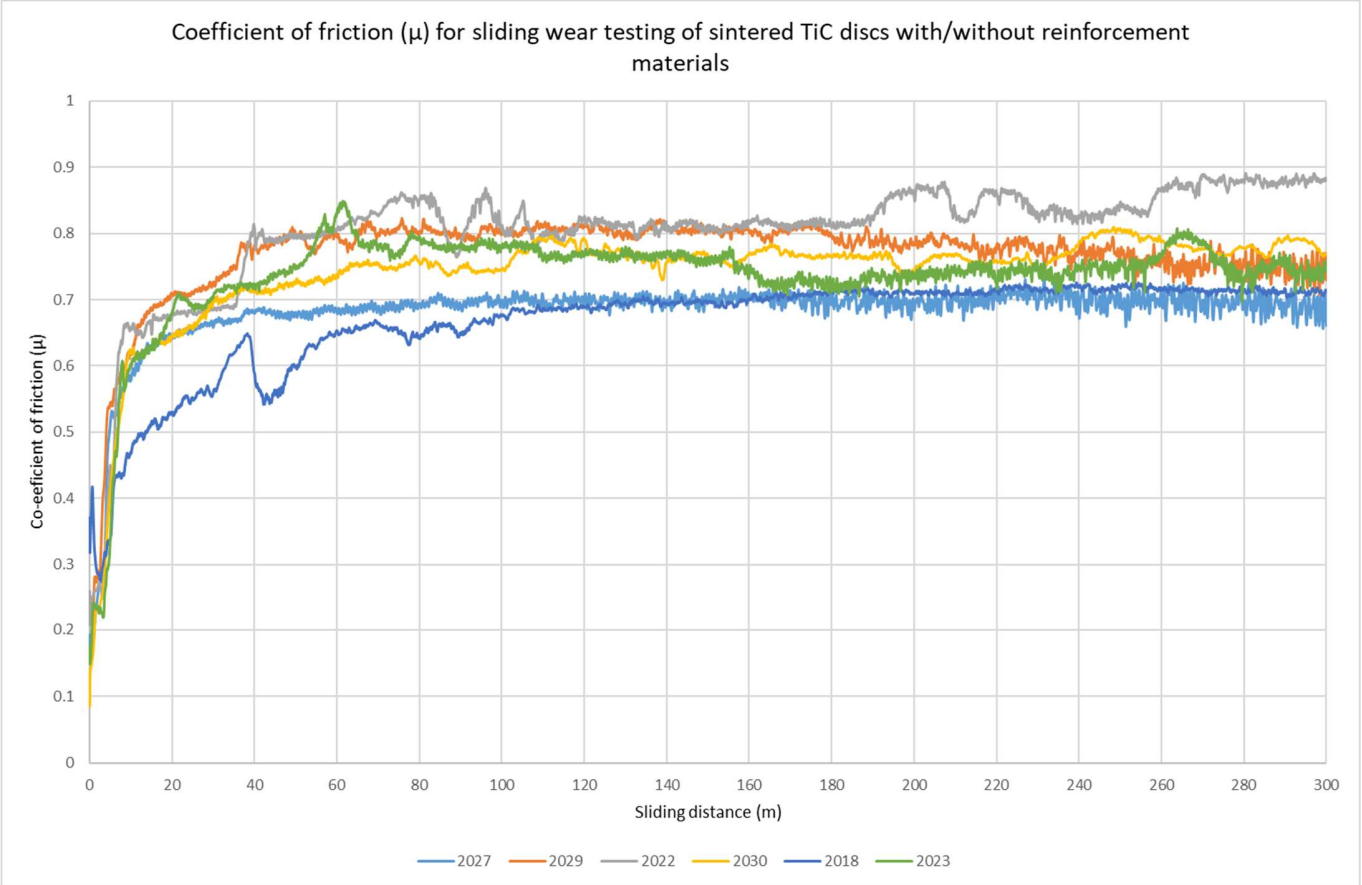


Figure 7.37 Graphs for results given by the CSM Tribometer for the sliding wear tests of the sintered TiC discs with/without reinforcements

Figure 7.37 shows the frictional coefficient as a function of the sliding distance registered during the wear tests of the sintered samples polished to a 1μm surface finish under dry conditions when worn against a AISI 52100 steel ball. Under a normal load of 10N.

Table 7.2 Coefficient of friction (μ) for the sliding wear testing of sintered TiC discs with/without reinforcement materials

Disc material	Start	Minimum	Maximum	Mean	Std. Deviation
85TiC-12Al_2O_3-3Y_2O_3	0.193	0.161	0.732	0.682	0.059
79TiC-11Al_2O_3-3Y_2O_3-7(10 vol.%) SiCw	0.170	0.153	0.823	0.769	0.070
73TiC-10Al_2O_3-3Y_2O_3-14(20 vol.%) SiCw	0.260	0.207	0.891	0.805	0.090
79TiC-4.5Al_2O_3-5.6Y_2O_3-4.9SiO_2-7.1(10 vol.%) SiCw	0.107	0.085	0.810	0.742	0.080
78.6TiC-3.5Al_2O_3-5.6Y_2O_3-4.9SiO_2-7.5 (10 vol.%) cBN	0.371	0.275	0.726	0.660	0.077
77.8TiC-6.9Al_2O_3-1.7Y_2O_3-14(20 vol.%) SiCw	0.175	0.149	0.849	0.737	0.079

The sample 85TiC-12Al_2O_3-3Y_2O_3 has the most stable coefficient of friction with the smallest standard deviation (0.059) due to the lack of reinforcement material. 73TiC-10Al_2O_3-3Y_2O_3-14 (20 vol.%) SiCw sample has the highest co-efficient of friction due to the roughness of the surface caused by the selective removal of the material around the SiC whiskers and the debonding of the whiskers themselves during the sliding wear testing. 78.6TiC-3.5Al_2O_3-5.6Y_2O_3-4.9SiO_2-7.5 (10 vol.%) cBN sample has the lowest mean co-efficient of friction (0.660) which can be explained by the examination of Figure 7.29 A and B which showed abrasive wear related to micro-cutting associated with the addition of cBN hard particles. The increase of SiC whisker content from 7 wt.% (10 vol.%) to 14 wt.% (20 vol.%) had caused an increase in the mean friction co-efficient due to the uneven wear of the contact surface. The addition of SiO_2 appears to have slightly decreased the co-efficient of friction for samples containing the same amount of SiC whiskers as reinforcement material. This might be due to the stronger bonds between the whiskers and the matrix preventing debonding and therefore decreasing surface roughness during the sliding wear tests.

8 CONCLUSIONS AND RECOMMENDATIONS

8.1 CONCLUSIONS

8.1.1 Results of the analysis of the TiC matrices with/without SiO_2

For the 85 wt. % TiC samples with Al_2O_3 and Y_2O_3 as liquid phase sintering aids; the density of the samples with the higher sintering pressures and higher temperatures were the closest to full density. The samples that had higher sintering pressures also had a lower percentage of open porosity than those sintered at the lower pressure. The samples that comprised 85 wt. % TiC and SiO_2 along with the other liquid phase sintering aids showed a different pattern of behaviours from those without SiO_2. Generally, there was a slight increase in density with the increase in sintering temperature but a slight decrease in density with an increase in pressure. The increase in pressure also increases the percentage of open porosity which was most likely due to the evaporation and/or squeezing out of the liquid phase. For the 90 wt. % TiC samples with Al_2O_3 and Y_2O_3 as liquid phase sintering aids; the density of the samples with the higher sintering pressures and higher temperatures were the closest to full density. The samples that were sintered at higher pressures also have a lower percentage of open porosity than those sintered at the lower pressure. The addition of SiO_2 caused a slight reduction in the percentage theoretical density and slight increase in percentage open porosity. At the higher pressure condition (70MPa) the 90TiC-2.5Al_2O_3-4Y_2O_3-3.5SiO_2 (86.9 vol.% TiC-3.01 vol.% Al_2O_3-3.8 vol.% Y_2O_3-6.29 vol.% SiO_2) composition which had less liquid phase sintering aids added was able to achieve higher percentage theoretical density.

Analysis of the hardness and fracture toughness of the sintered TiC matrix compacts with/ without SiO_2 concluded that the sintered sample with the highest Vickers hardness was found to be 90TiC-8Al_2O_3-2Y_2O_3 (88.28 vol.%TiC-9.79 vol.% Al_2O_3-1.93 vol.% Y_2O_3) SPS sintered at 1625°C, 70MPa and the sintered sample with the highest fracture toughness was determined to be 85TiC-12Al_2O_3-3Y_2O_3 (82.6 vol.%TiC-14.6 vol.% Al_2O_3-2.9 vol.% Y_2O_3) SPS sintered at 1625°C, 50MPa. From the XRD results it could be observed that the sintered material with the highest fracture toughness had formed YAP instead of YAG during SPS sintering. The addition of SiO_2 to the liquid phase of the 85-90 wt. % TiC reduced the hardness significantly and fracture toughness in both compositions to which it has been added regardless of the sintering parameters. This could be the result of the formation of large YAG grains which are weaker than the TiC grains and lower the mechanical properties of the sintered material. Also the presence of yttrium-aluminosilicate glass ($Y_2Si_2O_7$) which acted as a path of least resistance for cracks paths in the sintered material would also have lowered the fracture toughness of the material

8.1.2 Results of the analysis of the TiC Matrices with/without SiO_2 and the addition of SiC whiskers and cBN respectively

For the 85 wt.% TiC matrix composition there was a marked decrease in the density of the samples with the addition of 10 vol. % (7 wt. %) SiCw when compared with samples without the SiCw when sintered under the equivalent sintering temperature pressure and hold time. The decrease in density was due to the whiskers preventing the close packing of the matrix materials. By increasing the sintering temperature and pressure, the negative effects of the SiCw on the densification of the sample during sintering had been eliminated. The 85wt.%TiC powder mix with the addition of a higher volume of SiCw (20 vol. %/ 14 wt. %), resulted in a sintered sample with a dramatic drop in percentage theoretical density. The percentage open porosity also increased. At the higher sintering temperature (1610°C and 1600°C for the unreinforced and reinforced sintered samples respectively) and pressure of 70MPa, resulted in the percentage of theoretical density that were very similar for the unreinforced sintered material and the SiCw reinforced sintered materials.

Samples with the 14 wt. % SiCw reinforcement when then sintered for longer hold times in order to increase the densification by allowing more time for the sintering to reach completion but the extension of the sintering time resulted in a decrease of the relative density probably due to the evaporation of the liquid.

The 90 wt. % TiC samples with Al_2O_3 and Y_2O_3 as liquid phase sintering aids have densities between 88.81-98.57 percent of theoretical density. The density of the samples with the higher sintering pressures and higher temperatures are the closest to full density. The samples that have higher sintering pressures also have a lower percentage of open porosity than those sintered at the lower pressure. There is a noticeable decrease in the density of the samples with the addition of 10 vol.% (7 wt.%) SiCw when compared with the sample without the SiCw when sintered under the same sintering pressure, temperature and hold time. Similarly, with an increase in SiCw content from 10 vol.% (7 wt.%) to 20 vol.% (14 wt.%), the percentage of theoretical density decreased from 84.91 to 82.65 % and the percentage of open porosity increased 10.70 to 16.50%. To further increase the percentage of theoretical density of the 20 vol.% (14 wt.%) SiCw; the sintering hold time was increased from 10 min to 20 min resulting in an increase percentage theoretical density from 82.65% to 92.43% and a decrease in open porosity from 16.50% to 5.73%. Increasing the hold time during sintering had the equivalent effect to sintering at a higher temperature (1625°C) at the same pressure (70MPa).

The addition of 7 vol.% (5 wt.%) cBN to the 85 wt.% TiC matrix (without the addition of SiO_2) caused a significant decrease in the percentage of theoretical density at the same sintering pressure and temperature. Shorter hold times were used to prevent the conversion of cBN to hBN although this may have also contributed to the decrease in the density attained. Increasing the cBN content from 7 vol.% (5 wt.%) to 10 vol. % (7.4 wt.%) resulted in a drastic decrease in the percentage of theoretical density in the 85 wt.% TiC matrix.

The addition of cBN to a matrix containing 15 wt.% liquid phase sintering aids of which 11 wt.% was Al_2O_3 could cause a lowering in the densification rate as cBN has a suppressive effect on the grain boundary migration of Al_2O_3 during sintering. With the addition of SiO_2 of 85 wt. % TiC matrix changes the rate of densification. The addition of cBN in SPS sintered ceramic matrix composites usually decreased the relative density at equivalent pressures; but the addition of SiO_2 to the Al_2O_3-Y_2O_3 liquid phase sintering aids in the 85wt.% TiC matrix increased the densification rate possibly due to the formation $Y_2Si_2O_7$ as seen in Table 5.14.

The addition of 7 vol.% (5 wt.%) cBN to the 90 wt.% TiC matrix caused a significant decrease in the percentage in the percentage of theoretical density at the same sintering pressure and temperature. Shorter hold times were used to prevent the conversion of cBN to hBN. Increasing the cBN content from 7 vol.% (5 wt.%) to 10 vol. % (7.4 wt.%) resulted in a substantial decrease in the percentage of theoretical density in the 90 wt.% TiC matrix**.** At temperatures below 1575°C, pressures below 70 MPa and a hold time of less than 10 min during sintering was considered to be incomplete. With the addition of SiO_2 of 90 wt. % TiC matrix changes the rate of densification. The addition of cBN in SPS sintered ceramic matrix composites usually decreased the relative density at equivalent pressures; but the addition of SiO_2 to the Al_2O_3-Y_2O_3 liquid phase sintering aids in the 90wt.% TiC matrix had increased the densification rate possibly due to the formation of $Y_2Si_2O_7$. The addition of cBN in SPS sintered ceramic matrix composites usually decreased the relative density at equivalent pressures; but the addition of SiO_2 to the Al_2O_3-Y_2O_3 liquid phase sintering aids in the 90wt.% TiC matrix had increased the densification rate possibly due to the formation of YAG-$Y_3Al_5O_{12}$ as seen in Table 5.15.

In hot pressed SiC-whisker reinforced composites, the whiskers exhibit a preferred orientation as the longitudinal axes of the whiskers attempt to align perpendicularly to the hot pressing axis (Farkash et al., 1994). From the analysis of the microstructures of the SPS'd samples it can be noted that a similar preferred orientation has occurred in the whisker reinforced TiC composites. The anisotropy was taken into consideration when analyzing the fracture toughness by giving values for the cracks caused by the Vickers indentations that run both parallel and perpendicular to the pressing direction.

The addition of SiO_2 to the liquid phase of the 85 wt. % TiC matrices reduced the hardness significantly and fracture toughness in compositions with and without SiCw to which it had been added regardless of the sintering parameters. This could be the result of the formation of large YAG grains which are weaker than the TiC grains and lower the mechanical properties of the sintered material. Also the presence of yttrium aluminosilicate glass ($Y_2Si_2O_7$) which acts as a path of least resistance for cracks paths in the sintered material would also lower the fracture toughness of the material

Similarly, to the 85 wt.% TiC matrices the addition of SiO_2 to the liquid phase of the 90 wt. % TiC matrices reduced the hardness significantly and fracture toughness in compositions with and without SiCw to which it had been added regardless of the sintering parameters. This could be the result of the formation of large YAG grains which are weaker than the TiC grains and lower the mechanical properties of the sintered material.

The Vickers hardness and fracture toughness of 72.7 vol.% TiC-4.0 vol.% Al_2O_3-5.0 vol.% Y_2O_3-8.3 vol.% SiO_2-10 vol. % cBN sintered at 1575°C, 70MPa and a hold time of either 5 min or 10 min hold. The temperature was set at 1575°C as any temperature above this would have resulted in the conversion of cBN to hBN at this sintering pressure. (Will et al., 2000) The change in hold time caused a negligible difference in the Vickers hardness which was unexpected as there was a significant difference in the percentage theoretical density between the two, with density being 96.45% (5 min hold) and 85.43% (10 min hold) respectively. There was however a negligible difference in the fracture toughness. Parallel to the pressing direction the was no significant change in the fracture toughness and perpendicular to the pressing direction there was no real change in fracture toughness. From the XRD analysis we could see that the shorter hold time had resulted in the production of YAG and YAP which were not present in the samples sintered with the longer hold time which had TiB_2 and $Y_2Al_3Si_2$ as reaction products instead.

The Vickers hardness and fracture toughness of 78.2 vol.% TiC-2.7 vol.% Al_2O_3-3.4 vol.% Y_2O_3-5.7 vol.% SiO_2-10 vol.% cBN sintered at 1575°C, 70MPa and a hold time of either 5 min or 10 min hold. The change in hold time caused a large difference in the Vickers hardness with increasing hold time during sintering which was expected as there was a slight difference in the percentage theoretical density between the two, with density being 89.46% (5 min hold) and 91.50% (10 min hold) respectively. There was however a negligible difference in the fracture toughness. Parallel to the pressing direction although there was no significant change in the fracture toughness. Perpendicular to the pressing direction there was also no real change in fracture toughness. From the XRD analysis we could see that both of the hold times had resulted in the production of TiB_2, YAG and YAP. Neither $Y_2Si_2O_7$ nor $Y_2Al_3Si_2$ were detected in sample of either sintering hold condition.

8.1.3 Results of the analysis of the biaxial strength tests of sintered TiC samples with the best combination of density and fracture toughness.

The addition of 10 vol.% SiC whiskers to the unreinforced matrix samples with 85 wt.% TiC without the addition of SiO_2 to the liquid phase sintering aids (79TiC+11Al_2O_3-3Y_2O_3-7 (10 vol.%) SiCw) (74.6 vol.%TiC-13.1 vol.%Al_2O_3-2.6 vol.%Y_2O_3-10 vol.% SiCw) resulted in an increase in the ultimate stress at fracture and the Weibull moduli. These values are significantly higher than without the SiC whisker reinforcement. Further increase in the SiC whisker content to 20 vol.% (73TiC-10Al_2O_3-3Y_2O_3-14 (20 vol.%) SiCw) (66.1 vol.% TiC-11.6 vol.% Al_2O_3-2.3 vol.% Y_2O_3-20 vol.% SiCw) results in only a slight decrease in ultimate fracture strength and a slight increase in Weibull moduli possibly due to the more uniform distribution of whiskers throughout the matrix. However, the addition of SiO_2 to the matrix in addition the presence of 10 vol.% SiC whiskers (78.96TiC-3.48Al_2O_3-5.57Y_2O_3-4.48SiO_2-7.11 (10 vol.%) SiC_w) (76 vol.% TiC-4.0 vol.% Al_2O_3-5.0 vol.% Y_2O_3-5.0 vol.% SiO_2-10 vol.% SiCw) resulted in a decrease in the ultimate fracture while the Weibull moduli only underwent a slight increase. This result could have been due to the increased bonding strength at the interface between the fibres and the matrix as SiO_2 is known to form glassy phases at the interface.

Thus preventing fibre debonding or crack deflection which can slow crack propagation and absorb crack energy leading to fracture at lower stresses. The slight increase in reliability is due to the material behaving more homogeneously as the SiC whisker reinforcement behaves more like a part of the matrix and less like sites of potential flaws. When 10 vol.% cBN is added to the 85 wt.% TiC matrix with the addition of SiO_2 (78.70TiC-11.11Al_2O_3-2.79Y_2O_3-7.41 (10 vol.%) cBN) (72.7 vol.% TiC-4.0 vol.% Al_2O_3-5.0 vol.% Y_2O_3-8.3 vol.% SiO_2-10 vol.% cBN) there was a significant increase in the ultimate fracture strength and the Weibull moduli. Even compared to the equivalent volume fraction of SiC whisker reinforcement the fracture strength is lower but also had a large increase in the Weibull moduli. The increase in TiC content in the matrix from 85 wt.% to 90 wt.%, with 20 vol.% SiC whiskers and without the addition of SiO_2 as a liquid phase sintering aid (77.79TiC-6.86Al_2O_3-1.72Y_2O_3-14.24 (20 vol.%) SiCw) (70.7 vol.% TiC-7.8 vol.% Al_2O_3-1.5 vol.% Y_2O_3-20 vol.% SiCw); we find had the greatest ultimate fracture strength of 152.67 GPa and a Weibull modulus of 26.973 which is significantly higher than any unreinforced engineering ceramics but similar to other ceramic matrix composites especially those reinforced with ceramic fibres.

8.1.4 Results of the analysis of the friction and sliding wear tests of sintered TiC samples with the best combination of density and fracture toughness.

Investigation into the wear mode of the sintered TiC discs with and without reinforcements with a hardened AISI 52100 steel bearing as a counter showed that the general modes of wear for the discs was adhesion, a combination of adhesion and abrasion and abrasion. SEM micrographs as well as EDS analysis confirm the particular wear modes present. 78.6TiC-3.5Al_2O_3-5.6Y_2O_3-4.9SiO_2-7.5 (10 vol.%) cBN (72.7 vol.% TiC-4.0 vol.% Al_2O_3-5.0 vol.% Y_2O_3-8.3 vol.% SiO_2-10 vol.% cBN) was the only sintered sample that caused abrasive wear only with no adhesive wear visible at all. A comparison of the AISI 52100 steel bearings worn with the sintered TiC discs of various compositions show that the 78.6TiC-3.5Al_2O_3-5.6Y_2O_3-4.9SiO_2-7.5 (10 vol.%) cBN (72.7 vol.% TiC-4.0 vol.% Al_2O_3-5.0 vol.% Y_2O_3-8.3 vol.% SiO_2-10 vol.% cBN) caused a significantly larger removal of material from the steel ball bearing (4.530X10^{-4}g) as well as the highest specific wear rate (19.333X10^{-6} mm^3/Nm) for material removal. The friction co-efficient is measured as a function of the sliding distance registered during the wear test for the sintered materials when worn against the steel ball bearing. The mean co-efficient of friction μ was highest in the specimens with the lowest amount of the liquid sintering aids. Also the mean co-efficient of friction was higher in specimens containing the reinforcement material i.e. higher volume fraction of SiC whiskers the higher the frictional co-efficient which may be due to the maintaining surface roughness seen during the duration of the test instead of reducing as it does in unreinforced specimens. The debonding and subsequent delamination of the SiC whiskers also add to the continued roughness of the surface. The specimen containing cBN had a lower co-efficient of friction with very little deviation after the initial run in period.

Thus out of all the compositions tested the 78.6TiC-3.5Al_2O_3-5.6Y_2O_3-4.9SiO_2-7.5 (10 vol.%) cBN (72.7 vol.% TiC-4.0 vol.% Al_2O_3-5.0 vol.% Y_2O_3-8.3 vol.%SiO_2-10 vol.% cBN) removed the most material and had the lowest frictional coefficient making it the better of the materials created for the purpose of use as a cutting blade.

8.2 RECOMMENDATIONS

During testing certain parameters had to be fixed due to the nature of the materials interactions and the limitations of the sintering equipment. It would be our hope that for further research the following actions could be considered:

- Coating the SiC whiskers with boron nitride to decrease the matrix-fibre bonding and increase fracture toughness by encouraging debonding instead of bridging as a major mode of crack growth
- Decreasing the matrix-fibre bond would also allow for higher temperatures to be used in samples containing SiC whiskers (but no cBN) which could result in higher densities
- The SPS sintering machine used graphite dies which limited our sintering pressure due to their fragile nature. In future testing it may be wise to consider other materials and/or designs for the dies which increase the capability of the machine to over 100 MPa.
- Increasing the sintering pressure would allow for superior densification which opens up the option of increasing the volume of SiC whiskers added up to 30 vol.% which could significantly increase fracture toughness as well
- The sintering pressure could also affect the density of cBN reinforced matrices and allow for the possible inclusion of higher volume fractions of cBN
- With the improvement in densification we could also consider decreasing the volume of liquid phase sintering aids which were found to reduce hardness properties in the sintered material

BIBLIOGRAPHY

ALEMDAĞ1*, Y., PÜRÇEK1, G., & BEDER2, M. (2015). EFFECT OF AGE HARDENING ON THE WEAR BEHAVIOUR OF THE Al-7Si-4Zn-3Cu ALLOY. *1rst International Conference on Tribology (TURKEYTRIB'2015)*, 6.

Aluminum Oxide | Al2O3 Material Properties. (n.d.). Retrieved 16 December 2021, from https://accuratus.com/alumox.html

ASTM B962—15 Standard Test Methods for Density of Compacted or Sintered Powder Metallurgy (PM) Products Using Archimedes' Principle. (2015). In *ASTM Volume 02.05 Metallic and Inorganic Coatings; Metal Powders and Metal Powder Products* (p. 7). ASTM International. http://www.astm.org/cgi-bin/resolver.cgi?B962

Axén, N., Hogmark, S., & Jacobson, S. (2001). *13.1 The Importance of Testing in Tribology*.

Becher, P. F., Hsueh, C.-H., & Waters, S. B. (1995). Thermal expansion anisotropy in hot-pressed SiC-whisker-reinforced alumina composites. *Materials Science and Engineering: A*, *196*(1–2), 249–251. https://doi.org/10.1016/0921-5093(94)09687-2

Becher, P., & Hsueh, C. (1989). Theoretical and experimental analysis of the toughening behavior of whisker reinforcement in ceramic matrix composites. *Materials Science and …*, *107*, 257–259.

Bengisu, M., Inal, O., & Tosyali, O. (1991). On whisker toughening in ceramic materials. *Acta Metallurgica et Materialia*, *39*(11).

Benko, E., Barr, T. L., Hardcastle, S., Hoppe, E., Bernasik, a, & Morgiel, J. (2001). XPS study of the cBN–TiC system. *Ceramics International*, *27*(6), 637–643. https://doi.org/10.1016/S0272-8842(01)00011-6

Benko, E., Klimczyk, P., Morgiel, J., Włochowicz, a., & Barr, T. L. (2003). Electron microscopy investigations of the cBN–Ti compound composites. *Materials Chemistry and Physics*, *81*(2–3), 336–340. https://doi.org/10.1016/S0254-0584(03)00016-6

Benko, E., Stanisław, J., & Królicka, B. (1999). cBN–TiN, cBN–TiC composites: Chemical equilibria, microstructure and hardness mechanical investigations. *Diamond and Related …*, *8*, 1838–1846.

Bergs, T., Ohlert, M., Prinz, S., & Barth, S. (2020). Modeling of the Fracture Behavior of CBN Grains during Single Grain Dressing using FEM. *Procedia CIRP*, *93*, 1514–1519. https://doi.org/10.1016/J.PROCIR.2020.03.021

Bertram, B., & Gerhardt, R. (2011). Properties and Applications of Ceramic Composites Containing Silicon Carbide Whiskers. *Properties and Applications of Silicon …*, 197–230.

Börger, A., Supancic, P., & Danzer, R. (2002). The ball on three balls test for strength testing of brittle discs: Stress distribution in the disc. *Journal of the European Ceramic Society*, *22*(9–10), 1425–1436. https://doi.org/10.1016/S0955-2219(01)00458-7

Boron nitride | Sciencelearn Hub. (n.d.). Retrieved 9 April 2014, from http://www.sciencelearn.org.nz/Contexts/Ceramics/Sci-Media/Images/Boron-nitride

Boron Nitride (BN)—Properties and Information on Boron Nitride. (2001). http://www.azom.com/article.aspx?articleID=78

Carter, D. H., & Hurley, G. F. (1987). Crack Deflection as a Toughening Mechanism in SiC-Whisker-Reinforced MoSi2. *Journal of the American Ceramic Society*, *70*(4), C-79-C–81. https://doi.org/10.1111/j.1151-2916.1987.tb04992.x

Caslavsky, J. L., & Viechnicki, D. J. (1980). Melting behaviour and metastability of yttrium aluminium garnet (YAG) and YAlO3 determined by optical differential thermal analysis. *Journal of Materials Science*, *15*(7), 1709–1718. https://doi.org/10.1007/BF00550589

Chae, K., & Kim, D. (1993). Effect of Y2O3 additions on the densification of an Al2O3–TiC composite. *Journal of the American …*, *76*(195059), 1–4.

Chae, K., Kim, D., & Niihara, K. (1995). Sintering of Al2O3–TiC composite in the presence of liquid phase. *Journal of the American Ceramic …*, *78*(1), 257–259.

Chawla, K., & Meyers, M. (1999). *Mechanical behavior of materials*.

Chen, J., Li, W., & Jiang, W. (2009). Characterization of sintered TiC–SiC composites. *Ceramics International*, *35*(8), 3125–3129. https://doi.org/10.1016/j.ceramint.2009.04.022

Cheng, L., Xie, Z., & Liu, G. (2013). Spark plasma sintering of TiC ceramic with tungsten carbide as a sintering additive. *Journal of the European Ceramic Society*, *33*(15–16), 2971–2977. https://doi.org/10.1016/j.jeurceramsoc.2013.04.017

Cheng, L., Xie, Z., Liu, G., Liu, W., & Xue, W. (2012). Densification and mechanical properties of TiC by SPS-effects of holding time, sintering temperature and pressure condition. *Journal of the European Ceramic Society*, *32*(12), 3399–3406. https://doi.org/10.1016/j.jeurceramsoc.2012.04.017

Czichos, H., Becker, S., & Lexow, J. (1989). International multilaboratory sliding wear tests with ceramics and steel. *Wear*, *135*(1), 171–191. https://doi.org/10.1016/0043-1648(89)90104-X

Danzer, R., Lube, T., Supancic, P., & Damani, R. (2008). Fracture of Ceramics. *Advanced Engineering Materials*, *10*(4), 275–298. https://doi.org/10.1002/adem.200700347

Diouf, S., & Molinari, A. (2012). Densification mechanisms in spark plasma sintering: Effect of particle size and pressure. *Powder Technology*, *221*, 220–227. https://doi.org/10.1016/J.POWTEC.2012.01.005

Dolgopolsky, A., Karbhari, V., & Kwak, S. S. (1989). Microcrack induced toughening—An interaction model. *Acta Metallurgica*, *37*(5), 1349–1354. https://doi.org/10.1016/0001-6160(89)90165-X

Dusza, J., Šajgalik, P., & Bastl, Z. (1992). Properties of β-silicon nitride whiskers. *Journal of Materials …*, *11*, 2–5.

Evans, A. G., & Charles, E. A. (1976). Fracture Toughness Determinations by Indentation. *Journal of the American Ceramic Society*, *59*(7–8), 371–372. https://doi.org/10.1111/j.1151-2916.1976.tb10991.x

Evans, A. G., & Faber, K. T. (1984). Crack-Growth Resistance of Microcracking Brittle Materials. *Journal of the American Ceramic Society*, *67*(4), 255–260. https://doi.org/10.1111/j.1151-2916.1984.tb18842.x

Fabrichnaya, O., & Seifert, H. (2001). The assessment of thermodynamic parameters in the Al2O3-Y2O3 system and phase relations in the Y-Al-O system. *… Journal of Metallurgy*.

Farkash, M., Shafry, N., & Brandon, D. (1994). SiC-whisker-reinforced ceramics with modulated microstructures. *Materials Science and Engineering: A*, *177*, 277–281.

Fused Silica | SiO2 Material Properties. (n.d.). Retrieved 16 December 2021, from http://www.accuratus.com/fused.html

Gahr, K.-H. Z. (1998). Wear by hard particles. *Tribology International*, *31*(10), 587–596. https://doi.org/10.1016/S0301-679X(98)00079-6

Gahr, K.-H. Zum. (1987). *Microstructure and Wear of Materials*. Elsevier.

Garnier, V., Fantozzi, G., Nguyen, D., Dubois, J., & Thollet, G. (2005). Influence of SiC whisker morphology and nature of SiC/Al2O3 interface on thermomechanical properties of SiC reinforced Al2O3 composites. *Journal of the European Ceramic Society*, *25*(15), 3485–3493. https://doi.org/10.1016/j.jeurceramsoc.2004.09.026

Garrett, J. C., Sigalas, I., Wolfrum, A. K., & Herrmann, M. (2015). Effect of cubic boron nitride grain size in the reinforcing of α-Sialon ceramics sintered via SPS. *Journal of the European Ceramic Society*, *35*(2), 451–462. https://doi.org/10.1016/j.jeurceramsoc.2014.09.036

Gowayed, Y., Pierce, J., Buchanan, D., Zawada, L., John, R., & Davidson, K. (2018). Effect of microstructural features and properties of constituents on the thermo-elastic properties of ceramic matrix composites. *Composites Part B: Engineering*, *135*, 155–165. https://doi.org/10.1016/j.compositesb.2017.10.009

Guillon, O., Gonzalez-Julian, J., Dargatz, B., Kessel, T., Schierning, G., Räthel, J., & Herrmann, M. (2014). Field-Assisted Sintering Technology/Spark Plasma Sintering: Mechanisms, Materials, and Technology Developments. *Advanced Engineering Materials*, *16*(7), 830–849. https://doi.org/10.1002/ADEM.201300409

Guo, S., Liu, R., Jiang, X., Zhang, H., Zhang, D., Wang, J., & Pan, F. (2017). Statistical Analysis on the Mechanical Properties of Magnesium Alloys. *Materials*, *10*(11), 1271. https://doi.org/10.3390/ma10111271

Gyekenyesi, J., & Bansal, N. (2000). *High temperature tensile properties of unidirectional Hi-Nicalon/Celsian composites in air*.

Harrer, W., Danzer, R., & Morrell, R. (2012). Influence of surface defects on the biaxial strength of a silicon nitride ceramic – Increase of strength by crack healing. *Journal of the European Ceramic Society*, *32*(1), 27–35. https://doi.org/10.1016/j.jeurceramsoc.2011.07.019

Harrer, W., Danzer, R., & Supancic, P. (2011). Influence of Surface Quality on the Biaxial Strength of Silicon Nitride Specimens. *Practical Metallography*, *48*(10), 515–526. https://doi.org/10.3139/147.110130

Hay, R. S. (1994). Kinetics and Deformation during the Reaction of Yttrium-Aluminum Perovskite and Alumina to Yttrium-Aluminum Garnet. *Journal of the American Ceramic Society*, *77*(6), 1473–1485. https://doi.org/10.1111/j.1151-2916.1994.tb09745.x

Hotta, M., & Goto, T. (2008). Densification and microstructure of Al2O3-cBN composites prepared by spark plasma sintering. *Journal of the Ceramic Society of Japan*, *116*(1354), 744–748. https://doi.org/10.2109/jcersj2.116.744

Kendall, K., Alford, N., & Tan, S. (1986). Influence of toughness on Weibull modulus of ceramic bending strength. *Journal of Materials*. http://journals.cambridge.org/abstract_S0884291400096461

Kolitsch, U., Seifert, H. J., Ludwig, T., & Aldinger, F. (1999). Phase equilibria and crystal chemistry in the Y2O3–Al2O3–SiO2 system. *Journal of Materials Research*, *14*(02), 447–455. https://doi.org/10.1557/JMR.1999.0064

Lawn, B. R., & Swain, M. V. (1975). Microfracture beneath point indentations in brittle solids. *Journal of Materials Science*, *10*(1), 113–122. https://doi.org/10.1007/BF00541038

Li, S.-B., Xiang, W.-H., Zhai, H.-X., & Zhou, Y. (2008). Formation of TiC hexagonal platelets and their growth mechanism. *Powder Technology*, *185*(1), 49–53. https://doi.org/10.1016/j.powtec.2007.09.018

Liu, X. L., Wen, D. H., Li, Z. J., Xiao, L., & Yan, F. G. (2002). Cutting temperature and tool wear of hard turning hardened bearing steel. *Journal of Materials Processing Technology*, *129*(1–3), 200–206. https://doi.org/10.1016/S0924-0136(02)00651-9

Lundberg, R., Nyberg, B., Williander, K., Persson, M., & Carlsson, R. (1987). Processing of whisker-reinforced ceramics. *Composites*, *18*(2), 125–127. https://doi.org/10.1016/0010-4361(87)90491-5

Material: Titanium Carbide (TiC), Bulk. (n.d.). Retrieved 16 December 2021, from https://memsnet.org/material/titaniumcarbideticbulk/?keywords=titanium

Microstructure and Wear of Materials. (1987a). In *Tribology Series* (Vol. 10). Elsevier. https://doi.org/10.1016/S0167-8922(08)70722-3

Microstructure and Wear of Materials. (1987b). In *Tribology Series* (Vol. 10). Elsevier. https://doi.org/10.1016/S0167-8922(08)70724-7

Mitchell, M. R., Link, R. E., Quinn, G. D., Sparenberg, B. T., Koshy, P., Ives, L. K., Jahanmir, S., & Arola, D. D. (2009). Flexural Strength of Ceramic and Glass Rods. *Journal of Testing and Evaluation*, *37*(3), 101649. https://doi.org/10.1520/JTE101649

Neher, R., Herrmann, M., Brandt, K., Jaenicke-Roessler, K., Pan, Z., Fabrichnaya, O., & Seifert, H. J. (2011). Liquid phase formation in the system SiC, Al2O3, Y2O3. *Journal of the European Ceramic Society*, *31*(1–2), 175–181. https://doi.org/10.1016/j.jeurceramsoc.2010.09.002

Petrovic, J., Milewski, J., Rohr, D., & Gac, F. (1985). Tensile mechanical properties of SiC whiskers. *Journal of Materials Science*, *20*, 1167–1177.

Property of Silicon Carbide (SiC). (n.d.). Retrieved 16 December 2021, from http://qualitymaterial.net/news_list85.html

Quinn, G. D. (2016). *NIST Recommended Practice Guide Fractography of Ceramics and Glasses*. National Institute of Standards and Technology. https://doi.org/10.6028/NIST.SP.960-16e2

Radhika, N., Ramprasad, R., & Nivethan, S. (2018). Experimental Investigation on Adhesive Wear Behavior of Al–Si6Cu/Ni Coated SiC Composite Under Unlubricated Condition. *Transactions of the Indian Institute of Metals*, *71*(5), 1073–1082. https://doi.org/10.1007/s12666-017-1242-3

Raju, C., & Verma, S. (1997). SiC whiskers from rice hulls: Formation, purification, and characterisation. *British Ceramic Transactions*.

Rigney, D. A. (2003). *Sliding Wear of Metals*.

Samsonov, G., & Sergeev, N. (1971). Sintered titanium carbide hard alloys. *… Powder Metallurgy and …*, *9*(9), 714–716.

Sedriks, A. J., & Mulhearn, T. O. (1964). The effect of work-hardening on the mechanics of cutting in simulated abrasive processes. *Wear*, *7*(5), 451–459. https://doi.org/10.1016/0043-1648(64)90137-1

Seshadri, S. G., Srinivasan, M., & Keeler, K. M. (2008). Numerical Computation of the Toughening Increments Due to Crack Deflection in Particulate Composites. In *11th Annual Conference on Composites and Advanced Ceramic Materials: Ceramic Engineering and Science Proceedings* (pp. 671–684). John Wiley & Sons, Inc. https://doi.org/10.1002/9780470320402.ch23

Shahedi Asl, M., Ahmadi, Z., Sabahi Namini, A., Babapoor, A., & Motallebzadeh, A. (2019). Spark plasma sintering of TiC–SiCw ceramics. *Ceramics International*, *45*(16), 19808–19821. https://doi.org/10.1016/j.ceramint.2019.06.236

Shen, Z., Johnsson, M., Zhao, Z., & Nygren, M. (2002). Spark Plasma Sintering of Alumina. *Journal of the American Ceramic Society*, *85*(8), 1921–1927. https://doi.org/10.1111/j.1151-2916.2002.tb00381.x

Sorrell, C. A. (2001). *Low-cost synthesis and consolidation of titanium carbide*. Industrial Materials for the Future. http://www.nrel.gov/docs/fy01osti/28245.pdf

Tabor, D. (2000). *The Hardness of Metals*. OUP Oxford.

Titanium Carbide / TiC Chemical, mechanical, physical and environmental properties of materials. (n.d.). Retrieved 9 April 2014, from http://www.matbase.com/material-categories/ceramics-and-glasses/crystalline/technical/carbides/material-properties-of-titanium-carbide-tic.html#properties

Wei, G. C., & Becher, P. F. (1984). Improvements in Mechanical Properties in SiC by the Addition of TiC Particles. *Journal of the American Ceramic Society*, *67*(8), 571–574. https://doi.org/10.1111/j.1151-2916.1984.tb19174.x

Weisstein, E. W. (n.d.). *Spherical Cap*. Wolfram Research, Inc. Retrieved 28 February 2019, from http://mathworld.wolfram.com/SphericalCap.html

Will, G., Nover, G., & von der Gönna, J. (2000). New Experimental Results on the Phase Diagram of Boron Nitride. *Journal of Solid State Chemistry*, *154*(1), 280–285. https://doi.org/10.1006/JSSC.2000.8850

Xu, Y., Cheng, L., Zhang, L., Yin, H., & Yin, X. (2001). Mechanical properties of 3D fiber reinforced C/SiC composites. *Materials Science and Engineering: A*, *300*(1–2), 196–202. https://doi.org/10.1016/S0921-5093(00)01533-1

Ye, F., Hou, Z., Zhang, H., Liu, L., & Zhou, Y. (2010). Spark plasma sintering of cBN/β-SiAlON composites. *Materials Science and Engineering: A*, *527*(18–19), 4723–4726. https://doi.org/10.1016/j.msea.2010.04.034

Yeheskel, O., & Tevet, O. (1999). Elastic moduli of transparent yttria. *Journal of the American Ceramic Society*, *82*(1), 136–144. https://doi.org/10.1111/J.1151-2916.1999.TB01733.X

Yu, R., & Zhang, X. (2007). Elastic constants and tensile properties of Al2OC by density functional calculations. *PHYSICAL REVIEW B ….*

Zhang, J., Tu, R., & Goto, T. (2014). Cubic boron nitride-containing ceramic matrix composites for cutting tools. *Advances in Ceramic Matrix Composites*, 570–586. https://doi.org/10.1533/9780857098825.3.570

Zhao, Y., & Wang, M. (2009). Effect of sintering temperature on the structure and properties of polycrystalline cubic boron nitride prepared by SPS. *Journal of Materials Processing Technology*, *209*(1), 355–359. https://doi.org/10.1016/j.jmatprotec.2008.02.005

APPENDICES

Appendix A – Theoretical Density calculations

Table 1: Theoretical densities of TiC mixes with Al_2O_3 and Y_2O_3

95wt% TiC	**Wt.%**	**Mass (g)**	**Density (g/cm³)**	**Volume (cm³)**	**Vol.%**
TiC	95	95	4.93	19.27	94.08
Al_2O_3	4	4	3.95	1.01	4.94
Y_2O_3	1	1	5.01	0.20	0.97%
Total	**1.00**	**100**	**4.88**	**20.48**	**100.00**
90wt% TiC	**Wt.%**	**Mass (g)**	**Density (g/cm³)**	**Volume (cm³)**	**Vol.%**
TiC	90	90	4.93	18.26	88.28
Al_2O_3	8	8	3.95	2.03	9.79
Y_2O_3	2	2	5.01	0.40	1.93
Total	**1.00**	**100**	**4.84**	**20.68**	**100.00**
85wt% TiC	**Wt.%**	**Mass (g)**	**Density (g/cm³)**	**Volume (cm³)**	**Vol.%**
TiC	85	85	4.93	17.24	82.58
Al_2O_3	12	12	3.95	3.04	14.55
Y_2O_3	3	3	5.01	0.60	2.87
Total	**1.00**	**100**	**4.79**	**20.88**	**100.00**
80wt% TiC	**Wt.%**	**Mass (g)**	**Density (g/cm³)**	**Volume (cm³)**	**Vol.%**
TiC	80	80	4.93	16.23	76.99
Al_2O_3	16	16	3.95	4.05	19.22
Y_2O_3	4	4	5.01	0.80	3.79%
Total	**1.00**	**100**	**4.74**	**21.08**	**100.00**

Table 2: Theoretical densities of TiC mixes with the addition of Al_2O_3, Y_2O_3 and SiO_2

90wt% TiC (+SiO_2)	Wt.%	Mass (g)	Density (g/cm^3)	Volume (cm^3)	Vol.%
TiC	90.0	90	4.93	18.26	87.0
Al_2O_3	2.5	2.5	3.95	0.63	3.0
Y_2O_3	4.0	4	5.01	0.80	4.0
SiO_2	3.5	3.5	2.65	1.32	6.0
Total	**100.0**	**100**	**4.76**	**21.01**	**100.0**
85wt% TiC (+SiO_2)	**Wt.%**	**Mass (g)**	**Density (g/cm^3)**	**Volume (cm^3)**	**Vol.%**
TiC	85.0	85	4.93	17.24	81.0
Al_2O_3	4.0	3.75	3.95	0.95	4.0
Y_2O_3	6.0	6	5.01	1.20	6.0
SiO_2	5.0	5.25	2.65	1.98	9.0
Total	**100.0**	**100**	**4.68**	**21.37**	**100.0**

Appendix B – SPS sintering parameters for TiC mixes without SiO_2

SPS at 1450°C, 50MPa and 10 min holding time.

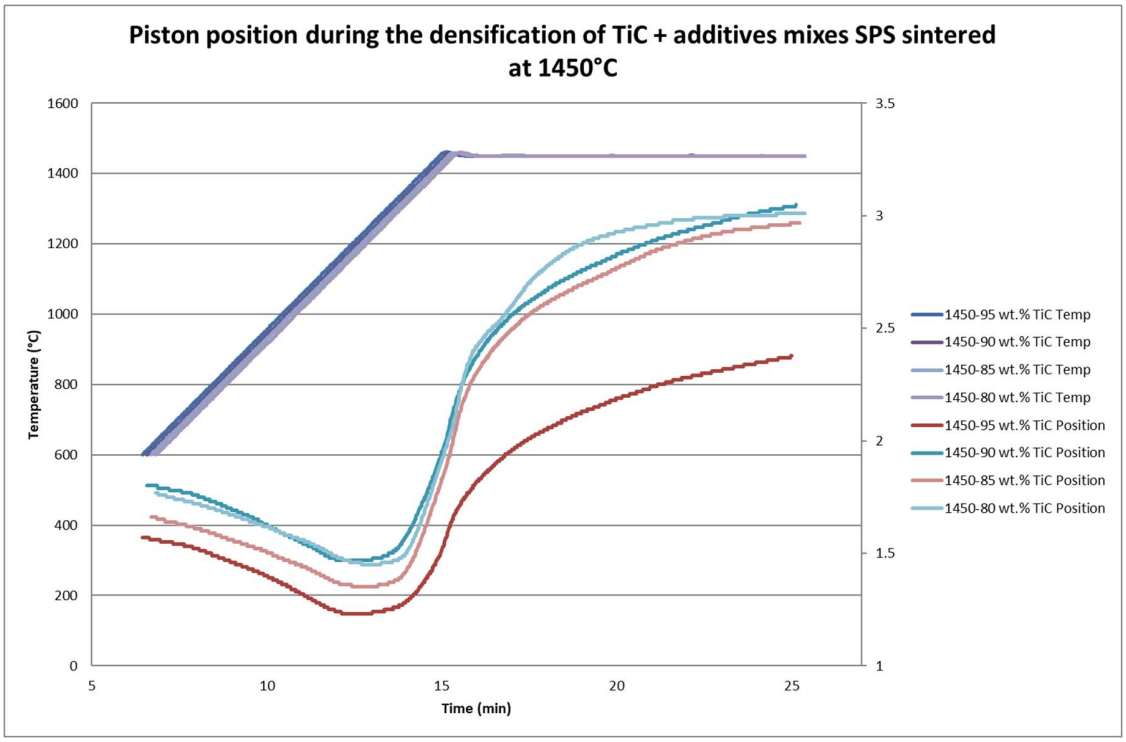


Figure 1 a) Piston position

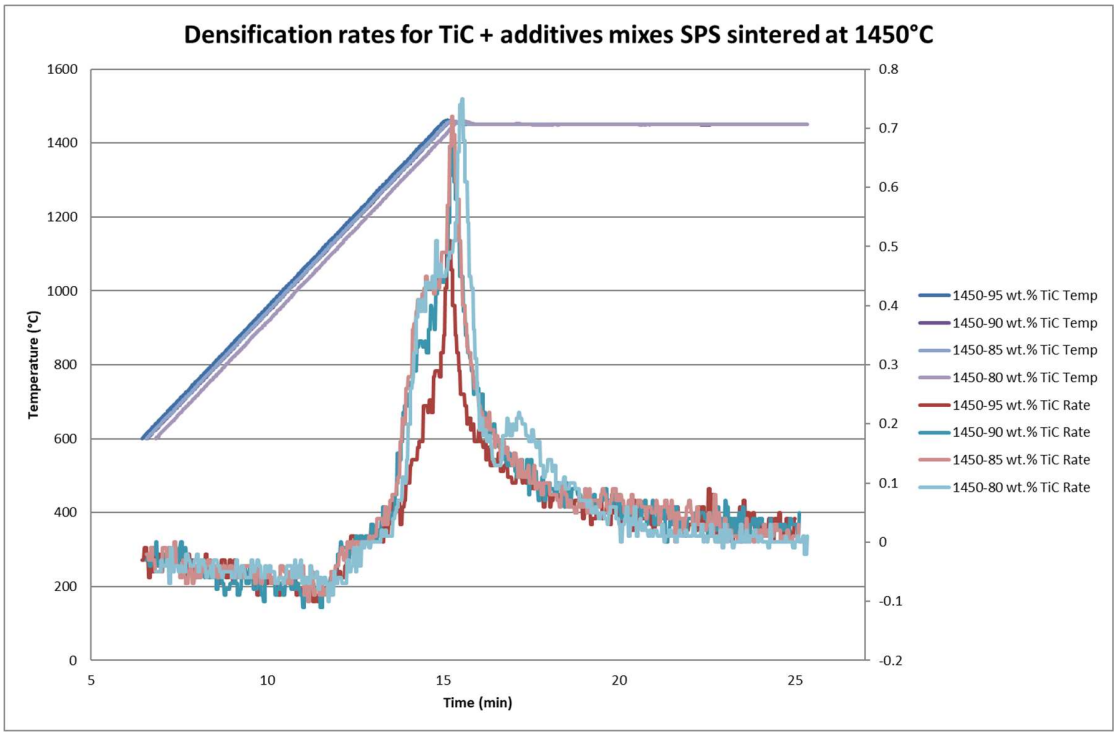


Figure 1 b) Densification rate

SPS at 1550°C, 50MPa and 10 min holding time.

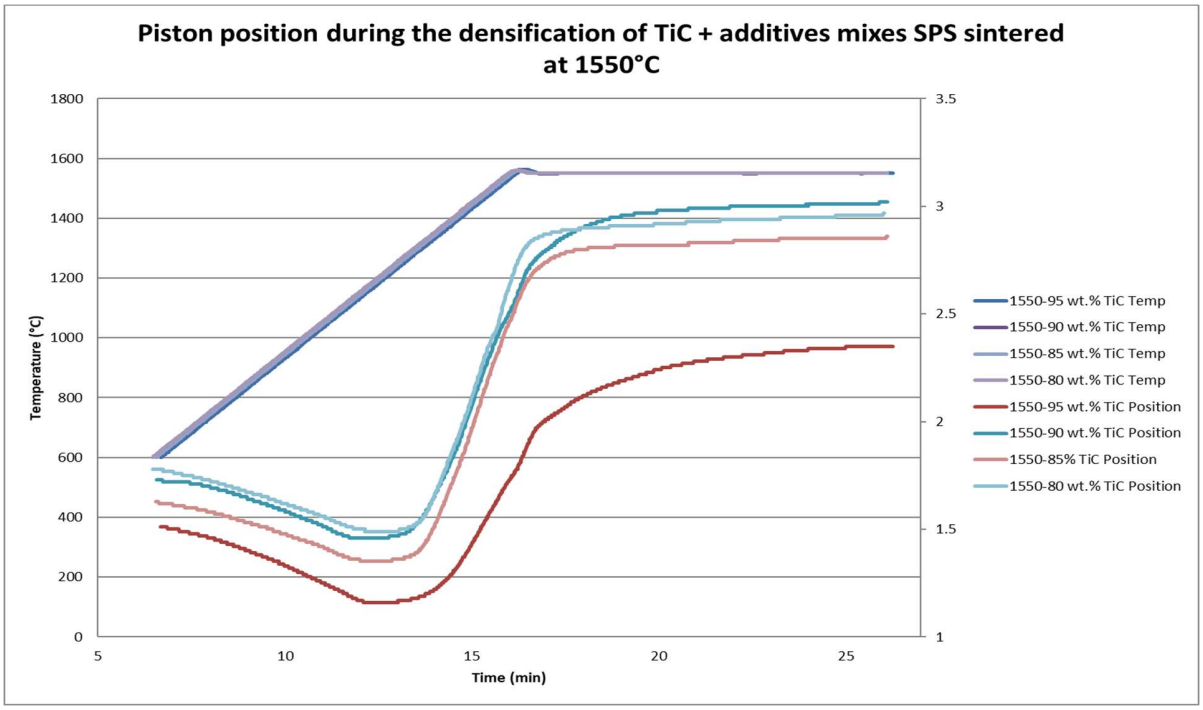


Figure 2 a) Piston position

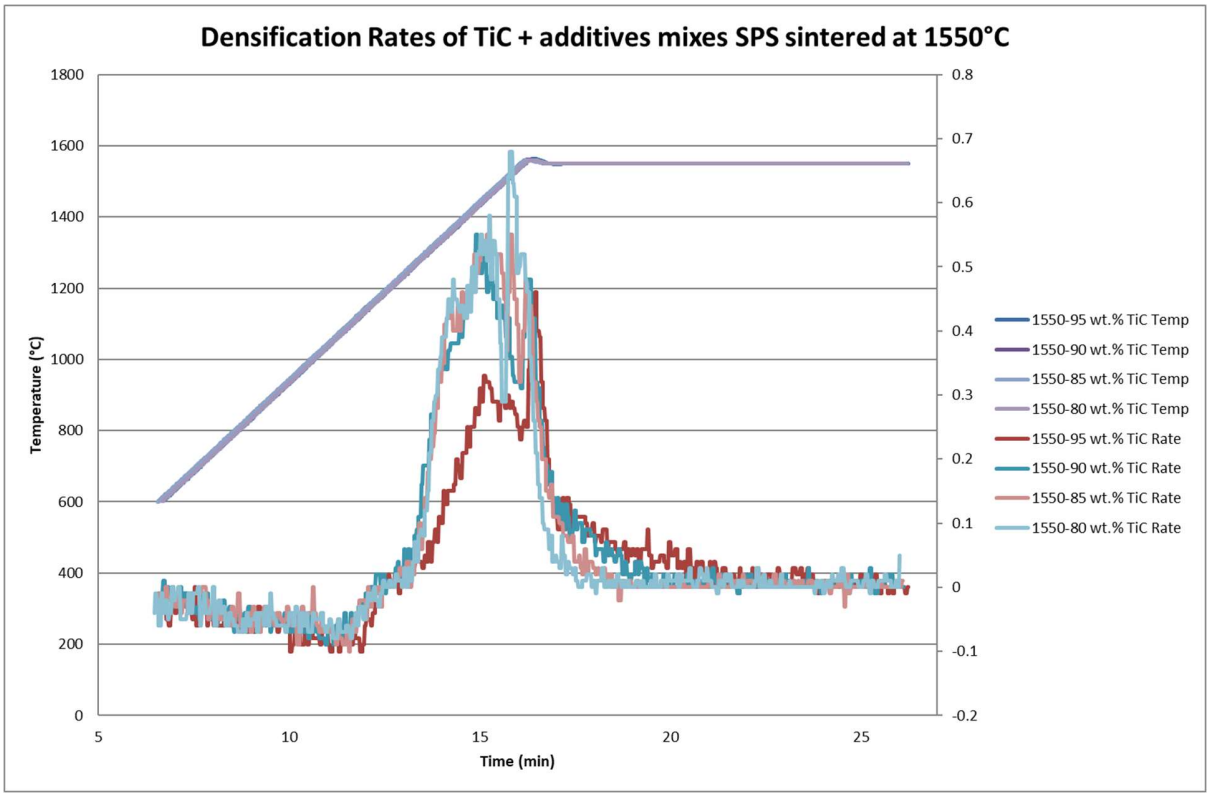


Figure 2 b) Densification rate

SPS at 1650°C, 50MPa and 10 min holding time.

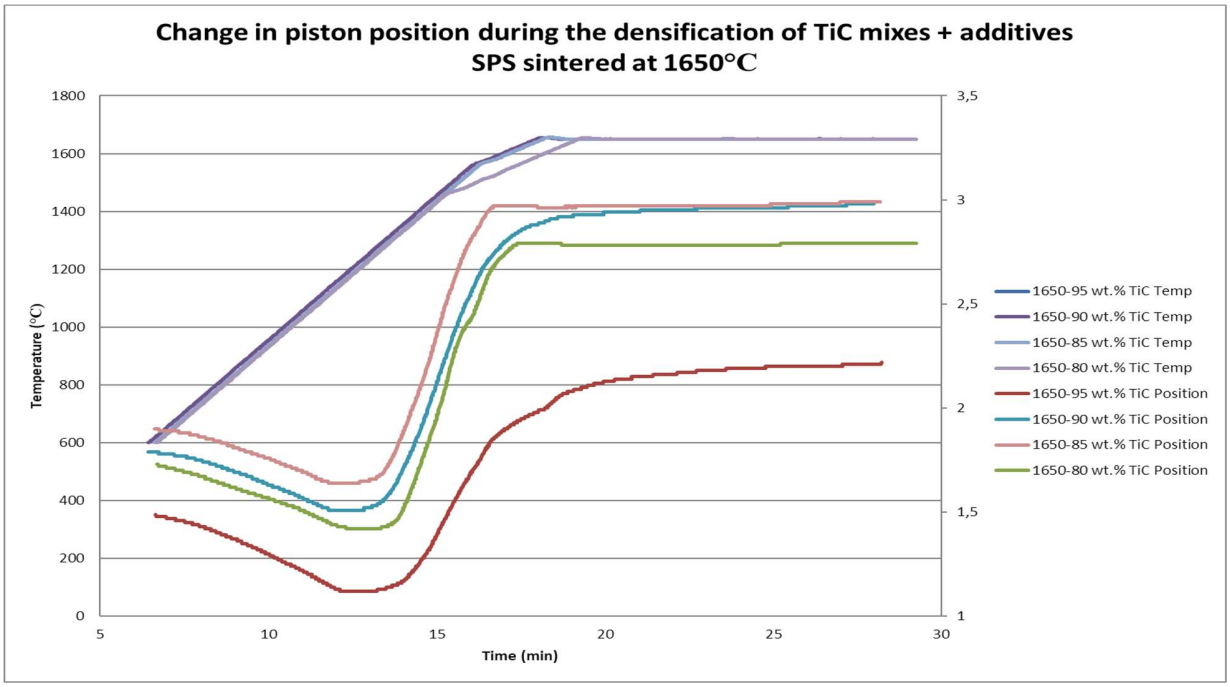


Figure 3 a) Piston position

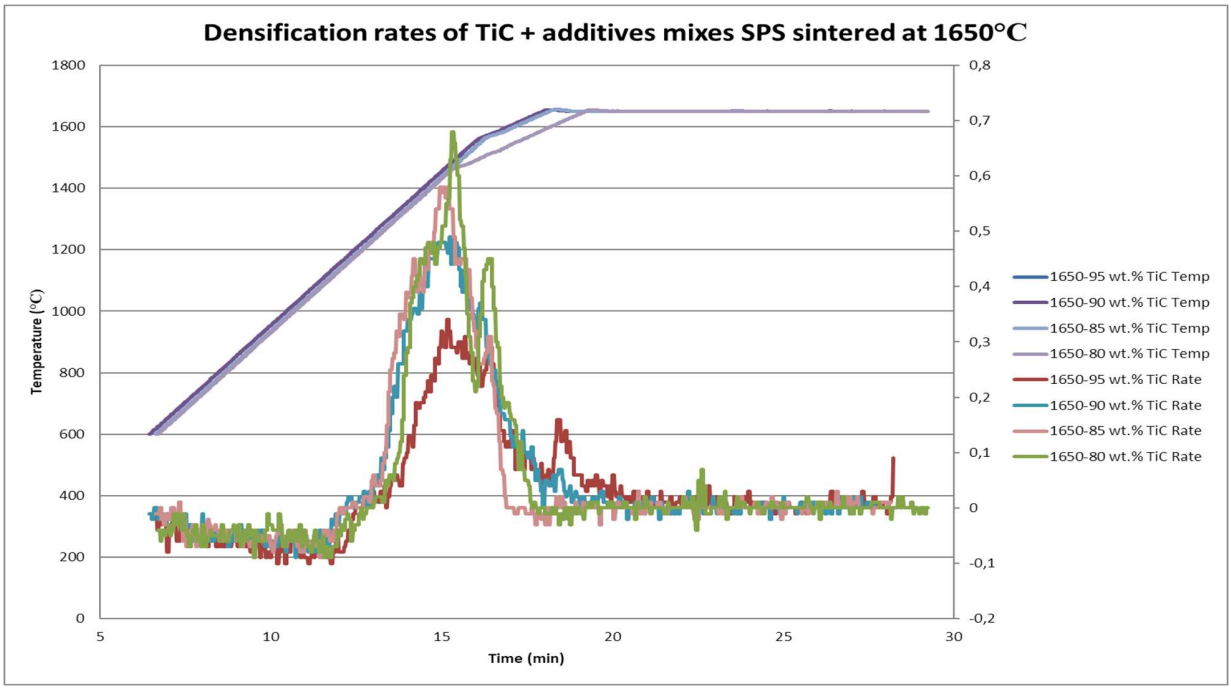


Figure 3 b) Densification rate

Appendix C – Preliminary Densification results of Sintered TiC mixes with Al_2O_3 and Y_2O_3

Preliminary Densification results of Sintered TiC mixes with Al_2O_3 and Y_2O_3 calculated via the Archimedes' Method. Values are the average values of 3 samples and the % values include the standard deviation.

Table 1: Average density measurements for samples of TiC mixes with Al_2O_3 and Y_2O_3 sintered at 1450°C

Mix name	Suspended Mass (g)	Wet Mass (g)	Dry Mass (g)	% of Full density	% of open porosity
95% TiC	3.18	4.14	4.09	86.30±0.28	5.92±0.19
90% TiC	3.96	5.03	5.02	96.73±0.04	1.07±0.09
85% TiC	4.09	5.19	5.18	98.58±0.49	0.75±0.14
80% TiC	4.03	5.12	5.11	99.26±0.06	0.03±0.10

Table 2: Average density measurements for samples of TiC mixes with Al_2O_3 and Y_2O_3 sintered at 1550°C

Mix name	Suspended Mass (g)	Wet Mass (g)	Dry Mass (g)	% of Full density	% of open porosity
95% TiC	3.12	3.93	3.93	99.05±0.22	0.33±0.07
90% TiC	4.05	5.11	5.11	98.95±0.04	0.56±0.08
85% TiC	4.10	5.19	5.19	99.10±0.04	0.43±0.03
80% TiC	3.98	5.05	5.04	99.08±0.33	0.70±0.16

Table 3: Average density measurements for samples of TiC mixes with Al_2O_3 and Y_2O_3 sintered at 1650°C

Mix name	Suspended Mass (g)	Wet Mass (g)	Dry Mass (g)	% of Full density	% of open porosity
95% TiC	3.04	3.83	3.83	99.21±0.24	0.26±0.10
90% TiC	4.07	5.13	5.13	99.13±0.11	0.28±0.07
85% TiC	4.05	5.13	5.13	99.14±0.05	0.36±0.01
80% TiC	4.15	5.27	5.26	98.75±0.11	0.47±0.09

Appendix D – SPS sintering parameters for TiC mixes with the addition of SiO_2

85 wt. % TiC, 70MPa and 10 min holding time

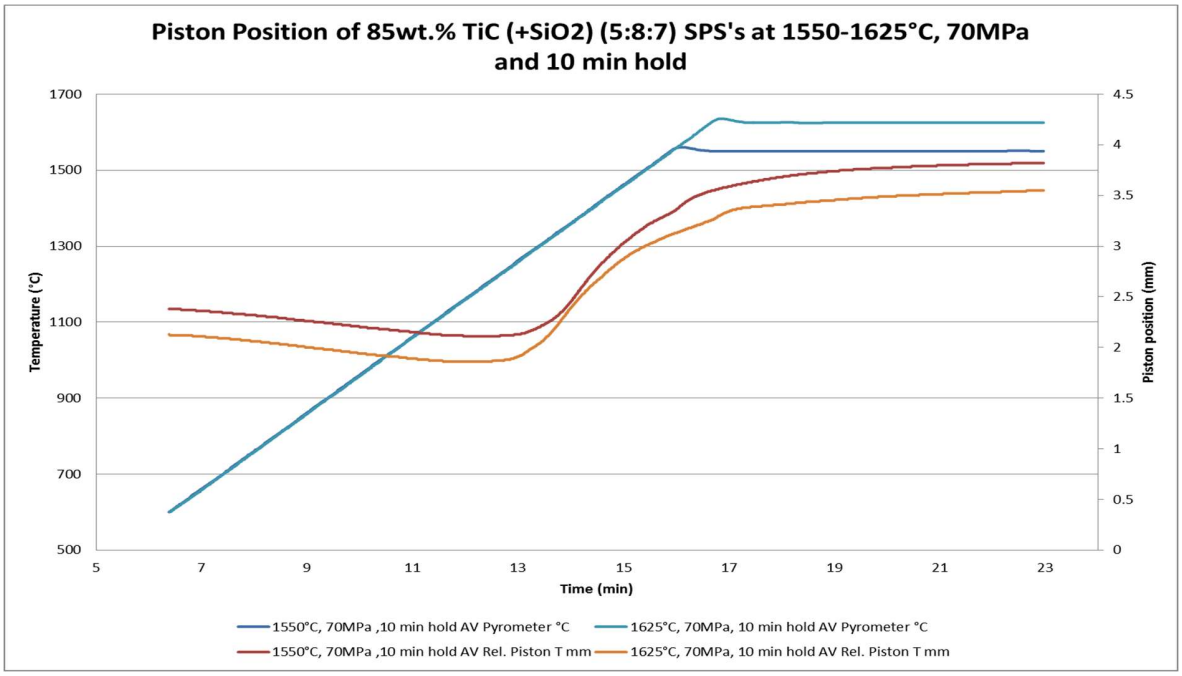


Figure 1 a) Piston position

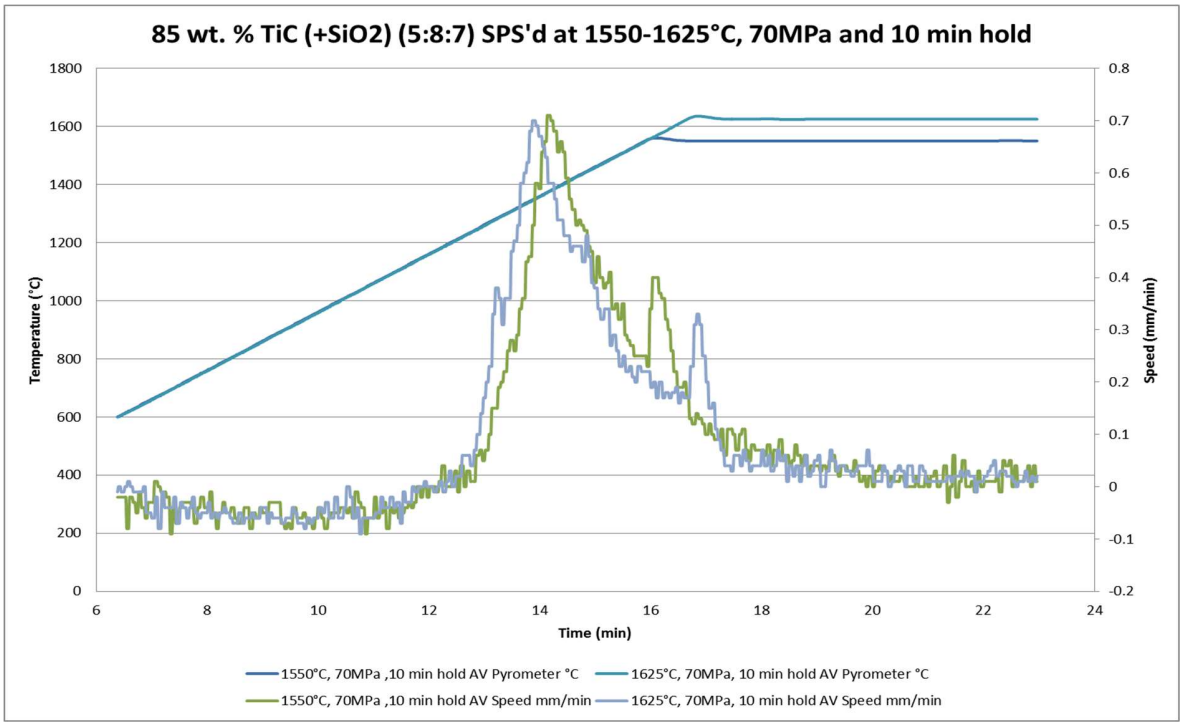


Figure 1 b) Densification rate

90 wt. % TiC, 70MPa and 10 min holding time

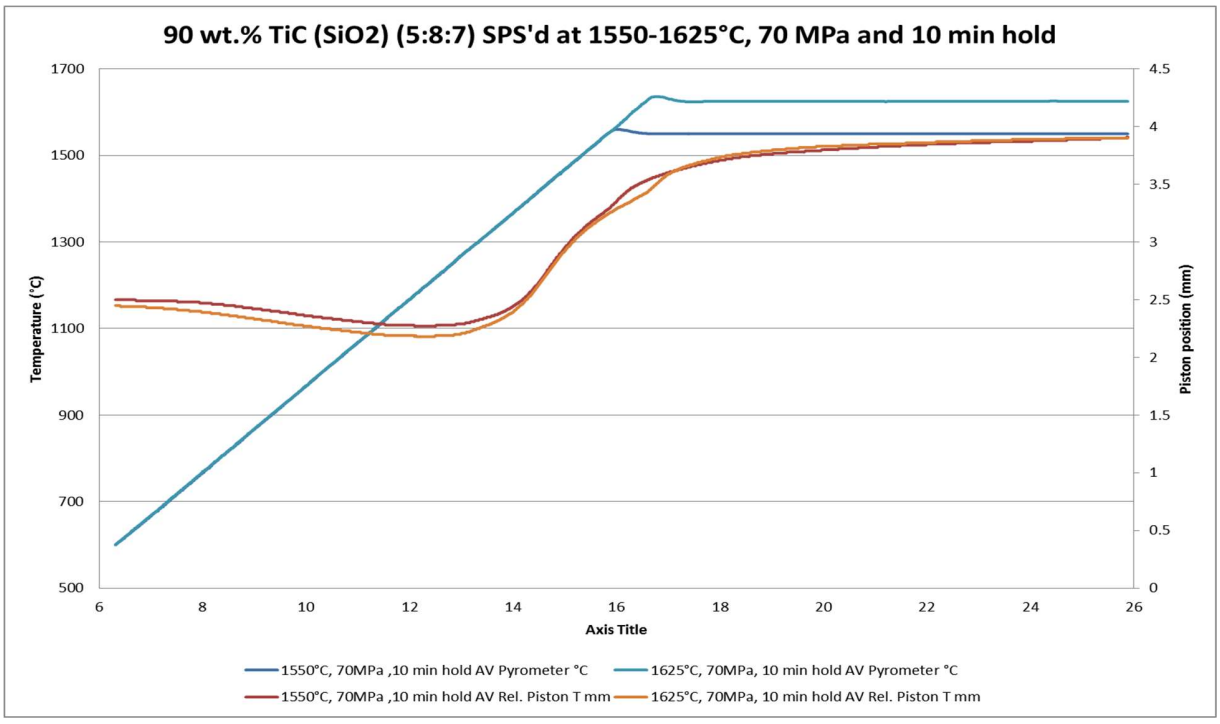


Figure 2 a) Piston position

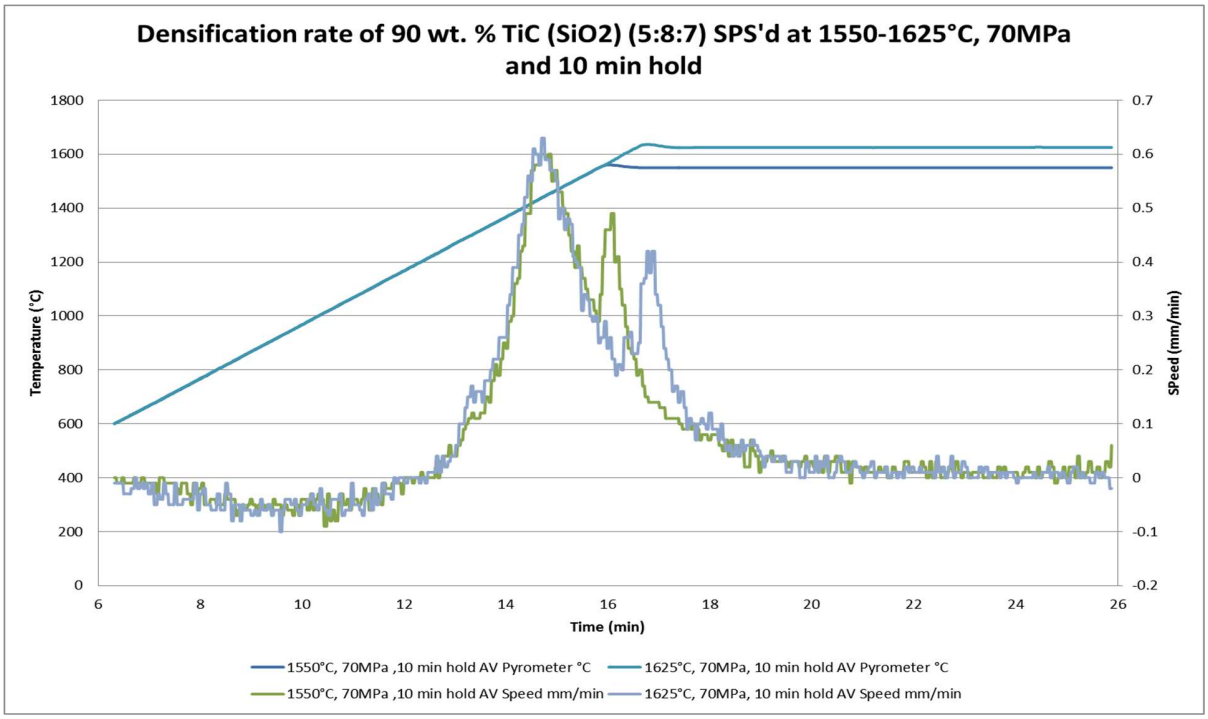


Figure 2 b) Densification rate

Appendix E - SPS sintering parameters for TiC mixes using TiC powder without SiO_2 and with the addition of cBN

TiC matrix mixes are SPS sintered at a rate of 100°C/min to a temperature of 1450- 1625°C, 50-70MPa and 10 min hold at the selected temperature.

85 wt. % TiC + 7 vol. % cBN: 1450, 1550, 1575 and 1625°C, 70 MPa and 10 min hold

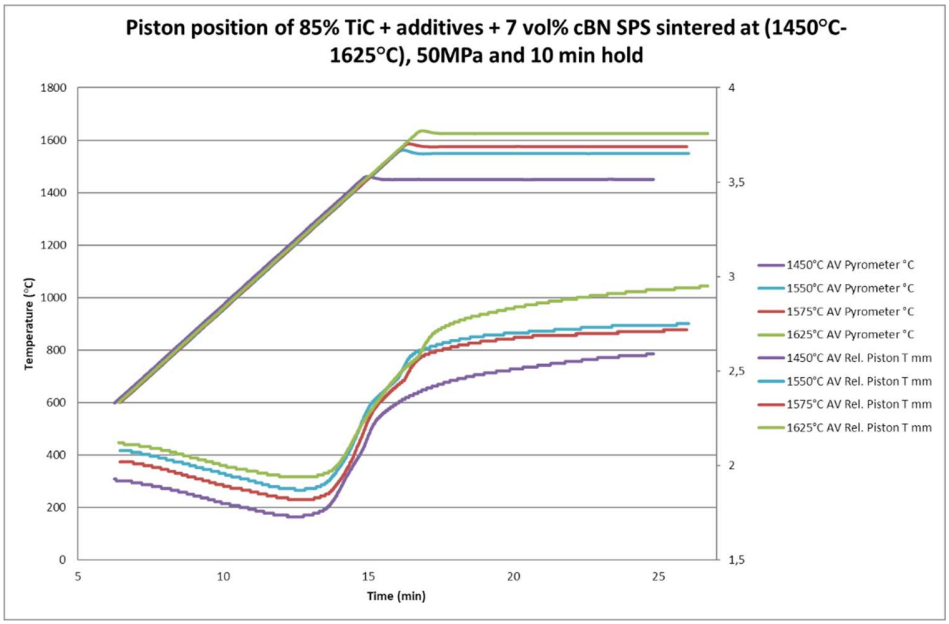


Figure 1 a) Temperature profile, piston position

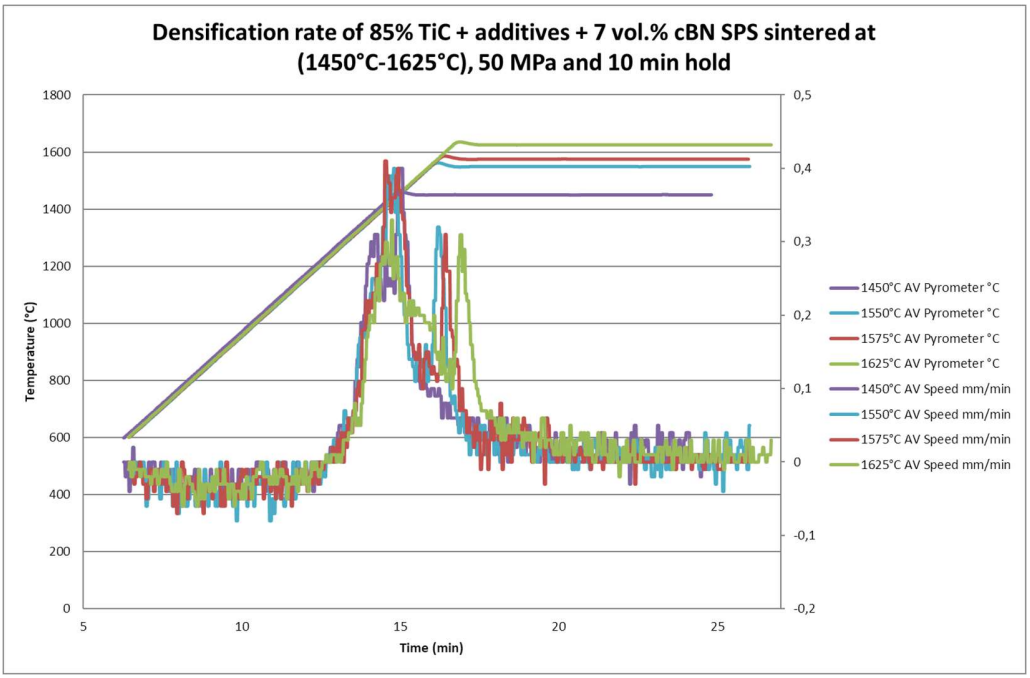


Figure 1 b) Densification rate

90 wt. % TiC + 7 vol. % cBN: 1450, 1550, 1575 and 1625°C, 70 MPa and 10 min hold

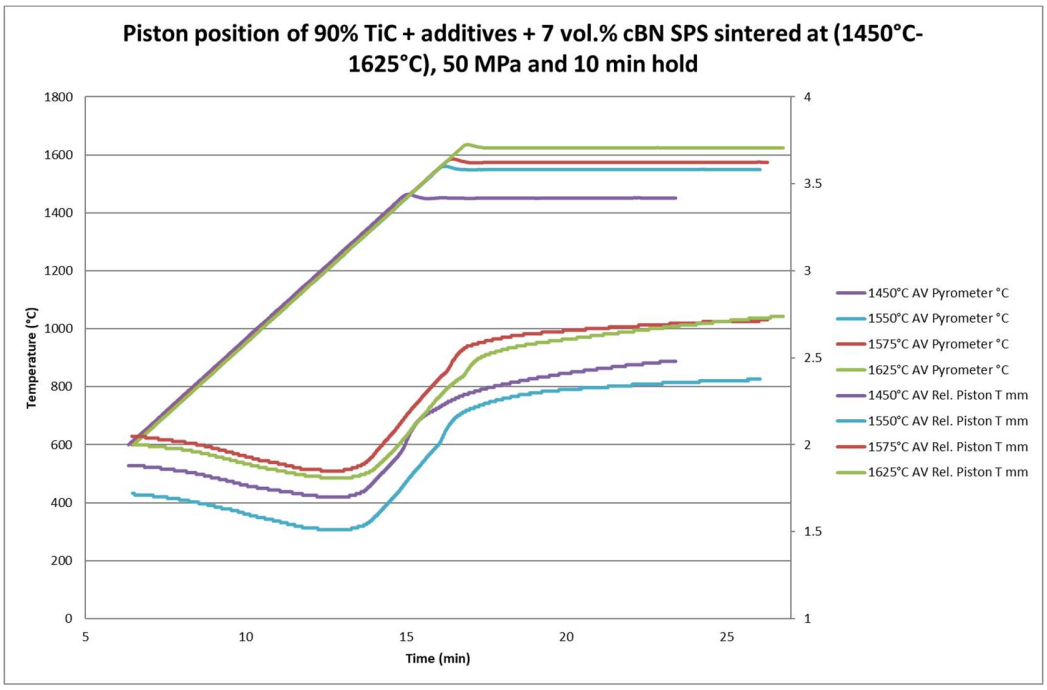


Figure 2 a) Piston position

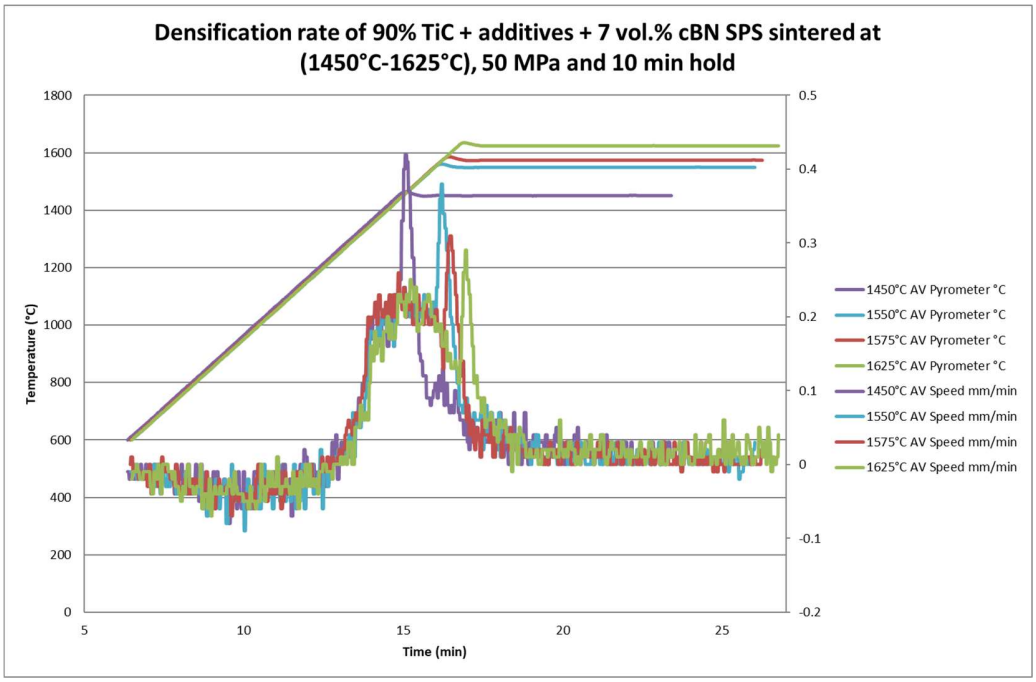


Figure 2 b) Densification rate

Appendix F - SPS sintering parameters for TiC mixes using TiC powder with SiO_2 and with the addition of cBN

TiC matrix mixes are SPS sintered at a rate of 100°C/min to a temperature of 1450- 1625°C, 70MPa and 5/10 min hold at the selected temperature. The graphs below show examples of the densification curves produced during the SPS sintering process.

85 wt. % TiC (SiO_2) + 10 vol. % cBN: 1575, 70 MPa and 5-10 min hold

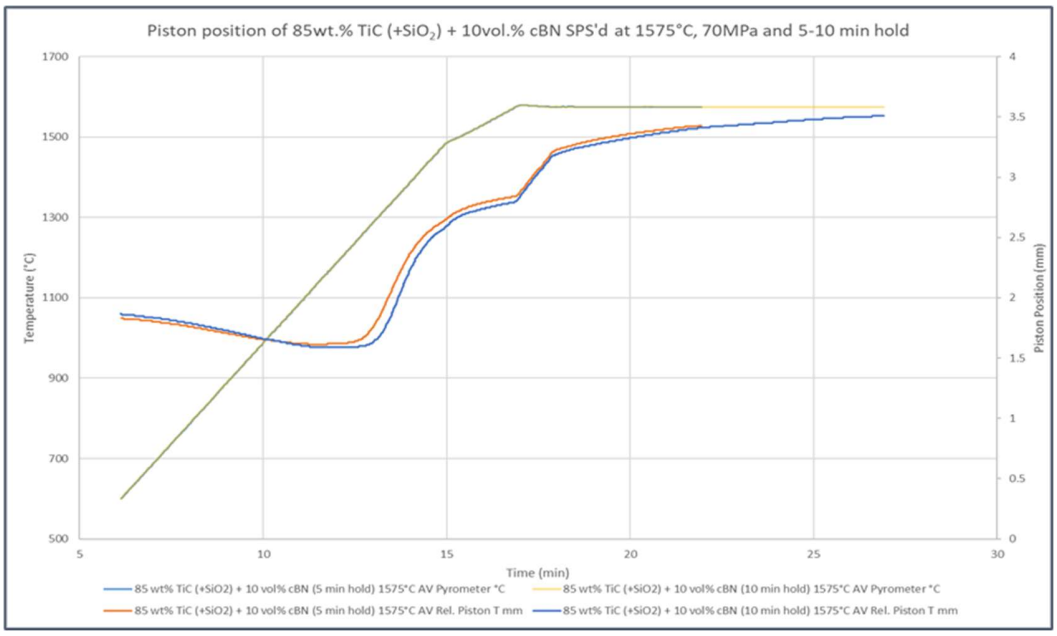


Figure 1 a) Piston position

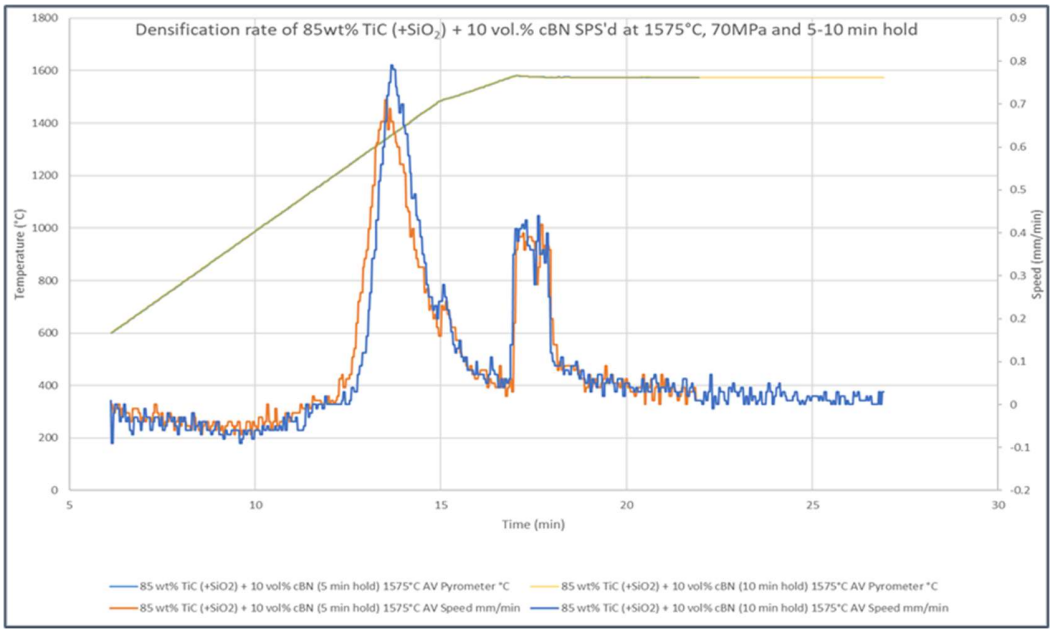


Figure 1 b) Densification rate

Appendix G -SPS sintering parameters for TiC mixes using 2µm TiC powder without SiO_2 and with the addition of SiC whiskers

TiC matrix mixes are SPS sintered at a rate of 100°C/min to a temperature of 1450- 1625°C, 70MPa and 10 min hold at the selected temperature. The graphs below show examples of the densification curves produced during the SPS sintering process.

90 wt. % TiC + 20 vol. % SiC_w: 1550 and 1625°C, 70 MPa and 10 min hold

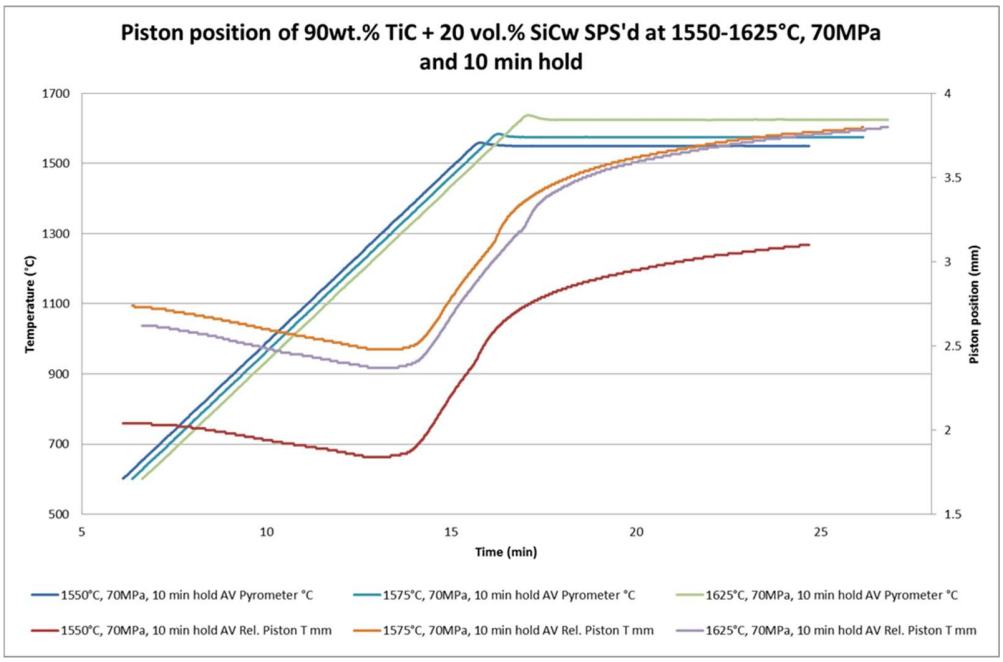


Figure 1 a) Piston position

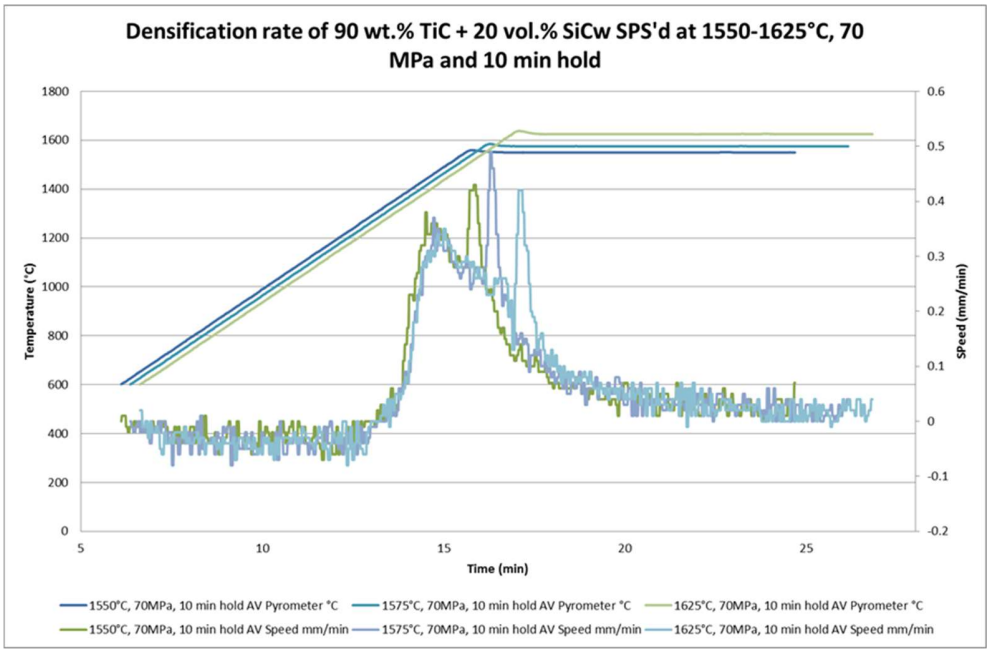


Figure 1 b) Densification rate

Appendix H -SPS sintering parameters for TiC mixes using TiC powder with SiO_2 and with the addition of SiC whiskers

TiC matrix mixes are SPS sintered at a rate of 100°C/min to a temperature of 1450- 1625°C, 70MPa and 10 min hold at the selected temperature. The graphs below show examples of the densification curves produced during the SPS sintering process.

90 wt. % TiC (+SiO_2) + 20 vol. % SiC_w: 1550 and 1625°C, 70 MPa and 10 min hold

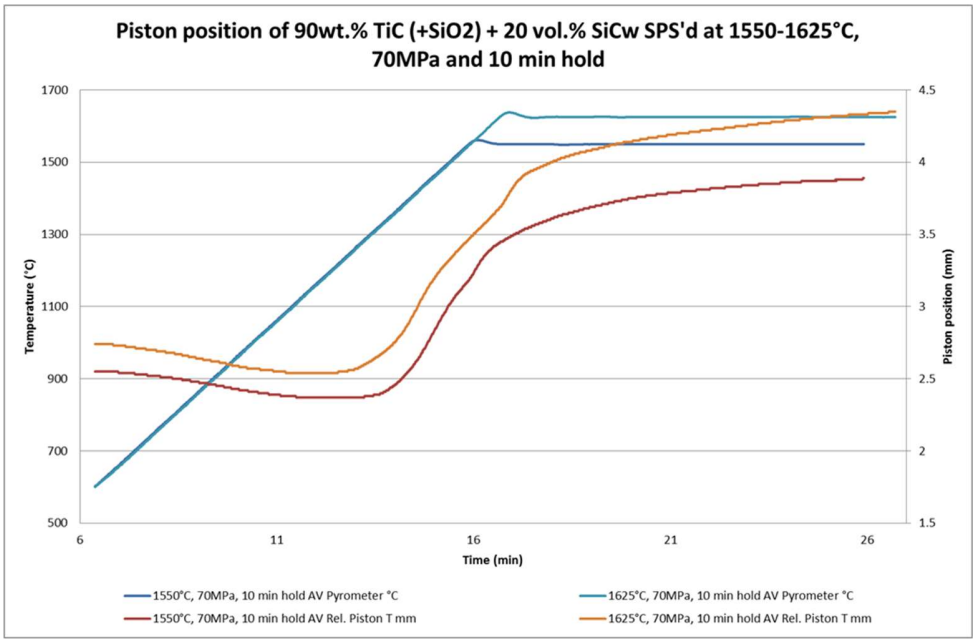


Figure 1 a) Piston position

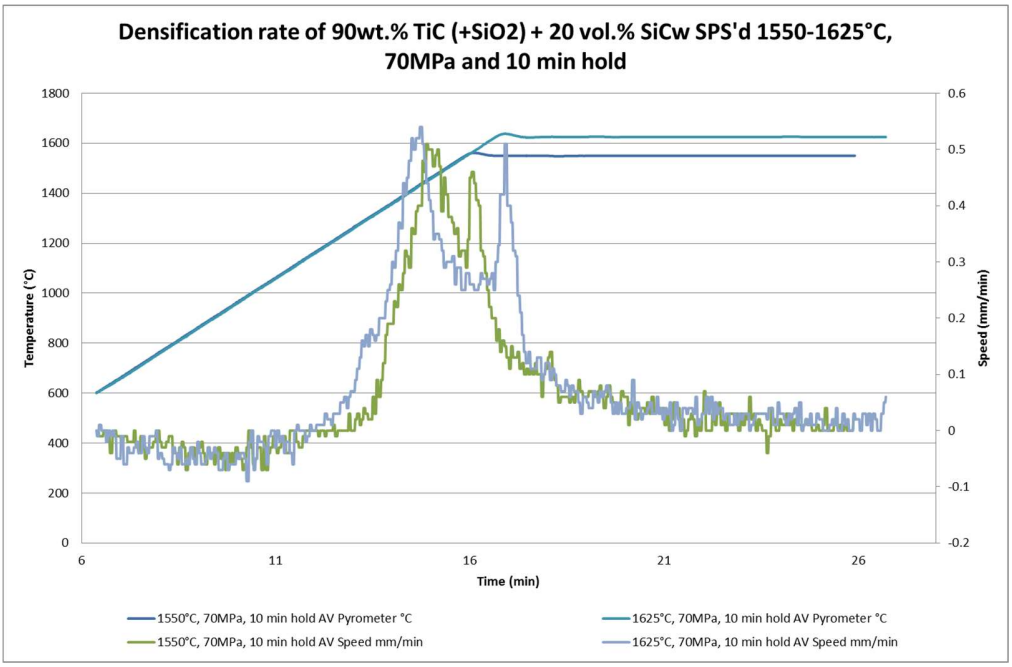


Figure 1 b) Densification rate